Role of intimacy in bifunctional catalysts for the production of light olefins : application to the Ox-Zeo process

Christophe Coudercy

N°d'ordre NNT : 2022LYSE1082

THESE de DOCTORAT DE L'UNIVERSITE DE LYON

opérée au sein de

l'Université Claude Bernard Lyon 1

Ecole Doctorale N° ED206

Ecole Doctorale de Chimie de Lyon

Spécialité de doctorat : **Chimie**

Discipline : **Catalyse**

Soutenue publiquement le 08/06/2022, par :

Christophe COUDERCY

Role of intimacy in bifunctional catalysts for the production of light olefins : application to the Ox-Zeo process

---

Devant le jury composé de :

MAUGE, Françoise	Directrice de recherche	Université de CAEN Normandie	Présidente
KHODAKOV, Andrei	Directeur de recherche CNRS	Université de Lille	Rapporteur
MAUGE, Françoise	Directrice de recherche	Université de CAEN Normandie	Rapporteuse
GIL, Sonia	Maître de Conférences	UCBL	Examinatrice
LORIDANT, Stéphane	Directeur de recherche CNRS	IRCELYON	Directeur de thèse
PAVEL, Afanasiev	Directeur de recherche CNRS	IRCELYON	Co-directeur de thèse
FONGARLAND, Pascal	Professeur	UCBL	Invité
LE VALANT, Anthony	Maître de Conférences	Université de Poitiers	Invité

Table of content

Introduction

Light (C2-C4) olefins are important chemicals for polymers production. They are produced at 200 Mt/year via Steam Cracking and Fluid Catalytic Cracking processes. However, change in feedstock leads to the development of a gap between production and demand especially for propylene, known as the propylene gap. To fill this gap, dedicated processes to produce light olefins are developed such as Fischer-Tropsch to Olefins (FTO) and Methanol To Olefins (MTO). Those processes are mostly using syngas feed, that comes from fossil resources and biomass. However, Fischer Tropsch which is one of the leading processes for the conversion of syngas suffers from limitation of selectivity to light olefins and MTO from fast deactivation of catalysts, requiring frequent regeneration.

Since 2016, the Ox-Zeo process has been emerging as a very selective and stable process for light olefins production. It combines a hydrogenating oxide and an acidic zeotype catalysts. The most important limitation is the high selectivity to CO_2 (30-45%) and current research mainly focuses on this bottleneck by optimising the oxide and zeotype properties. However, the bifunctionality of Ox-Zeo catalyst introduces an additional parameter which is the intimacy, rarely addressed in the literature.

The role intimacy in bifunctional catalysis has been investigated for many years especially for hydrocracking/hydroisomerisation. The study of the effect of the distance between the hydrogenating metallic and the acidic functions led to definition of the Weisz criterion. This criterion can be expressed as ‘the closer the better’ for catalytic properties. However, recent studies evidenced that selectivity to hydroisomerisation products is higher when the two functions are separated by few hundreds of nanometers, leading to definition of the nanoscale intimacy. Recent progress paves the way to study the role of intimacy from the atomic to the millimeter scale for various catalytic systems and bifunctional reactions.

This PhD work has been performed in the framework of the ANR INCH project (2017-2022) gathering teams of IRCELYON, IC2MP and LGPC. The main objectives of this project were to better

understand the effect on selectivity of the density of contact and of the distance between two functions of a bifunctional catalyst. It dealts with the direct conversion of syngas to lower olefins by the Syngas-to Dimethyl ether-To Olefins (SDTO) and Ox-Zeo processes over (Cu/ZnO, SAPO-34) and (Oxide, SAPO-34) bifunctional catalysts, respectively. This PhD work was focused on the MnOx-SAPO-34 catalytic system for the Ox-Zeo process.

In **Chapter 1,** we review the light olefins market and the industrial production routes and explain the reasons for the development of on-purpose processes for the production of light olefins. Then, main studies and concept on the role of intimacy in bifunctional catalysis are presented. Finally, the literature related to the Ox-Zeo process is reviewed, leading us to define the objective of the thesis.

Chapter 2 describes the techniques and the methods used to characterize the oxide and zeotype catalysts applied in this work. We also provide a description of the catalytic testing apparatus, and of the analytical method for catalytic measurements.

Chapter 3 provides the results on the Ox-Zeo process obtained with reference catalyst. In particular, the impact of various reaction parameters on the catalytic properties and kinetic parameters are determined. It relies on preparation and a detailed characterization before and after reaction of MnO_x reference samples and four SAPO-34 materials. Then, an *in situ* DRIFT study is presented to identify the key reaction intermediate and better draw the reaction scheme which was a pre-requisite before undertaking the study of the role of intimacy.

Chapter 4 investigates the role of intimacy for the Ox-Zeo process by varying the distance between the two functions from the millimeter to the atomic scale. For that purpose, various bed arrangements, the effect of dilution were studied. For the nanometric intimacy, $MnO_x@SiO_2$ core shell structures with modulated shell thickness were prepared by different methods, characterized and some of them were selected to be tested in combination with SAPO-34 samples. Finally, suspension mixtures and ionic exchanged SAPO-34 were prepared, characterized and evaluated.

Chapter 1 : Literature survey

1) Light Olefins market

1.1) Definition and usage

Light olefins are defined as the group of C2-C4 alkenes containing linear and branched isomers. These molecules are produced in large quantities over the world by petroleum industries. For example, the ethylene market represents 208 Mt per year and the propylene one 110 Mt per year.[1–7] They are usually produced by Fluid Catalytic Cracking (FCC) and Steam Cracking (SC) plants[1–7] which represent more than 50% of the production. Light olefins are widely used for the production of polymers such as polyethylene or polypropylene, as shown in **Figure 1**, for which the demand is constantly increasing. Aside from the polymers synthesis, light olefins are also used for fine chemistry industry and polymer precursor synthesis. Therefore, light olefins are important molecules and efforts have to be done to fill the gap between production and demand.

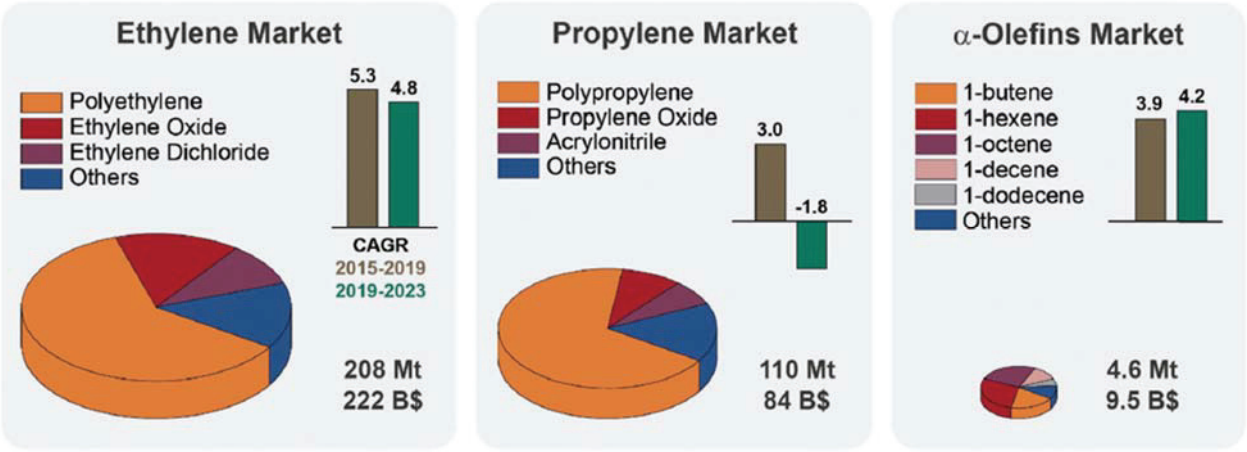

Figure 1: Light olefin market and usage in 2019; reproduced from Monai and coll.[1]

1.1.1) Propylene gap

During the past decade, the worldwide propylene demand has increased rapidly due to population growth and life standards improvement and it is expected to grow from 110 Mt in 2019 to 165 Mt by 2030.[1,3,6] However, the production through the traditional processes did not increase

as fast leading to the so-called 'propylene gap' as shown in **Figure 2**. Indeed, the SC feedstock has moved from naphtha and liquid petroleum to ethane decreasing drastically the selectivity toward propylene.[1,3,6–8] The propylene gap has provoked an increase in the propylene price. Therefore, on-purpose processes such as propane dehydrogenation and methanol to olefins (MTO) have become more economically viable whereas others are under development.[3,5,8] In the on-purpose processes, the Methanol to olefin (MTO) also aims directly at reducing the CO_2 emissions of propylene production by using feedstock such as syngas or CO_2.[3,5–9]

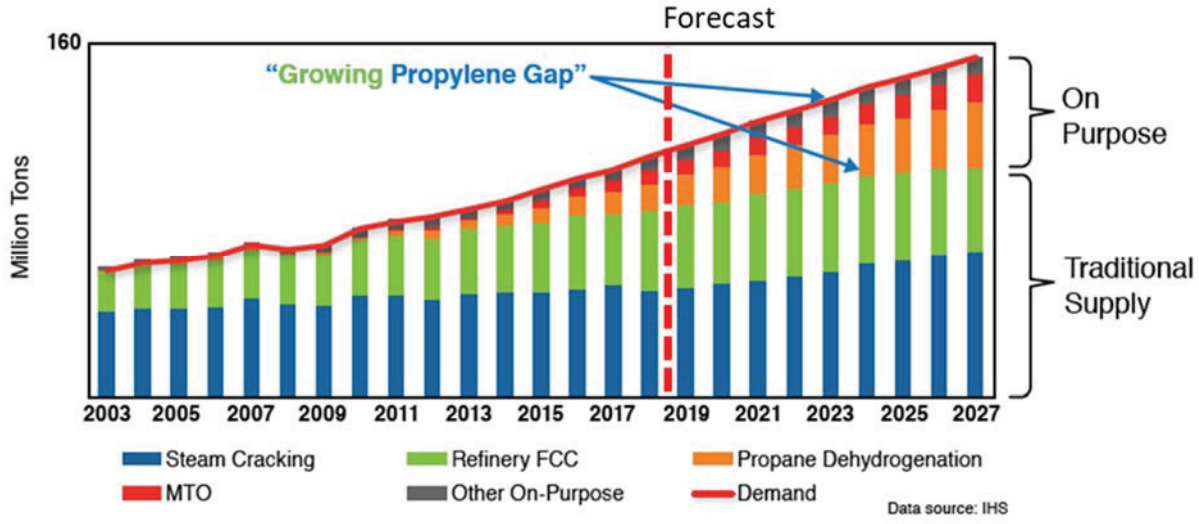

Figure 2: Demand evolution and propylene production from different processes. Reproduced from Marsh and coll[10].

1.2) Production

1.2.1) Traditional production

a) Steam Cracking

Steam Cracking (SC) is a traditional process that produces ethylene from naphtha or ethane. SC works at high temperature, above 650 °C, and leads to high energy consumption due to the endothermicity of the reaction shown in **Figure 3** using ethane as a feedstock.[7,11,12]

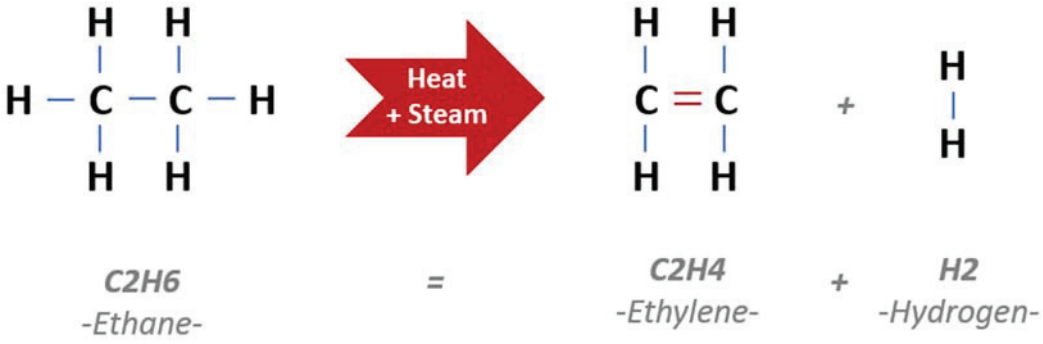

Figure 3: The main reaction occurring in an ethane-fed steam cracker.

Before the shale gas development, the SC units used naphtha as feedstock leading to selectivity toward ethylene, propylene and butylene of 30, 13 and 5%, respectively.[12] However, the SC feedstock has shifted toward ethane in the last decade due to the shale gas availability. It has led to a decrease in the propylene and butylene production. Nowadays, the propylene and butane selectivity in the ethane SC units are around 2 and 1%, respectively while the ethylene selectivity is ca 80%.[12] This shift in selectivity is one of the reasons for the propylene gap. However, SC remains one of the main sources for propylene production due to the high ethylene demand.[7,12]

b) Fluid Catalytic Cracking refinery

Fluid catalytic cracking (FCC) is a process designed to produce gasoline for energy, transport and other usages. In this process using an acid catalyst, naphtha is upgraded to gasoline at high temperature, above 500 °C.[7,13] The catalyst used in the conventional FCC units is the zeotype Y or UZY.[7,13] In those conditions, light olefins are produced as byproducts. Nowadays, modifications of the reaction conditions and of the catalyst are undertaken to shift the product selectivity toward light olefins.[13–17]

1.2.2) On purpose production

To fulfill the demand, new processes dedicated to the production of light olefins have been developed. Some of them already exist at the industrial scale while others are still at the research stage.

a) Industrial scale processes

i) Paraffin dehydrogenation

Paraffin dehydrogenation processes have been developed to convert selectively light paraffins, mainly propane, into olefins. Propane originating from the shale gas is mainly used as a feedstock for propylene production. The dehydrogenation reaction is carried out above 600 °C, and at low partial pressure of propane over a Pt or Cr - based catalyst, leading to high selectivity toward propylene (> 90 %).[3,6,7,18] However the propane partial pressure is limited and cannot be increased to maintain the selectivity leading to decreased productivity.

Current research focuses on improving the process energy efficiency and productivity. Catalyst properties are usually tuned to allow the use of higher propane partial pressure.[18]

Among several emerging processes such as K-PRO^{TM} FCDh or ADHO,[19] for propane dehydrogenation, Oleflex and Catofin have been industrialised and most widely applied: they produced 0.5 Mt of propylene in 2014, volume which is expected to raise due to the construction of novel plants.[3,19]

ii) Methanol to olefins

Methanol To Olefins (MTO) process produces olefins by dehydration of methanol. Syngas for the methanol synthesis can originate from either methane reforming, coal or biomass gasification.[20,21] Syngas is converted to methanol over a Cu-ZnO/Al_2O_3 catalyst. The MTO reaction takes place above 400 °C on an acidic catalyst such as the mainly industrially used zeotype H-SAPO-34. At full methanol conversion, a selectivity to C2-C4 olefins above 90% can be obtained.[20,22–24] Many other zeotypes with various pore opening sizes can be used to tune the chain length of the produced olefins driving selectivity toward higher olefins or aromatics.

Current studies focus on improving the MTO catalysts by reducing coke deposition. For that purpose, the zeotype crystal size has been reduced to the nanometer scale and metals were added as dopants improving both the selectivity and the catalyst lifetime.[23–26]

One of the first plants was built in Belgium in 2009 using the UOP/hydro MTO process. This first commercial unit was able to convert 10 tons of methanol per day.[20] Later on, many commercial

scale pilot were built in china.[25] The most notorious one being the DMTO-I in Baotou which converted 1.8 Mt of methanol in 2010.[25]

iii) Methane oxidative coupling

Oxidative coupling of methane is a process that produces ethylene from methane and oxygen using a mixed oxide catalyst at high temperature, typically 800 °C. Research on this process have been pushed by the wide availability of natural gas and the development of shale gas extraction.[27]

It faces a great challenge due to the low selectivity toward ethylene. The O_2 partial pressure has to be precisely monitored to avoid over-oxidation into either CO or CO_2. Nowadays research , from a chemistry stand point, focuses mainly on improving the selectivity toward ethylene.[27–30] Right now, one of the few viable oxidative coupling plants is a pilot demonstrated by Siluria Technologies in 2012 which achieves an ethylene production of 350 ton per year.[30]

iv) Ethanol dehydration

The dehydration of ethanol is a process that converts ethanol into ethylene through dehydration over an acidic catalyst. The reaction usually takes place above 300 °C and is very selective toward ethylene. This process developed due to the large availability of bioethanol in certain region is considered as a local solution to ethylene shortage. However, a low ethanol price is needed to have an economically viable process.[6] Low ethanol price in Brazil allowed for the construction of an industrial plant by Braskem in 2010 which produces 200 kt/year of ethylene from sugar cane based ethanol.[31] The biggest plant have been developed by Axens in collaboration with Total and produces up-to 400 kt/year of ethylene.[31]

b) Research- scale processes

i) Oxidative dehydrogenation of alkanes

Oxidative dehydrogenation (ODH) is a process that has been developed to address some of paraffin dehydrogenation limitations. ODH is achieved by reaction of O_2 with paraffins leading to formation of olefins and water molecules (instead of H_2 formation that occurs in conventional dehydrogenation). Exothermicity of this reaction allows to decrease the reaction temperature and the global energy cost of the process.[32,33]

The active phases commonly used for the ODH catalysts are V, Ni and Mo based oxides, often doped with halogens to mitigate the hydrogenation capacity of the catalyst.[33]

Nowadays such process is not used at an industrial scale due to two major factors. First, the selectivity reached with ODH are equivalent to those of the actual dehydrogenation process and do not justify to invest in a new system. Second, with halogenated catalysts, metallic reactors suffer from corrosion and must be replaced frequently.[32]

ii) Fischer Tropsch Synthesis

Fischer Tropsch Synthesis (FTS) is a process that allows to convert directly syngas into a large variety of hydrocarbons. It has been discovered by Franz Fischer and Hans Tropsch in 1922 and the first industrial plant was built in Germany in 1936. In the 1940s, this process was mainly used to produce liquid fuel from coal in Germany. Nowadays light olefins, alcohols or acetone can be also produced from syngas by this process.[34–38] The syngas feed can be produced either by natural gas reforming or coal or biomass gasification.[39,40] Furthermore, even considering its high investment cost FTS has become attractive due to the increase in the crude petroleum price.

The FTS reaction is a surface polymerization reaction that produces hydrocarbons with size distributed along the Anderson–Schulz–Flory (ASF) distribution as shown in **Figure 4**. Two main elements are used in the FTS catalysts: Fe and Co. Fe is usually promoted by alkali metals and used with low H_2/CO ratio.[34,35] On the other hand, Co is promoted with alkali earth metals and fed with high H_2/CO reactant flow.[34,35,37,38,41]

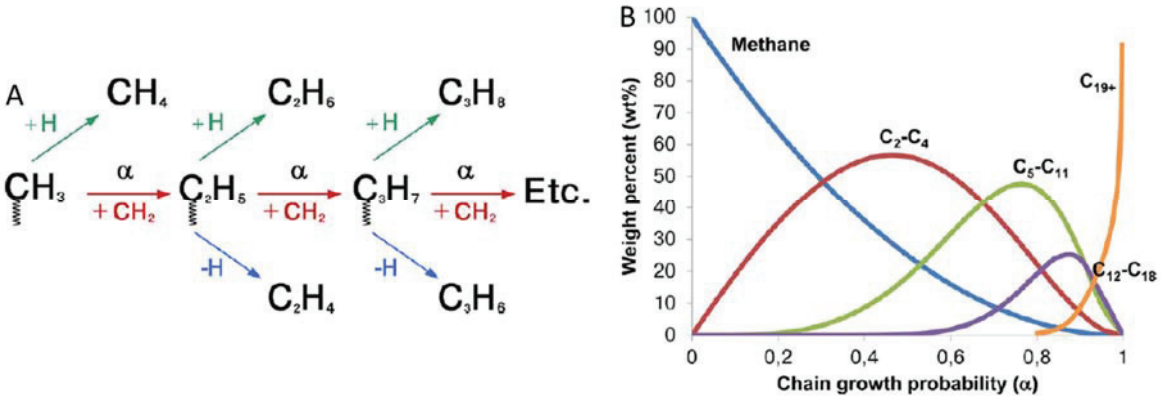

Figure 4: A) Fischer-tropsch reaction mechanism B) Anderson-Schulz-Flory (ASF) model for the prediction of the product distribution, Reproduced from Ref.5.

The main challenge for the production of light olefins from FTS is to reduce the selectivity to methane at low chain growth.[36] A solution to this problem is the coupling of FTS catalyst with zeotype: reaction conditions are then chosen to favor a high chain growth probability on the FTS catalyst and the zeotype cracks the long olefins that are produced into light olefins.[35,36]

iii) Syngas to hydrocarbon

The syngas to hydrocarbon (STH, STO for olefins) process aims to convert syngas into hydrocarbons or light olefins in one reactor by mixing two catalysts. Usually, the catalyst is composed of a methanol synthesis catalyst coupled with an acidic catalyst to produce hydrocarbons. Such process is particularly interesting to produce light hydrocarbons because their selectivity is not limited by the ASF distribution.[40,42,43] The syngas used for this process can be produced from coal gasification, natural/shale gas reforming or biomass gasification.[39,40] The use of various zeotypes with different pore and cage sizes allows to change the length of the produced hydrocarbons.[43]

A first publication on STH can be found in 1985: Fujimoto and coll.[39] reported a CO conversion as high as 16.4% with selectivity toward hydrocarbons of 66% obtained with a mixture of Pd/SiO_2 as a methanol synthesis catalyst and H-ZSM-5 as C-C coupling agent at 350 °C and 2 bar. The main hydrocarbons produced were C2 and C3 paraffins. Later, other bifunctional systems were developed over the years by mixing the "best" catalyst for each function. Zhang and coll[44] reported that a CuZnO catalyst mixed with H-ZSM-5 gave a CO conversion as high as 71% and a selectivity toward hydrocarbons of 54% at 325 °C and 2 bar with a selectivity of 46 % toward CO_2. The main hydrocarbons produced were C2-C4 paraffins. Later, Chen and coll. [24] reported CO conversion of 60% with a selectivity toward hydrocarbons of 60% for $CuO\text{-}ZnO\text{-}Al_2O_3$ and SAPO-34 mixture at 400 °C and 3 bar. The main products were still C2-C4 paraffins.

In 2016, Jiao and coll. reported a selectivity to hydrocarbons of 50% at 16% of CO conversion with an olefin/paraffin ratio of 6.5 using a mixture of $ZnCrO_x$ and M-SAPO-34 (SAPO-34 containing mesoporosity).[45] This bifunctional catalyst was one of the first to produce C2-C4 olefins with high selectivity. Such bifunctional catalyst named Ox-Zeo catalyst paved the way for numerous works on a large variety of similar catalysts. Such process attracted great interest in China where coal is

used as a feedstock for syngas production, leading to the demonstration of a 1000 ton/year pilot plant.[46]

2) Intimacy in bifunctional catalysis

The development of new processes for the synthesis of important chemicals such as olefins led to the design of bifunctional processes. Those new processes often apply mixing two catalysts into one bed. This helps to reduce the number of synthesis steps by avoiding separation steps and transportation of chemicals leading to greener process with higher energy efficiency and reduced soil artificialization. As an example, a FTS catalyst can be mixed with a zeotype to shift the product distribution toward lighter olefin as explained in **part 1.2.2.b.ii**. Depending on the catalyst used for both steps, long hydrocarbons can be produced and cracked to produce light olefins, or isomerize them to produce valuable fuels.

The attractiveness of those new processes led to many studies on the influence of different parameters on the overall efficiency. In particular, a question arises about the degree of catalysts mixing. To collaborate in one reactor, two functions should use common reaction products and therefore to be close in space. However, the scale of this spatial proximity might vary strongly, from many centimeters (in a multi-bed reactor) to nanometers (in a co-supported catalyst). What is the optimal distance between the two functionalities depends on the reaction scheme, being often not clear. Therefore, the impact of the distance between the two functions on the catalytic properties should be studied. Such property was defined as the intimacy of a (bifunctional) catalyst. Nano intimacy is a recently coined term, related to the distance between different types of catalytic sites at the nano scale.[47] Application of “nano intimacy” term implies that the distance between the catalytic sites at the nanoscale affects the catalytic activity. Nano intimacy is a concept stemming from several assumptions and applicable to a limited number of catalytic processes. From the most general viewpoint, in order for nano intimacy to be a relevant concept, at least two conditions should be fulfilled, namely:

- Two or more types of catalytic sites should be present, i.e. bifunctional (or more complex) catalysts are only considered. As explained before the bifunctionality is generally considered when two or more reactions are combined into one to optimize the production

condition. Generally the reaction intermediate between the two function can be isolated.

- Diffusion limitations must exist in the system at some (nanoscopic) level. This condition can possibly be realized via two scenarios. Either, the transfer of “normal” stable intermediates between different types of sites should be hindered by diffusion or certain short-live (surface) intermediates should be important for the reaction rate (and/or for the catalyst deactivation).

Diffusion limitations between the two functions are obviously necessary for the distance to become an important parameter. Indeed, if all the catalytic sites are available to all the present reactants and intermediates in such manner that no external diffusion limitations exist, then kinetic regime is realized for all reaction steps. In this case the micro kinetic equations describing the system do not include diffusion pathways and the nano intimacy consideration does not make sense. In other words, it becomes unimportant, how fine is the mixture of catalysts: they both work in kinetic regime.

It follows from the above said that not a geometric distance between the sites (as measured, for example by microscopy), but a diffusion path must be considered as a measure of the “distance” for the nano intimacy discussion. It immediately follows further, that nano intimacy is not an absolute property of a (composite) catalyst but it should depend on the media diffusivity and by consequence on the conditions such as temperature and pressure. Thus, for a combination of a macroporous oxide and a microporous zeotype that have comparable geometric size, the most part of the diffusion path would obviously belong to zeotype. Moreover, this relative path in zeotype might be by orders of magnitude greater for a liquid media than for light gases. Therefore parameters of nano intimacy have no sense without a precise description of the reaction system and conditions.

There are several simple situations which can qualitatively illustrate the possible impact of nano intimacy: in a bifunctional catalyst two types of sites are present, A and B, where the sites A produce an intermediate for the sites B, whereas the sites B produce a desired target product. Then if the sites of type A and B are localized too far apart, the reaction does not proceed optimally. Note this is the simplest, but in some sense a trivial case of nano intimacy. There is just a maximal

distance to respect, “the closer the better”. On the practical side that means that the sites should be mixed as well as possible, to achieve the optimal performance. In other words, the activity curve as a function of distance between the sites is monotonously decreasing, but has a plateau at some (small enough) distances. The extent of this plateau corresponds to the nano intimacy criterion.

In these lines, the intimacy criterion has been first developed for hydrocracking catalysts that contain hydrogenating and acid functions. In the hydrocracking mechanism, first dehydrogenation reaction occurs on the metal sites to generate olefinic intermediates and then they migrate towards the acid sites where cracking occurs, (as well as isomerization and cycle opening) as represented in **Figure 5**.

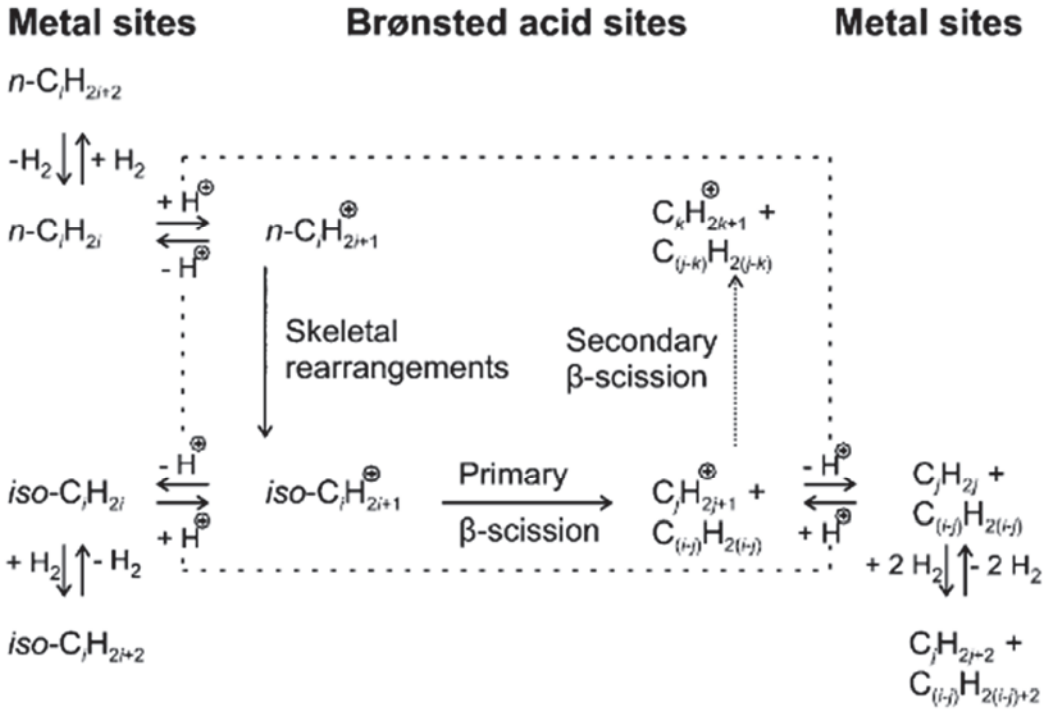

Figure 5: Mechanism of isomerization and hydrocracking of an n-alkane on a bifunctional catalyst comprising metal sites for dehydrogenation/hydrogenation and Brønsted acid site, Reproduced from Ref.[48].

Metal and acid sites should be sufficiently close to ensure that the diffusion of the olefinic intermediates does not impede the kinetics. Yet in 1962 Weisz[49] introduced the so-called “intimacy criterion”, defining a critical condition in a polystep reaction (note that no “nano” intimacy were

discussed at this time as Weisz mostly studied the micro-intimacy). This criterion was constructed by dividing the consumption rate by the diffusion rate of the intermediate.

$$\frac{Reaction\ rate}{Diffusion\ rate} = \frac{dN}{dt} * \frac{1}{[B_{eq}]} * \frac{R^2}{D} < 1$$

Where dN/dt is the reaction rate; [Beq] is the partial pressure for the intermediate species that provide connection between the different types of sites; R and D are respectively the distance to travel in a porous medium and the diffusion coefficient for this intermediate species.

This is a general condition from which "critical pressure", "critical diffusion coefficient" or "critical distance" could be derived ad hoc.[49] In those conditions, the diffusion of the intermediate is at least as fast as the consumption of such intermediate on the catalyst. Thus, it does not limit the apparent reaction rate.

Other parameters being fixed by the reaction system, "critical distance" for the hydrocracking reaction was introduced:

$$R^2 < 1.2 * 10^{-5} * \frac{P_0 D_0}{T} * \frac{dt}{dN}$$

Below this distance, the catalyst activity is not influenced by the diffusion of intermediates in the system studied by Weisz. For this type of catalysts a concept of "well-balanced" catalyst is commonly used, meaning that the catalyst contains enough dehydrogenating sites to achieve quasi equilibrium of olefins formation and fulfills the intimacy criterion.[50,51]

In the recent years however, the concept "closer the better" has been revisited. There are cases for which intimacy criterion is relaxed and the catalytic sites could be rather distant.[52]

Zečević and coll.[47] studied nano intimacy in the hydroconversion of paraffins with bifunctional catalysts, Pt/Al_2O_3-USY zeotype systems. They reported negative effect of closer distances between the two functions on the isomerization selectivity and attributed it to the long residence time of the molecules inside the zeotype pores, increasing the amount of undesirable cracking products. In agreement with this study, Samad and coll.[53] showed detrimental effect of atomic-

scale closeness between silica alumina, the acid function, and Pt functions in the n-heptane isomerization.

These studies suggest that less trivial effects of the nano intimacy exist, than a simple diffusion limitation. Conceptually, several general schemes could be conjectured that would give rise to a complex shape of activity vs. distance curve. For example, if a short-live intermediate is formed on sites A that could produce coke on the sites B and deactivate them (but this intermediate is not required for the target reaction), then too close distance between different sites would lead to a rapid coking of the catalyst as exposed in **Figure 6.1**. However, if the sites A and B are located too far, the performance decreases according to Weisz (cf. the first example) and as depicted in **Figure 6.2**. This case, if realized, should be more challenging for the practical design of catalysts, because an optimal distance between the sites should be then respected.

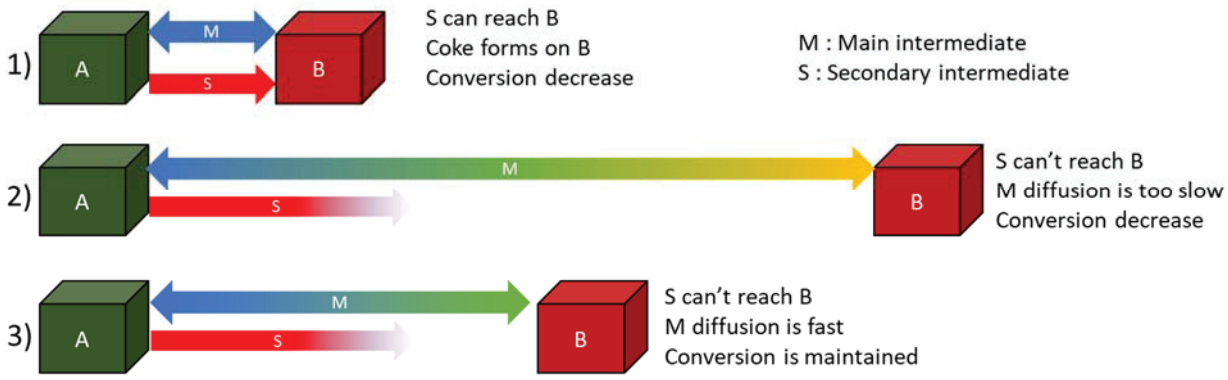

Figure 6: Schematic representation of an example case where a distance optimum can be observed.

2.1) Design of catalysts to study nano intimacy

In order to study nano intimacy in the bifunctional catalysts, specially designed catalytic materials should be synthesized. The morphology control in such materials should be finer than in the conventional systems (impregnated catalysts or composite catalysts containing mechanical mixtures).

Thus, in the impregnated bifunctional catalysts (e.g. noble metals supported on aluminosilicates), metal particles are randomly distributed over the support and the distance

between two catalytic functions, namely hydrogenating Pt sites and acidic aluminosilicate centers, is not controlled. These bifunctional catalysts are working industrial systems, but we ignore how the nano intimacy would impact their properties. Indeed, maximal mixing of sites is always implemented in them and the distance between acidic and metallic functions never controlled.

Another type of bifunctional catalysts contains mechanical mixtures such as hydrocracking catalysts, containing a zeotype as an acidic component and a supported NiMo sulfide as a (de)hydrogenating one. In the mechanical mixtures, nano intimacy is difficult to achieve as the granulometric size of particles is often much greater, microns or even millimeters scale. To obtain nanometric scale intimacy, dedicated preparation are required (e.g. ball milling). But even then, if the particle size will be randomly distributed in a wide range, the distance between the functionalities will vary broadly from nano intimacy at the interface to many micrometers as represented in **Figure 7.a)**. For such systems, also applied in industry it is implicitly supposed that the size of the grains is sufficiently small to provide rapid exchange of the products between the components and therefore further morphology control would not impact the performance. Again, this assumption is made as the distance was never varied systematically, because of the lack of appropriate materials.

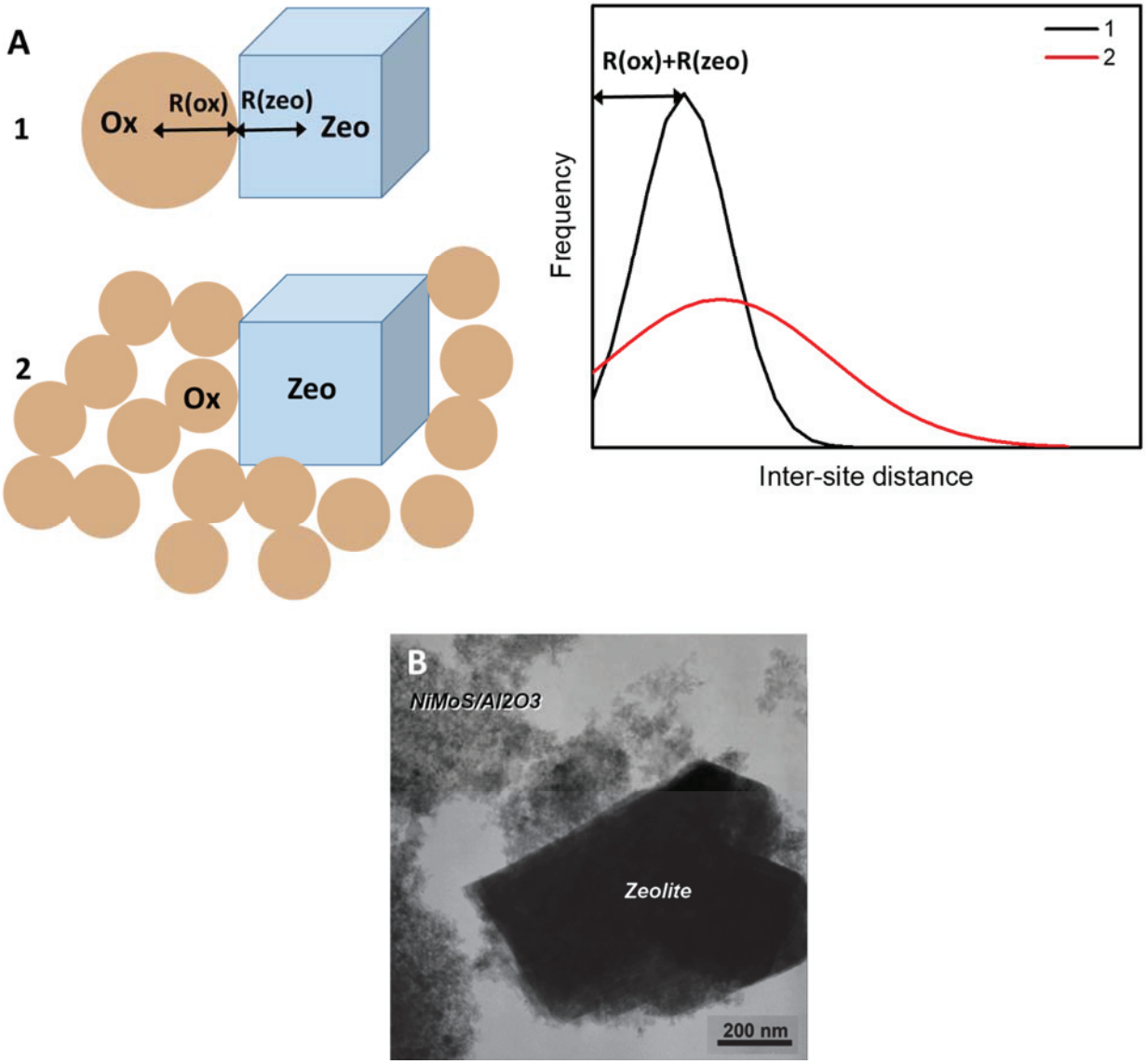

Figure 7: a) Schematic sketch showing the diversity of diffusion path depending on textural properties of the catalyst; (b) industrial hydrocracking catalyst containing a mixture of large crystals of microporous zeotype Y and nanoparticles of mesoporous hydrotreating catalyst. Most part of diffusion path is on zeotype side. The distance between functionalities is ill-defined. Adopted from Ref. [54].

In order to quantify the diffusion path and to study fine effects of nano intimacy, mechanical mixtures as depicted in **Figure 7 b)** are used leading to the demonstration of only rough qualitative effect. To study nano intimacy effects, novel catalytic materials with a well-controlled separation between two functions are necessary. Such materials would contain size-controlled grains of oxide and zeotype particles, separated with a controlled-thickness porous membrane.

3) Ox-Zeo process

It appears from Part 1 of this chapter that no process is able to convert selectively in one reactor syngas into C2-C3 olefins. Using FTS catalysts, the selectivity to light olefins remains low and high quantity of CH_4 is produced due to the ASF distribution.[34–37] Therefore, bifunctional systems combining a methanol synthesis catalyst and a MTO one have been developed and this process is called Syngas To Olefins (STO).[39,40,42–44,55,56] However, the olefin selectivity is limited even when using a catalyst very efficient for methanol synthesis (such as $Cu/ZnO/Al_2O_3$) because of strong hydrogenating properties.

A bifunctional system able to convert syngas directly into light olefins with high selectivity was firstly reported in 2016.[45] It was composed of $ZnCr_2O_4$ oxide catalyst used for the high temperature methanol synthesis[45] and SAPO-34 acidic zeotype used to convert MeOH/DME into hydrocarbons (a C-C coupling catalyst).[20,24,26,57] The corresponding process was called Ox-Zeo. It gave unexpected results, with CO conversion as high as 17% and a selectivity to C2-C4 hydrocarbons of 54% with an olefin/paraffin ratio of 5.7. Those selectivity and conversion values were achieved with a CH_4 selectivity as low as 2% and a CO_2 selectivity of 43%. The main drawback compared to FTS was the high selectivity toward CO_2 impeding the sustainability of such process. However, the Ox-Zeo process appeared as a serious alternative to FTS for the production of light olefins and gave rise to a lot of studies. Later, most of the studies were focused on improving the conversion, O/P ratio and decreasing the CO_2 selectivity.[58] Some studies also tried to diversify the products produced by using large pore zeotypes to produce gasoline range hydrocarbons.[59–63]

3.1) Mechanisms

In the Ox-Zeo process, the main role of the oxide is to hydrogenate CO into an intermediate. On the other hand, the zeotype role is to further convert the formed intermediate into light olefins by C-C coupling via the hydrocarbon pool. The overall process corresponds to the reaction equation Eqn (1):

$$xCO + 2xH_2 \rightarrow C_xH_{2x} + xH_2O \quad (1)$$

Parallel to this main reaction path, both functions can catalyze side reactions: the adsorbed intermediate can be converted on the oxide into methane, which is the main product observed in absence of the zeotype.[45,64,65] Water-Gas-Shift (WGS) reaction can occur on the oxide surface leading to the formation of CO_2.[66] On the zeotype acid site, coke can be formed from the intermediate conversion and olefins can be hydrogenated.[67–69] All those reactions combined lead to a simplified reaction mechanism as shown in **Figure 8**.

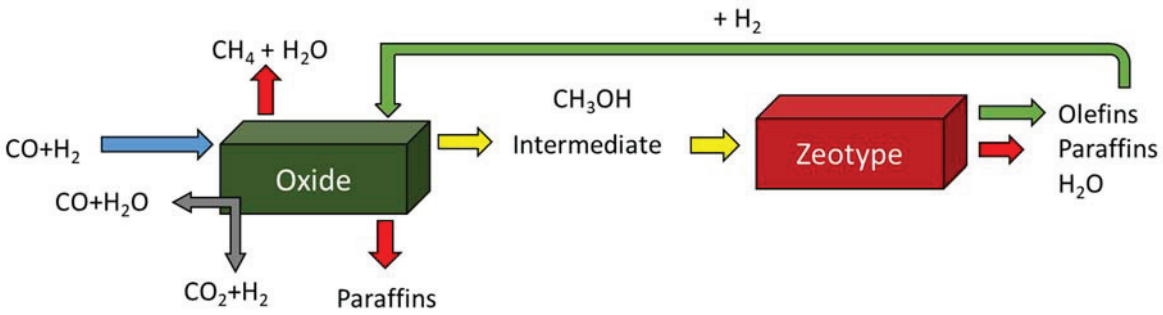

Figure 8: Simplified reaction scheme for the Ox-Zeo process.

3.1.1) Oxide phase

Oxide phase with moderate hydrogenating properties is supposed to initiate the reaction due to hydrogenation of syngas into the intermediate. Formation of the intermediate on the oxide phase have been studied on simple oxides like MnO[64], ZnO[70,71] and ZrO_2[72] and mixed oxides such as $ZnCr_2O_4$.[45]

Nowadays, either CH_3OH (MeOH) or CH_2CO (ketene) are considered as intermediate: MeOH formation is supposed to occur on the oxide through CO adsorption on either O-vacancy or Lewis acid and successive hydrogenation as depicted in **Figure 9** on $ZnZrO_2$ surface.[71–75] Here, CO adsorbed species react with surface hydroxyl groups to form formates that have been observed by *in situ* DRIFT study.[72] Then, successive hydrogenation occurs to form surface methoxy species and then methanol which is desorbed. Before desorption of methanol, it can undergo further hydrogenation forming CH_4 and H_2O.[71]

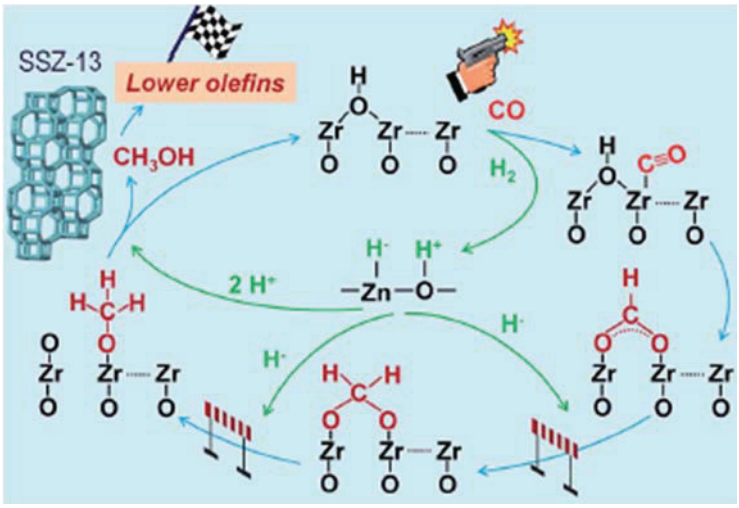

Figure 9: Methanol formation on oxide via reaction with Lewis acid as proposed by Liu and coll.[74]

Alternatively, ketene is formed through the Boudouard reaction as depicted in **Figure 10** on MnO surface.[64,76] First a CO molecule is adsorbed on the surface of the oxide and reacts with a gaseous CO to form gas phase CO_2 and adsorbed C*. The adsorbed C* species undergoes hydrogenation to produce CH_2* which reacts with another CO molecule to form CH_2CO. The formation of CH_4 here is done by pursuing the hydrogenation of the CH_2* species.

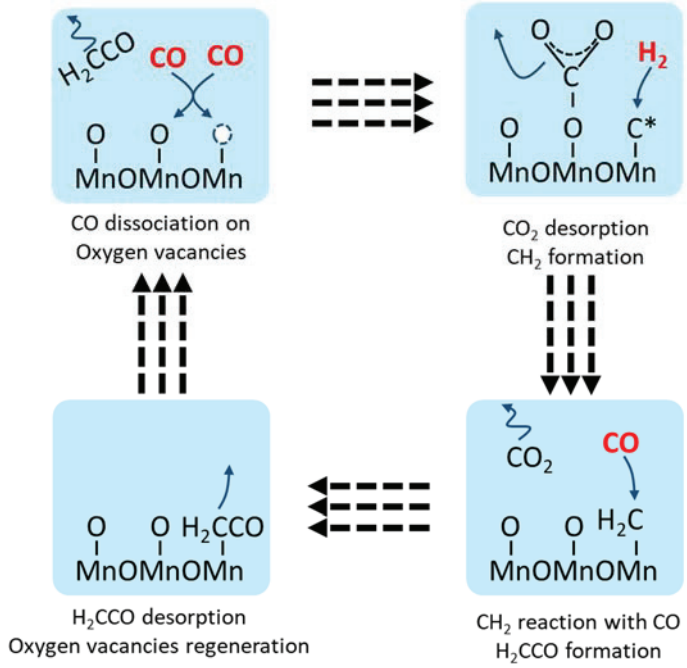

Figure 10: Boudouard reaction on MnO surface using O vacancy as described by Zhu and coll.[64]

Methanol and dimethyl ether (DME) formation in significant amounts was evidenced over ZnO,[77] $ZnZrO_x$,[74,77] $ZnAlO_x$,[78,79] Zn spinels[75] and ZrInOx.[73] In fact, the nature of key intermediate (ketene versus methanol) may vary with different metal oxides and reaction conditions[46] and both mechanisms could occur in parallel.[80] Pan and coll[46] supposed that a selectivity of 50 % toward CO_2 imply that ketene is the main intermediate and WGS do not occur not on the surface. However other literature work made by Huang and coll.[81] and Yang and coll.[63] do not support such claim as they supposed a methanol intermediate for $ZnCr_2O$/SAPO-34 and $ZnCr_2O$/ZSM-5 systems, respectively, with CO_2 selectivity of 50%.

3.1.2)Zeotype phase

The role of the zeotype is to convert the intermediate into light olefins through C-C coupling. The first step of the reaction is decomposition of the intermediate on an acid site, producing CH_3^+ species.[20,22,82,83] H_2O is produced in the case of methanol and CO is produced in the case of ketene. After this step, for both intermediates, the CH_3^+ species will react with hydrocarbon pool species inside zeotype microspores either through the olefin carbon pool cycle or aromatics carbon pool cycle (**Figure 11**).[20,22,82,83]

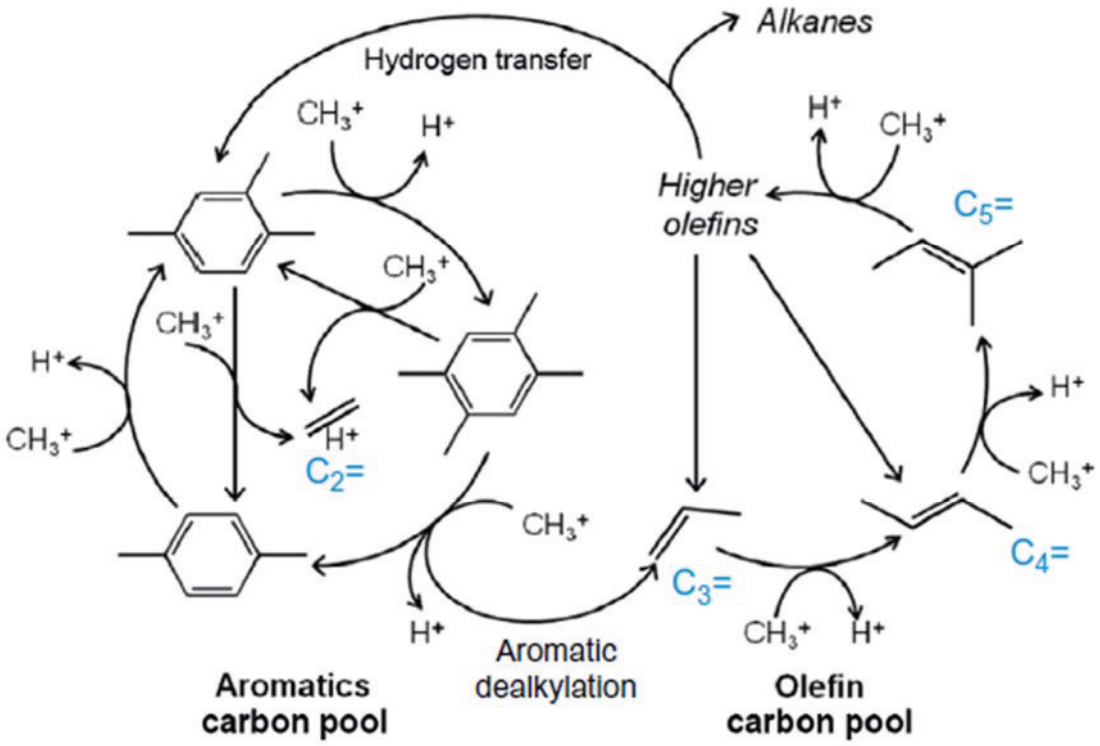

Figure 11: Dual cycle hydrocarbon pool mechanism, Reproduced from Ref.[20].

3.1.3)Synergy of the two function

Alone the conversion of the oxide is usually low (around 3 %) and produce mainly CH_4, methanol and C5+ hydrocarbon.[45,64,74] On the other side zeolite alone is not able to convert syngas. It is the mix of those two function that allow to convert syngas into light olefin. However the catalytic properties of the system is not a linear combination of both catalytic properties. If that was the case the conversion of the oxide alone and the oxide-zeolite mix should be the same.

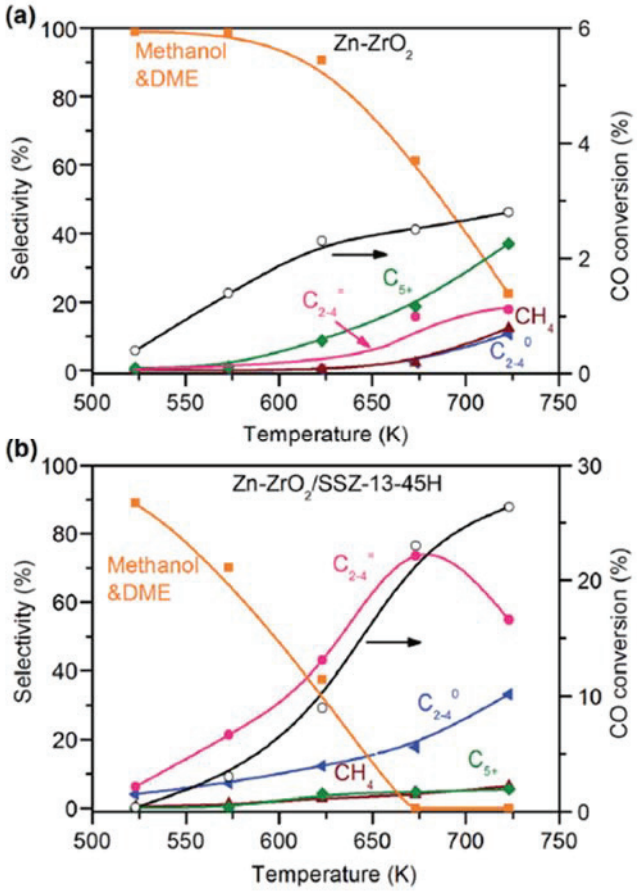

Figure 12: Effect of temperature on a) $Zn\text{-}ZrO_2$ and b) the $Zn\text{-}ZrO_2$/SSZ-13 system. Reaction condition m($Zn\text{-}ZrO_2$)=0.2 g, m($Zn\text{-}ZrO_2$/SSZ-13)=0.6 g, H_2/CO=2, P=3 MPa, F 30 nml/min^{-1}. Measure were taken after 10 h on stream. Reproduced from [74]

The mix of those two phases lead to a synergetic effect that improve greatly the conversion along with the selectivity toward light olefin as shown in **Figure 12**. Such synergetic effect is usually maximal when all the intermediate, here methanol, that is produced by the oxide is consumed. Such condition are met at 400 °C for the $Zn\text{-}ZrO_2$/SSZ-13 system. It is worth noting that such effect have been observed in every Ox-Zeo system.[45,46,64]

The large increase in conversion is supposed to be due to the consumption of the formed intermediate. The consumption of the intermediate draw the thermodynamic equilibrium of the intermediate formation improving the conversion. Such equilibrium is well known in methanol synthesis and this synergetic effect have already been evidenced in syngas to hydrocarbon process.[39]

3.2) Influence of the reaction conditions and catalyst composition

3.2.1) Reaction conditions

Usually, the parameters that are varied for a gas phase process are the contact time, the temperature, the pressure and the feed composition. Ox-Zeo catalysts are not exception and these parameters are optimized in the literature works. Their impact on the catalytic properties are discussed in this part.

a) Contact time

The impact of contact time was studied earlier.[75] An increase in contact time increases the conversion of syngas and decreases the olefins to paraffins (O/P) ratio while the CH_4 selectivity increases only slightly. For the MnO+SAPO-34 system studied by Zhu and coll.,[64] the conversion rose from 13% to 16% by dividing the GHSV by two. In the same time, the O/P ratio decreased from 4.7 to 3.0 and the CH_4 and CO_2 selectivity was approximately constant, at ca 1% and 42%, respectively.

b) Temperature

The reaction temperature has been varied from 250 °C to 500 °C.[58,74,75] Usually, methanol can be observed only below 400 °C.[58,74,75] The CH_3OH selectivity decreases with the temperature in favor of hydrocarbons and CO_2. Above 400 °C, while the conversion increases, a decrease in O/P ratio is observed with an increase in CH_4 selectivity. The CO_2 selectivity is usually constant above 400 °C.[58,74,75] Thus the temperature must be kept as low as possible while allowing for complete consumption of the intermediate.

c) Pressure

The impact of the reaction pressure have been studied by Wang and coll.[43] and Liu and coll.[74]. Using $Zn_{0.3}Ce_{1.0}Zr_{1.0}O_4$ and SAPO-34, it was observed that the increase in total pressure from 0.1 MPa to 2 MPa at 300 °C allows to increase slightly the conversion from 6% to 8%. Meanwhile, the CO_2 selectivity increased from 6% to 12% while CH_3OH and DME selectivity decreased from 5% to 1% and from 8% and 2%, respectively. The O/P ratios decreased from 28 to 6 increasing the pressure[58]. Those results show clearly that working at lower pressure reduces the CO_2 production by WGS reaction. Similar results were found for $ZnZrO_2$ combined with SSZ-13.[74]

d) Feed composition

The feed composition can be modified by changing the H_2/CO ratio of the inlet.[45,74] An increase of the H_2/CO ratio promotes the hydrogenation of olefins into paraffins and increases the CH_4 selectivity while the conversion increases. On the other hand, a decrease in the H_2/CO ratio increases the O/P ratio and decreases the CH_4 selectivity, while the conversion decreases.[45,74] Usually H_2/CO ratio of 2 or 2.5 are used.[58,66,74,84–87]

3.2.2) Ox-Zeo balance

In a bifunctional catalyst, a function A produces an intermediate that reacts with a function B to give a target product. The balance of formation and consumption of an intermediate is crucial. Therefore, the proportion of two functions might be varied to optimize catalytic properties. For the Ox-Zeo process, many studies[45,64,74–77] have tuned the proportion of catalysts in the solid mixtures to optimize the conversion and the O/P ratio. Two different methods have been used. The first method is to set the global mass of the mixture constant and vary its composition.[45,64,76] The second one consist of setting the oxide mass constant and varying the number of acid sites by adding different masses of zeotype or changing its acidity by ionic exchange with alkali cations.[74,75,77]

a) Constant global mass

As the same mass (volume) of Ox-Zeo catalyst is used with this method, the contact time is constant. In the literature several studies have used this method.[45,64,66,76]

Jiao and coll. optimized the balance between ZnCrOx and M-SAPO (SAPO-34 containing mesoporosity)[45]. Two volcano-type curves were obtained for the conversion and the O/P ratio. For both curves the maximal value was obtained with a 1/1 mixture as shown in **Figure 13**. With a zeotype rich mix, the conversion and the O/P ratio decrease greatly. For an oxide-rich mix, the conversion and the O/P ratio also decrease greatly and moreover the CH_4 selectivity increases. Similar trends were obtained with other systems optimised with this method.[64,76]

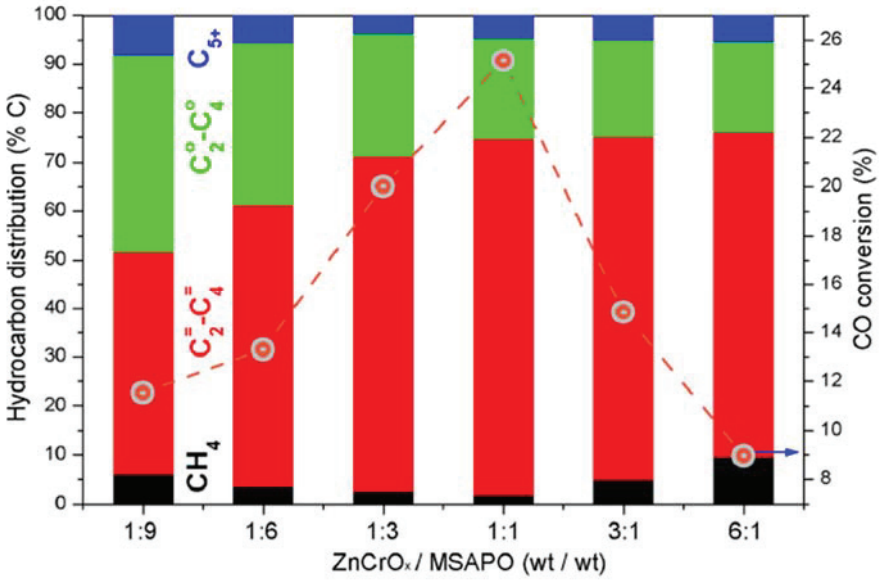

Figure 13: Catalytic results as a function of mass ratios of $ZnCrO_x$/MSAPO Reaction conditions: 400 °C, 2.5 MPa and GHSV 5143 ml/h.$g_{cat,}$ reproduced from Ref.[45]

At each extremity of the curve, one function is kinetically limiting the formation of olefins. For an oxide-rich mix, not enough acid sites are available to convert the intermediate into olefins. For a zeotype-rich mix, the quantity of intermediate produced is limited by the number of hydrogenating sites, and the conversion is decreased. Specific properties of each solid can also come out at the extremities. For instance, a decrease in O/P ratio is observed for a zeotype-rich mixture which suggests hydrogenating properties of the zeotype under the reaction feed. It has been attributed to hydrogen transfer from the hydrocarbon pool formed in the zeotype pores.[67–70] Those results show the importance to find the balance between the two functions. It is worth noting that this optimum is specific to each oxide-zeotype mixture. Usually, mass ratios are reported in the literature, but for correct representation the ratios of the numbers of sites should

be rather used, that depend on the densities of active sites and on the specific surface areas of the corresponding solids.

b) Constant oxide mass

In this approach, the contact time is kept constant with respect to the oxide. Such method was used extensively in literature.[62,70,74,77,87,88] Wang and coll.[77] studied $ZrZnO_x$+SAPO-34 mixture with such methods. The mass of oxide and zeotype were kept constant but the density of acid sites was varied by varying the composition of SAPO-34 and by ball milling the solid for different times. The ball milling is known to change the acidity of zeotype due to collapse of the crystalline structure and modification of local environment around Brønsted acid site.[89–94]

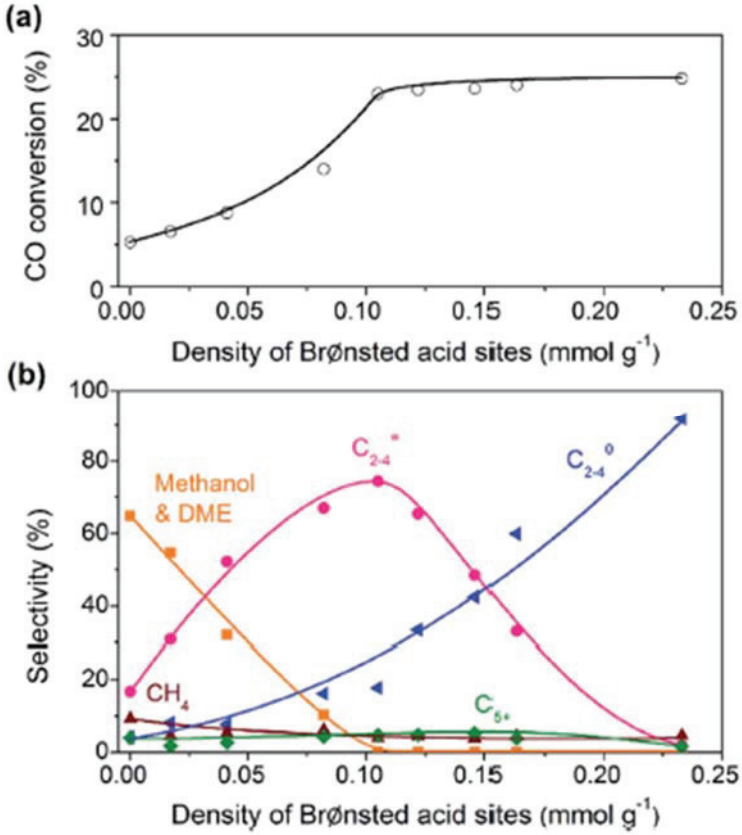

Figure 14 : Effect of density of Brønsted acid site on the catalytic properties of Zn-ZrO_2/SSZ-13 catalyst with a) CO conversion and b) product selectivity, reproduced from Ref.[74].

Similar work was published by Liu and coll.[74] with a Zn-ZrO_2/SSZ-13 mixture. The authors modified the zeotype by Na ion exchange to decrease the acid site density. An increase in conversion was observed increasing the density for value lower than 0.1 mmol.g^{-1}. At higher

density, the conversion was constant. The O/P ratio curve had a maxima at 0.1 mmol.g^{-1}. It was concluded that below this value, the C-C coupling is the limiting step of the process, whereas above it the CO hydrogenating function was the limiting step leading to a plateau in conversion. This method has a clear advantage for determination of the apparent kinetic constants of the intermediate formation on the oxide. At the conversion plateau, reactions on the oxide represent the limiting step and the conversion can be used for the kinetic constant determination on the oxide.

3.2.3)Oxides optimization

Different works on the Ox-Zeo process aim to improve the conversion and O/P ratio of the process by mitigating the hydrogenation properties of the oxide catalyst.[45,58,66,75,78,85,95] Recently, the reduction of the CO_2 selectivity induced by the WGS reaction was a major target .[58] The oxide can be either a simple oxide or a mixed oxide inspired by methanol synthesis catalysts. Usually Oxide with good CO adsorption and H2 dissociation are used or mixed together to optimize the oxide.

a) Simple oxides

Even if simple oxides do no lead to the best catalytic performances for the Ox-Zeo process, they were used in theoretical studies and preliminary screening for the development of mixed oxides. Theoretical studies focused on the impact of oxide properties such as the crystallite size and crystalline phase on the overall catalytic properties.

The impact of the crystallite size on the catalytic properties was studied by Ni and coll.[70] with ZnO. For that purpose, ZnO samples were prepared with a crystallite size ranging from 23 nm to 79 nm and tested in combination with SAPO-34. The conversion decreased from 31.9% to 6.5% upon increasing the crystallite size, while the O/P ratio also decreased from 4.9 to 2.1 and the hydrocarbon selectivity increased from 58% to 68%. Hence, a smaller crystallite size of ZnO improves catalytic properties. Such results were linked to an increase in defect density of ZnO. The density of defects that are Lewis acid sites was measured by NH_3-TPD.

The effect of crystalline phase of ZrO_2 on catalytic properties for the Ox-Zeo process was studied by Wang and coll.[72]. In this work, monoclinic and tetragonal crystalline ZrO_2, m-ZrO_2 and t-ZrO_2 respectively, were prepared and tested with ZSM-5 zeotype to produce aromatics. It has been shown that m-ZrO_2 is twice as active as t-ZrO_2, with similar selectivity as shown in **Table 1**. This difference in conversion was attributed to higher CO adsorption ability observed for m-ZrO_2 as represented in **Figure 15**.This higher adsorption capability was correlated to a higher density of hydroxyl groups on the oxide surface.

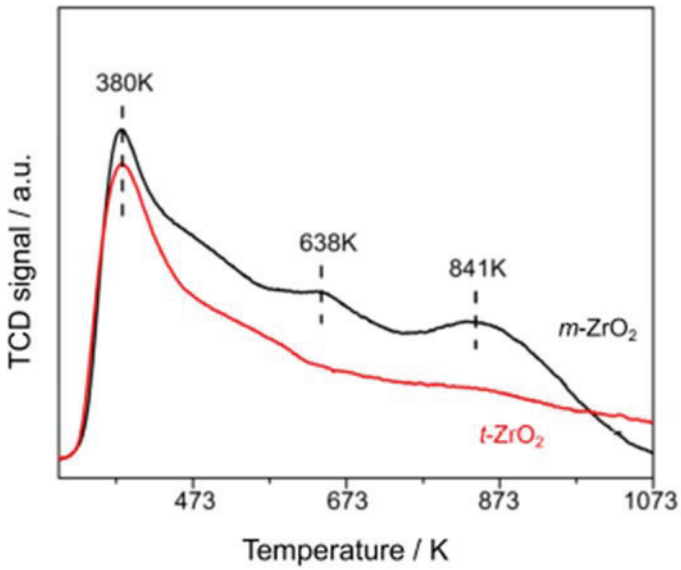

Figure 15 : CO-TPD profile of m-ZrO2 and t-ZrO2. Reproduced from Wang and coll[72]

Table 1 : Catalytic results of m-ZrO_2 and t-ZrO_2 alone and with the addition of HZSM-5 (ratio 1:1). Reaction condition H_2/CO=1/1, F=25 ml/min^{-1}, P=3.8 MPa, T=673 K after 8 h on stream. Reproduced from Wang and coll[72]

Catalyst	CO conv. (%)	CO_2 sel. (%)	Product Selectivity (%)				
			CH_4	C2-C4=	C2-C4°	C5+	Ar
m-ZrO_2	12.9	38.3	5.4	57.8	6.7	30.1	-
t-ZrO_2	8.6	36.9	29.5	26.1	19.3	25.1	-
m-ZrO_2/HZSM-5-mix	24.0	36.4	4.3	2.7	21.4	4.2	67.4
t-ZrO_2/HZSM-5-mix	14.2	33.5	4.9	2.6	20.6	6.9	65.0

The effect of the initial oxidation state was studied for MnO_x by Zhu and coll.[64]. Three manganese oxides with different oxidation states (MnO, Mn_2O_3 and MnO_2) were prepared and tested with SAPO-34. All oxides exhibited similar activity at 400 °C and 25 bar with conversion ranging from 7.3 to 8.5% and $C2^{=}$-$C4^{=}$ (olefins with carbon number ranging from 2 to 4) selectivity around 44%. DRX diffractogram of the used catalysts showed the presence of MnO after testing, suggesting that it corresponds to the active phase. XPS spectra of MnO before and after activation under H_2 or syngas have also been performed. For both types of activation, partial reduction occurred on the MnO surface. The active sites were attributed to oxygen vacancies appearing due to partial reduction.

b) Mixed oxides

Mixed oxides were developed for the Ox-Zeo process to finely tune the hydrogenation and CO activation properties and to maximize the CO conversion while maintaining a high O/P ratio. For that purpose, one site able to activate CO and another site able to dissociate H_2 are required in the mixed oxide.

Such strategy was used for the development of Zr-based catalysts. ZrO_2 is able to activate CO [71,74,77,96,97] and a high conversion can be obtained by adding another element capable of adsorbing and dissociating H_2. Zr-Zn mixed oxides were studied in combination with SSZ-13. [74,77] Mixtures of ZrO_2 and SSZ-13 led to a low conversion, around 3.9%, with a high C2-C4 selectivity of 50% and an O/P ratio of 8.5. The CH_4 selectivity was as low as 1.6%. For ZnO and SSZ-13, a higher conversion was observed, 6.2%, with a C2-C4 selectivity of 45% and an O/P ratio of 0.5. The CH_4 selectivity was higher (5.4%). Those results suggested better hydrogenating properties of ZnO compared to ZrO_2 leading to the production of methane and paraffins in high quantity. Small addition of Zn in zirconia, with a Zr/Zn ratio of 64/1, gave a conversion of 17% with a C2-C4 selectivity of 50% and an O/P ratio of ca 7. Here Zn, used as a dopant, was able to greatly improve the catalytic properties of ZrO_2 as shown in **Figure 16**. It is supposed that ZnO has greater H_2 dissociative capability.[98–100] By adding more Zn, the conversion increased up to 29% with a Zr/Zn ratio of 1 and then decreased. The highest O/P ratio for the Zr-Zn mixed oxides was obtained with a Zr/Zn ratio of 64.

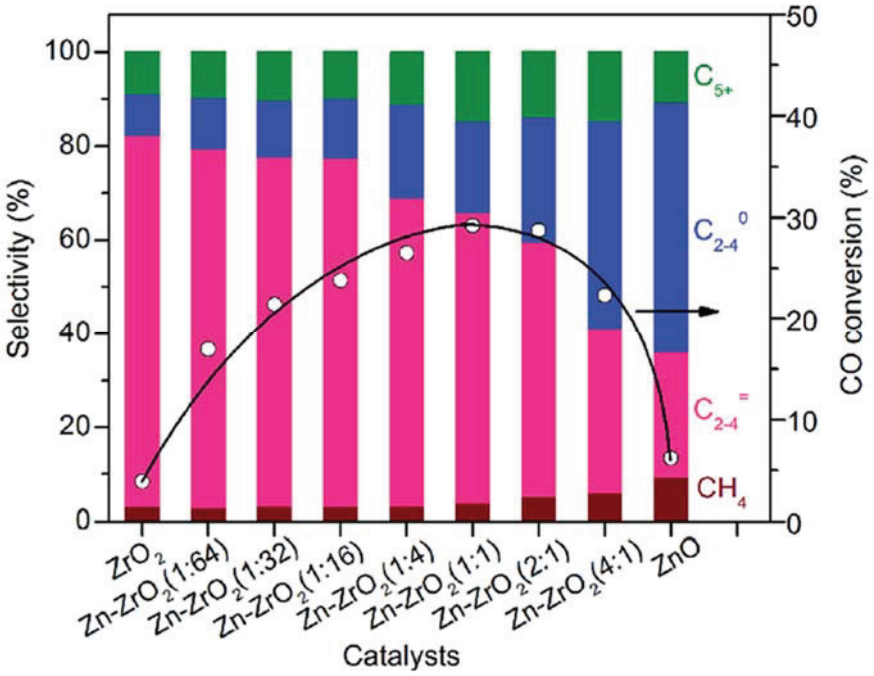

Figure 16 : Effect of Zn/Zr ratio on catalytic properties of Zn-Zr/SSZ-13 system. The CO_2 selectivity was constant in the range 41-45 %.[74]

Similar studies were undertaken with mixed zirconium indium oxide by Su and coll..[73] It was shown that a In/Zr ratio of 2/1 was optimal for both the conversion and the O/P ratio. Those mixed oxides were developed with the same idea as Zr-Zn oxides, implying that Zr provides the CO activation function whereas In is responsible for the H_2 dissociative adsorption function. Other works have been done by preparing various Zn based spinel structures with Cr, Ga or Al.[45,58,66,75,78,85,95] Other Mn based catalysts were developed by doping them with Zn or Ga as an H_2 dissociative adsorption agent.[76,84]

3.2.4)Zeotype optimization

Different studies were focused on the optimization of the zeotype.[60–63,65,74,86,87] Indeed, some important characteristics such as its structure, chemical composition, acidity and morphology have a strong impact on the catalytic properties of the mixture.

a) Structure

The zeotype structure has a great impact on the distribution of the reaction products. The structure of zeotype can be defined by the dimensionality (connectivity) of the channel system,

either 3D, 2D or 1D, the cage size and the pore opening size. The pore opening affects mainly the diffusion rate of a molecule from the gas phase into the zeotype structure. The cage size can modify the reaction pathway and the dimensionality affects the overall accessibility of the acid sites.[88]

Different studies have shown that smaller pore opening of zeotypes like SAPO-34,[45] SAPO-18,[87] SAPO-35,[87] SSZ-39,[65] MOR,[86] and SSZ-13[74] allows to produce mainly C2-C4 hydrocarbons with a high C3 proportion. For example, SSZ-39 mixed with $ZnCrO_x$ led to a C2-C4 selectivity of 44%.[65] The C5+ selectivity was limited to about 6% due to the small pore opening.[65] Moreover, the carbon content in the zeotype after reaction showed that very little quantities of aromatic intermediates are produced inside the SSZ-39 zeotype. Those results suggest that the MTO reaction in small cages occurs mainly through the olefin carbon pool cycle part.[65]

A Larger pore size of zeotypes like ZSM-11,[59] SAPO-11,[59] ZSM-22[59] and ZSM-5[60–63] allows the production of C5+ and gasoline range hydrocarbons. As an example, the ZSM-5 structure was tested with $ZnZrO_x$ by Wang and coll.[61] , this mixture gave a C5+ selectivity of 75% among hydrocarbons including 96% of aromatics. The C2-C4 hydrocarbon selectivity was of 23%. Here the proportion of aromatics is controlled by fine-tuning the structure. 1D structure with 10 MR pore opening lowers the aromatic proportion rendering operational gasoline mixture.[59]

These results clearly show that the Ox-Zeo process is versatile in terms of available hydrocarbons distribution. By selecting carefully the zeotype structure, the selectivity can be modulated from light hydrocarbons mainly composed of C3, up to gasoline range hydrocarbons.

The structure and pore opening of the zeotype can also impact the catalyst lifetime as shown by Huang and coll..[88] In this study, two structures were compared, namely AEI and LEV that correspond to SAPO-18 and SAPO-35 zeotype, respectively. Those two structures have been chosen for the difference in dimensionality: a 3D structure for SAPO-18 and a 2D one for SAPO-35 (**Figure 17**). This difference implies that a blockage of a pore entrance in SAPO-35 leads to a greater loss of accessibility to cages. Also, NH_3-TPD measurements showed that SAPO-35 presented stronger strong acid sites than SAPO-18. A stronger acidity favors the formation of coke at the pore entrance during the MTO process leading to faster deactivation: after only 100 min on stream, the

activity has dropped to 2.5% for SAPO-35 while it remained stable at 12% for SAPO-18 and even after 6000 min on stream the catalytic properties using SAPO-18 remained the same.[88]

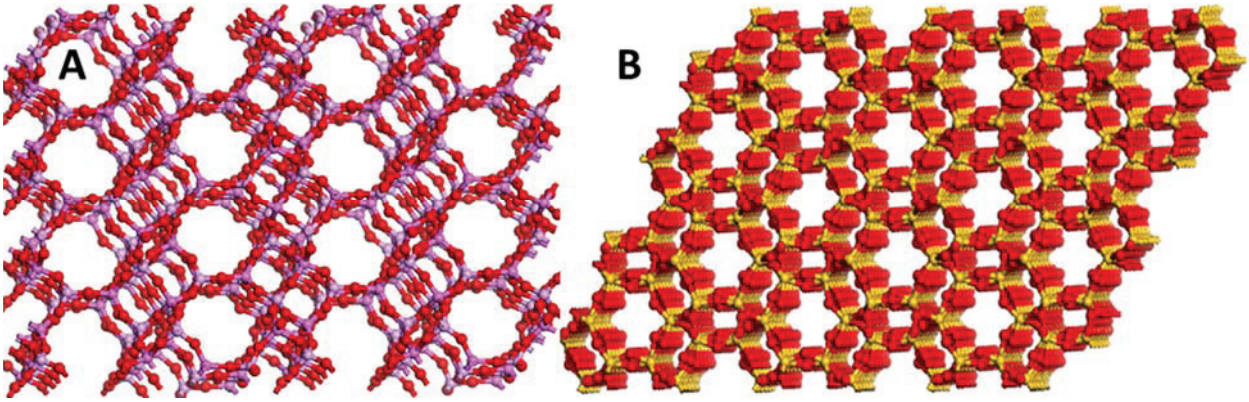

Figure 17: A) AEI orthorhombic 3D structure viewed along [001] axis; B) LEV 2D structure along [001] axis.

b) Acid strength

In addition to the density of acid sites which determines the optimized balance between the oxide and the zeotype, a crucial property of the zeotype is its acid site strength. It is usually characterized by multiple techniques, including model catalytic tests (e.g. isooctane cracking) or NH_3 temperature programmed desorption (TPD) measurements. The temperature at which NH_3 is desorbed is characteristic of the acid strength of adsorption sites: a higher desorption temperature reveals stronger acid sites.

The impact of the acid strength on the O/P ratio has been first evidenced for the Ox-Zeo process by Jiao and coll.[45] SAPO-34 samples with different strength of acid sites were prepared and tested in mixtures with $ZnCrO_x$. All those zeotypes had a NH_3 desorption temperature comprised between 350 and 400 °C. An O/P ratio of 4.75 was obtained for the weakest acid sites while it was only 1.50 for the strongest as shown in **Figure 18**. Therefore, too strong acidity is deleterious for the target Ox-Zeo process selectivity.

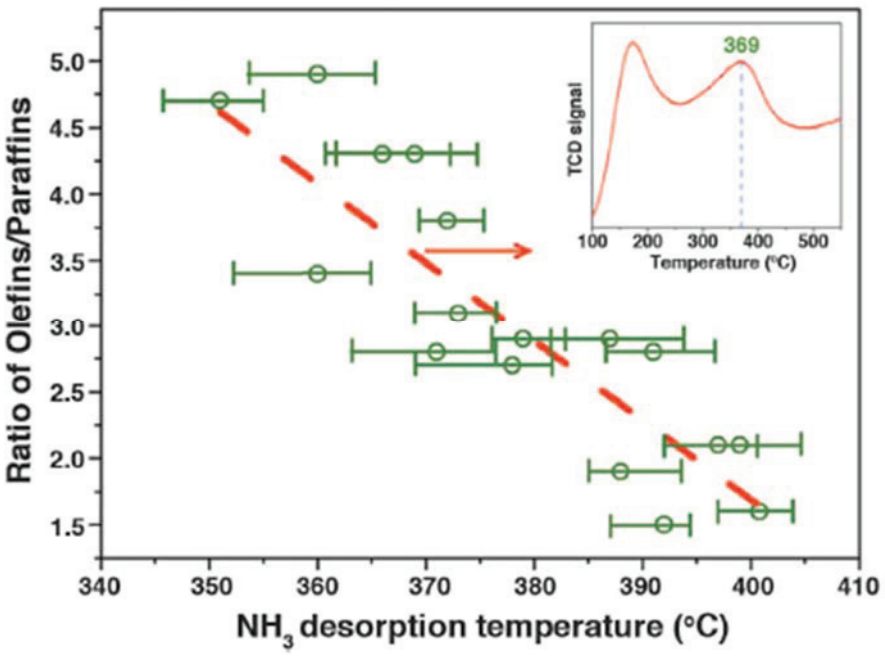

Figure 18 : Ratio O/P as a function of the NH_3 desorption peak temperature for a selection of SAPO-34. The inset corresponds to a typical NH_3-TPD profile, reproduced from Ref.[45].

In another study reported by Li and coll.[65] the same trend was observed using SSZ-39 or SAPO-34 mixed with $ZnCrO_x$. The higher O/P ratio obtained with SAPO-34 was related to the presence of weaker sites compared to SSZ-39 (NH_3-desorption temperature of 375 and 500 °C, respectively).

The impact of the acid strength on the O/P ratio is related to the ability of the zeotype to hydrogenate olefins. This property has been observed for the hydrogenation of ethene and propene.[67–69,101,102] Li and coll.[65] showed that both SSZ-39 and SAPO-34 are able to hydrogenate propene to propane. It occurs through protonation of propene on a Brønsted acid site. Then gaseous H_2 reacts with the ethoxy species to produce the corresponding alkane and regenerate the acid site as described in Eqn (2) and (3).[67–69]

$$C_2H_4 + HO - Z => HCH_2 - CH_2 - O - Z \quad (2)$$

$$H - H + CH_3 - CH_2 - O - Z => CH_3 - CH_3 + HO - Z \quad (3)$$

It is also stated in numerous paper concerning Ox-Zeo[63,87] that hydrogen transfer occur in the zeotype participating in the formation of alkane. Those transfer occur generally between higher

olefin compound forming alkane and aromatic compound that participate in the hydrocarbon pool[68,103–106].

3.2.5)Bed stacking

As the Ox-Zeo process uses two catalytic phases, various spatial organizations of the catalyst bed are possible. As this organization can have a great impact on the catalytic properties, various arrangements have been made from a dual-bed catalyst to an oxide deposited on a zeotype catalyst.

In a Dual layer (DL) arrangement, the oxide and the zeotype are physically separated and placed one on top of the other. Usually, the oxide layer is placed before the zeotype because the zeotype cannot convert syngas at all. An inert spacer can be inserted between the two layers to increase the distance between the two functions. The main interest of those types of arrangement is that the products formed on the zeotype are not in contact again with the oxide, avoiding contact of olefin with two solid capable of hydrogenation.

In a multi-layer (ML) arrangement, the bed consist of alternating layers of oxide and zeotype. The products formed on the zeotype can then pass through one or more layers of oxide. The higher the number of layers, the closer the oxide and the zeotype and the higher the number of contacts. As for a DL, an inert spacer can be used inside a ML.

In the Randomly Mixed (RM) Bed, the particles of two sieved solids are randomly mixed. Usually two solids have a similar particle size and similar density, so that the distribution of both types of particles remains homogeneous (absence of sedimentation).

For the ball milled (BM) bed, the two powders are ball milled together leading to the formation of strong contact between the two phases. In the case of the Ox-Zeo process, degradation of the zeotype properties was reported after ball milling.[77,89–94,107]

One phase can also be deposited on the other leading to a supported arrangement (SA). Some products or intermediates pass through a specific phase to reach the other phase. Core-shell structures (CS) also called capsules can also be prepared by using a binder, like silica to favor

deposition of zeotype on the surface of oxide.[108] All these arrangements are represented in **Figure 19**.

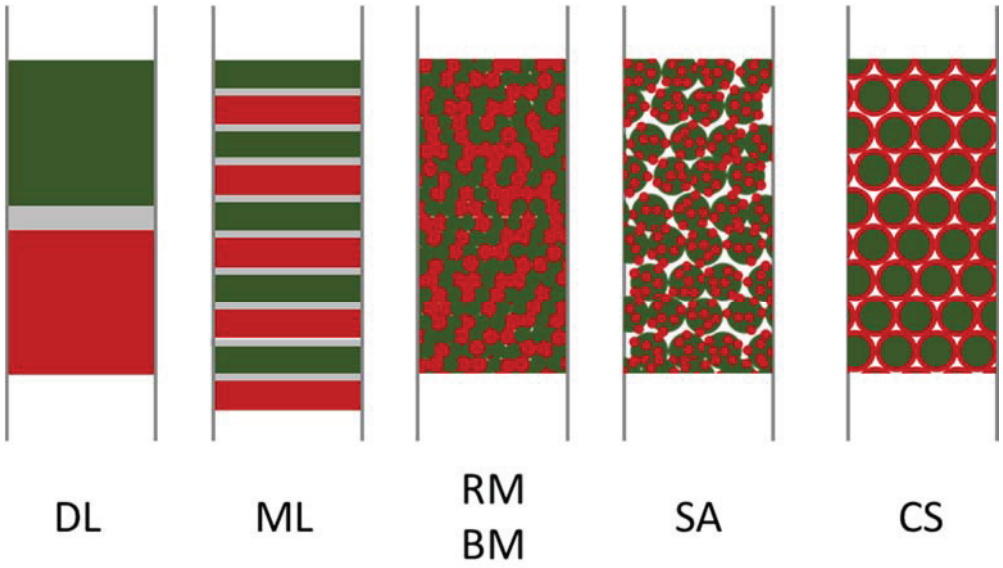

Figure 19: Various bed arrangements possible for an Ox-Zeo bifunctional catalyst.

The studies on the bed arrangement have been published usually focusing on DL, ML, RM and BM. Jiao and coll.[45] reported a net variation of catalytic properties of $ZnCr_2O_4$+SAPO-34 mixture from DL to RM. It was observed that a higher conversion can be achieved with a higher O/P ratio by increasing the intimacy in the catalytic bed. A conversion of 9% was obtained for a DL and 35% for a RM while the O/P ratios were 0.5 and 3.45, respectively. Liu and coll.[74] published similar results with the $ZnZrO_x$+SSZ-13 system that represented in **Figure 20**. They showed that mortar mixing of the two phases for 10 min improve catalytic properties. The CO conversion raised from 2% to 28% and the O/P ratio was improved from 0.12 to 4.5.

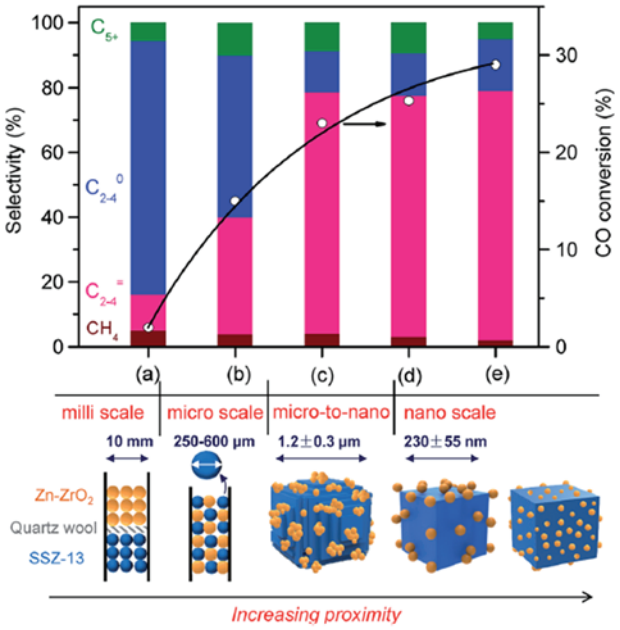

Figure 20 : Effect of proximity in the Zn-ZrO_2/SSZ-13 (1:2 ratio) on the catalytic properties. a) Dual layer, b) simple powder mix c) Zn-ZrO_2 (8.9 nm)/micro-SSZ-13, d) Zn-ZrO2 (8.9 nm)/nano-SSZ-13 and e) Zn-ZrO_2 (4.8 nm)/nano-SSZ-13.reproduced from Liu and coll.[74]

Usually for the Ox-Zeo process an increase in contact from DL to RM is benefic in terms of conversion, O/P ratio and C2+ hydrocarbon selectivity for all catalytic systems. An intimate mixing of the oxide and the zeotype allows to decrease the gas phase intermediate concentration shifting the thermodynamic equilibrium toward the olefin production. The increase in the C2+ hydrocarbon selectivity could be also related to the decrease in the intermediate partial pressure. This decrease limits the quantity of intermediates that can further react with the oxide to produce methane. From those results it can be concluded that good contact between the two phases is needed to improve the catalytic properties in the Ox-Zeo process.

4) Conclusion

In this chapter, we have shown that the Ox-Zeo process allows production of light olefins from alternative feedstock. This process combines two steps: in the first step methanol or ketene is produced on an oxide as intermediate. In the second step, the intermediate is converted over a zeotype to light olefins. Various combinations of oxides and zeotypes were shown to be efficient for the Ox-Zeo process and a $C2^{=}$-$C4^{=}$ selectivity above 40% was obtained at 30% of conversion with $ZnCr_2O_4$ and SAPO-34. From those studies Zn-based oxide coupled with moderate acidic

zeotype seems to be the most promising as the ZnZrCe oxide that allow selectivity toward CO_2 as low as 12% compared to the 45% obtained with $ZnCr_2O_4$. Some studies have also shown a synergy between the activity of the oxide and the zeotype: the zeotype shifts the thermodynamic equilibrium of the intermediate synthesis thus increasing the CO conversion over the oxide. The importance of the catalyst bed arrangement has also been studied. It has been shown that a greater intimacy between the two phases improves the catalytic properties for the Ox-Zeo process.

5) Objective of the thesis

Based on this literature survey, this PhD work was focused on the role of intimacy in the Ox-Zeo process. MnO_x was selected as the oxide and SAPO-34 as the zeotype. To access different scales of intimacy, we shall investigate multi-layer beds and mechanical mixtures of MnO_x and SAPO-34 functions. Dilution of a mechanical mixture with an inert spacer will be also applied at the micrometer scale. At the nanometer scale, we will synthesize core-shell structures consisting of an oxide core covered by a permeable inert shell. It will allow to determine the impact of the distance between the oxide and zeotype functions on catalytic properties for the Ox-Zeo process. This work on intimacy is the purpose of Chapter 4.

However, a study of the catalytic properties of reference MnO+SAPO-34 mixtures for the Ox-Zeo process was needed to decorrelate the effect of intimacy. This work will be presented in Chapter 3 in which important catalytic properties such as the activation energy, the partial reaction orders and the dependence against a selection of reaction parameters will be determined. An *in situ* DRIFT study will be also conducted to identify the key reaction intermediate for the Ox-Zeo process using MnO+SAPO-34 mixtures.

But before presenting those results, the experimental methods including the characterization techniques and catalytic measurements will be detailed in Chapter 2. All the preparation methods of catalysts will be provided in Chapter 3 and 4.

6) References

1. Monai, M., Gambino, M., Wannakao, S. & Weckhuysen, B. M. Propane to olefins tandem catalysis: a selective route towards light olefins production. *Chem. Soc. Rev.* **50**, 11503–11529 (2021).
2. Bender, M. An Overview of Industrial Processes for the Production of Olefins - C $_4$ Hydrocarbons. *ChemBioEng Reviews* **1**, 136–147 (2014).
3. Amghizar, I., Vandewalle, L. A., Van Geem, K. M. & Marin, G. B. New Trends in Olefin Production. *Engineering* **3**, 171–178 (2017).
4. Gao, Y. *et al.* Recent Advances in Intensified Ethylene Production—A Review. *ACS Catal.* **9**, 8592–8621 (2019).
5. Torres Galvis, H. M. & de Jong, K. P. Catalysts for Production of Lower Olefins from Synthesis Gas: A Review. *ACS Catal.* **3**, 2130–2149 (2013).
6. Zhao, Z., Jiang, J. & Wang, F. An economic analysis of twenty light olefin production pathways. *Journal of Energy Chemistry* **56**, 193–202 (2021).
7. Zacharopoulou, V. & Lemonidou, A. Olefins from Biomass Intermediates: A Review. *Catalysts* **8**, 2 (2017).
8. Agarwal, A., Sengupta, D. & El-Halwagi, M. Sustainable Process Design Approach for On-Purpose Propylene Production and Intensification. *ACS Sustainable Chem. Eng.* **6**, 2407–2421 (2018).
9. Zhao, Z. *et al.* Low-carbon roadmap of chemical production: A case study of ethylene in China. *Renewable and Sustainable Energy Reviews* **97**, 580–591 (2018).
10. Marsh, M. & Wery, J. Filling the Propylene Gap – Shaping the Future with On-Purpose Technologies. *Honeywell UOP* (2019).
11. Amghizar, I., Dedeyne, J. N., Brown, D. J., Marin, G. B. & Van Geem, K. M. Sustainable innovations in steam cracking: CO $_2$ neutral olefin production. *React. Chem. Eng.* **5**, 239–257 (2020).
12. Akah, A., Williams, J. & Ghrami, M. An Overview of Light Olefins Production via Steam Enhanced Catalytic Cracking. *Catal Surv Asia* **23**, 265–276 (2019).
13. Akah, A. & Al-Ghrami, M. Maximizing propylene production via FCC technology. *Appl Petrochem Res* **5**, 377–392 (2015).
14. Corma, A. *et al.* Crude oil to chemicals: light olefins from crude oil. *Catal. Sci. Technol.* **7**, 12–46 (2017).
15. Blay, V. *et al.* Engineering Zeolites for Catalytic Cracking to Light Olefins. *ACS Catal.* **7**, 6542–6566 (2017).
16. Rahimi, N. & Karimzadeh, R. Catalytic cracking of hydrocarbons over modified ZSM-5 zeolites to produce light olefins: A review. *Applied Catalysis A: General* **398**, 1–17 (2011).
17. Sadrameli, S. M. Thermal/catalytic cracking of liquid hydrocarbons for the production of olefins: A state-of-the-art review II: Catalytic cracking review. *Fuel* **173**, 285–297 (2016).
18. Bricker, J. C. Advanced Catalytic Dehydrogenation Technologies for Production of Olefins. *Top Catal* **55**, 1309–1314 (2012).
19. Chen, S. *et al.* Propane dehydrogenation: catalyst development, new chemistry, and emerging technologies. *Chem. Soc. Rev.* **50**, 3315–3354 (2021).

20. Nesterenko, N., Aguilhon, J., Bodart, Ph., Minoux, D. & Dath, J.-P. Methanol to Olefins. in *Zeolites and Zeolite-Like Materials* 189–263 (Elsevier, 2016). doi:10.1016/B978-0-444-63506-8.00006-9.
21. Rodríguez-Vallejo, D. F., Guillén-Gosálbez, G. & Chachuat, B. What Is the True Cost of Producing Propylene from Methanol? The Role of Externalities. *ACS Sustainable Chem. Eng.* **8**, 3072–3081 (2020).
22. Tian, P., Wei, Y., Ye, M. & Liu, Z. Methanol to Olefins (MTO): From Fundamentals to Commercialization. *ACS Catal.* **5**, 1922–1938 (2015).
23. Ali, M. A. *et al.* A Comprehensive Review Covering Conventional and Structured Catalysis for Methanol to Propylene Conversion. *Catal Lett* **149**, 3395–3424 (2019).
24. Chen, D., Moljord, K. & Holmen, A. A methanol to olefins review: Diffusion, coke formation and deactivation on SAPO type catalysts. *Microporous and Mesoporous Materials* **164**, 239–250 (2012).
25. Yang, M., Fan, D., Wei, Y., Tian, P. & Liu, Z. Recent Progress in Methanol-to-Olefins (MTO) Catalysts. *Adv. Mater.* **31**, 1902181 (2019).
26. Zhong, J. *et al.* Recent advances of the nano-hierarchical SAPO-34 in the methanol-to-olefin (MTO) reaction and other applications. *Catal. Sci. Technol.* **7**, 4905–4923 (2017).
27. Galadima, A. & Muraza, O. Revisiting the oxidative coupling of methane to ethylene in the golden period of shale gas: A review. *Journal of Industrial and Engineering Chemistry* **37**, 1–13 (2016).
28. Gambo, Y., Jalil, A. A., Triwahyono, S. & Abdulrasheed, A. A. Recent advances and future prospect in catalysts for oxidative coupling of methane to ethylene: A review. *Journal of Industrial and Engineering Chemistry* **59**, 218–229 (2018).
29. Takanabe, K. Catalytic Conversion of Methane: Carbon Dioxide Reforming and Oxidative Coupling. *J. Jpn. Petrol. Inst.* **55**, 1–12 (2012).
30. Liu, J. *et al.* From fundamentals to chemical engineering on oxidative coupling of methane for ethylene production: A review. *Carbon Resources Conversion* **5**, 1–14 (2022).
31. Mohsenzadeh, A., Zamani, A. & Taherzadeh, M. J. Bioethylene Production from Ethanol: A Review and Techno-economical Evaluation. *ChemBioEng Reviews* **4**, 75–91 (2017).
32. Cavani, F., Ballarini, N. & Cericola, A. Oxidative dehydrogenation of ethane and propane: How far from commercial implementation? *Catalysis Today* **127**, 113–131 (2007).
33. Gärtner, C. A., van Veen, A. C. & Lercher, J. A. Oxidative Dehydrogenation of Ethane: Common Principles and Mechanistic Aspects. *ChemCatChem* **5**, 3196–3217 (2013).
34. Gholami, Z., Tišler, Z. & Rubáš, V. Recent advances in Fischer-Tropsch synthesis using cobalt-based catalysts: a review on supports, promoters, and reactors. *Catalysis Reviews* **63**, 512–595 (2021).
35. Jahangiri, H., Bennett, J., Mahjoubi, P., Wilson, K. & Gu, S. A review of advanced catalyst development for Fischer–Tropsch synthesis of hydrocarbons from biomass derived syn-gas. *Catal. Sci. Technol.* **4**, 2210–2229 (2014).
36. Sartipi, S., Makkee, M., Kapteijn, F. & Gascon, J. Catalysis engineering of bifunctional solids for the one-step synthesis of liquid fuels from syngas: a review. *Catal. Sci. Technol.* **4**, 893–907 (2014).
37. Dry, M. E. The Fischer–Tropsch process: 1950–2000. *Catalysis Today* **71**, 227–241 (2002).

38. Mirzaei, A., Arsalanfar, M., Bozorgzadeh, H. & Samimi, A. A review of Fischer-Tropsch synthesis on the cobalt based catalysts. *PCR* **2**, (2014).
39. Fujimoto, K., Saima, H. & Tominaga, H. Synthesis gas conversion utilizing mixed catalyst composed of CO reducing catalyst and solid acid. *Journal of Catalysis* **94**, 16–23 (1985).
40. Ereña, J., Arandes, J. M., Bilbao, J., Aguayo, A. T. & de Lasa, H. I. Study of Physical Mixtures of Cr_2O_3 −ZnO and ZSM-5 Catalysts for the Transformation of Syngas into Liquid Hydrocarbons. *Ind. Eng. Chem. Res.* **37**, 1211–1219 (1998).
41. Delparish, A. & Avci, A. K. Intensified catalytic reactors for Fischer-Tropsch synthesis and for reforming of renewable fuels to hydrogen and synthesis gas. *Fuel Processing Technology* **151**, 72–100 (2016).
42. Onel, O., Niziolek, A. M. & Floudas, C. A. Optimal Production of Light Olefins from Natural Gas via the Methanol Intermediate. *Ind. Eng. Chem. Res.* **55**, 3043–3063 (2016).
43. Nieskens, D. L. S., Ciftci, A., Groenendijk, P. E., Wielemaker, M. F. & Malek, A. Production of Light Hydrocarbons from Syngas Using a Hybrid Catalyst. *Ind. Eng. Chem. Res.* **56**, 2722–2732 (2017).
44. Zhang, Q., Li, X., Asami, K., Asaoka, S. & Fujimoto, K. Synthesis of LPG from synthesis gas. *Fuel Processing Technology* **85**, 1139–1150 (2004).
45. Jiao, F. *et al.* Selective conversion of syngas to light olefins. *Science* **351**, 1065–1068 (2016).
46. Pan, X., Jiao, F., Miao, D. & Bao, X. Oxide–Zeolite-Based Composite Catalyst Concept That Enables Syngas Chemistry beyond Fischer–Tropsch Synthesis. *Chem. Rev.* **121**, 6588–6609 (2021).
47. Zecevic, J., Vanbutsele, G., de Jong, K. P. & Martens, J. A. Nanoscale intimacy in bifunctional catalysts for selective conversion of hydrocarbons. *Nature* **528**, 245–248 (2015).
48. Weitkamp, J. Catalytic Hydrocracking—Mechanisms and Versatility of the Process. *ChemCatChem* **4**, 292–306 (2012).
49. Weisz, P. B. Polyfunctional Heterogeneous Catalysis. in *Advances in Catalysis* vol. 13 137–190 (Elsevier, 1962).
50. Batalha, N., Pinard, L., Bouchy, C., Guillon, E. & Guisnet, M. n-Hexadecane hydroisomerization over Pt-HBEA catalysts. Quantification and effect of the intimacy between metal and protonic sites. *Journal of Catalysis* **307**, 122–131 (2013).
51. Francis, J. *et al.* Design of improved hydrocracking catalysts by increasing the proximity between acid and metallic sites. *Applied Catalysis A: General* **409–410**, 140–147 (2011).
52. Gutierrez-Acebo, E., Leroux, C., Chizallet, C., Schuurman, Y. & Bouchy, C. Metal/Acid Bifunctional Catalysis and Intimacy Criterion for Ethylcyclohexane Hydroconversion: When Proximity Does Not Matter. *ACS Catal.* **8**, 6035–6046 (2018).
53. Samad, J. E., Blanchard, J., Sayag, C., Louis, C. & Regalbuto, J. R. The controlled synthesis of metal-acid bifunctional catalysts: The effect of metal:acid ratio and metal-acid proximity in Pt silica-alumina catalysts for n-heptane isomerization. *Journal of Catalysis* **342**, 203–212 (2016).
54. Henry, R. *et al.* Vacuum gas oil hydrocracking performance of bifunctional Mo/Y zeolite catalysts in a semi-batch reactor. *Catalysis Today* **220–222**, 159–167 (2014).
55. Chen, Y. *et al.* C_2 - C_4 hydrocarbons synthesis from syngas over CuO-ZnO-Al_2O_3/SAPO-34 bifunctional catalyst : Hydrocarbons synthesis from syngas over bifunctional catalyst. *J. Chem. Technol. Biotechnol.* **90**, 415–422 (2015).

56. Li, J., Pan, X. & Bao, X. Direct conversion of syngas into hydrocarbons over a core–shell Cr-Zn@SiO2@SAPO-34 catalyst. *Chinese Journal of Catalysis* **36**, 1131–1135 (2015).
57. Zhou, Y. *et al.* Methanol-to-olefin induction reaction over SAPO-34. *Chinese Journal of Catalysis* **37**, 1496–1501 (2016).
58. Wang, S. *et al.* Direct Conversion of Syngas into Light Olefins with Low CO_2 Emission. *ACS Catal.* **10**, 2046–2059 (2020).
59. Li, N. *et al.* High-Quality Gasoline Directly from Syngas by Dual Metal Oxide–Zeolite (OX-ZEO) Catalysis. *Angew. Chem. Int. Ed.* **58**, 7400–7404 (2019).
60. Yang, J. *et al.* Enhanced aromatic selectivity by the sheet-like ZSM-5 in syngas conversion. *Journal of Energy Chemistry* **35**, 44–48 (2019).
61. Cheng, K. *et al.* Bifunctional Catalysts for One-Step Conversion of Syngas into Aromatics with Excellent Selectivity and Stability. *Chem* **3**, 334–347 (2017).
62. Yang, J., Pan, X., Jiao, F., Li, J. & Bao, X. Direct conversion of syngas to aromatics. *Chem. Commun.* **53**, 11146–11149 (2017).
63. Yang, X. *et al.* The influence of alkali-treated zeolite on the oxide–zeolite syngas conversion process. *Catal. Sci. Technol.* **8**, 4338–4348 (2018).
64. Zhu, Y. *et al.* Role of Manganese Oxide in Syngas Conversion to Light Olefins. *ACS Catal.* **7**, 2800–2804 (2017).
65. Li, G. *et al.* Selective conversion of syngas to propane over ZnCrO -SSZ-39 OX-ZEO catalysts. *Journal of Energy Chemistry* **36**, 141–147 (2019).
66. Kirilin, A. V. *et al.* Conversion of Synthesis Gas to Light Olefins: Impact of Hydrogenation Activity of Methanol Synthesis Catalyst on the Hybrid Process Selectivity over Cr–Zn and Cu–Zn with SAPO-34. *Ind. Eng. Chem. Res.* **56**, 13392–13401 (2017).
67. Kanai, J. On the nature of the active sites for ethylene hydrogenation in metal-free zeolites. *Journal of Catalysis* **133**, 527–543 (1992).
68. Senger, S. & Radom, L. Zeolites as Transition-Metal-Free Hydrogenation Catalysts: A Theoretical Mechanistic Study. *J. Am. Chem. Soc.* **122**, 2613–2620 (2000).
69. Vityuk, A. *et al.* Room-Temperature Ethene Hydrogenation Activity of Transition-Metal-Free HY Zeolites. *ACS Catal.* **9**, 839–847 (2019).
70. Li, N. *et al.* Size Effects of ZnO Nanoparticles in Bifunctional Catalysts for Selective Syngas Conversion. *ACS Catal.* **9**, 960–966 (2019).
71. Fu, X., Li, J., Long, J., Guo, C. & Xiao, J. Understanding the Product Selectivity of Syngas Conversion on ZnO Surfaces with Complex Reaction Network and Structural Evolution. *ACS Catal.* **11**, 12264–12273 (2021).
72. Wang, S., Fang, Y., Huang, Z., Xu, H. & Shen, W. The Effects of the Crystalline Phase of Zirconia on C–O Activation and C–C Coupling in Converting Syngas into Aromatics. *Catalysts* **10**, 262 (2020).
73. Su, J. *et al.* Direct Conversion of Syngas into Light Olefins over Zirconium-Doped Indium(III) Oxide and SAPO-34 Bifunctional Catalysts: Design of Oxide Component and Construction of Reaction Network. *ChemCatChem* **10**, 1536–1541 (2018).
74. Liu, X. *et al.* Design of efficient bifunctional catalysts for direct conversion of syngas into lower olefins *via* methanol/dimethyl ether intermediates. *Chem. Sci.* **9**, 4708–4718 (2018).

75. Liu, X. *et al.* Tandem Catalysis for Hydrogenation of CO and CO_2 to Lower Olefins with Bifunctional Catalysts Composed of Spinel Oxide and SAPO-34. *ACS Catal.* **10**, 8303–8314 (2020).
76. Zhang, P. *et al.* Excellent selectivity for direct conversion of syngas to light olefins over a Mn–Ga oxide and SAPO-34 bifunctional catalyst. *Catal. Sci. Technol.* **9**, 5577–5581 (2019).
77. Cheng, K. *et al.* Direct and Highly Selective Conversion of Synthesis Gas into Lower Olefins: Design of a Bifunctional Catalyst Combining Methanol Synthesis and Carbon–Carbon Coupling. *Angew. Chem.* **128**, 4803–4806 (2016).
78. Raveendra, G., Li, C., Cheng, Y., Meng, F. & Li, Z. Direct transformation of syngas to lower olefins synthesis over hybrid Zn–Al_2O_3/SAPO-34 catalysts. *New J. Chem.* **42**, 4419–4431 (2018).
79. Ni, Y. *et al.* Realizing and Recognizing Syngas-to-Olefins Reaction via a Dual-Bed Catalyst. *ACS Catal.* **9**, 1026–1032 (2019).
80. Huang, Z.-Q., Li, T.-H., Yang, B. & Chang, C.-R. Role of surface frustrated Lewis pairs on reduced CeO2(110) in direct conversion of syngas. *Chinese Journal of Catalysis* **41**, 1906–1915 (2020).
81. Huang, Y. *et al.* Role of nanosized sheet-like SAPO-34 in bifunctional catalyst for syngas-to-olefins reaction. *Fuel* **273**, 117771 (2020).
82. Khadzhiev, S. N., Magomedova, M. V. & Peresypkina, E. G. Mechanism of olefin synthesis from methanol and dimethyl ether over zeolite catalysts: A review. *Pet. Chem.* **54**, 245–269 (2014).
83. Wang, W., Buchholz, A., Seiler, M. & Hunger, M. Evidence for an Initiation of the Methanol-to-Olefin Process by Reactive Surface Methoxy Groups on Acidic Zeolite Catalysts. *J. Am. Chem. Soc.* **125**, 15260–15267 (2003).
84. Yang, G., Meng, F., Zhang, P., Yang, L. & Li, Z. Effects of preparation method and precipitant on Mn–Ga oxide in combination with SAPO-34 for syngas conversion into light olefins. *New J. Chem.* **45**, 7967–7976 (2021).
85. Yuxuan Huang, Weixin Qian, Hongfang Ma, Haitao Zhang & Weiyong Ying. Impact Of Zn/Cr Ratio On Zncrox-Sapo-34 Bifunctional Catalyst For Direct Conversion Of Syngas To Light Olefins. *International Journal of Chemical, Materials and Biomolecular Sciences* **12**, 557–563 (2018).
86. Jiao, F. *et al.* Shape-Selective Zeolites Promote Ethylene Formation from Syngas via a Ketene Intermediate. *Angew. Chem.* **130**, 4782–4786 (2018).
87. Li, G. *et al.* Role of SAPO-18 Acidity in Direct Syngas Conversion to Light Olefins. *ACS Catal.* **10**, 12370–12375 (2020).
88. Huang, Y. *et al.* Utilization of SAPO-18 or SAPO-35 in the bifunctional catalyst for the direct conversion of syngas to light olefins. *RSC Adv.* **11**, 13876–13884 (2021).
89. Kosanović, C. *et al.* Mechanochemistry of zeolites: Part 1. Amorphization of zeolites A and X and synthetic mordenite by ball milling. *Zeolites* **13**, 261–268 (1993).
90. Kosanović, C. *et al.* Mechanochemistry of zeolites. Part 4: Influence of cations on the rate of amorphization of zeolite A by ball milling. *Zeolites* **15**, 632–636 (1995).
91. Kosanović, C., Subotić, B. & Čižmek, A. Thermal analysis of cation-exchanged zeolites before and after their amorphization by ball milling. *Thermochimica Acta* **276**, 91–103 (1996).
92. Kosanovic, C., Subotic, B. & Smit, I. Thermally induced phase transformations in cation-exchanged zeolites 4A, 13X and synthetic mordenite and their amorphous derivatives obtained by mechanochemical treatment. *Thermochimica Acta* **317**, 25–37 (1998).

93. Saepurahman & Hashaikeh, R. Insight into ball milling for size reduction and nanoparticles production of H-Y zeolite. *Materials Chemistry and Physics* **220**, 322–330 (2018).
94. Kosanović, C. *et al.* Mechanochemistry of zeolites: Part 2. Change in particulate properties of zeolites during ball milling. *Zeolites* **15**, 247–252 (1995).
95. Chen, Z. *et al.* The carboxylates formed on oxides promoting the aromatization in syngas conversion over composite catalysts. *Chinese Journal of Catalysis* **42**, 835–843 (2021).
96. Silver, R. The role of lattice anion vacancies in the activation of CO and as the catalytic site for methanol synthesis over zirconium dioxide and yttria-doped zirconium dioxide. *Journal of Catalysis* **118**, 400–416 (1989).
97. Jung, C. *et al.* Different support effect of M/ZrO2 and M/CeO2 (M=Pd and Pt) catalysts on CO adsorption: A periodic density functional study. *Catalysis Today* **111**, 322–327 (2006).
98. Meyer, B. First-principles study of the polar O-terminated ZnO surface in thermodynamic equilibrium with oxygen and hydrogen. *Phys. Rev. B* **69**, 045416 (2004).
99. Mun, B. S., Liu, Z., Motin, M. A., Roy, P. C. & Kim, C. M. In situ observation of H2 dissociation on the ZnO (0001) surface under high pressure of hydrogen using ambient-pressure XPS. *International Journal of Hydrogen Energy* **43**, 8655–8661 (2018).
100. Traeger, F., Kauer, M., Wöll, Ch., Rogalla, D. & Becker, H.-W. Analysis of surface, subsurface, and bulk hydrogen in ZnO using nuclear reaction analysis. *Phys. Rev. B* **84**, 075462 (2011).
101. Ebitani, K. Activation of molecular hydrogen into protonic acid sites over metal-free H-ZSM-5 catalyst. *Journal of Catalysis* **138**, 750–753 (1992).
102. Gounder, R. & Iglesia, E. Catalytic hydrogenation of alkenes on acidic zeolites: Mechanistic connections to monomolecular alkane dehydrogenation reactions. *Journal of Catalysis* **277**, 36–45 (2011).
103. Xin, Y., Qi, P., Duan, X., Lin, H. & Yuan, Y. Enhanced Performance of Zn–Sn/HZSM-5 Catalyst for the Conversion of Methanol to Aromatics. *Catal Lett* **143**, 798–806 (2013).
104. Schulz, H. “Coking” of zeolites during methanol conversion: Basic reactions of the MTO-, MTP- and MTG processes. *Catalysis Today* **154**, 183–194 (2010).
105. Yu, L. *et al.* Transformation of Isobutyl Alcohol to Aromatics over Zeolite-Based Catalysts. *ACS Catal.* **2**, 1203–1210 (2012).
106. Zhang, G. Q., Bai, T., Chen, T. F., Fan, W. T. & Zhang, X. Conversion of Methanol to Light Aromatics on Zn-Modified Nano-HZSM-5 Zeolite Catalysts. *Ind. Eng. Chem. Res.* **53**, 14932–14940 (2014).
107. Gao, P. *et al.* Direct conversion of CO2 into liquid fuels with high selectivity over a bifunctional catalyst. *Nature Chem* **9**, 1019–1024 (2017).
108. Tan, L. *et al.* Design of a core–shell catalyst: an effective strategy for suppressing side reactions in syngas for direct selective conversion to light olefins. *Chem. Sci.* **11**, 4097–4105 (2020).

Chapter 2 : Experimental methods

1) Introduction

In this chapter we will describe the experimental methods used along this thesis. X-Ray Diffraction and N_2 adsorption were used to characterise the crystalline phases and the specific surface area of each solid. Attenuated reflectance Infrared spectroscopy was used to follow the decomposition of our solid's precursor and the deposition of silica on MnO. Raman spectroscopy was used to further characterize the reference oxide phases. Then Inductively Coupled Plasma – Optical Emission Spectrometry was used to determine the composition of the prepared zeolite. Solid state Nuclear Magnetic Resonance was used to determine the local environment of framework atom and used in conjunction with NH_3-TPD to express the acidity of the prepared zeolite. Spent catalyst were characterized by ^{13}C NMR, CHONS, TGA and GC-MS to determine the proportion and nature of trapped species in zeolite. Later on, surface species in Ox-Zeo were observed with in-situ DRIFT experiment. The prepared core-shell structure was characterized with TEM and FX to determine the core size, shell thickness and the proportion of free silica. MEB images were used to observe the intimacy and its evolution in random mixes. Finally, the catalytic test outlet was followed with a GC-TCD analyser.

2) Characterization techniques

2.1) Elemental analysis

2.1.1) Inductively Coupled Plasma – Optical Emission Spectrometry (ICP-OES)

Inductively Coupled Plasma-Atomic Emission Spectrometry (ICP-AES) is a method used to determine the elemental composition of a sample. The sample is dissolved in a specific matrix (usually mixture of acids) and is then injected, vaporized and decomposed into a radiofrequency (RF)-induced argon plasma. The excited atoms and ions in the discharge plasma create a unique emission spectrum specific to each element. The spectra are recorded using a spectrometer

equipped with a Charge Coupled Device (CCD) detector allowing to determine the proportion of each element.

This technique has been used for quantification of Si, Al, P and Mn on an ICP-OES Activa spectrometer (Horiba). For Al, P and Mn quantification, the solid was firstly dissolved in H_2SO_4+HNO_3+HF at boiling point before being injected into the analysis apparatus. For Si, the solid has been fused with lithium tetraborate into a Pt-Au crucible at 1100 °C. The obtained solid was then dissolved into a 20% HCl solution before injection.

2.1.2)Fluorescence X spectroscopy

Fluorescence X (FX) spectroscopy is a non-destructive method using the emission spectrum generated under an X-ray beam and characteristic of each atom to determine the composition of a sample. An incident X-Ray beam which is sent to the sample ejects an electron of the inner shell of the atom with an energy Ex. A second electron (with an energy Ey such as Ey > Ex) fills the hole caused by the first electron ejection as represented in **Figure 1**. This creates the emission of a photon whose wavelength ranges in the X-rays. The energy of this photon depends on the energy difference Ey-Ex and thus, is characteristic of the atom. By counting the number of photons at each energy, it is possible to quantify chemical elements present in the sample, using a calibration curve.

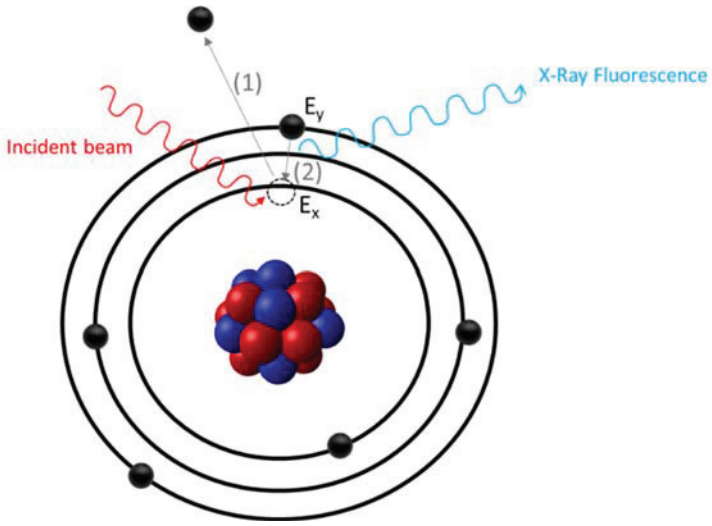

Figure 1: principle of FX spectroscopy.

FX was mainly implemented to determine the proportion the Mn and Si in the core-shell structures and the nature of impurities in some precursors. For that purpose, an Epsilon 4

(Panalytical) spectrometer was used with an Ag 15 W-3 mA X-ray source and a resolution of 135 eV (Mn Kα).

2.1.3)CHNS elemental analysis

CHNS analysis is a method used to determine the proportion of C, H, N and S in a sample. For that purpose, a crucible containing the sample is introduced into an oven heated at 950 °C and containing enough O_2 to achieve a complete combustion of the sample. The gases produced during the combustion are sent through two catalytic layers to be completely converted to NO_2, CO_2, H_2O and SO_2. Then, the outlet flow is usually analysed by a GC equipped with a TCD detector.

The measurements have been performed with a Flash 2000 elemental analyser equipped with a MAS200R autosampler (Thermo Fisher Scientific).

2.2) X-ray diffraction

X-Ray Diffraction (XRD) is a bulk technique used to identify and quantify the crystalline phases present in a solid. A monochromatic X-ray beam is sent to a sample at variable incident angles θ. The X-rays are diffracted by atomic planes of a crystalline structure according to the Bragg's law: $n\lambda = 2d(hkl)\sin(\Theta)$ where d(hkl) is the spacing between diffracting planes, θ the incident angle, n any integer and λ the wavelength of the X-ray beam, as represented in **Figure 2**. By scanning the sample through a range of θ angles, all possible diffraction directions of the crystalline lattice should be attained due to the random orientation of the powdered material. Conversion of the diffraction angles to d-spacings followed by comparison with a standards library allows identification of the crystalline phases present in the solid.

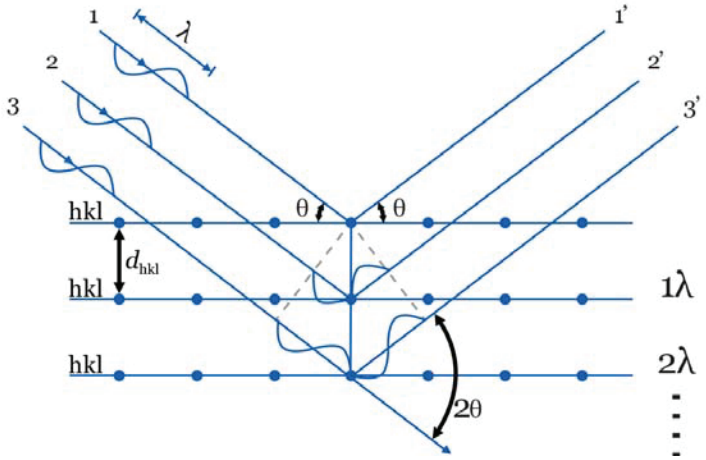

Figure 2: X-Rays diffraction by atomic planes.

XRD diffractograms were achieved between 4 and 80° (2Θ) on a Bruker D8 Advance A25 diffractometer equipped with a Ni filter (Cu K_α radiation: 0.154184 nm) and a one-dimensional multistrip detector (Lynxeye, 192 channels on 2.95°). The counting per point was 0.5 s. The International Center for Diffraction Data (ICDD) library was used for phase identification.

Furthermore, the crystallite size was determined using the Scherrer equation:

$$D = \frac{K\lambda}{\beta_i * \cos(\theta)} \quad (1)$$

Where D is the crystallite size, λ the wavelength of the X-ray beam, β_i the full width half maximum corrected of the instrumental width (0.06°) and θ the diffraction peak angle.

2.3) Spectroscopic techniques

2.3.1) Infrared (IR) spectroscopy

Vibrational modes of chemical entities depend on the symmetry and on the bond strength. Infra-Red (IR) spectroscopy is vibrational spectroscopy that measures absorption or emission of an IR beam. A vibrational mode could be detected by IR spectroscopy if the dipolar moment of the molecule/crystal is modified during vibration. Fourier Transform IR (FTIR) spectrometers that simultaneously collect spectral data over a wide spectral range are commonly used for their short acquisition time. Two different analytical methods, namely attenuated total reflection and diffuse reflectance have been used in this work.

a) Attenuated Total Reflection (ATR)

Attenuated total reflection (ATR) is an IR sampling method allowing fast analysis with minimal requirements for sample preparation. The sample is placed and pressed against a high reflectance crystal. An IR beam is passed through the crystal at an angle allowing total reflectance. The reflected light at sample/crystal interface is partially adsorbed by the sample and recorded to collect an IR spectrum.

ATR spectroscopy has been used to follow the decomposition of precursors and templates of the prepared catalysts. It has also been used to observe surface species present on the surface of MnO_x cores prior to the SiO_2 shell deposit.

The spectra were recorded with a Cary 630 FTIR spectrometer (Agilent) equipped with a diamond crystal. The spectral resolution was 2 cm^{-1} from 4000 cm^{-1} to 650 cm^{-1}.

b) Diffuse Reflectance Infrared Fourier Transform (DRIFT)

Diffuse Reflectance Infrared Fourier Transform (DRIFT) spectroscopy is a simple and effective method for the analysis of powders: an IR beam is sent to a powder sample and diffused light is collected by an integration sphere. Different *in situ* and *operando* cells have been designed to characterize solid catalysts [1,2]. Usually, a gas flow goes through the powder sample put in a crucible that can be heated. The cell contains a dome with IR transparent windows to send the IR beam to the sample and recollect the diffused light (**Figure 3**).

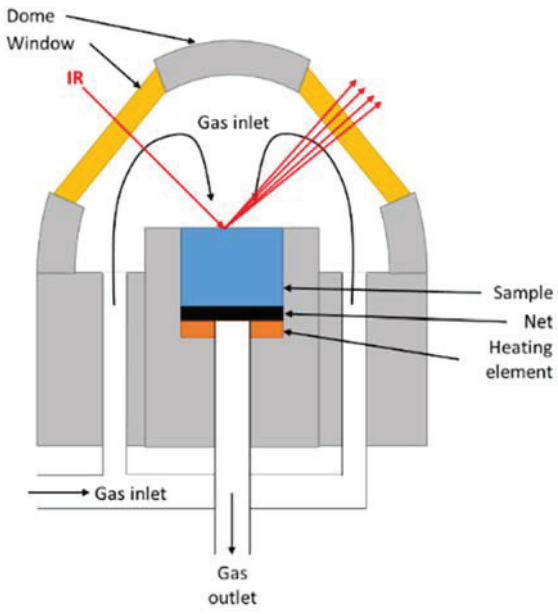

Figure 3: Schematic representation of a DRIFT *in situ* cell.

DRIFT spectroscopy was implemented to follow the evolution of surface species over MnOx and MnO_x+SAPO34 mechanical mixture under CO and CO/H_2 flows at temperature ranging fro - 2 °C to 450 ° C at atmospheric pressure. The spectra were recorded using a Nicolet 6700 FTIR spectrometer (Thermo Fisher Scientific) equipped with Praying Mantis High Temperature Reaction Chamber (Harrick, model HVC DRP 4, ZnSe windows) and a MCT detector cooled by liquid N_2. The spectral resolution was 4 cm^{-1}. The gradient of temperature between the regulation thermocouple and the upper part of the powder bed was calibrated and corrected.

2.3.1)Raman spectroscopy

Raman spectroscopy is a vibrational spectroscopy that uses two processes occurring when an incident monochromatic light is sent to a sample:

- A photon excites an electron from the fundamental state to a vibrational one via a virtual state leading to scattering a photon with lower energy (Stokes Raman effect).
- A photon excites an electron from a vibrational state to the fundamental one via a virtual state leading to scattering a photon with higher energy (anti-Stokes Raman effect).

The knowledge of the photon energy loss (Stokes) or gain (anti-Stokes) provides the energy (wavenumber) of the vibrational states of the studied matter. Thus, Raman spectroscopy is a

vibrational spectroscopy similarly to IR and it is possible to characterize chemical bonds in a molecular or crystalline structure and obtain information on the structural symmetry or on the force constants and bonds strength.

Raman spectroscopy was implemented to characterize the structure of MnO_x sample under H_2 at various temperatures. Raman spectra were obtained with a LabRAM HR spectrometer (Horiba) equipped with a CCD open electrode detector cooled at -75 °C. The exciting line at 514.53 nm of an Ar^+ ion laser was focused on samples with an X50 objective which also recollected the diffused light before dispersion with a diffraction grating (spectral resolution of 4 cm^{-1}). The power at sample was limited to 100 µW to avoid laser heating. A THMS600 cell coupled with a TM594 programmer (Linkam) was used for *in situ* measurements. The gradient of temperature between the heating sole and the top layer of the sample was calibrated and corrected.

2.3.2)Nuclear Magnetic Resonance

Nuclear Magnetic Resonance (NMR) spectroscopy is a technique used to determine the chemical environment of magnetic nuclei present in the analysed sample. Shortly, in a nucleus having non-zero (usually odd) spin. If put in an external magnetic field, the energy levels are split (Zeeman effect). Therefore, an energy transfer becomes possible between the ground state and higher energy levels (generally a single energy gap). In NMR spectroscopy, the energy transfer takes place at a wavelength that corresponds to radio frequencies. Absorption of energy by nuclei occurs during a short radio wave pulse, in a narrow window of frequencies (resonance effect). Then, during the relaxation of the nuclei a radio frequency characteristic of the nuclei and its environment is emitted and recorded to get NMR spectra. Unequal screening of nuclei by their electron shells in the chemical species leads to inequality of the resonance frequencies and allows fine analysis of chemical structures.

NMR spectroscopy has been used to determine the chemical structure of SAPO-34 through the ^{27}Al, ^{31}P and ^{29}Si atoms. Spectra were recorded using a Bruker Advance III 500WB. ^{31}P MAS NMR analysis were performed using a 4 mm triple channel probe at B_0=7,56 T (Larmor frequency ν_0=130.29 MHz). Samples were spun at a rate of 12 KHz. Free Induction Decays (FID) were collected with 3.25 µs radiofrequency pulse and a recycle time of 60 s. H_3PO_4-85% was used as a reference

for the chemical shift. ^{27}Al MAS NMR spectra were obtained using a 4 mm double channel probe at B_0=18,24 T (Larmor frequency ν_0=202.4 MHz). Samples were spun at rate of 12 KHz. FID data were collected with 0.8 µs radiofrequency pulse and a recycle time of 800 ms. $Al(NO_3)_3$ 1 M in D_2O was used as a reference for the chemical shift. ^{29}Si MAS NMR spectra were performed using a 4 mm double channel probe at B_0=11,74 T (Larmor frequency ν_0=99.34 MHz). Samples were spun at rate of 10 KHz. FID data were collected with 4 µs radiofrequency pulse and a recycle time of 60 s. Octakis(trimethylsiloxy)silsesquioxane (Q8M8) was used as a reference for the chemical shift. 13C NMR was also used to determine the chemical nature of trapped species in spent catalyst. Analysis were performed using a 4 mm double channel probe at B0=11.74 T (Larmor frequency v0=125.73 MHz). Samples were spun at a rate of 10 KHz. FID were collected with 2.5 µs radiofrequency pulse and a recycle time of 5 s. Adamantane was used as a reference for the chemical shift.

2.4) Electron microscopy

2.4.1) Transmission electron microscopy

Transmission electron microscopy (TEM) is a technique used to observe nanosized objects, to determine their morphology and crystal structure. It consists of sending an electron beam toward the sample. An image is formed from the interaction of the electrons with the sample as the beam is transmitted through this sample. It is then magnified and focused onto an imaging device, such as a scintillator attached to a CCD camera. TEM has been implemented to determine the size of core-shell particles and SAPO-34 crystals through statistical treatment of TEM images. The dimension of the object were measured using ImageJ software and statistical analysis were done on the measurement to determine the mean value and the uncertainty.

Images were acquired using a JEOL 2010 with a 200 kV accelerating voltage equipped with a LaB6 source and a CCD Gatan camera. The spatial resolution was 0.19 nm. The TEM device is coupled with energy dispersive (EDS) spectrometer (Oxford Instruments) that analyses X-rays released due to excitation of core levels of elements present in the sample by high energy electrons. Analysis of that X-rays allows to carry out semi-quantitative chemical analysis of the observed particles.

2.4.2)Scanning electron microscopy

Scanning electron microscopy (SEM) is a technique used to determine the morphology, topography and the 'surface' (few microns) composition of a sample. Images are obtained by scanning the surface with a focused beam of electrons. The impact of incident electrons produces Secondary Electrons (SE), Back Scattered Electron (BSE) and X-rays. The SE and BSE are used to get images, whereas X-rays are used to determine the elemental composition of the analysed sample (same EDS principle as in TEM).

These analyses have been used to follow the textural evolution of the catalyst mixture after activation and after catalytic test. SEM images were recorded using a FEI ESEM-XL30 device with a 15 kV accelerating voltage.

2.5) Textural analyses by N2 adsorption

Nitrogen physisorption at liquid N_2 temperature is used to determine textural properties of a sample such as its specific surface area, pore volume and pore size distribution. Shortly, the solid is exposed to N_2 at a step wisely changing pressure and 77 K. The quantity of N_2 necessary to obtain a pressure equilibrium is used to determine the quantity of adsorbed N_2. From those measurements, the BET method[3] is used to determine the BET surface area, the BJH method[4] to determine the pore volume and size and the t-plot method[5] to determine microporosity.

Textural analyses of MnOx oxides and SAPO-34 zeotypes were performed on a micromeritic ASAP 2020 instrument after desorption of the solid at 400 °C for 2 h under vacuum of 0.1 Pa.

2.6) Temperature programmed desorption of NH3 (NH3-TPD)

NH_3-TPD is used to determine the quantity and strength of acid sites in a solid. For that purpose, NH_3 is first chemisorbed at the surface of a solid and then desorbed upon linear heating. Shortly, after sample outgassing at a specific temperature, NH_3 is adsorbed at low temperature (from room temperature to 100 °C). Then the excess (physiosorbed and/or weakly chemisorbed) of NH_3 is flushed under He and the temperature is increased at a specific heating rate. The quantity of desorbed NH_3 is determined at the outlet of the reactor to get a TPD curve.

NH_3-TPD measurements were performed to determine the quantity and strength of acid sites in different SAPO-34 samples using a BelCat-M (Bel Japan Inc.) apparatus equipped with a TCD detector, as represented in **Figure 4**. First around 60 mg of solid was flushed under He flow at 400 °C for 1 h to remove adsorbed molecules and the solid was exposed to 50 nml.min $^{-1}$ of 1% NH_3-He for 30 min. After flushing the sample under He at 100 °C until a stable TCD signal was observed, the temperature was raised at a rate of 10 °C/min under 50 nml.min^{-1} of He. The number of acid sites was determined by integration over time of the quantity of NH_3 desorbed.

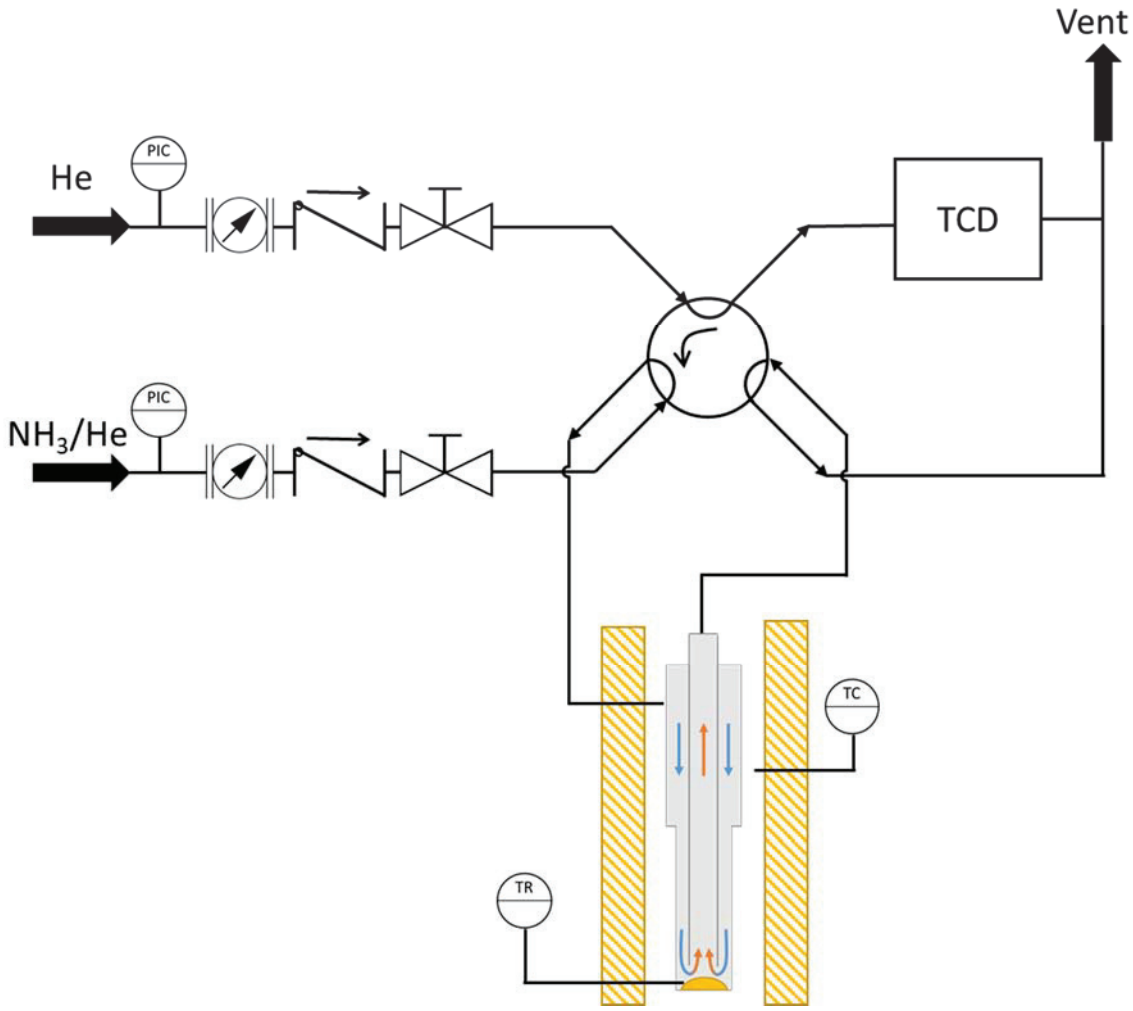

Figure 4 : Scheme of the TPD-NH_3 workbench.

2.7) Thermo-gravimetric analysis

Thermogravimetric analysis (TGA) consists of following the mass variation and heat exchange of a solid as a function of temperature under a controlled atmosphere.

TGA has been used to access thermal evolution processes (removal of water and other volatile compounds, carbonate decomposition...) in spent MnO_x-SAPO-34 mixtures. Approximately 5 mg of sample was put in an alumina crucible and then introduced into the oven of a TGA Mettler Toledo apparatus. The sample was flushed in N_2 or air and then the temperature was increased at a specific rate.

2.8) Coke extraction and characterisation

The analysis of the coke composition in the spent was conducted in two step. First the coke located on the external surface was extracted by washing the solid with CH2Cl2 at 313 K and under 100 bar of nitrogen for 10 minutes in a Dionex ASE 350 apparatus. Then the extraction of the trapped molecule was conducted by dissolution of the zeolite structure. The spent catalyst was dissolved in a hydrofluoric acid (HF) solution in water (51 % vol) at room temperature for 20 min. After that the HF was neutralized by the addition of acid boric and sodium hydrogen carbonate. The left residue were extracted with CH2Cl2. The two fraction of soluble coke in CH2Cl2 are mixed together and dried. These soluble coke are then analysed by GC-MS (Thermoelectron DSQ). The low temperature of treatment by HF, the short contact time of the acid solution and the coke components as well as the very small contact area between mineral and organic phases allow to avoid any change of coke composition.

3) Catalytic measurements

3.1) Catalytic testing apparatus

3.1.1) Description

The apparatus can be divided into 3 parts as shown in **Figure 5** the reactor and furnace are located in part I. A set of 3 manual valves are used to send the inlet gas mixture toward the reactor or directly to the output allowing a bypass test. A manual pressure regulator place connected at the outlet was set at 25 bar. To perform a pre-treatment at atmospheric pressure, a vent was placed before the pressure regulator; it was closed during a catalytic testing. A manometer located before the reactor allows checking the pressure inside the system. All the lines in Part I were heated at 100 °C to avoid condensation of liquid products. A straight tubular steel reactor (internal

diameter of 6 mm) containing powder samples was used. A thermowell with an external diameter of 1.6 mm pass through the whole reactor allowing temperature measurement across the whole catalytic bed. The catalytic bed was centre in the reactor using quartz wool and can be as long as 10 cm.

Part II contains the reaction and pre-treatment gas inlet lines of Ar, CO, H_2 and N_2. Each line is composed of a Brooks 5850 TR flow regulator, a manometer and a stop valve.

Part III composed of two microGC is used for analysing the effluent gas. It is located after the pressure regulator and measurements are achieved at atmospheric pressure. The sampling for analysis is made by pumping the gas from the outlet line into a sampling line.

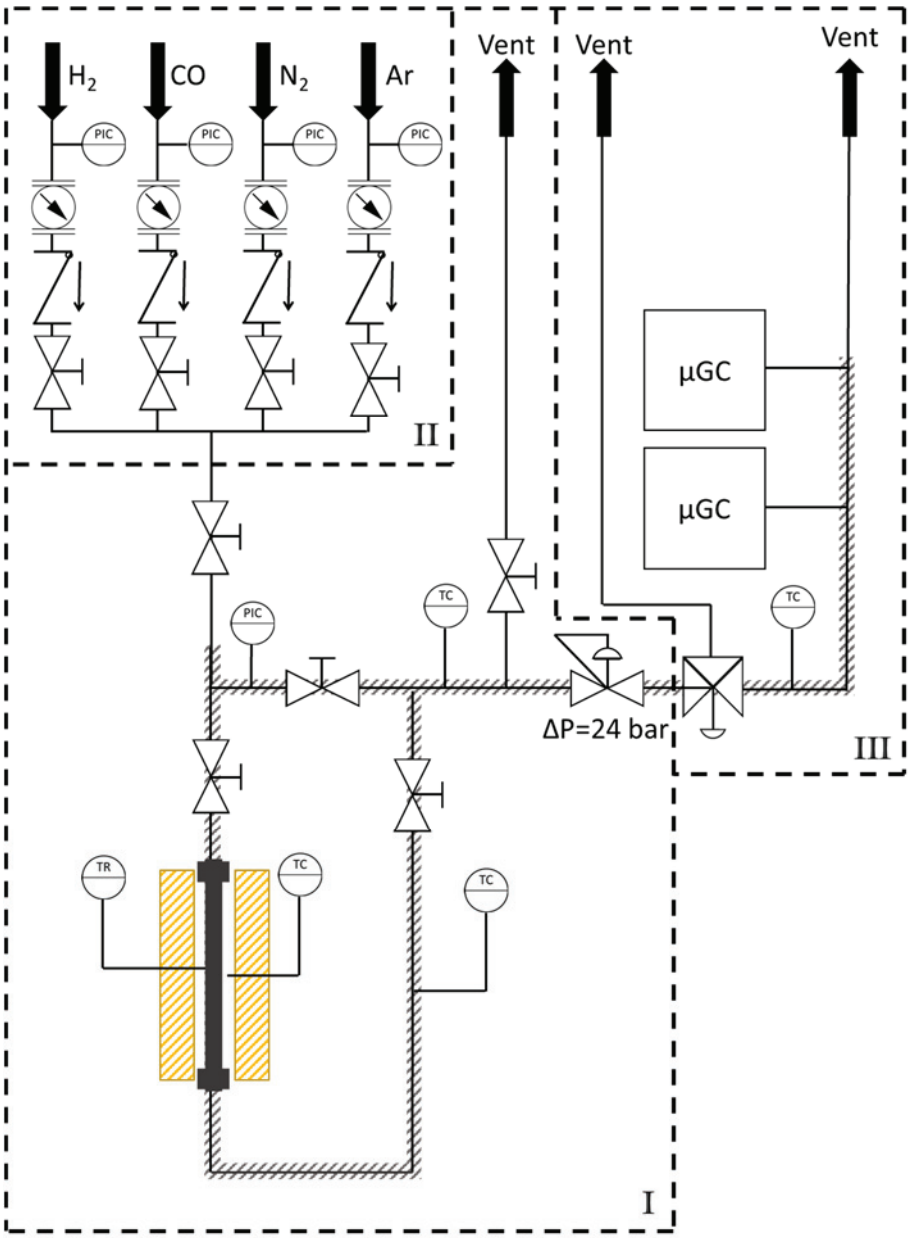

Figure 5: PID Scheme of the catalytic testing apparatus.

3.1.2)Control experiments

a) Furnace

A profile of temperature measured across the reactor using the reactor thermowell is presented in **Figure 6**. The regulation temperature for the oven was set at 400 °C. The temperature ranges from 269 °C to 412 °C with a parabolic curve center around 11 cm which corresponds to the center of the oven. By accepting a 3% error margin, a catalytic bed as long as 10 cm can be used.

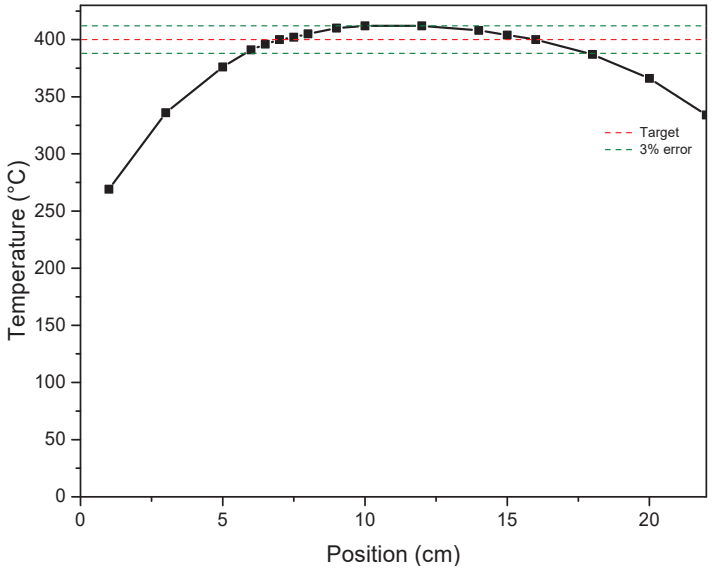

Figure 6: Evolution of the temperature with the position in the furnace.

b) Reactor

A validation of the reactor has been done by checking that no diffusion limitation occurred during catalytic tests and to determine the activity of the empty reactor in the reaction conditions. For that purpose, the Thiele modulus has been determined assuming a first order reaction law leading to **Equation 2**:

$$\phi = L_C \sqrt{\frac{k}{D_{CO}}} \qquad (2)$$

With Lc a characteristic distance for the diffusion, here the width of the static layer, k=0.01 s^{-1} the apparent kinetic constant estimated from Zhu and coll.[6] at 400 °C and D_{CO}=9x10^{-6} m^2/s the diffusion coefficient of CO in gas phase. To check external diffusion limitations, the width of the static layer was overestimated at 1 µm based on the fact that gases are used. ϕ is then equal to 3x10^{-5} which is negligible compare to 1. It means that the diffusion rate with a static layer of 1 µm is much faster than the observed reaction rate and no diffusion limitation should be observed.

3.2) Catalytic testing

The catalytic testing has been performed as follows: the reactor is placed inside the oven with quartz wool as insulating material placed at both extremities of the oven. The catalyst is pre-

treated at atmospheric pressure, using the atmospheric vent, under H_2 at a temperature ranging from 410 °C to 450 °C. Then, the reactor is flushed under N_2 and the atmospheric vent is closed increasing the pressure in the system. When the reaction pressure is reached, the reaction temperature is set up at the reaction temperature and the reactants are preloaded in their respective inlet lines to the reactor pressure. When the reactants (H_2 and CO) reached the reactor pressure, the flow of CO, N_2 and H_2 are set to their initial values and the inlet valves are opened. At this moment the µGC begins to sample from the atmospheric outlet line determining the composition of the outlet flow. Usually, the experiment lasts for at least 14 h to reach a steady state after what operation conditions as, the temperature, the gas feed composition and the contact time can be modified.

3.3) Reaction conditions

The activation step was performed under H_2 flow at atmospheric pressure varying the temperature from 410 °C up to 450 °C. The flow of H_2 per mass of catalyst was kept at 66,67 $nml.g_{cat}^{-1}.min$ (typically 300 mg catalyst and a H_2 flow of 20 $nml.min^{-1}$).

The reaction temperature was ranged from 390 °C to 450 °C and pressure was kept at 25 bar. The inlet flow could vary for each component, for H_2 up to 20 $nml.min^{-1}$, for CO up to 10 $nml.min^{-1}$, for N_2 up to 17 $nml.min^{-1}$ and for Ar up to 70 nml/min. In standard conditions, the H_2/CO ratio was kept around 2 and 10% of N_2 in the flow was used and the WHSV was 88.7 $nml.g_{cat}.min^{-1}$. Ar was used as diluent.

The GC analysis has been performed with two microGC that were directly linked to the outlet line. The first µGC, a Fusion/Chemlys, is equipped with a molecular sieve for CO, H_2, CH_4 and N_2 quantification and an alumina Na_2SO_4 column allowing quantification of hydrocarbons ranging from C2 to C6. The second microGC, a 3000/Inficon, was equipped with a Plot-U-column for the quantification of CO_2. Both microGC are equipped with a TCD detector.

Carbon balance was determined using the GC analysis and kept at 100 ±5 %

3.4) Activity of the empty reactor

Finally, a blank test has been performed loading the reactor only with quartz wool to determine the empty reactor activity. A conversion of 0.73 % was measured with a CH_4 selectivity of 50% and CO_2 selectivity of 33%. Selectivity of 12% for C2 hydrocarbons, 4.5% for C3, 0.04% of C4 and 0.05% C5+ were observed. This allows us to conclude that almost no reaction occurs from the reactor alone.

3.5) Catalyst properties

Catalytic properties have been determined from the microGC measurements. The conversion of CO was determined from the sum of yield for each product as described in **Equation 3**:

$$X = \frac{\sum_i \frac{\nu_{CO}}{\nu_i} x_i}{x_{COs} + \sum_i \frac{\nu_{CO}}{\nu_i} x_i} \quad (3)$$

Where x_i corresponds to the molar percent determined by GC analysis, ν_i to the stochiometric factor for the component i and x_{COs} to the molar percent of CO in the outlet. The denominator for **Equation 3** was chosen for two reasons. First, all the carbon containing products were detected with the GC analysis allowing us to complete the carbon mass equation (carbon balance close to 100%). Second, a slight deviation of inlet CO proportion have been observed over time leading to inaccuracy when using X_{COe}.

The selectivity value was determined by **Equation 4**:

$$S_i = \frac{\frac{\nu_{CO}}{\nu_i} x_i}{\sum_i \frac{\nu_{CO}}{\nu_i} x_i} \quad (4)$$

The ratio of Olefins to Paraffins (ratio O/P) was determined by calculating the ratio of olefins molar percent to the paraffin molar percent. Usually, the O/P Ratio for hydrocarbons ranging from C2 to C4 is presented.

$$\frac{O}{P} = \frac{\sum_o x_o}{\sum_p x_p} \quad (5)$$

The activation energy (Ea) was determined from the Arrhenius law using the **Equation 6** and **Equation 7**. The kinetic constant k was determined at multiple temperatures and used to determine the Ea linear regression of ln(k)=f(1/T).

$$k = Ae^{-\frac{Ea}{RT}} \tag{6}$$

$$\ln(\mathrm{k}) = \ln(\mathrm{A}) - \frac{Ea}{RT} \tag{7}$$

The apparent partial reaction orders were determined from the kinetic law described in **Equation 8**.

$$r_i = [H_2]^{ai}[CO]^{bi}k_i \tag{8}$$

Experiments were performed keeping constant [CO] while [H_2] varied for determination of the apparent partial order for H_2 with $k' = [CO]^{bi}k_i$.

$$\ln(r_i) = a_i * \ln[H_2] + \ln\left(k^{'}\right) \tag{9}$$

Other experiments were performed keeping constant [H_2] while [CO] varied for determination of the partial order for H_2 with $k'' = [H_2]^{ci}k_i$.

$$\ln(r_i) = b_i * \ln[CO] + \ln\left(k^{''}\right) \tag{10}$$

4) References

1. Meunier, F. C. Pitfalls and benefits of *in situ* and *operando* diffuse reflectance FT-IR spectroscopy (DRIFTS) applied to catalytic reactions. *React. Chem. Eng.* **1**, 134–141 (2016).
2. Meunier, F. C. The design and testing of kinetically-appropriate operando spectroscopic cells for investigating heterogeneous catalytic reactions. *Chem. Soc. Rev.* **39**, 4602 (2010).
3. Brunauer, S., Emmett, P. H., Teller, E. Adsorption of Gases in Multimolecular Layers. *J. Am. Chem. Soc.* **60**, 309–319 (1938).
4. Barrett, E. P., Joyner, L. G., Halenda, P. P. The Determination of Pore Volume and Area Distributions in Porous Substances. I. Computations from Nitrogen Isotherms. *J. Am. Chem. Soc.* **73**, 373–380 (1951).
5. de Boer, J. H., Lippens, B. C., Linsen, B. G., Broekhoff, J. C. P., van den Heuvel, A., Osinga, Th. J. Thet-curve of multimolecular N_2-adsorption. *J. Colloid Interface Sci.* **21**, 405–414 (1966).
6. Zhu, Y., Pan, X., Jiao, F., Li, J., Yang, J., Ding, M., Han, Y., Liu, Z., Bao, X. Role of Manganese Oxide in Syngas Conversion to Light Olefins. *ACS Catal.* **7**, 2800–2804 (2017).

Chapter 3 : Reference study on the Ox-Zeo process

1) Introduction

Before beginning to study the impact of intimacy on the Ox-Zeo process, reference data were needed. Therefore, the evolution of catalytic properties as a function of various parameters such as the activation and reaction temperatures, time on stream and reactant partial pressures have been determined. Furthermore, the relationship between the conversion and the selectivity values have been established and kinetic parameters such as the apparent activation energy and the partial reaction orders have been determined and compared to relevant literature. Finally, *in situ* DRIFT study has been conducted on the reference MnO_x and MnO_x+SAPO-34 mixtures to observe the surface species present during the reaction, allowing to give insight into the reaction intermediates on the surface of MnO+SAPO-34 system.

2) Preparation and characterization of reference solids

To study the catalytic behavior of the Ox-Zeo process, MnO_x oxide was chosen due to its simplicity compared to mixed oxides and H-SAPO-34 zeotype for both its commercial availability and simple synthesis protocols. These reference solids have been prepared and characterized in detail.

2.1) MnOx oxide.

2.1.1) Preparation

$MnCO_3$ (Aldrich ref. 377449, 99.9%) was used as precursor for the preparation of reference MnO_x according to the protocol reported by Zhu and coll.[1] 20 g of $MnCO_3$ was introduced into a borosilicate glass tubular reactor and placed in an oven. The solid was treated at 410 °C (heating rate 10 °C.min^{-1}) under 20% H_2-N_2 flow for 12 h. After this treatment the solid was cooled down to room temperature under H_2/N_2 mixture. At room temperature, the solid was kept under flowing air for 1 h until the solid turned from light green to brown suggesting passivation phenomenon. This sample is labelled MnOx-Ref in the following.

2.1.2)Characterization

The reference oxide was characterized by several physical techniques to verify the complete decomposition of the carbonate species and to determine the phase composition and the Mn oxidation state.

The decomposition of $MnCO_3$ was followed by ATR-FTIR spectroscopy. $MnCO_3$ spectra before and after calcination under H_2/N_2 are presented in **Figure 1**. The spectrum of $MnCO_3$ before calcination shows the characteristic bands of carbonate at 1469, 1390, 860 and 724 cm^{-1}.[2,3] After treatment under H_2 at 410 °C, no bands were observed above 800 cm^{-1} confirming total decomposition of the $MnCO_3$ into MnO_x.

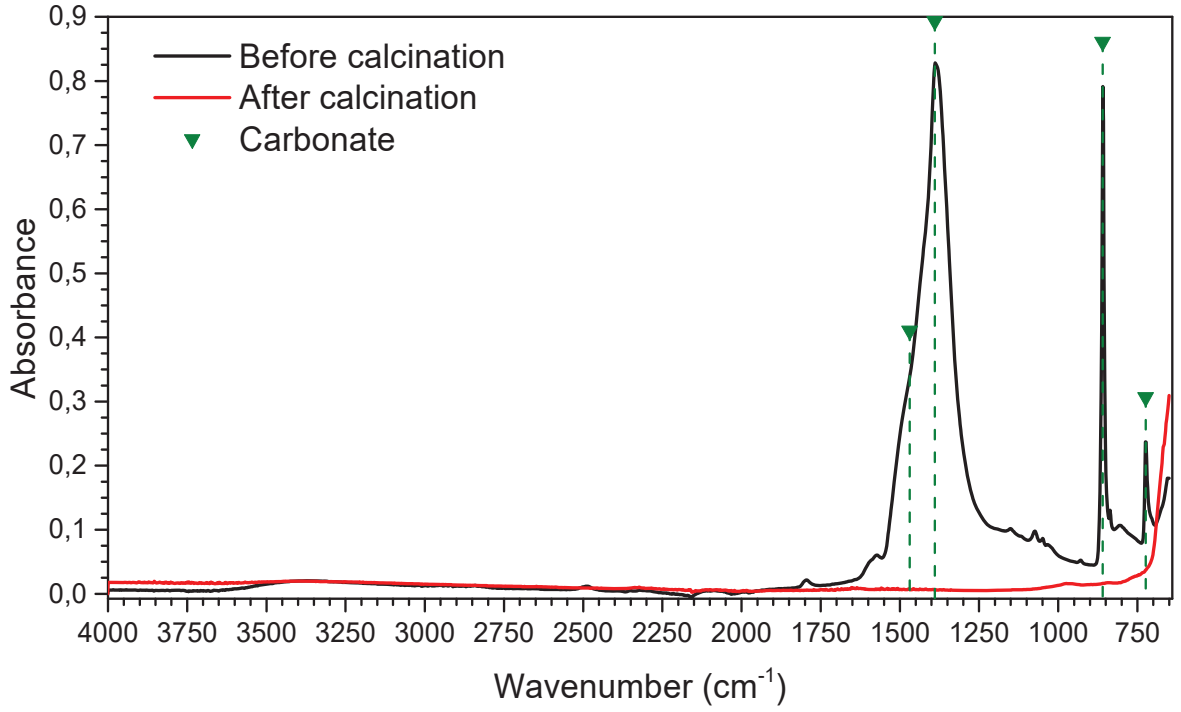

Figure 1: ATR-FTIR spectra of $MnCO_3$ sample before and after thermal treatment under 25%H_2/N_2 flow at 410 °C for 12 h.

XRD analysis was performed on MnO_x-Ref to determine the phase composition. The diffractogram displayed in **Figure 2A** shows characteristic peaks for cubic MnO phase(PDF 75-1090 ICDD pattern) with no other crystalline phases. Using the Scherrer equation, a crystallite size of 21 nm was found.

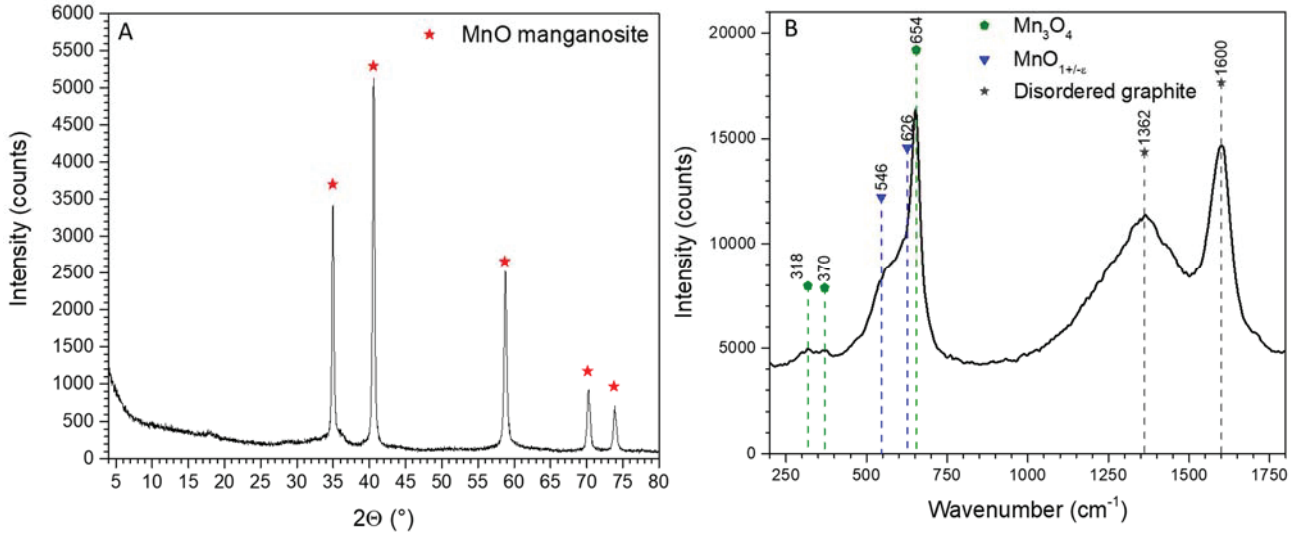

Figure 2: A) XRD diffractogram and B) Raman spectrum of MnO_x-Ref.

The Crystallite Specific Surface (CSS) can be estimated from this value assuming a perfect cubic crystal using **Equation 1**:

$$CSS = \frac{6}{a * \rho} \quad \textbf{(1)}$$

Where a is the crystallite size and ρ its volume weight (5.45 $g.cm^{-3}$).

It leads to a CSS value of 48 $m^2.g^{-1}$ while the BET specific surface area was 23 $m^2.g^{-1}$. The difference indicates that the MnO crystallites are slightly aggregated into larger particles.

Raman spectroscopy revealed the presence of Mn_3O_4 (bands at 318, 370 and 654 cm^{-1})[4–6] in addition to MnO feature around 550 cm^{-1} [7–9] and disordered graphite near 1360 and 1600 cm^{-1} [10,11]as shown in **Figure 2B**. The high relative intensity of the Raman bands of disordered graphite is due to a resonance effect and not to a high quantity. Note that the presence of 1.2% of C was revealed by elemental analysis and hence some part was present as disordered graphite. It is assumed to be formed from traces of hydrocarbons present in the H_2 flow used during thermal treatment. Because Mn_3O_4 phase is not visible in the XRD diffractogram it is supposed that the Mn_3O_4 is formed in ambient air and corresponds to a surface passivation layer which is amorphous or nanocrystallized. This explains the modification of the solid color from light green characteristic of MnO to brown characteristic of Mn_3O_4. This allows us to conclude that MnO_x-Ref is composed of bulk MnO covered by Mn_3O_4 layer at the surface.

2.2) SAPO-34 samples

Four SAPO-34 samples have been tested during this work. One of them was purchased from ACS material (SAPO-com), one was provided by Dr. S. Gil from IRCELYON (SAPO-GIL) and two others were prepared in our laboratory: one containing potassium (SAPO-K) and one without potassium (SAPO-sK).

2.2.1) Preparation

a) Commercial SAPO-34 (SAPO-com)

Commercial SAPO-34 was purchased from ACS material (SAPO-34-100 g, lot n° 220317) in its protonated form.

b) SAPO-GIL

The synthesis protocol of this solid and characterization was previously reported.[12] Briefly, TetraEthylAmmonium Hydroxide (TEAOH) was mixed with aluminium isopropoxide in a Teflon recipient for 90 min. Then silica was added to the recipient and stirred for 30 min. Finally, a phosphoric acid solution was added and the final suspension was stirred for 30 min at room temperature. The recipient was then closed and sealed inside of a stainless-steel autoclave which was introduced in an oven at 200 °C for 96 h. After that, the autoclave was quenched and the solid inside was recovered and wash-centrifuged with water until pH 7 and finally dried at 100 °C for 6 h. The dried solid was then calcinated under an air flow (Q=4.5 $L.h^{-1}$) primarily with a ramp of 1 °C/min and a 2 h step at 200 °C and then with a 0.5 °C ramp and a second step for 6 h at 550 °C.

c) SAPO-34 with potassium (SAPO-K)

The presence of potassium in this solid was caused by impurity in TEAOH, found only later in this work due to the absence of mention on the package. Elemental analysis showed the presence of 3% of potassium (potassium phosphate) in a freshly opened bottle of TEAOH. It seems that potassium phosphate is either a residue of the synthesis process or a stabilizing agent.

The preparation was carried out as follows: 84 g of Al-isopropoxide (Sigma Aldrich, 220418, ≥ 98%) and 170 ml of TEAOH (Sigma Aldrich, 86633-500 ml, 40 wt% in H_2O) were mixed in a Teflon recipient for 1h30 at room temperature. After that, 3.7 g of silica (Evonik, Aerosil 200 153070413, ≥99.99%) was added to the mixture and mixed for 1 h. Finally, 47 g of H_3PO_4 (Honeywell Fluka, 30417-1L, ≥85%) and 68 g of H_2O were added to the mixture and stirred for 3 h at room temperature. Then the Teflon recipient was closed and placed in a stainless-steel autoclave. The autoclave was heated to 100 °C for 12 h without stirring, for ageing. Finally, the autoclave was heated to 200 °C and maintained at this temperature for 48 h under autogenous pressure. After this step, the suspension was recovered and washed by water with repetitive centrifugation. The recovered solid was dried at 100 °C overnight and then calcinated. The calcination was done in two steps: first, the solid was heated under air to 200 °C with a ramp of 1 °C.min^{-1} and this temperature was maintained for 2 h. Then, the temperature was increased slowly up to 550 °C with a ramp of 0.5 °C.min^{-1}. The solid was kept at this temperature for 6 h. After the calcination the solid was sieved between 120 and 180 µm.

d) SAPO-34 without potassium (SAPO-sK)

The preparation of SAPO-sK was carried out using the same procedure as for SAPO-K. 39 ml of Potassium –free TEAOH (Alfa Aesar, 43023, 35 wt% in H_2O) and 8.7 g of H_2O were used in the synthesis and the total amounts of the other reactants were divided by five.

2.2.2) Characterization

a) Elemental analysis

Elemental analysis allow to determine the (Si+P)/Al, which can give information on the dominating type of substitution. If inferior or equal to 1 it is supposed that type II substitution mainly occurs. [13,14] In cases extra framework alumina is present the ratio can be inferior to 1. [13,14] On the other hand if the ratio is superior to 1 it is usually considered that type III substitution is favored.

Elemental analysis presented in **Table 1** shows that SAPO-Gil, SAPO-K and SAPO-sK have (Si+P)/Al ratio below 1, suggesting that the Si atoms were mainly present in the type II substitution (**Figure 3**).[13,14] On the other hand, SAPO-com presents a (Si+P)/Al ratio above 1 meaning that Si atoms have undergone type II and III substitutions leading to the formation of Si islands (Fig.3):[13,14] Type II substitution is the replacement of an Si atom with an P atom. On the other hand, in type III substitution an Si atom replaces an Al atom.

For both SAPO-Gil and SAPO-K elemental analysis has shown that those solids contain K coming from the TEAOH used in the synthesis. The presence of K might affect their acidic properties.

Table 1: Elemental composition of the SAPO-34 samples determined by ICP-OES.

	Mass composition (wt%)				Molar composition				
Sample	Si	Al	P	K	Si	Al	P	K	(Si+P)/Al
SAPO-Com	4.1	18.2	17.8	0	0.22	1	0.85	0	1.07
SAPO-Gil	2.5	17.0	16.0	3.0	0.14	1	0.82	0.12	0.96
SAPO-K	3.5	23.0	18.0	3.0	0.15	1	0.68	0.09	0.83
SAPO-sK	3.3	20.8	16.2	0	0.15	1	0.68	0	0.83

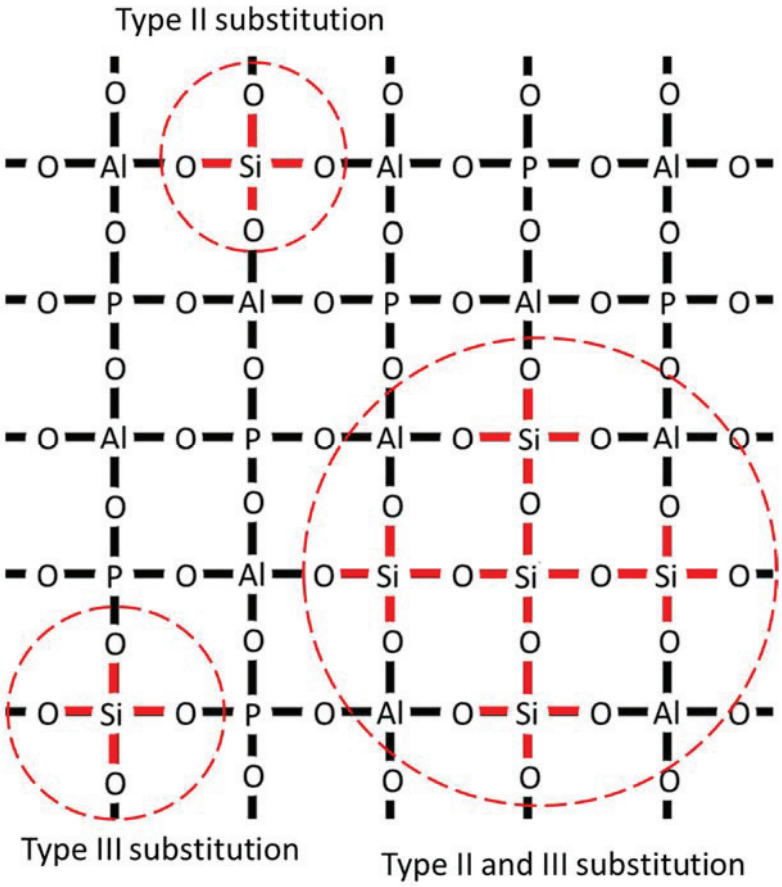

Figure 3: Scheme of the types of Si substitution in an AlPO framework.

b) XRD

XRD analysis of SAPO-K and SAPO-sK before calcination shows that two phases were present, as shown in **Figure 4** and **Figure 5**, respectively. SAPO-34 was already formed and aluminium hydroxide was also present in a small quantity. After calcination, the SAPO-34 structure was retained and the aluminium hydroxide peaks disappeared suggesting that this phase was decomposed into amorphous alumina. The slight shift and change of relative intensity of peaks were due to the removal of organic species during calcination, leading to slight modification of the crystalline structure.[15]

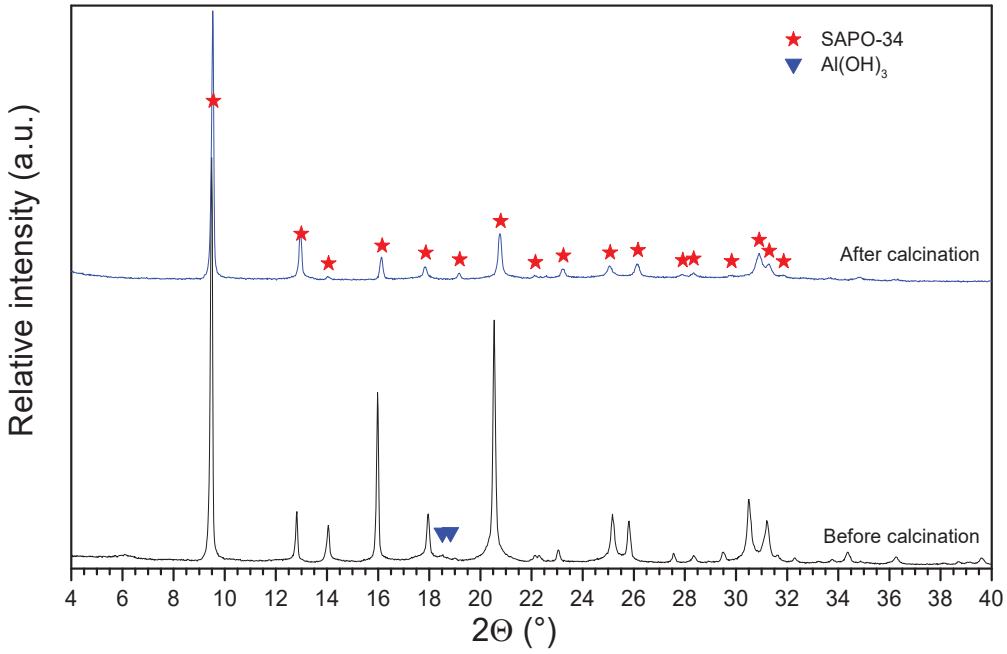

Figure 4: XRD patterns of SAPO-K sample before and after calcination at 550 °C. The diffraction peaks were indexed with the PDF 47-0429 ICDD pattern corresponding to crystalline SAPO-34 with composition Si/Al/P:0.22/1/0.75 and the PDF 85-1049 ICDD pattern corresponding to $Al(OH)_3$.

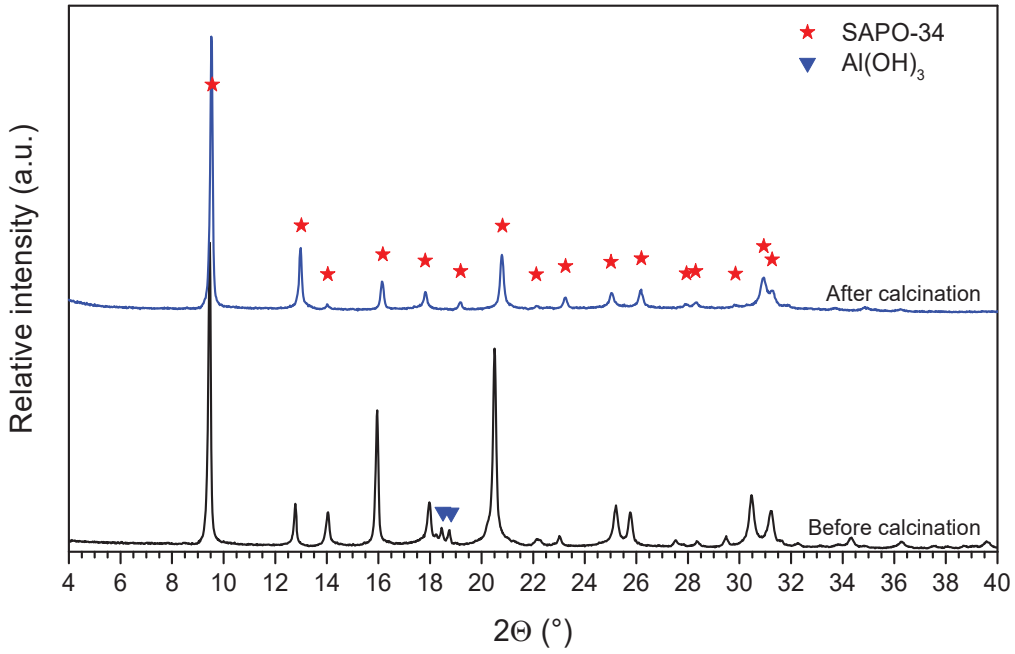

Figure 5: XRD patterns of SAPO-sK before and after calcination at 550 °C. The diffraction peaks were indexed with the PDF 47-0429 ICDD pattern corresponding to crystalline SAPO-34 with composition Si/Al/P:0.22/1/0.75 and the PDF 85-1049 ICDD pattern corresponding to $Al(OH)_3$.

Figure 6 compares the XRD patterns of the four calcined samples. They all contained the diffraction peaks of SAPO-34 at similar angles except for the SAPO-Gil. In the SAPO-Gil small variation of the diffraction angle are observed that maybe due to composition variation.[13]

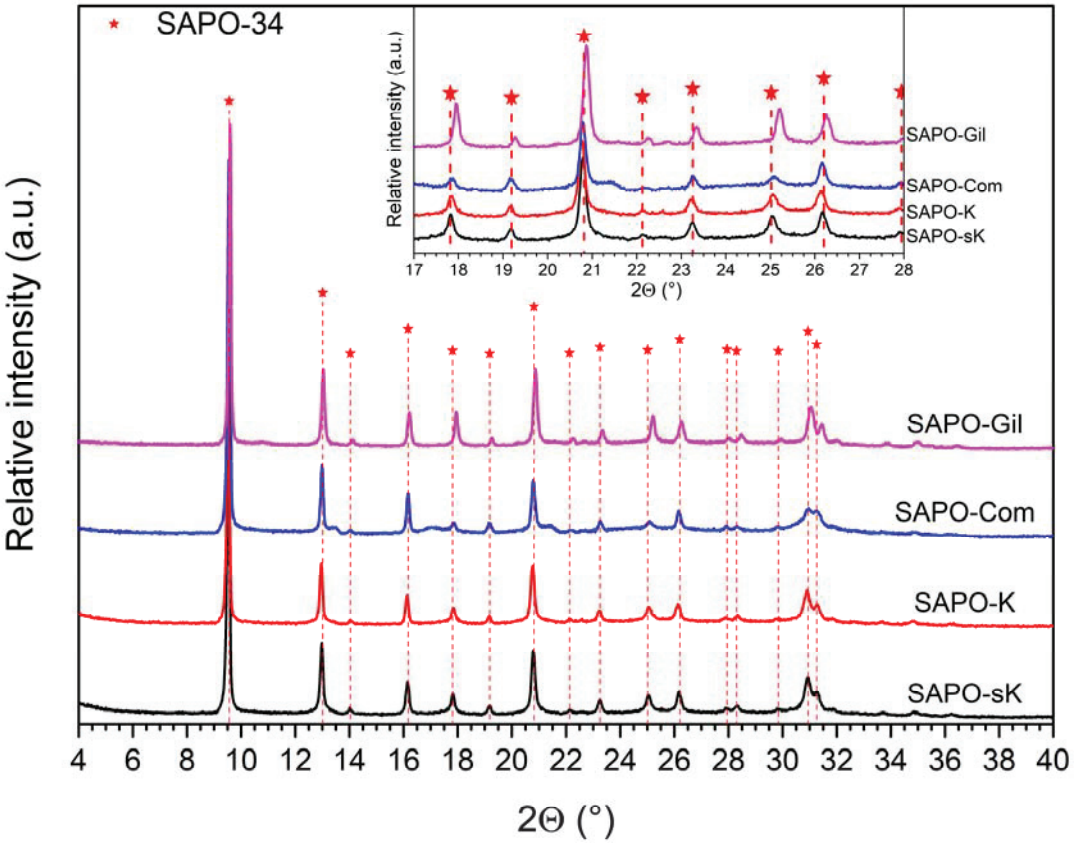

Figure 6: XRD patterns of the four SAPO-34 calcined samples. The diffraction peaks were indexed with the PDF 47-0429 ICDD pattern corresponding to crystalline SAPO-34 with composition Si/Al/P:0.22/1/0.75.

c) Solid state NMR

^{31}P, ^{29}Si and ^{27}Al NMR analyses have been performed on the solids at stake. For all elements, chemical shifts of the species have been compared to the structural and extra-framework P species. ^{31}P NMR spectra of all the four SAPO-34 samples presented in **Figure 7B** show a $P(OAl)_4$ local structure with a chemical shift near -27 ppm.[13,14,16] Contrarily to SAPO-com, the three in-lab prepared solids contained different amounts of $P(OAl)_x(H_2O)_y$ hydrated local structures with a chemical shift of -18 ppm.[16] SAPO-K owned the highest proportion of $P(OAl)_x(H_2O)_y$. Those species correspond to framework defects or species present at the outer surface of the crystals.[13,16] It

suggests that SAPO-K contained higher proportion of defects or smaller crystals than the other SAPO samples.

Concerning the ^{27}Al NMR spectra, structural and extra-framework Al species are present in all the solids as shown in **Figure 7A**. The proportion of $Al(OP)_x(H_2O)_y$ hydrated local structures and extra framework Al_2O_3 seems to be higher for SAPO-K and SAPO-sK.

Hence, the ^{27}Al and ^{31}P spectra attest relative purity of the commercial SAPO-34 solid and the presence of Al_2O_3 in all three lab-made samples.

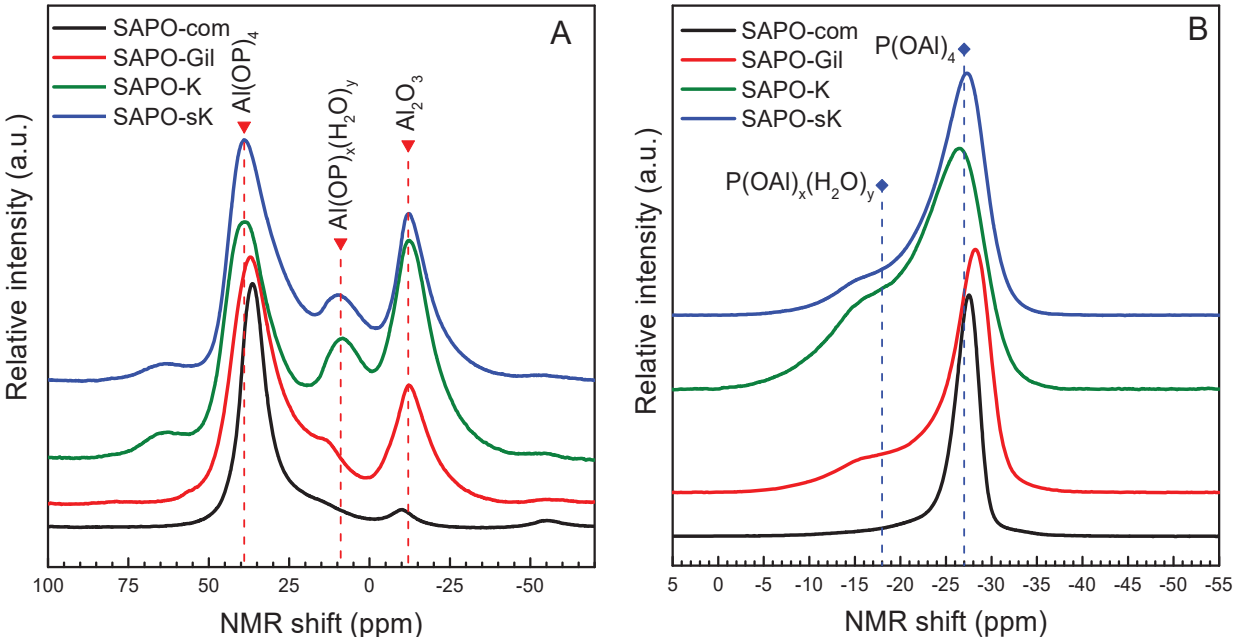

Figure 7: A) ^{27}Al NMR and B) ^{31}P NMR normalized spectra of the four SAPO-34 samples.

^{29}Si NMR allows observing the local environment of Si and estimating the number of silicon and aluminum atoms in the direct vicinity to silicon atoms. It is noteworthy that Si-O-P bonds have never been observed in ^{29}Si NMR and only Si-O-Al bonds were observed.[13] Therefore, five types of Si environment can be observed in our samples as depicted in the **Figure 8**: $Si(OAl)_4$, $Si(OAl)_3(OSi)$, $Si(OAl)_2(OSi)_2$, $Si(OAl)(OSi)_3$ and $Si(OSi)_4$. Their distribution can affect the acid sites density and strength of SAPO-34.[13,14,16]

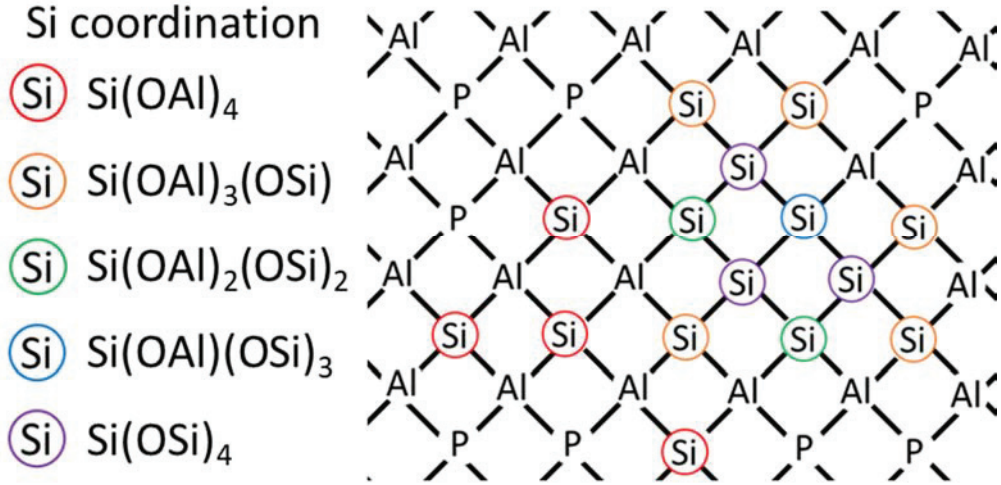

Figure 8: Scheme showing the five types of environment existing around framework Si atoms.

Isolated Si atoms have been observed in every SAPO-34 with a chemical shift in the -89 ppm to -92 ppm region[13,14,16] as shown in **Figure 9**. For the SAPO-com sample, the signals of $Si(OAl)_3(OSi)$, $Si(OAl)_2(OSi)_2$, $Si(OAl)(OSi)_3$ and $Si(OSi)_4$ have been observed with chemical shifts of -97 ppm, -102 ppm, -107 ppm and -112 ppm respectively, as described in the literature.[13,14,16] Only isolated Si atoms were observed for SAPO-K, SAPO-sK and SAPO-Gil.

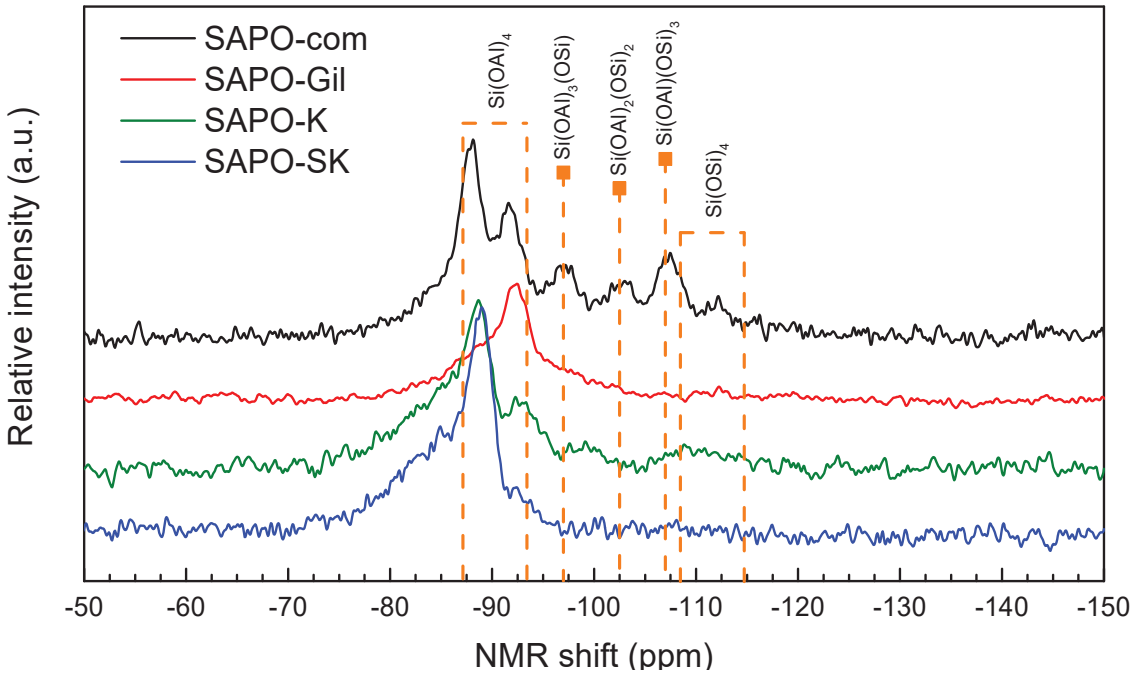

Figure 9: ^{29}Si NMR spectra of the four SAPO-34 calcined samples.

The presence of SiO_2 in SAPO-com and SAPO-GIL might be related to a higher proportion of Si in the solid (Table 1). No other peaks that might correspond to Si-O-P linkages were observed in the ^{29}Si NMR spectra. Those linkages are highly unstable[13,17,18] and it is supposed that isolated Si-Al substitution is impossible and type III substitution requires formation of a Si island[13,17,18] as depicted in **Figure 3**.

d) NH3-TPD

NH_3-TPD curves plotted in **Figure 10** show two desorption peaks for each solid , one around 180 °C and one around 400 °C corresponding to weak and strong acid sites, respectively [13,19]. The temperature of the second peak varies from one solid to another: it is higher for the potassium-free sample, SAPO-sK and SAPO-com (near 420 °C for both) whereas it is lower for SAPO-K and SAPO-Gil (400 and 380 °C respectively). Similarly, the area of the second peak is higher for SAPO-sK and SAPO-com.

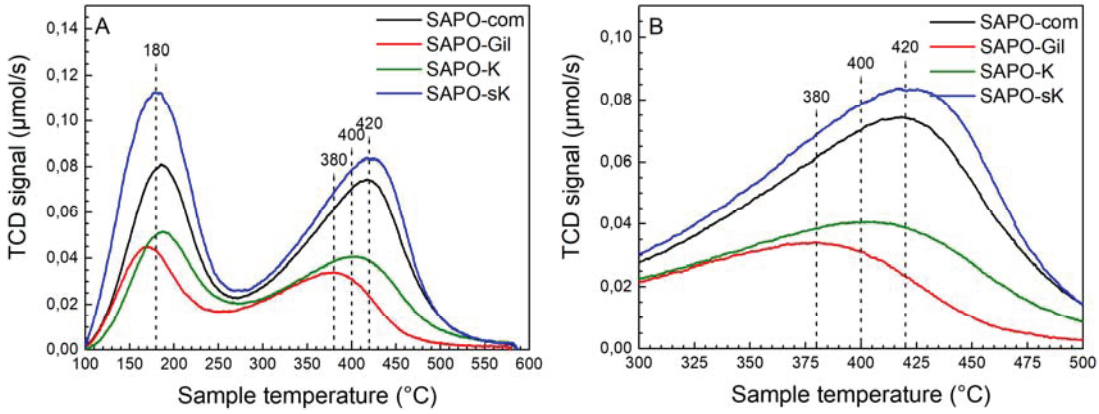

Figure 10: NH_3-TPD curves of the four SAPO-34 samples, A) on the whole studied temperature range B) zoom between 300 and 500 °C.

SAPO-sK and SAPO-com have the highest strong acid site densities with 925 and 1007 µmol.g^{-1}, respectively (**Table 2**). On the other hand, SAPO-K and SAPO-Gil have less strong acid sites with 572 and 551 µmol.g^{-1}. We only discussed the strong acid site density here because literature have shown that those are the main reaction site for the C-C coupling.[20–24]

Table 2: Strong and weak acid site density determined from NH_3-TPD curves for the four SAPO-34 samples.

	Density (µmol.g-1)		
Sample	Total acid sites	Weak acid sites[a]	Strong acid sites[b]
SAPO-Gil	1066	515	551
SAPO-com	1749	742	1007
SAPO-K	1019	447	572
SAPO-sK	1819	894	925

[a] quantified by integration between 100 and 270°C

[b] quantified by integration between 280 and 550 °C

These differences in acidity can be related to the presence of K in SAPO-K and SAPO-Gil. The K^+ cations might have partially exchanged the acid sites inside the SAPO-34 framework leading to a decrease in the acid sites density.

e) Textural properties

Table 3 reports the BET surface areas, the microporous surface areas (deduced from the t-plot) for the four SAPO-34 samples. The mesoporous surface areas correspond to the difference between the two values.

Table 3: BET, microporous and mesoporous surface areas for the four SAPO-34 samples.

	Surface area ($m^2.g^{-1}$)		
Sample	BET	Microporous	Mesoporous
SAPO-com	534	518 (97%)	16 (3%)
SAPO-Gil	485	455 (94%)	30 (6%)
SAPO-K	450	387 (86%)	63 (14%)
SAPO-sK	581	524 (90%)	57 (10%)

All the solids are mostly microporous. However, the proportion of mesoporosity was higher for the two in-lab prepared SAPO-34, especially SAPO-K (14%).

TEM images recorded for the four zeotypes show cubic-shaped particles for all samples (**Figure 11-14**). SAPO-com, SAPO-Gil and SAPO-K contained crystals that were micro-sized while they were in the 100 to 300 nm range for SAPO-sK. For SAPO-K and SAPO-sK, extra framework alumina was additionally observed as well as KPO_3 for SAPO-K. The KPO_3 phases is present in minor amount as evidenced by ICP analysis

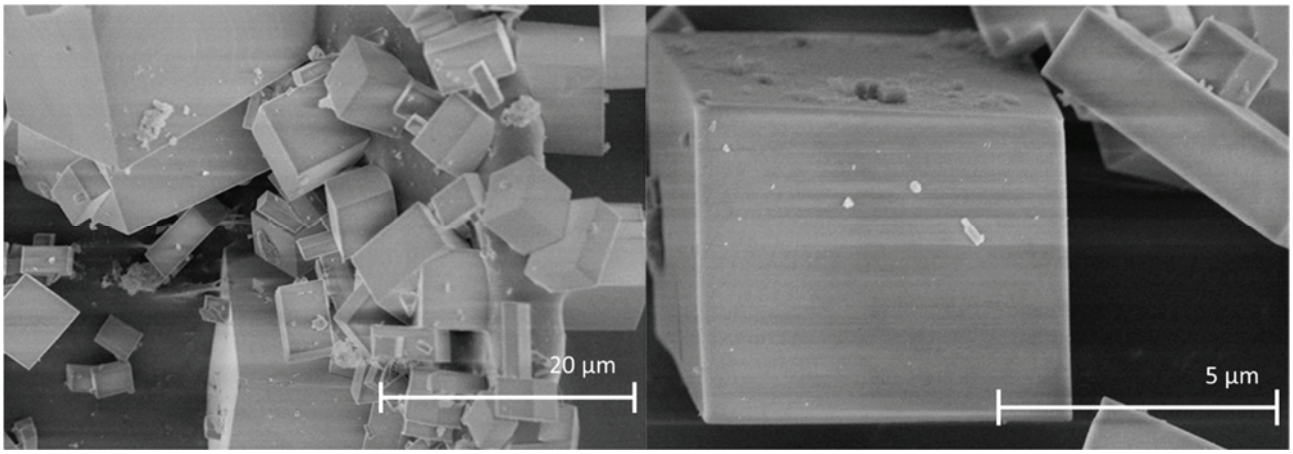

Figure 11: MEB image of SAPO-com sample. Source ACS Material: SAPO-34

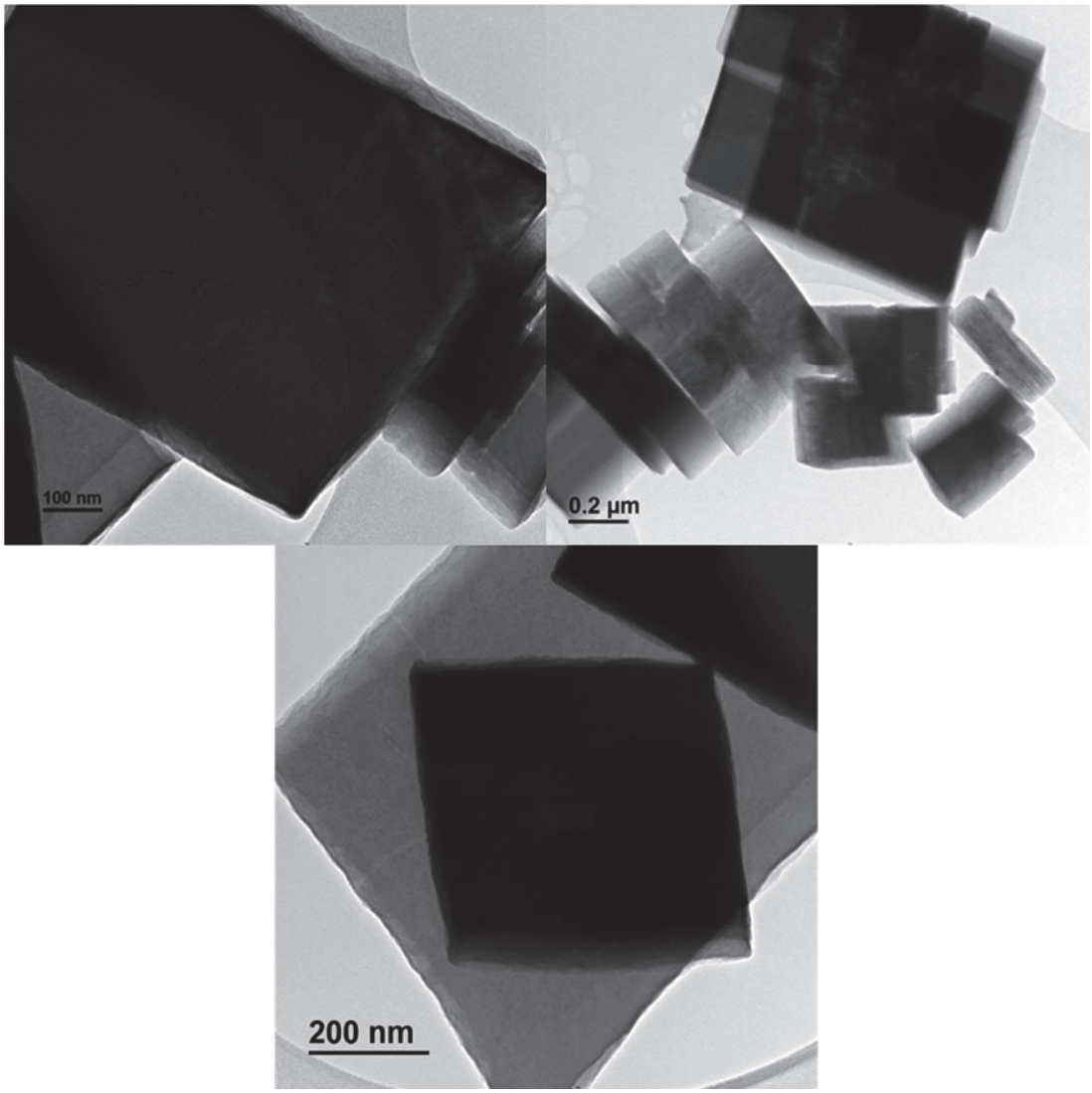

Figure 12: TEM images of SAPO-Gil sample.

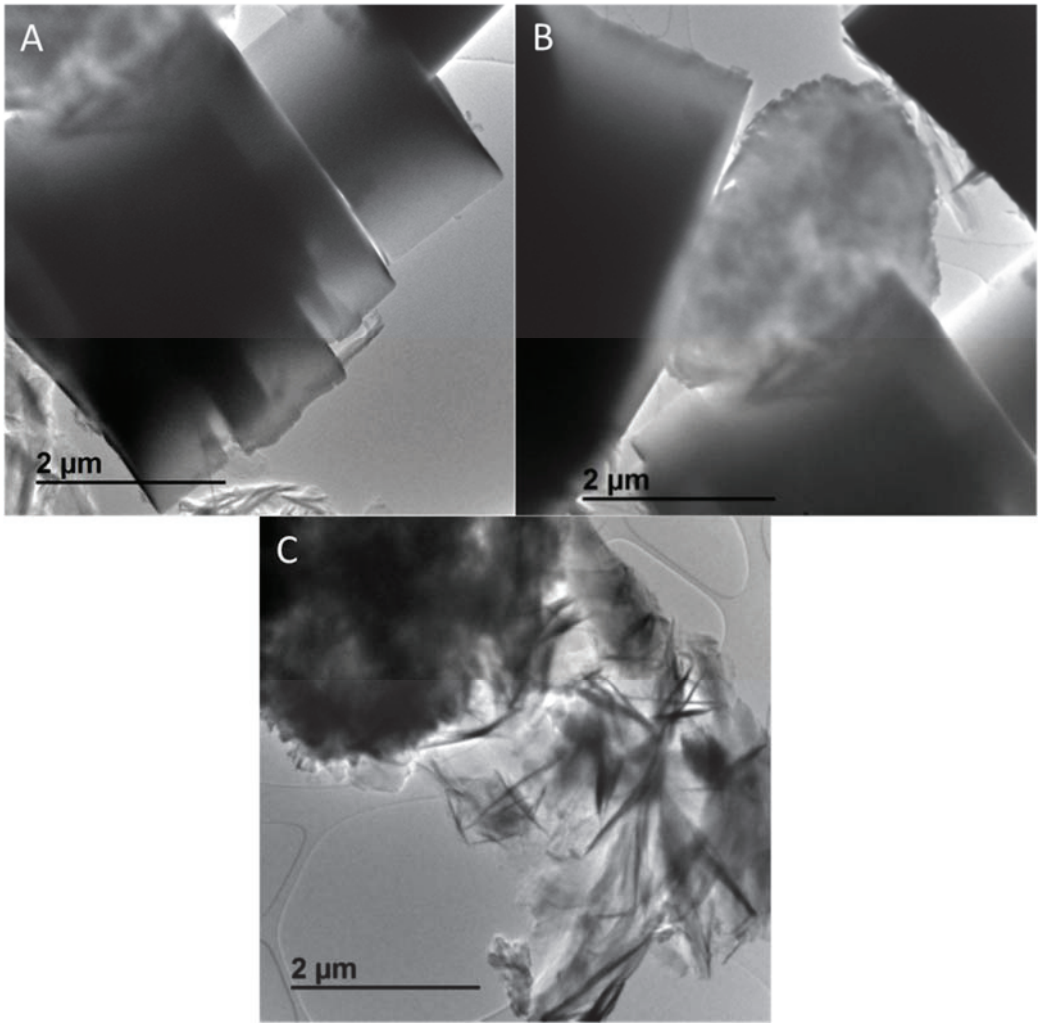

Figure 13: TEM images of SAPO-K sample showing A) SAPO-34 crystals, B) extra-framework alumina with SAPO-34 crystals and C) $KHPO_3$ needles.

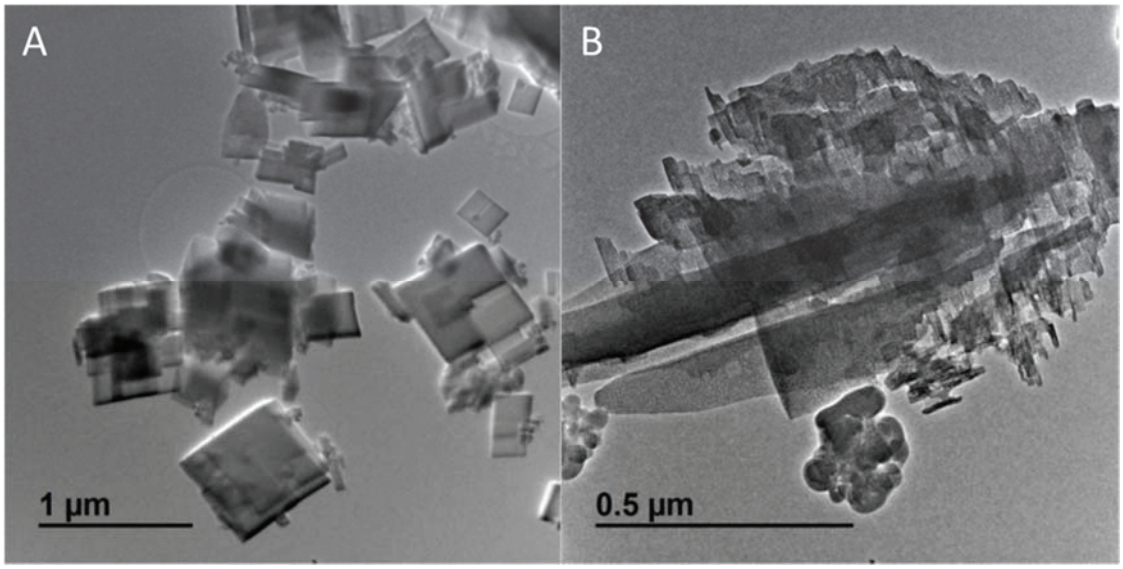

Figure 14: TEM images of SAPO-sK sample showing A) zeolite crystals and B) extra-framework alumina.

As conclusion, the four SAPO-34 materials had different properties: all of them were mainly microporous but SAPO-K contained the highest proportion of mesoporosity (14%). SAPO-Gil and SAPO-sK were nano-sized while the two others were micro-sized. SAPO-K and SAPO-sK contained extra framework Al_2O_3, SAPO-Gil and SAPO-K contained K in significant amount which decreased the strong acid sites density and their strength.

3) Preliminary catalytic study

A preliminary catalytic study was carried out to fix the most important parameters of the reaction such as the time on stream necessary to reach a stationary state, the activation temperature and the most appropriate SAPO-34.

3.1) Temporal evolution of catalytic properties

The aim of these first tests was to determine the time evolution of activity and selectivity. A mechanical mixture of MnOx-Ref and SAPO-K (33 wt%) was used.

We observed that the conversion and the selectivity values varied mostly during the first 14 h on stream (**Figure 15**): The conversion increased during ca. 2 h of testing before slowly decreasing and appearing to stabilize after 14 h at 5.8%. The CO_2 and C4 selectivity decreased for the benefit of the C3 and then the C2 one. All selectivity values became rather stable after 14 h. The C3 and C2 hydrocarbon were the main hydrocarbon products during the whole test whereas C4, C5+ hydrocarbons and CH_4 were minor, with yields not exceeding 5%.

Concerning the C2-C4 O/P (olefin to paraffin) ratio, it increased from 2 to 3 during the first 14 h. The O/P ratios for C2, C3 and C4 hydrocarbons evolved independently: it increased continuously for C4 and C3 hydrocarbons while it increased during the first 4 h of test for C2 hydrocarbons and then steadily decreased.

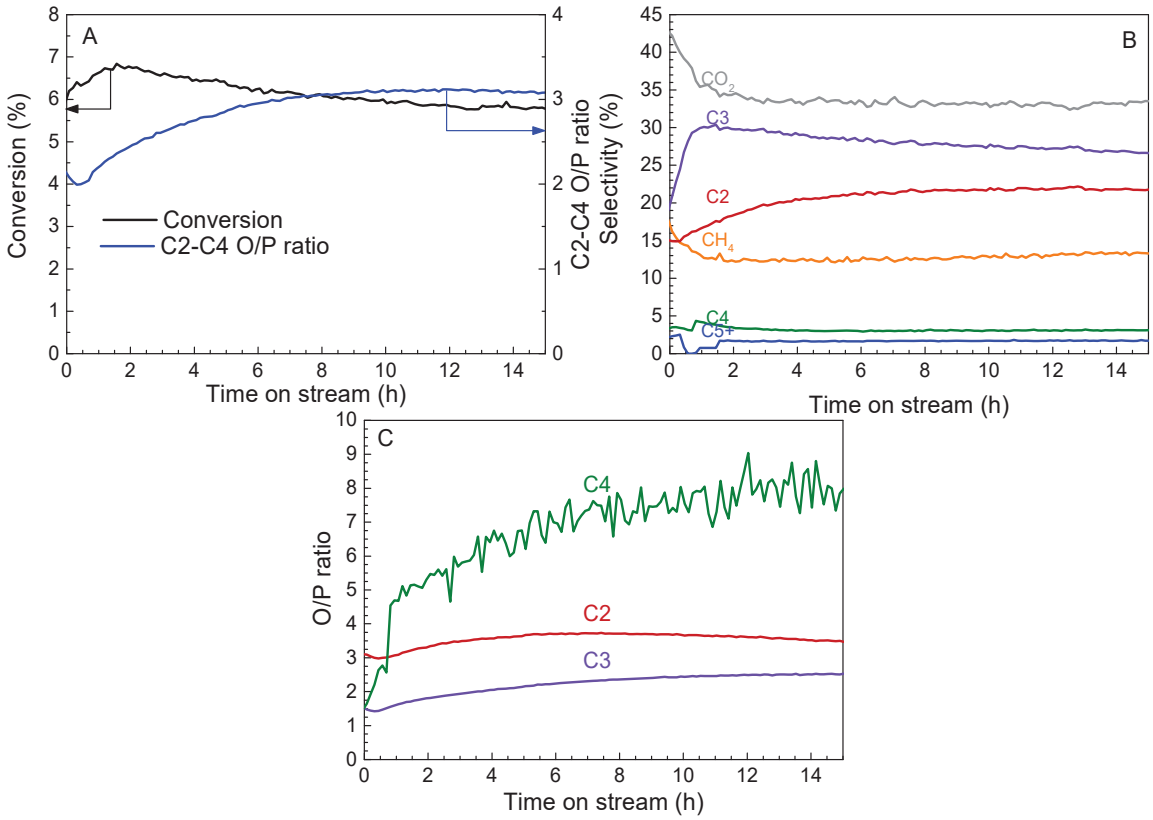

Figure 15: A) Evolution of the conversion and C2-C4 O/P ratio, B) Evolution of the CO_2, CH_4 and hydrocarbon selectivity and C) Evolution of the O/P ratio for C2, C3 and C4 hydrocarbons with time on stream. Reaction conditions: m(MnO_x-Ref)=200 mg, m(SAPO-K)=100 mg, P=25 bar, T=410 °C, $H_2/CO/N_2$=60/30/10, WHSV 87 $mL.min^{-1}.g^{-1}$.

These results suggest that equilibration of diffusion processes in SAPO-34 occurs during the first hour, prior to achieving the steady state regime and during this period strong variations of selectivity were observed. Overall, the stationary state in the Ox-Zeo process in our conditions is attained approximately after 14 h.

3.2) Influence of the activation temperature

Prior to the catalytic test, the catalyst was activated for 1 h in hydrogen flow. The goal of activation is to transform the surface layer of Mn_3O_4 into MnO and to create surface oxygen vacancies which are believed to be the hydrogenation sites.[1]

The activation temperature before the catalytic test has been varied from 410 °C to 450 °C. As shown in **Figure 16**, the activation temperature has no strong effect on the conversion and the

hydrocarbon distribution. A minimum of the C2-C4 O/P ratio was observed at 430 °C (**Figure 16A**) associated with a maximal CH_4 selectivity (**Figure 16B**). However, this minimum is small considering the accuracy of this parameter and could be explained by a slightly higher conversion.

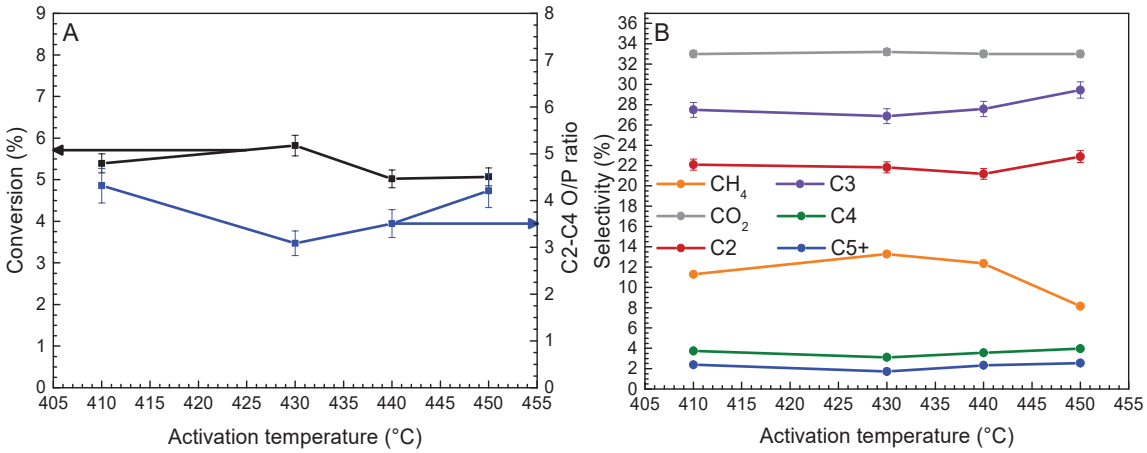

Figure 16: A) Evolution of the conversion and C2-C4 O/P ratio and B) Evolution of the CO_2, CH_4 and hydrocarbon selectivity with activation temperature. Reaction conditions: m(MnO_x)=200 mg, m(SAPO-K)=100 mg, P=25 bar, T=410 °C, H_2/CO/N_2=60/30/10, WHSV 87 mL.min^{-1}.g^{-1}. Data were taken after 14 h on stream.

In situ Raman spectra recorded at RT for the MnOx-Ref sample at the initial state and after treatment under 10%H_2-N_2 flow at different temperatures are compared in **Figure 17**. Mn_3O_4 which was present at the initial state became more crystallized upon increasing the temperature to 360 °C (thinner bands) before disappearing at higher temperatures. Then, the spectra contained mainly two broad bands at 546 and 626 cm^{-1}. The former was attributed to the 2TO (Transverse Optical) or LO (Longitudinal Optical) mode of MnO[7,9] while the other one is not observed for single crystals. Its observation could be related to the nanocrystallinity and/or non-stoichiometry ($MnO_{1\pm\varepsilon}$).

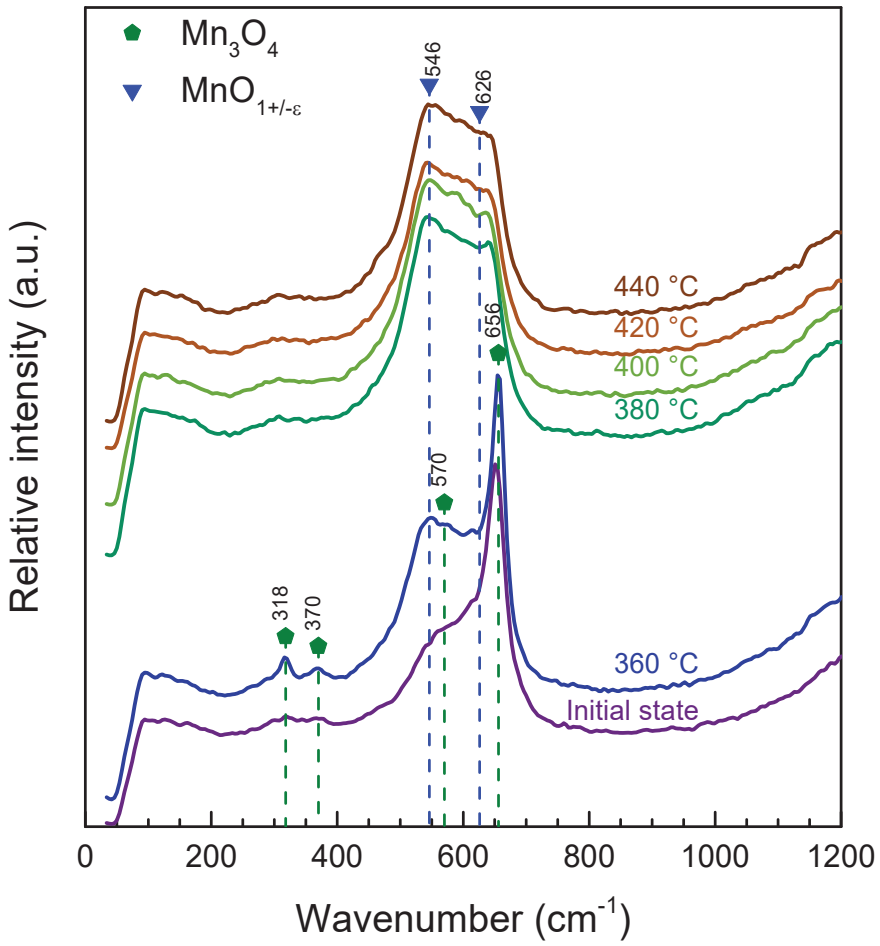

Figure 17: *In situ* Raman spectra recorded at RT of MnOx-ample at the initial state and after treatment for 15 min under 50 NmL.min^{-1} of 10%H_2-N_2 flow at different temperatures.

Considering the catalytic and Raman results, the activation temperature has been set at 430 °C for the rest of this work.

3.3) Influence of SAPO-34 properties

First, SAPO-com and SAPO-Gil were tested to evaluate their catalytic properties when mixed with MnO_x-Ref. The results are shown in **Figure 18**. At 410 °C, close conversions (5.6% and 6.5%, respectively) were obtained with a much higher C2-C4 O/P ratio for SAPO-Gil than for SAPO-Com (6.1 and 1.5, respectively). Interestingly, the C3 O/P ratio was higher than the C2 O/P one for SAPO-Gil contrarily to SAPO-com. Basing on these results, we decided to prepare SAPO-34 by reproducing the SAPO-Gil protocole[12] (with and without K) leading to SAPO-K and SAPO-sK samples.

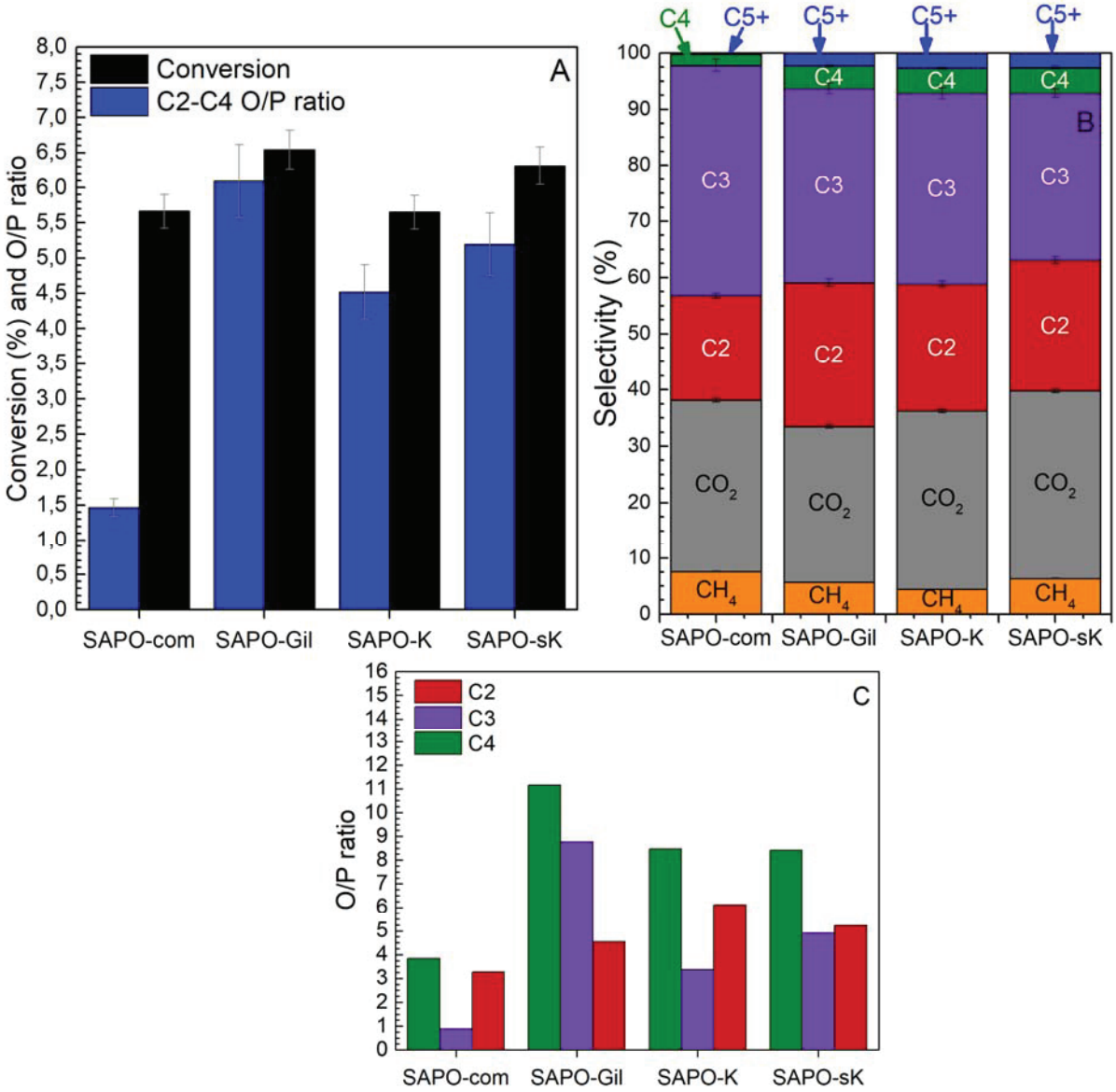

Figure 18 : A) Conversion and C2-C4 O/P ratio and B) CO_2, CH_4 and hydrocarbon selectivity and C) O/P ratio for C2, C3 and C4 hydrocarbons determined for MnOx-Ref mixed with the four SAPO-34 samples. Reaction conditions: m(MnO_x-Ref)=200 mg, m(SAPO-34)=100 mg, P=25 bar, T=410 °C, $H_2/CO/N_2$=60/30/10, WHSV 87 $mL.min^{-1}.g^{-1}$. Data were taken after 14 h on stream.

The two prepared zeolites, SAPO-K and SAPO-sK combined with MnO_x-Ref exhibited conversion of 5.6% and 6.3%, respectively which are close to the conversions obtained with the SAPO-com and SAPO-Gil samples. SAPO-Gil exhibited the lowest CO_2 selectivity (27.9%) while it was 30.6 %, 31.9% and 33.4% for SAPO-com, SAPO-K and SAPO-sK, respectively. SAPO-K led to the lowest CH_4 selectivity (4.4%) compared to 7.6%, 5.6% and 6.4% for SAPO-com, SAPO-Gil and SAPO-sK, respectively. The hydrocarbons distribution was similar for the four tested SAPO-34 samples.

They mainly produced C3 hydrocarbons with the selectivity of 41%, 35%, 34% and 30% for SAPO-com, SAPO-Gil, SAPO-K and SAPO-sK, respectively. Next are the C2 hydrocarbons with the selectivity of 19%, 26%, 23% and 23%, respectively. The C4 hydrocarbons were minor products with the selectivity of 4.0% for SAPO-Gil, SAPO-K and SAPO-sK and 1.9% for SAPO-com. Finally the rest of hydrocarbons were C5+ products.

The O/P ratios were lower for SAPO-K and SAPO-sK (4.5 and 5.2, respectively) than for SAPO-Gil (6.1). The O/P ratios for C2, C3 and C4 strongly varied with the zeotype.

The O/P ratio was reported to depend on the surface density and strength of acid sites with an optimal value.[22,25,26]In the present study, high O/P ratios were obtained for SAPO-Gil and SAPO-K which contain lower amounts of strong acid sites. However, contradictory results were obtained for SAPO-com and SAPO-sK which contain higher amounts of acid sites but show very different O/P ratios (1.5 and 5.2, respectively). This difference could be related to the nature of acid sites (Brønsted vs Lewis). It could also arise from the crystal size which was much smaller for SAPO-sK limiting deeper hydrogenation.

As a summary, the preliminary study has permitted to fix some parameters of the Ox-Zeo reaction: first, all the catalytic results presented further are measured after 14 h on stream when a stationary state is reached. SAPO-K was firstly chosen as the reference zeotype and was used for the following parametric study in combination with MnO_x-Ref. The presence of potassium in SAPO-K was discovered after most of this parametric study was already done. SAPO-sK was then synthetized and a comparative study was undertaken to determine the impact of K on the catalytic property.

4) Parametric study

In this section, we investigate the influence of several reaction parameters on the activity and selectivity of MnO_x-Ref–SAPO-K mixtures in the Ox-Zeo process. The studied parameters include the contact time, the reaction temperature, the composition of the reaction feed and the mass balance of the two catalysts in the mixture. While in such a multiparametric system a full-factor experiment is not possible, the partial reaction orders were calculated and major trends were revealed. The goal was to provide an overall picture of the parametric sensitivity of this system

and to select the working range of parameters, where the variations of intimacy parameter should be studied.

4.1) Contact time

The contact time was varied by changing the total flow, all the other parameters of the test being kept constant. The variations of the contact time naturally influence the catalytic conversion and by consequence, the O/P ratio and the hydrocarbons selectivity.

4.1.1) MnOx-Ref and SAPO-34 individual phases

For the sake of comparison with MnO_X-SAPO-34 mixtures, we studied the catalytic properties on MnO_x-Ref alone as the oxide component. Its supposed role in the bifunctional mixture is to provide a hydrogenation function. Therefore, it could be expected that hydrogenation should be predominant on sole MnO_x, in a wide range of conditions.

The influence of contact time was studied on MnO_x-Ref alone, as depicted in **Figure 19**. The conversions are several times lower than for the MnO_x-ref-SAPO-34 mixtures. MnO_x-Ref exhibits high selectivity to CH_4 and CO_2 (43% and 33%, respectively). The high CH_4 selectivity naturally appears at the expense of the hydrocarbon selectivity values which are 9.6%, 7.6%, 5.8% and 2.6% for C2, C5+, C3 and C4, respectively. Therefore, the addition of SAPO-34 to MnO_x-Ref leads to a strong shift in selectivity due to the C-C coupling that probably occurs via the intermediate species reactions inside the SAPO-34 pores. The selectivity towards hydrocarbons and CO_2 seems to not be impacted by the increase in conversion.

The C2-C4 O/P decreases from 1.5 to 0.5 when the conversion increases from 1 to 3%. The O/P ratio is considerably lower on sole MnO_x-Ref than on the MnO_x-Ref-SAPO34 mixtures. As for the C2-C4 O/P ratio, an increase in overall conversion leads to a decrease in the O/P ratio for C2 and C3 hydrocarbons.

The samples of individual SAPO-34 phase did not show any detectable conversion of syngas in the standard reaction conditions.

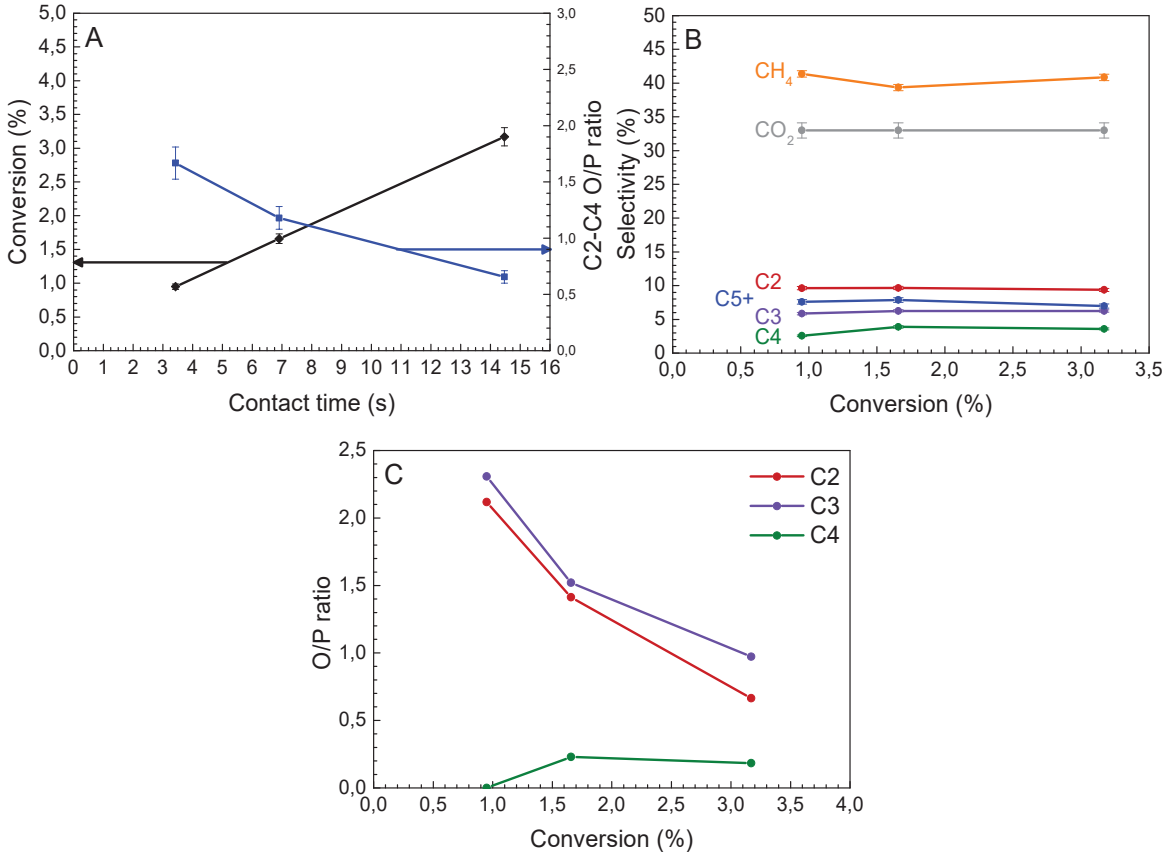

Figure 19: A) Evolution of the conversion and C2-C4 O/P ratio with contact time; B) evolution of the CO_2, CH_4 and hydrocarbon selectivity; C) evolution of the O/P ratio for C2, C3 and C4 hydrocarbons with conversion. Reaction conditions: m(MnO_x-Ref)=300 mg, P=25 bar, T=410 °C, H_2/CO/N_2=60/30/10. Data were taken after 14 h on stream.

4.1.2)MnOx-Ref+SAPO-K

The contact time was varied for a MnO_x-Ref+SAPO-K mechanical mixture and the corresponding catalytic properties are depicted in **Figure 20**. An increase in contact time leads to an expected increase in conversion, whereas the C2-C4 O/P ratio decreases in step. As for the C2-C4 O/P ratio, the O/P ratios for C2, C3 and C4 hydrocarbons decrease with an increase in conversion. The higher contact time allows more olefins to be hydrogenated either on the oxide or on the zeolite. An increase in the CH_4 selectivity occurs with the contact time in parallel with the decrease in the O/P ratio: the C1 intermediate and the C2-C4 olefins produced on the oxide are hydrogenated.

While the overall conversion increases with the contact time, the CO_2 selectivity decreases slightly. The C2, C4 and C5+ selectivity values decrease with increasing conversion while the C3 and CH_4 ones increase. For the C3 selectivity, the increase might be explained by a higher contact time of the C2 olefins with the SAPO-34 component allowing further methylation.

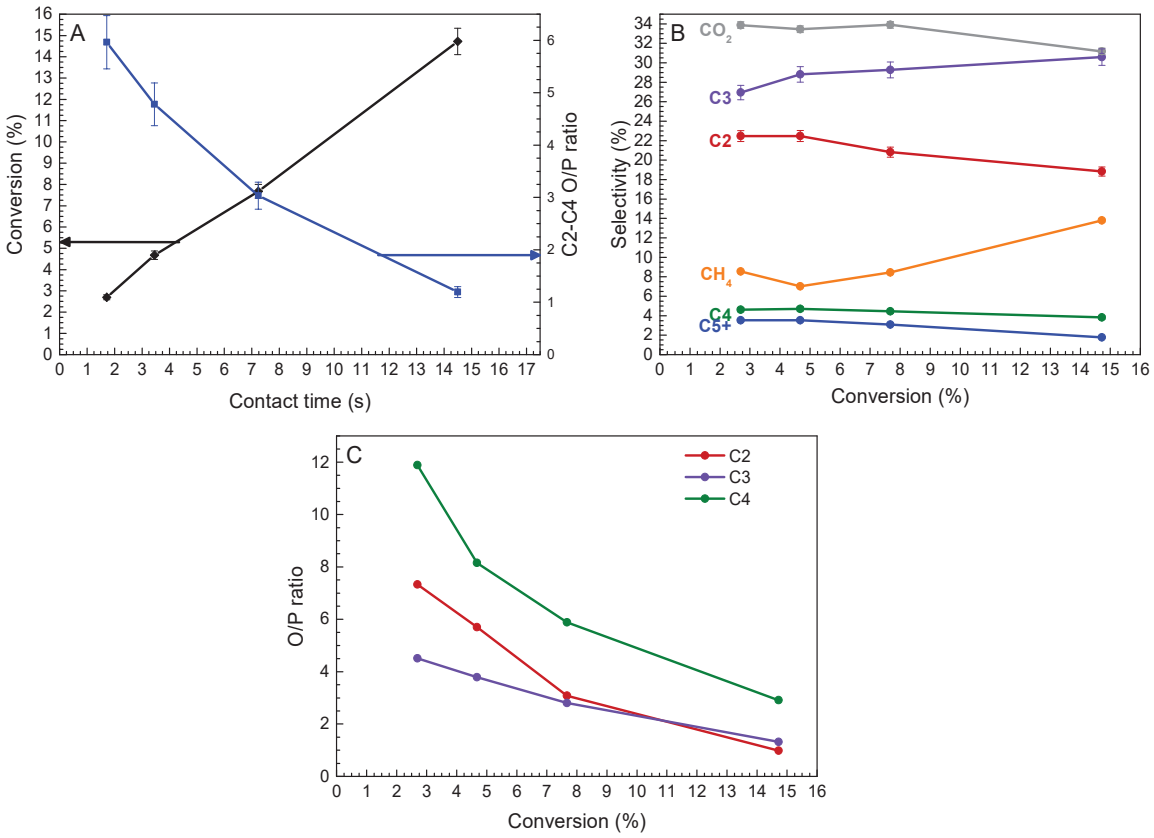

Figure 20: A) Evolution of the conversion and C2-C4 O/P ratio with contact time and B) evolution of CO_2, CH_4 and hydrocarbon selectivity and C) O/P ratio for C2, C3 and C4 hydrocarbons with conversion. Reaction conditions: m(MnO_x-Ref)=240 mg, m(SAPO-K)=60 mg, P=25 bar, T=410 °C, $H_2/CO/N_2$=60/30/10. Data were taken after 14 h on stream.

4.2) MnOx-Ref-SAPO-K balance

The mass proportion of SAPO-K in the catalytic mixtures was varied from 0 to 50 wt%. The evolution of catalytic properties with the mass proportion of zeolite is depicted in **Figure 21**. An optimal conversion (5.7%) is observed for 20wt% of SAPO-K in the catalyst mixture. Beyond 20 wt% of zeotype, the conversion slightly decreases. The highest O/P ratio of 7 is obtained for 5 wt% of SAPO-K. The CO_2 selectivity is almost independent on the mass proportion of SAPO-K. The CH_4

selectivity is constant for zeotype mass proportion ranging from 10 to 30 wt%. At 5 and 50 wt% of SAPO-K, the CH_4 selectivity increases at the expense of the C2-C4 hydrocarbon selectivity. The O/P for each hydrocarbon has an optimum at 5 wt% of SAPO-K and then continuously decreases with its proportion.

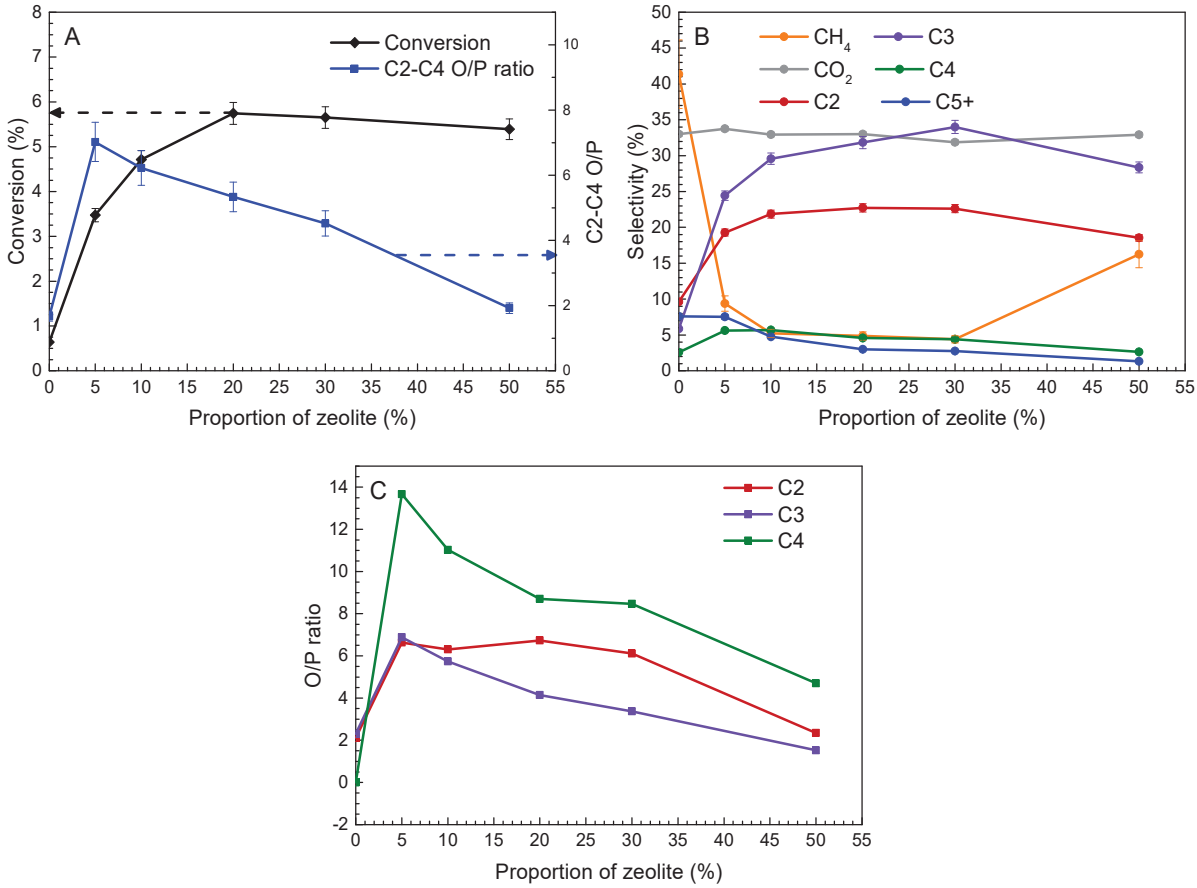

Figure 21: A) Evolution of the conversion and C2-C4 O/P ratio with mass proportion of zeolite; B) evolution of the CO_2, CH_4 and hydrocarbon selectivity with mass proportion of zeolite; C) evolution of O/P ratio for C2, C3 and C4 hydrocarbons C2 to C4 with mass proportion of zeolite. Reaction conditions: m(MnO_x-Ref+SAPO-K)=300 mg, P=25 bar, T=410 °C, H_2/CO/N_2=60/30/10, WHSV 87 $mL.min^{-1}.g^{-1}$. Data were taken after 14 h on stream.

These results show that a small quantity of SAPO-34 is sufficient to change drastically the catalytic properties of the mixture, compared to MnO_x-Ref alone. An increase in conversion, O/P ratio and selectivity to hydrocarbons are observed due to zeotype addition. Apparently, the introduction of SAPO-34 allows to convert the reaction intermediate (methanol or ketene, according to the literature)[1,20,27–30] toward C2+ hydrocarbons. This leads to a shift in the

thermodynamic equilibrium of the intermediate production allowing an increase of the overall CO conversion. Moreover, The SAPO-34 component converts the intermediate into light olefins leading to an increase in the O/P ratio.

Further increase in the zeotype proportion until the optimum of conversion only draws further the shift of the thermodynamic equilibrium of the intermediate production, leading to an increase in conversion at the detriment of the O/P ratio. Beyond 20 wt% of SAPO-K, both the overall conversion and the O/P ratio progressively decrease. It seems that as far as the amount of zeotype is sufficiently large, the conversion rate of the intermediate on it becomes higher than the reaction rate on the oxide, leading to a decrease in conversion. At this point, the reaction on the oxide is probably the limiting step. Moreover, at a large mass excess, the zeotype might contribute to the hydrogenation of the olefins toward the corresponding paraffins, additionally decreasing the O/P ratio.[31–35]

The independence of the CO_2 selectivity on the mass proportion of zeotype can be explained by considering the global reaction equation. For one mole of CO that is converted into a light olefin or CH_4, one mole of H_2O is produced.

$$CO + 3\,H_2 \rightarrow\ CH_4 + H_2O$$

$$xCO + 2x\,H_2 \rightarrow\ C_xH_{2x} + xH_2O$$

H_2O undergoes the water-gas-shift reaction with CO on the oxide, producing CO_2.

$$CO +\ H_2O\ \leftrightarrow\ CO_2 + H_2$$

As a consequence, the conversion of CO into either methane or hydrocarbons implies the production of a specific proportion of CO_2. More generally, any CO hydrogenation reaction in these conditions generates the amount of CO_2 proportional to the amount of consumed carbon monoxide. Therefore the selectivity to CO_2 remains constant. However equilibrium of WGS reaction is not reached. At this temperature the equilibrium constant, K_{WGS} is of 10 while our reaction quotient, Q, is about 2 at our conversion (calculation is described in the Equation S1). Thus the conversion rate of H_2O via WGS is not sufficient in our system to reach the equilibrium.[36] If the equilibrium was reached the CO_2 selectivity would be close to 45 %.

The same series of experiments with varying mass proportion of zeotype was carried out with SAPO-sK for the mass proportions from 2.5% to 35%; the results are shown in **Figure 22**. A maximum of conversion is observed with 10 wt% of zeotype and a maximum of O/P ratio is observed with 5 wt%. As for SAPO-K, the maxima of conversion and O/P ratio are observed at different zeotype proportions. Decreasing the proportion of zeotype below 10 wt% leads to an increase in CH_4 selectivity at the expense of the other hydrocarbons. As for SAPO-K, the CO_2 selectivity is independent of the proportion of SAPO-sK. The O/P ratios for C2, C3 and C4 hydrocarbons are maximal at 5 wt% of zeotype and decrease at higher proportion.

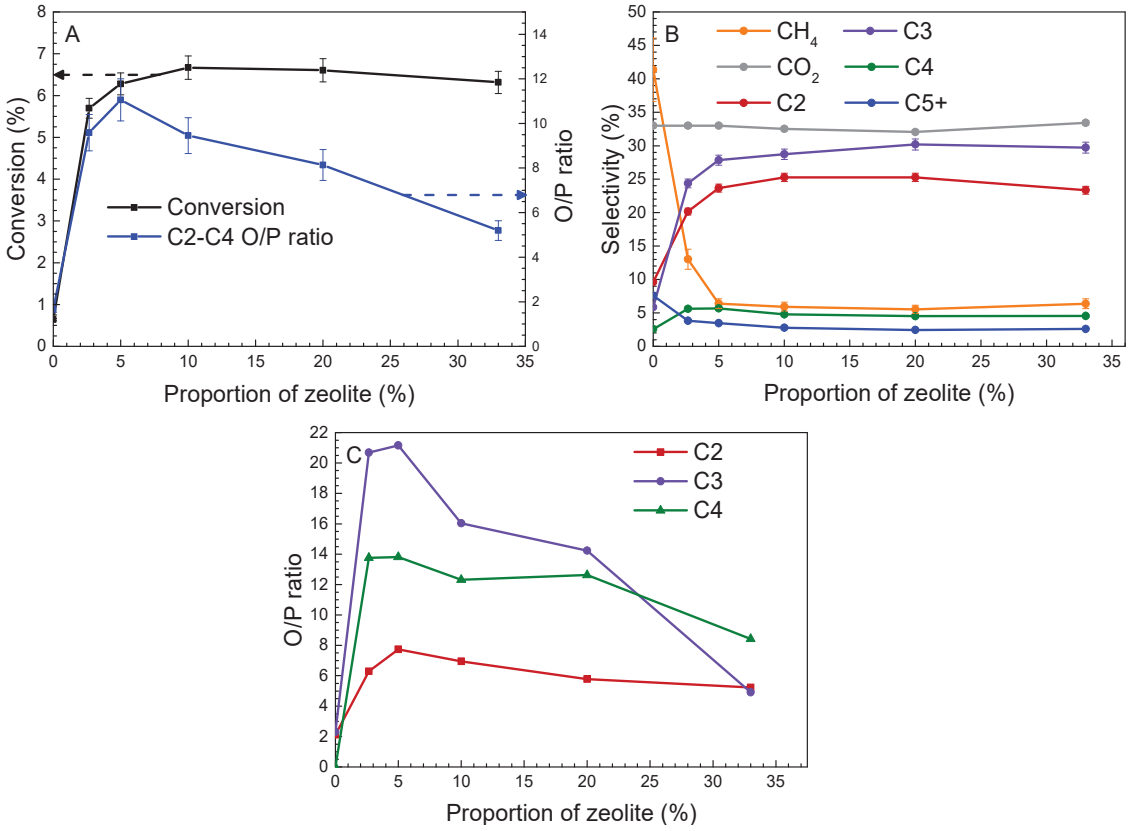

Figure 22: A) Evolution of the conversion and C2-C4 O/P ratio with mass proportion of zeolite; B) evolution of CO_2, CH_4 and hydrocarbon selectivity with mass proportion of zeolite; C) evolution of the O/P ratios for C2, C3 and C4 hydrocarbons with mass proportion of zeolite. Reaction conditions: m(MnO_x-Ref+SAPO-sK)=300 mg, P=25 bar, T=410 °C, H_2/CO/N_2=60/30/10, WHSV 87 $mL.min^{-1}.g^{-1}$. Data were taken after 14 h on stream.

The results for the SAPO-K and SAPO-sK bear considerable similarity: the addition of small quantity of zeotype greatly increases the conversion and the O/P ratio. The CH_4 selectivity decreases greatly in favor of hydrocarbons.

However, a significant difference exists between the potassium-free and potassium-containing SAPO-34: only 10 wt% of SAPO-sK is necessary to reach the maximum of conversion, compared to the 20 wt% necessary for SAPO-K. This can be related to the difference in density of acid sites between the two zeotypes, the density of SAPO-sK (1819 $\mu mol.g^{-1}$, Table 2) being nearly twice higher than the density of SAPO-K (1019 $\mu mol.g^{-1}$). Both zeolites exhibit hydrogenation properties as described in the literature.[21,31–35]

4.3) Reaction temperature

The impact of the reaction temperature on the MnO_x-Ref+SAPO-K catalytic properties was studied and the results are presented in **Figure 23**. An increase in temperature leads to an increase in conversion and a decrease in C2-C4 O/P ratio. At the same time, a CH_4 selectivity increase is observed along with temperature. The O/P ratio for each hydrocarbon decreases with increasing temperature. The decrease in CO_2 selectivity with temperature can be explained by the exothermic enthalpy of the WGS reaction which is around -41 kJ/mol according to the literature.[37–39] The equilibrium constant decrease slightly with temperature from 13 at 390 °C to 9 at 430 °C reducing the driving force for CO_2 formation at higher temperature.

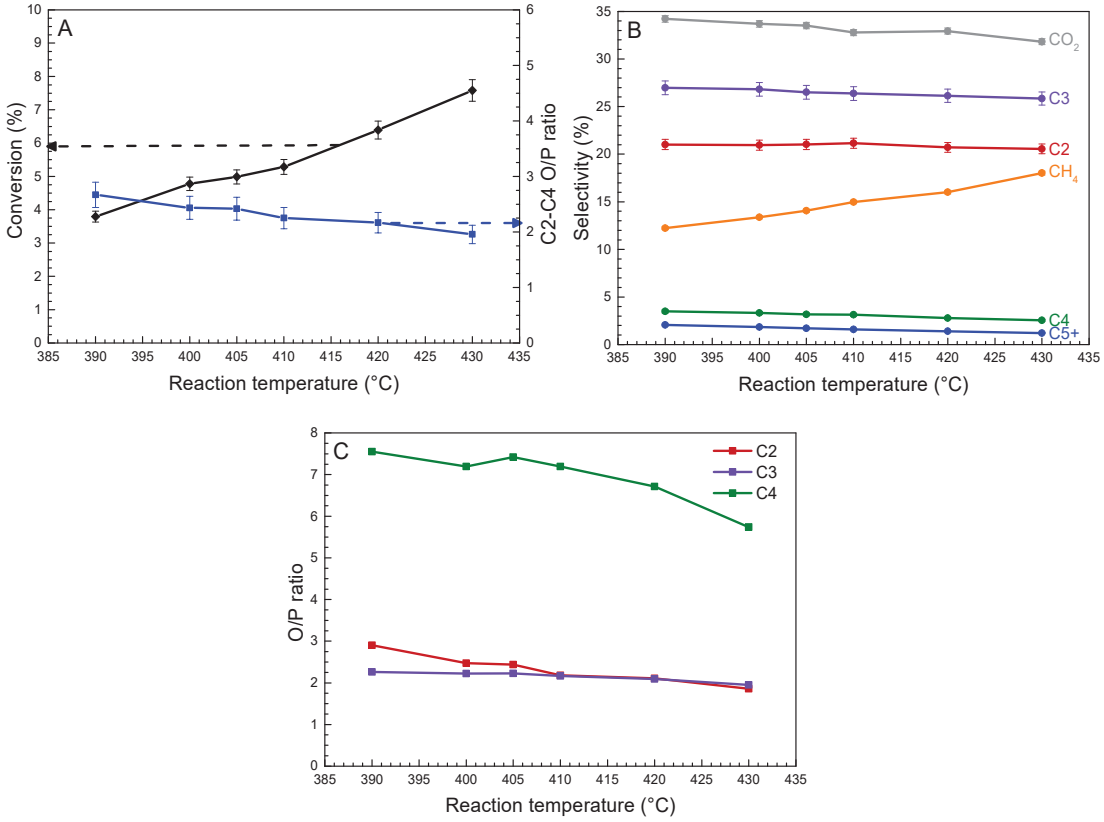

Figure 23: Evolution of the catalytic properties with temperature: A) conversion and C2-C4 O/P ratio; B) CO_2, CH_4 and hydrocarbon selectivity; C) O/P ratio for C2, C3 and C4 hydrocarbons. Reaction conditions: m(MnO_x-Ref)=200 mg, m(SAPO-K)=100 mg, P=25 bar, H_2/CO/N_2=60/30/10, WHSV 87 $mL.min^{-1}.g^{-1}$. Data were taken after 14 h on stream.

4.3.1)Activation energy

The activation energy can be determined by drawing an Arrhenius plot, ln(k)=f(1000/T), depicted in **Figure 24**. The CO reaction rates (ln(k)) were calculated from the conversion values determined from 390 and 430 °C (**Figure 24A**). A linear fitting has been applied to this figure with a R^2 of 0.99. The slope of the linear fit is 8.7244 K and an apparent activation energy of 70 $kJ.mol^{-1}$ was obtained.

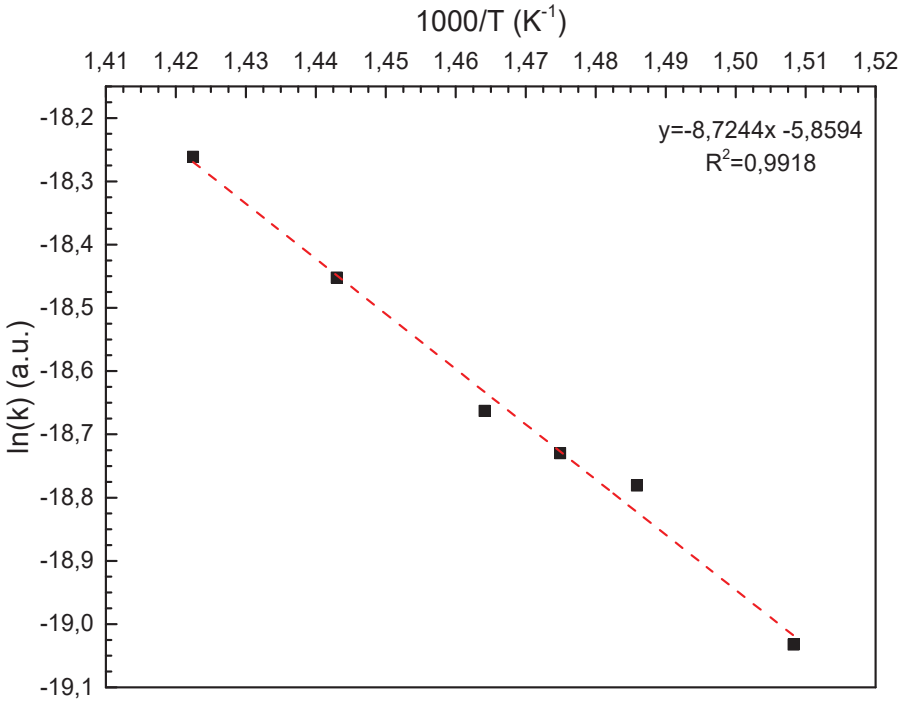

Figure 24: Arrhenius plot for the MnO_x-Ref+SAPO-K catalytic system. Reaction conditions: m(MnO_x-Ref)=200 mg, m(SAPO-K)=100 mg, P=25 bar, H_2/CO/N_2=60/30/10, WHSV 87 mL.min^{-1}.g^{-1}. Data were taken after 14 h on stream.

This value can be compared with the apparent activation energy of methanol synthesis on Cu/ZnO/Al_2O_3 and MTO autocatalytic phase on SAPO-34 that are 56 kJ.mol^{-1} [40] and 332 kJ.mol^{-1},[41] respectively. It can be seen that the apparent activation energy of MnO_x-Ref+SAPO-K is closer to the former value. Furthermore, the difference of activation energy with MTO confirms that the intermediate synthesis on MnO_x-Ref might be the limiting step with 33 wt% of SAPO-34. Moreover, this suggests that methanol is probably the intermediate in our bifunctional system.

4.4) Reactant composition

4.4.1) CO proportion in the CO/H2 mixture

The inlet CO partial pressure was varied at constant total pressure to determine its impact on the catalytic properties of MnO_x-Ref+SAPO-K as shown in **Figure 25** and to calculate the partial reaction order (see part 4.4.3). An increase in CO partial pressure from 1 to 8 bar leads to a decrease in conversion from 18 to 6%. At the same time, the C2-C4 O/P ratio increases from 1.5 to 3.0 (Fig. 25A). The same increase in CO pressure leads to decrease in CH_4 selectivity from 55% to

13% for the benefit of the others hydrocarbons (from 34 to 58%) and CO_2 (from 11 to 29%, Fig. 25B). In line with the global C2-C4 O/P ratio, the O/P ratios for C2 and C3 hydrocarbons increase with the CO partial pressure (Fig. 25C).

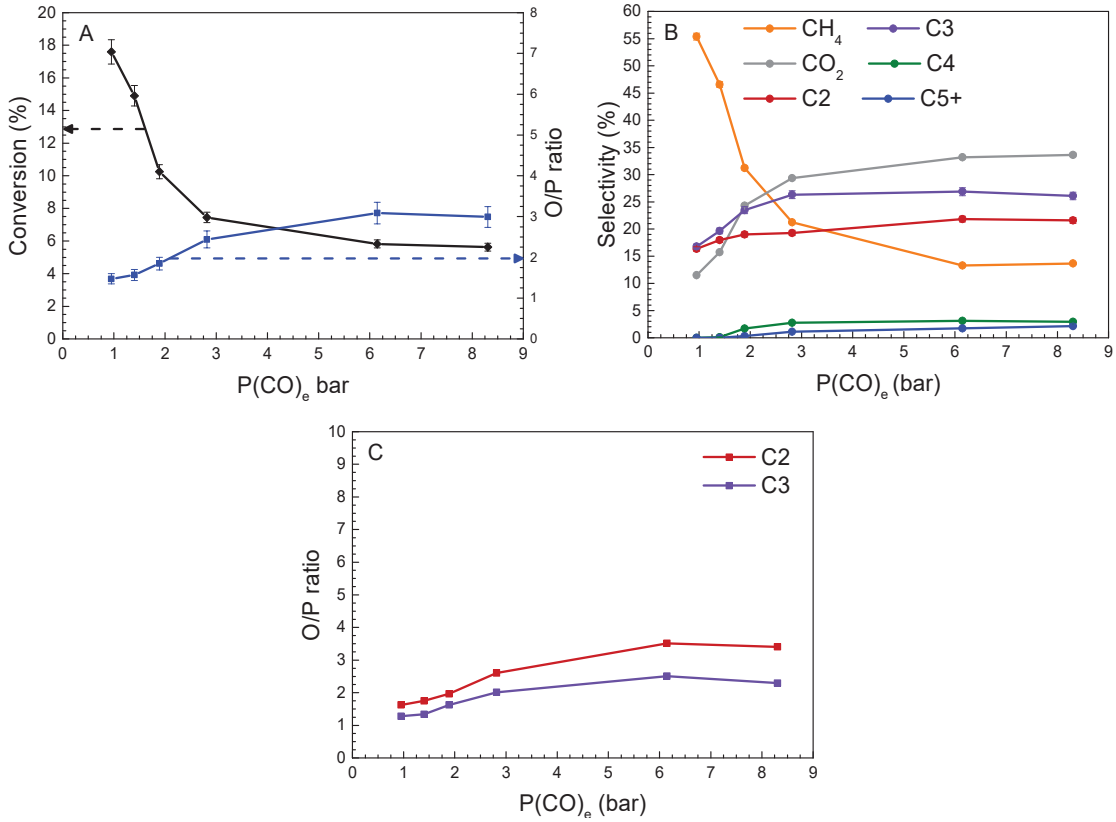

Figure 25: Evolution of the conversion and selectivity values as a function of CO partial pressure ($P(CO)_e$): A) conversion and C2-C4 O/P ratio; B) evolution of CO_2, CH_4 and hydrocarbon selectivity; C) O/P ratio for C2; C3 and C4 hydrocarbons. Reaction conditions: m(MnO_x-Ref)=200 mg, m(SAPO-K)=100 mg, P=25 bar, x_{H2}=60%, N_2 was set to complete the CO proportion , WHSV 87 $mL.min^{-1}.g^{-1}$. Data were taken after 14 h on stream.

The variation of CO_2 evolution can be explained by the shift of the thermodynamic equilibrium. In agreement with the Le Chatelier's principle,[42–44] an increase in the CO partial pressure should shift the equilibrium towards higher conversion of CO and H_2O into CO_2 through the WGS reaction.

4.4.2)H2 proportion

The inlet H_2 partial pressure was varied to determine its impact on catalytic properties of MnO_x-Ref+SAPO-K as depicted in **Figure 26** and to calculate the partial reaction order (see Part 4.4.3). An increase in the H_2 partial pressure leads to an increase in CO conversion (from 2.7% to

5.8%) with a concomitant decrease in the C2-C4 O/P ratio from 5.3 to 2.9 (**Figure 26A**). The O/P ratios for C2 and C3 hydrocarbons also decrease with the H_2 partial pressure (**Figure 26C**) as the CO_2 and C5+ selectivity values (**Figure 26B**). The C3 selectivity increases beyond 10 bar. A maximum in CH_4 selectivity can be observed at 10 bar of H_2. C2 selectivity seems to be stable with the H_2 partial pressure.

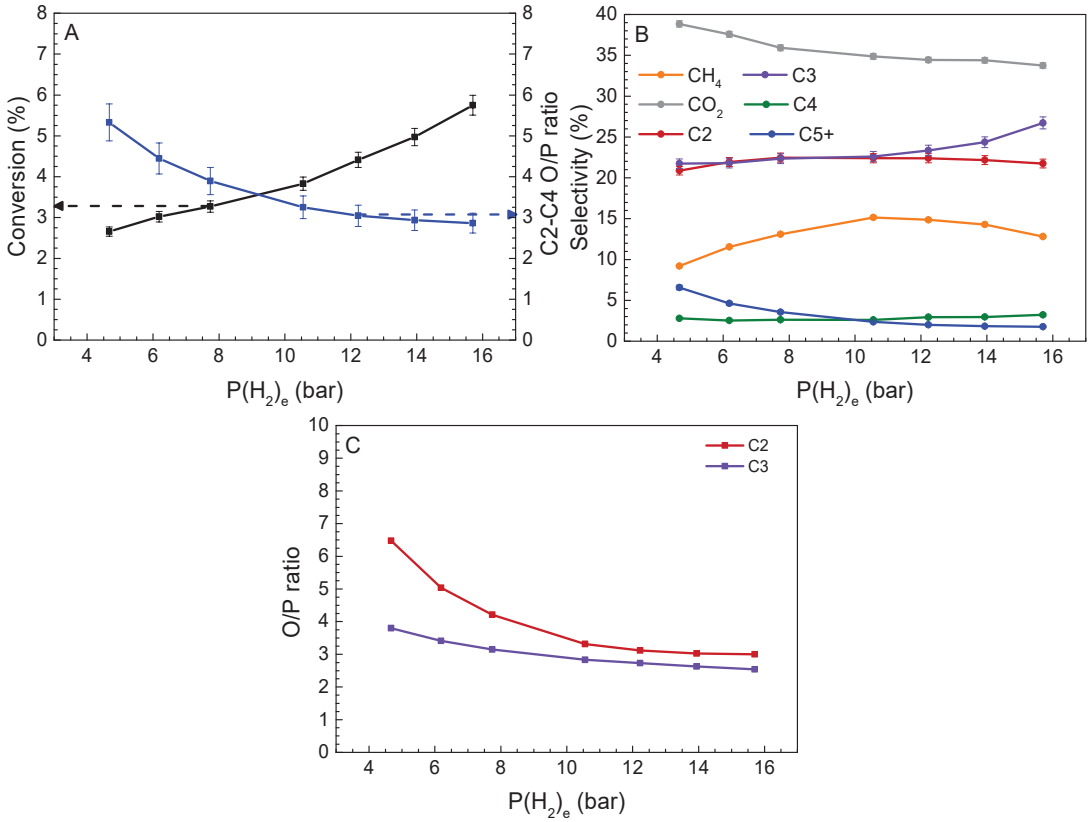

Figure 26: Evolution of the conversion and selectivity values vs. the H_2 partial pressure, $P(H_2)_e$: A) conversion and C2-C4 O/P ratio; B) evolution of CO_2, CH_4 and hydrocarbon selectivity; C) O/P ratio for C2 and C3 hydrocarbons with H_2 partial pressure. Reaction conditions: m(MnO_x-Ref)=200 mg, m(SAPO-K)=100 mg, P=25 bar, x_{CO}=20%, N_2 was set to complete the H_2 proportion, WHSV 87 $mL.min^{-1}.g^{-1}$. Data were taken after 14 h on stream.

The effects of CO and H_2 partial pressure are expectedly opposite. The increase in H_2 partial pressure seems to improve greatly the hydrogenation of CO either into an intermediate or CH_4. However, the maximum of CH_4 selectivity cannot be explained by this effect and should be further studied. Concerning the O/P ratio, the introduction of H_2 in greater quantity increases the reaction rate for olefin hydrogenation either on the zeotype or the oxide leading to a decrease in O/P ratio.

By the same token as for the CO pressure, the effect of H_2 pressure, leading to decrease in CO_2 selectivity (Fig. 26B) can be explained by a shift in the thermodynamic equilibrium of the WGS reaction.

4.4.3) Partial reaction orders

From the experiments using variable partial pressures of the reactants, partial reaction orders were determined for both H_2 and CO. To do so, logarithm of the reaction rate ln(ri) has been plotted against logarithm of the partial pressure of the reactants, as depicted in **Figure 27**. The slope of the linear regression curve corresponds to the partial order (toward either CO or H_2).

Partial orders with respect to CO have been determined for the production of CH_4, CO_2 and the sum of hydrocarbons as to be 0, 1 and 1, respectively. Surprisingly, CH_4 partial order vs CO is null, meaning that the rate of CH_4 formation does not depend on the CO partial pressure.

The partial orders with respect to H_2 for the production of CH_4, CO_2 and the hydrocarbons are 1, 0.5 and 0.5, respectively.

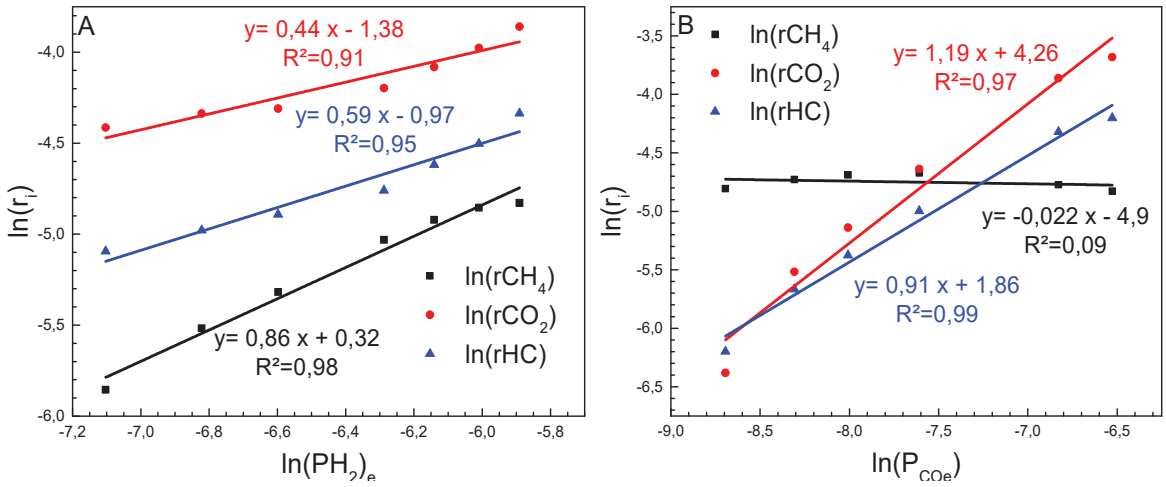

Figure 27: Formation reaction rates plotted as a function of partial pressure of A) H_2 and B) CO for CO_2, CH_4 and other hydrocarbons.

From these results we can divide the reaction products into two groups with respect to their specific reaction orders: the CO_2 and C2+ hydrocarbons group which has the same partial reaction order for H_2 and CO (0.5 and 1, respectively) and CH_4 with partial reaction order toward H_2 and CO of 1 and 0 respectively:

$$r_{HC} = k_{HC} * [H_2]^{0.5} * [CO]$$

$$r_{CO2} = k_{CO2} * [H_2]^{0.5} * [CO]$$

$$r_{CH4} = k_{CH4} * [H_2]$$

The partial reaction order for the formation of CO_2 and hydrocarbons with respect to H_2 equal to 0.5 suggests that H_2 could undergo a dissociative adsorption on the oxide allowing CO hydrogenation. In such process if the adsorption of H_2 is limiting the hydrocarbon production rate then the partial order of the H_2 dissociation might appear in the apparent kinetic law. The H_2 dissociative adsorption was also reported as an important step in the Ox-Zeo process. Oxides known for their ability to dissociate H_2 were added to oxides capable of activating CO.[20,25,45–50] For instance, Ga_2O_3, known for its H_2 dissociation capability,[51–53] has been added to MnO to improve the H_2 dissociation capabilities of the oxide[54,55] and thus the catalytic activity.

4.5) Conclusion on the parameters study

This study allowed to gain insight into the dependence of the catalytic properties on the main reaction parameters. Several common trends have been revealed: generally, an increase in conversion is accompanied with a decrease in the O/P ratio. On the other hand, the CH_4 selectivity increases at the expense of the C2+ hydrocarbons. These rules are common, whether the conversion is modified by variations of contact time, temperature or reactants partial pressure. Among the studied parameters, the most influential one is the contact time that strongly impacts all the measured catalytic properties. It is important to maintain correct reaction conditions to favor both conversion and olefin selectivity. The CO_2 selectivity varies due to the WGS thermodynamic equilibrium, only if the temperature or H_2 or CO partial pressures are varied. Otherwise, the conversion variation does not affect the CO_2 selectivity.

From the data obtained at variable temperatures and partial pressures, activation energies and partial reaction orders have been determined. The apparent activation energy in our study is of 72 $kJ.mol^{-1}$, comparable to the one usually found for the methanol synthesis. The partial reaction orders of CO_2 and C2+ hydrocarbons formation are 1 and 0.5 with respect to CO and H_2,

respectively, whereas formation of CH_4 has reaction order of 0 and 1 toward CO and H_2, respectively.

5) In situ DRIFT study

Diffuse Reflectance Infrared Fourier Transform (DRIFT) spectroscopy was used to study the evolution of the surface species present after the activation step and during catalytic reaction.

5.1) MnOx-Ref

5.1.1) Surface species after activation

The spectra of MnO_x-Ref treated at 430 °C under either He or H_2 are shown in **Figure 28**. The spectrum of He treated sample contains bands at 3680, 3630 and 863 cm^{-1} attributed to surface hydroxyl[56] and carbonate species,[57,58] respectively. The two bands at 1431 and 1565 cm^{-1} were attributed to carbonate species and or second-order vibrations of MnO_x-Ref. Interestingly, the relative absorbance of the bands at 3680 cm^{-1} was enhanced for the H_2-treated, sample revealing increased hydroxylation.

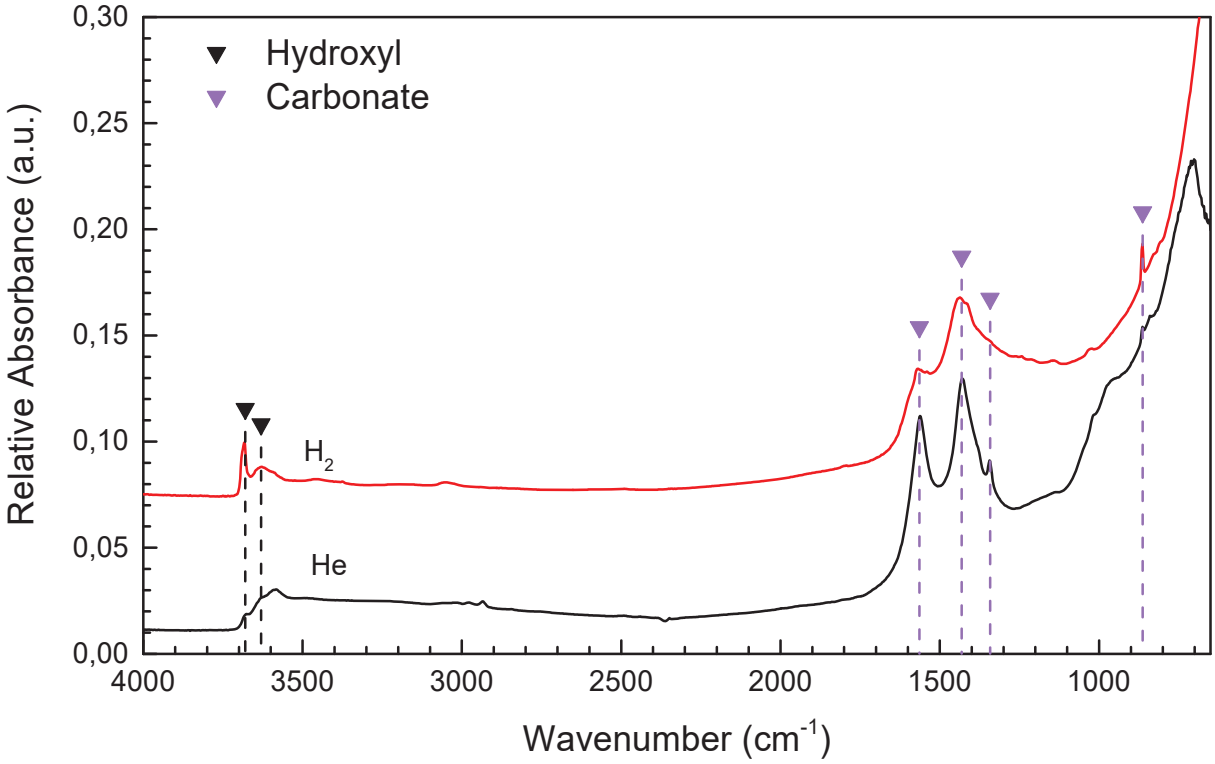

Figure 28: *In situ* DRIFT spectra of MnO_x-Ref recorded at room temperature under 20 nml.min^{-1} of He after treatment at 430 °C under either H_2 or He. The background signal was subtracted, corresponding to the spectrum of dehydrated KBr powder recorded at the same temperature.

As shown in **Figure 29**, no effect of the H_2 activation temperature on both hydroxylation and carbonatation was observed between 380 and 450 °C.

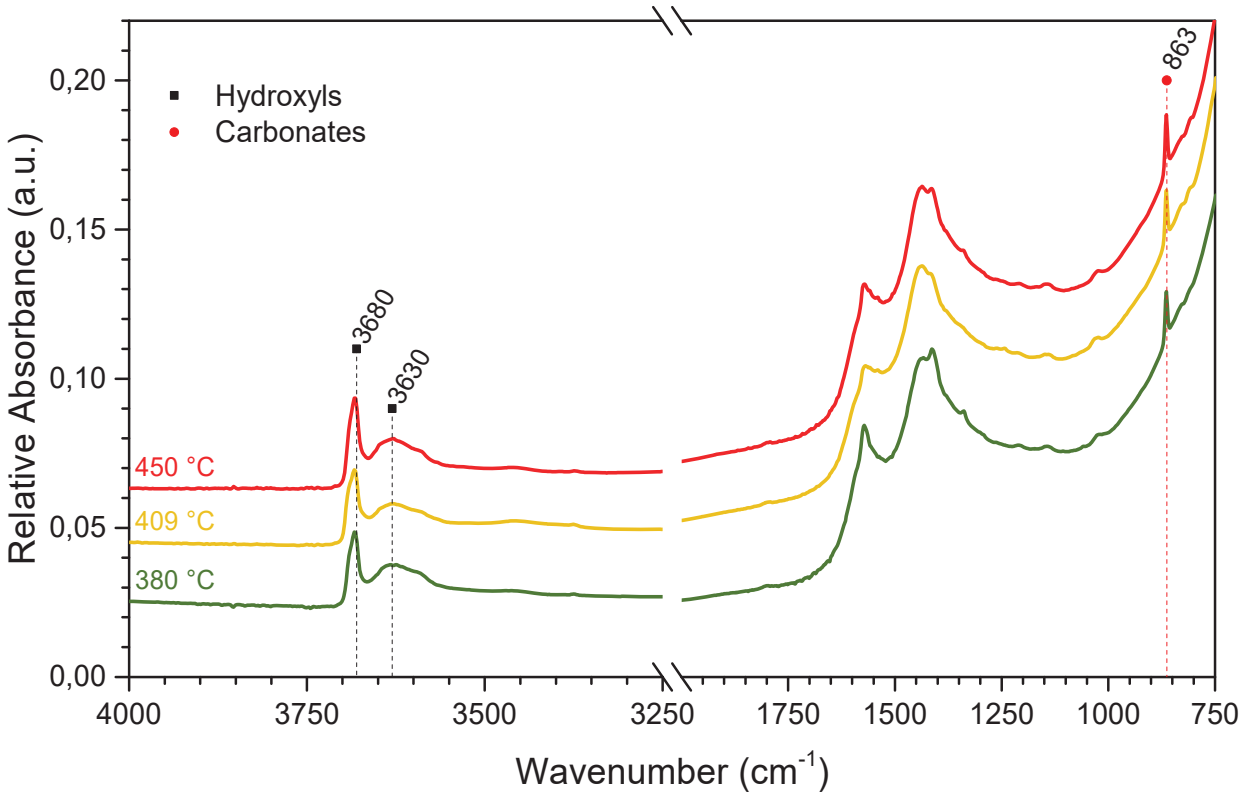

Figure 29: *In situ* DRIFT spectra of MnO_x-Ref recorded under 20 NmL.min^{-1} of H_2 flow at different temperatures. The backgrounds corresponded to the spectra of dehydrated KBr powder recorded at the same temperatures.

5.1.2) CO adsorption at low temperature

Activation of MnO_x-Ref under H_2 flow at 410 °C enabled to absorb CO at -2 °C as revealed by IR bands at 2062, 2038, 1984, 1962, 1927 and 1917 cm^{-1} (**Figure 30**) corresponding to $Mn_y(CO)_x$ species.[59–61] Note that contrarily to Zhu and coll.[1] no signals corresponding to linearly absorbed CO were observed on both fresh sample and those reduced at different temperatures.

However, no CO adsorption was evidenced after activation under He at the same temperature, showing that the Mn_3O_4 passivation layer does not adsorb CO. It was concluded that reduction of Mn_3O_4 leads to formation of oxygen vacancies at the surface of MnO_x able to adsorb CO. Zhu and coll.[1] have tested three oxides with different Mn oxidation states, MnO, MnO_2 and Mn_3O_4. They were all active but were all reduced during the catalytic test towards MnO (as characterized by XRD), which is the only stable crystalline phase in the reaction conditions. Our DRIFT results

suggest that MnO is the active phase since it is able to adsorb CO. This phase is probably non-stoichiometric as shown by *in situ* Raman spectra (see part 3.2).

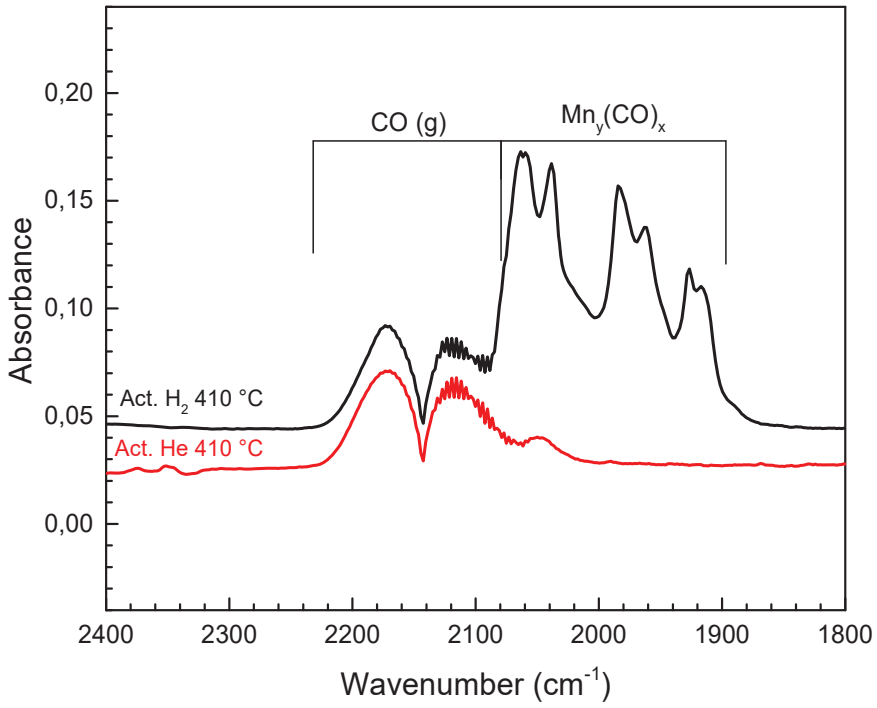

Figure 30: *In situ* DRIFT spectra of MnO_x-Ref sample recorded at -2 °C under 20 NmL.min^{-1} of 2.5%CO-He flow. The backgrounds corresponded to the spectra recorded under 20 NmL.min^{-1} of He flow at -2 °C after activation at 410 °C under 20 NmL.min^{-1} He or H_2 flow for 30 min.

The evolution of *in situ* DRIFT spectra recorded over time at -2 °C under 20 mL.min^{-1} of 2.5% CO-He flow is plotted in **Figure 31**. the bands corresponding to $Mn_x(CO)_y$ species were observed immediately and they increased for the first 12 min before being strongly decreased afterwards. At the same time, additional bands rose between 900-1100 cm^{-1} and 1200-1700 cm^{-1}. Those bands were attributed to ν1 and ν3 vibrations, respectively of monodentate, chelating bridging and bridging bidentate carbonates.[57] Note that the splitting of the degenerate ν3 vibration (E mode for free carbonate with D_{3h} symmetry) is typical of each species and that the ν1 vibration is slightly IR active due to the loss of symmetry compared to D_{3h}.[57] The intensity of carbonate bands continued to grow after 12 min when $Mn_x(CO)_y$ species began to disappear. Formation of

carbonates species over activated MnO_x was already reported by Zhu and coll. [1] and attributed to the Boudouart reaction:

$$2CO^* \rightarrow C^* + {CO_2}^*$$

By interaction with surface O^{2-} species adsorbed CO_2* is transformed to carbonate anion. The surface carbon species C* can be further converted into ketene, methanol or methane by reacting with H_2 (and CO). Note that this exothermic reaction is thermodynamically favourable (+172 kJ.mol^{-1})[62–64] but could be kinetically limited at -2 °C.

Alternatively, it would imply a redox mechanism during which lattice oxygen is consumed to form carbonates and electrons ($CO + 2O^{2-} \rightarrow CO_3^{2-} + 2e^-$) leading to reduction of MnO_x. Finally, it was confirmed that carbonates are stable[1] since they were still observed in flowing He at 200 °C.

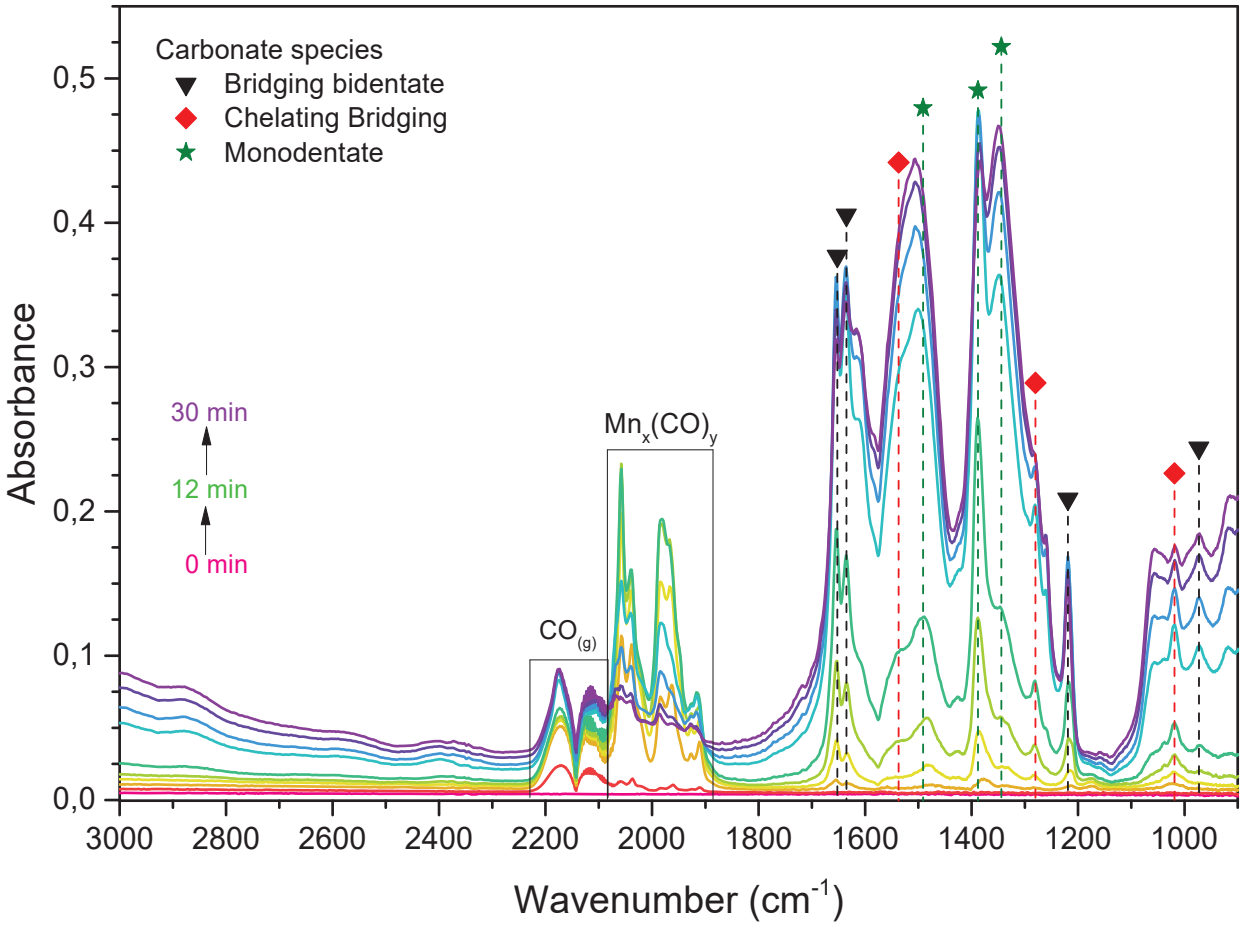

Figure 31: *In situ* DRIFT spectra of MnOx-Ref sample recorded over time for 30 min at -2 °C under 20 mL.min^{-1} of 2.5%CO-He flow. The background corresponded to the spectrum recorded

under 20 mL.min^{-1} of He flow at -2 °C after activation at 430 °C under 20 mL.min^{-1} H_2 flow for 30 min.

5.1.3) Surface species under H2/CO reaction mixture at 410 °C

Furthermore, *in situ* DRIFT experiments were carried out under H_2/CO flow at the reaction temperature. The spectral evolution of MnO_x-Ref sample recorded over time at 410 °C under 20 mL.min^{-1} of 2.5%CO/7.5%H_2/90%He flow is plotted in Fig. 32: some bands typical of formate species were unambiguously observed at 2820 and 2715 cm^{-1} (ν(C-H) and ν_s(O-C-O)+δ(C-H), respectively).[65–67] These formate bands rose for 10 min and then remained constant. Furthermore, bands observed around 2143 and 2349 cm^{-1} were attributed to CO and CO_2 molecules in the gas phase, respectively.[58,68]

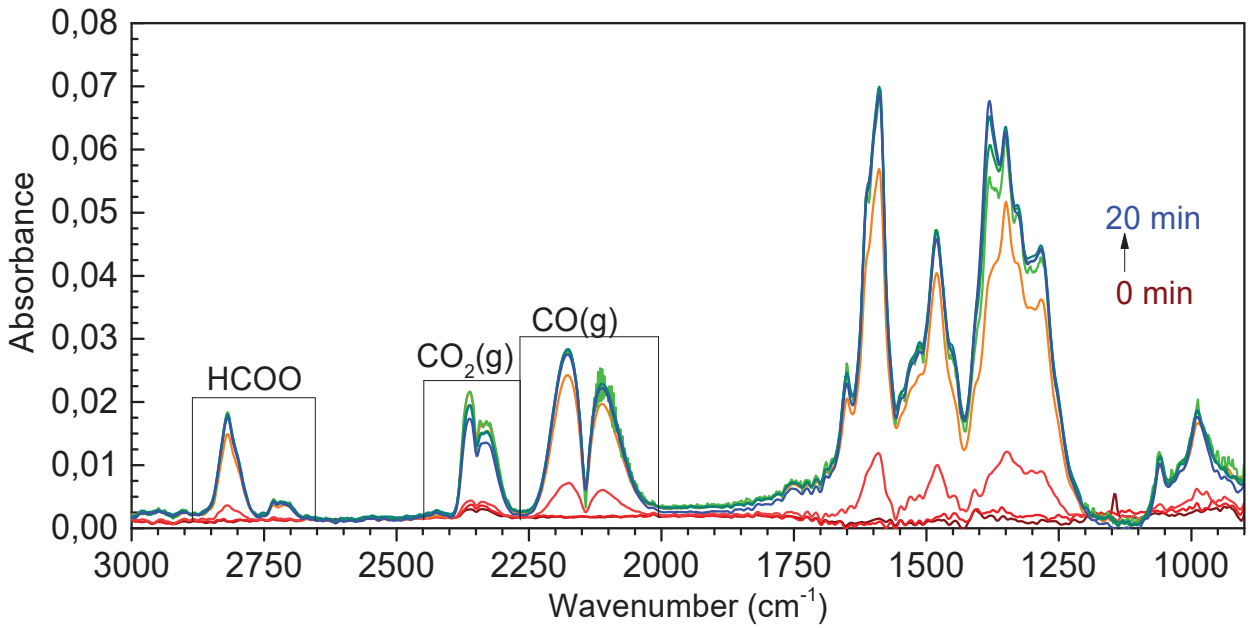

Figure 32: *In situ* DRIFT spectra of MnO_x-Ref sample recorded over time at 410 °C under 20 mL.min^{-1} of 2.5%CO/7.5%H_2/90%He flow. The background corresponded to the spectrum recorded under 20 mL.min^{-1} of He flow at 410 °C after activation at 430 °C under 20 mL.min^{-1} H_2 flow for 30 min.

As for CO adsorption at -2 °C, numerous bands were observed at 1700-1200 cm^{-1}. They could either be attributed to formates,[65–67] or to carbonates.[57] Furthermore, the bands at 1060, 988 cm^{-1} could also correspond to these species as well as methoxy ones.[66,69,70] However, as the main

bands evolved with the same rate as the bands at 2820 and 2715 cm^{-1}, they were attributed to formates. In particular, the bands at 1651 and 1614 cm^{-1} corresponded to ν_{as}(O-C-O) vibrations, the ones at 1384, 1353 cm^{-1} to ν_s(O-C-O) and δ(OC-H) and the ones at 1060, 988 cm^{-1} to δ(OC-H)[71]. Formate species have been reported as intermediates leading to methanol formation.[25,45,47] However, the $\nu_{as}(CH_3)$ band at 2900-2900 cm^{-1} [66,69,70] typical of methoxy species was not observed in the DRIFT spectra. This feature was explained by a slower formation rate of methoxy species from formates and their rapid transformation to methanol.[28]

5.2) MnOx-Ref+SAPO-K mixture

5.2.1) Surface species after activation

MnO_x-Ref+SAPO-K mixtures were analyzed by *in-situ* DRIFT after activation under H_2 at 410 °C as illustrated in **Figure 33** for 75%MnO_x-Ref+25%SAPO-K. Compared to MnO_x-Ref, broad additional bands were observed at 1215, 1100, 730 cm^{-1} which were attributed to asymmetric and symmetric stretching vibrations of the SAPO-34 framework.[72] Second order bands of the SAPO-34 T-O-T framework atom (T either Si, AL or P) were also observed at 2200 and 2300 cm^{-1}. The ν(OH) spectral range was significantly different with a main band at 3600 cm^{-1} due to acidic OH groups of SAPO-34.[13] It is worth noting that the fine band at 863 cm^{-1} that was observed on the spectrum of MnO-Ref is no longer visible on the MnO-Ref+SAPO-34 one. This might be due to acid-base reaction of the surface carbonates with Brønsted sites of SAPO-34.

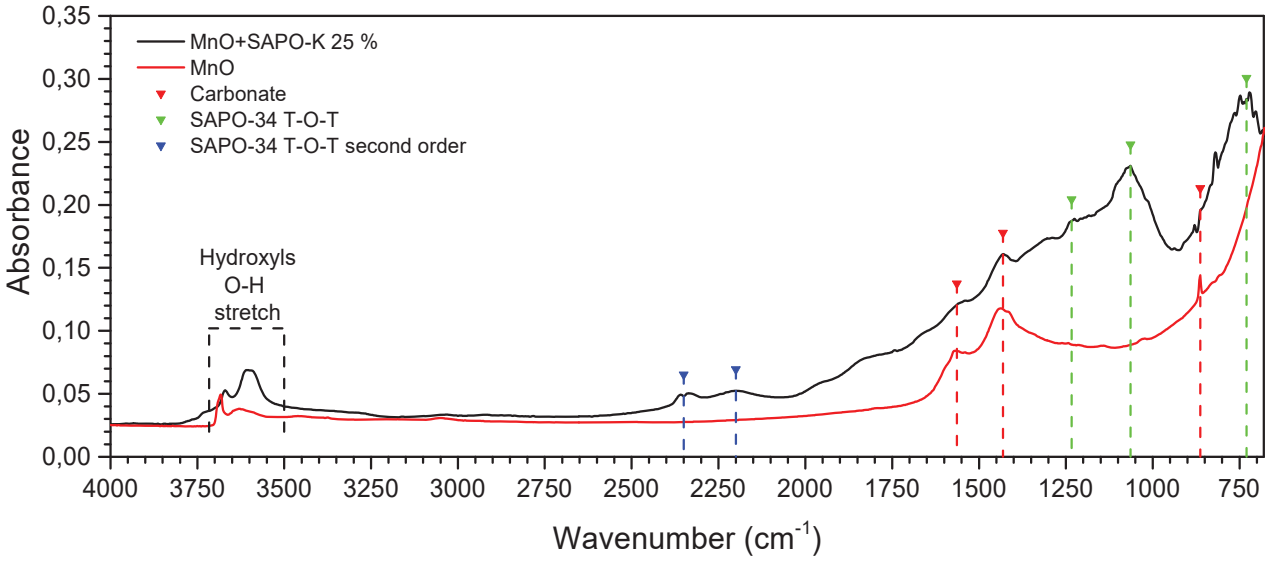

Figure 33: *In situ* DRIFT spectra of MnO_x-Ref and 75%MnO_x-Ref+25%SAPO-K recorded under 20 NmL.min^{-1} of H_2 flow at 410 °C. The background corresponds to the spectrum of dehydrated KBr powder recorded in the same conditions.

5.2.2) Surface species under H_2+CO at 410 °C

a) Catalyst mixture composition

Addition of only 10% wt. of SAPO-34 to MnO_x-Ref led to a drop of absorbance of formates bands by 2 times whereas after addition of 25% wt. of SAPO-34, the formates bands became by 4 times less intense (**Figure 34**). This evidenced a strong decrease of the steady state concentration of formate species caused by addition of zeotype, probably due to methanol conversion over SAPO-34. On the opposite, the carbonate species do not seem to be consumed by SAPO-34. This might indicate that they are only spectator species on the surface and their surface coverage do not depend on the overall conversion.

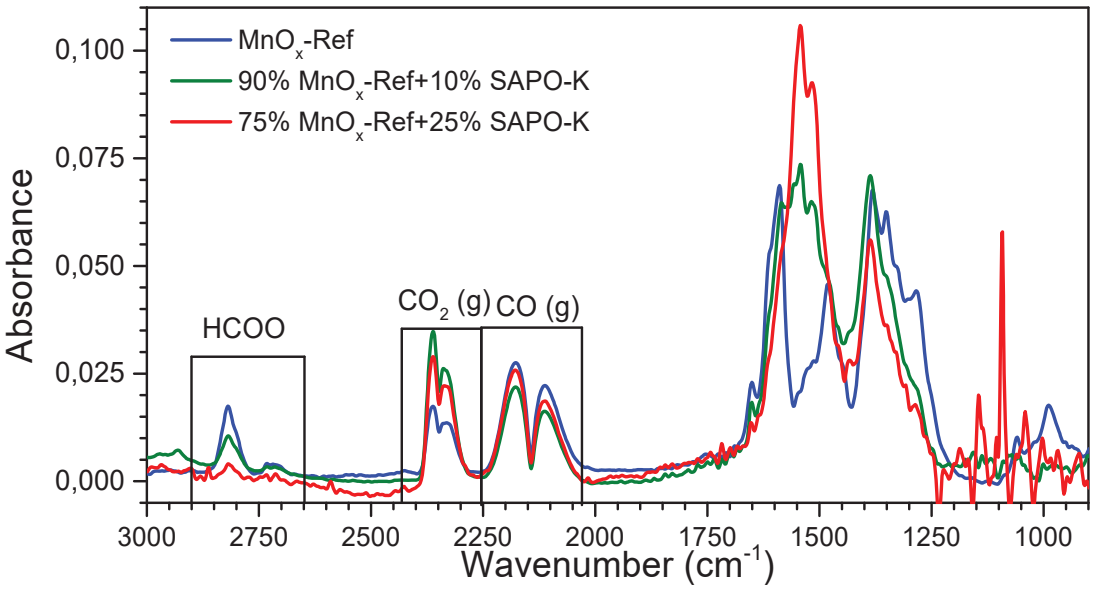

Figure 34: *In situ* DRIFT spectra of MnO_x-Ref, 90%MnO_x-Ref-10%SAPO-K and 75%MnO_x-Ref-25%SAPO-K samples recorded at 410 °C after 10 min under 20 mL.min^{-1} of 2.5%CO/7.5%H_2/90%He flow. The backgrounds corresponded to the spectra recorded under 20 mL.min^{-1} of He flow at 410 °C and activation at 430 °C under 20 mL.min^{-1} H_2 flow for 30 min.

From these observations we propose that methanol is the main intermediate for the formation of the olefins over MnO_x+SAPO-34 mixtures. Surface carbonates could come from both the WGS and Boudouard reactions occurring on the oxide surface.

b) Temperature effect

The adsorbed species have been studied from 250 to 400 °C and the recorded spectra are depicted in **Figure 35**. It can be seen that the formate bands at 2900 cm^{-1} and 2655 cm^{-1} increased when the reaction temperature was decreased. It was related to the lowering in CH_3OH conversion shifting the reaction equilibrium toward the formates and confirms that methanol is a key reaction intermediate produced on MnOx-Ref that reacts with SAPO-34 to produce light olefins, which results in a synergistic effect between two catalytic functions.

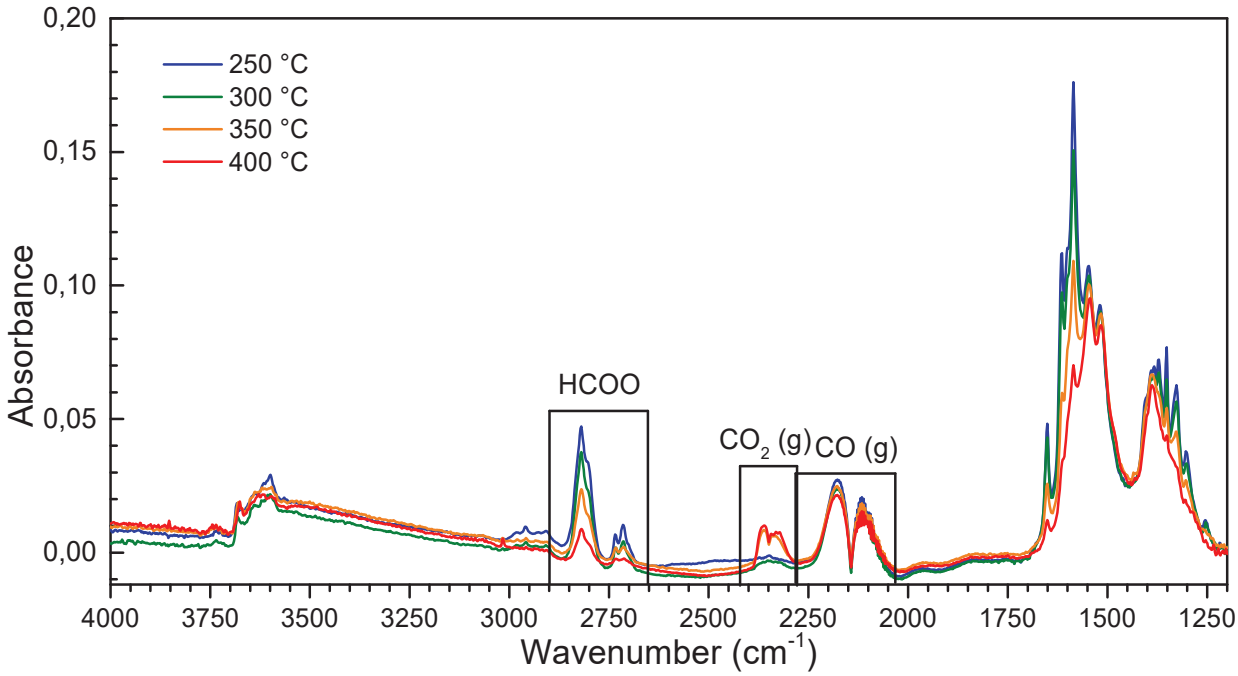

Figure 35: *In situ* DRIFT spectra of 75%MnO_x-Ref-25%SAPO-K sample recorded at various temperatures under 20 NmL.min^{-1} of 2.5%CO/7.5%H_2/90%He flow. The backgrounds corresponded to the spectra recorded under 20 NmL.min^{-1} of He flow after activation at 430 °C under 20 NmL.min^{-1} H_2 flow for 30 min.

6) Characterization of spent catalysts

XRD analysis was carried out on 80%MnO-Ref+20%SAPO-K mixture after 14 h of test. The characteristic peaks of MnO (PDF 75-1090 ICDD pattern) and of SAPO-34 (PDF 47-0429 ICDD pattern) were observed (**Figure 36**). The amorphous background observed in the diffractogram is probably due to the presence of fused quartz fibers (added when filling the reactor).

By using the Scherrer equation on the diffraction peaks corresponding to MnO, the crystallite size was shown to increase from 21 nm to 25 nm during the test, revealing a slight sintering.

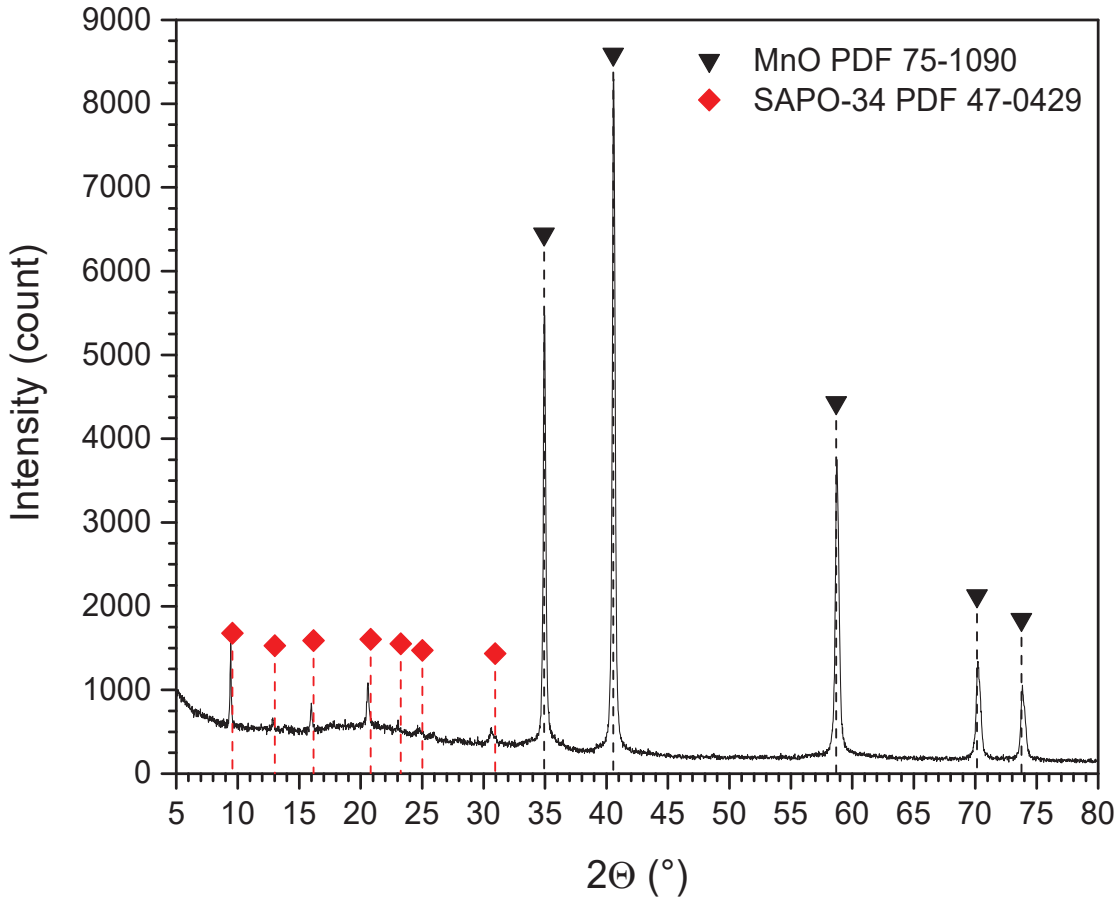

Figure 36: XRD diffractogram of 80%MnO-Ref+20%SAPO-K spent catalyst.

Another question was the proportion of carbon accumulated on the catalytic mixture during the test. A CHONS analysis was performed on a fresh and used catalyst. As already said, 1.2% of carbon was already present before test. Carbon is present as carbonate surface species in the oxide as shown by *in situ* DRIFT spectrum in **Figure 28** and highly disordered graphite as shown by Raman spectrum of the fresh oxide in **Figure 2**. Interestingly, the amount of carbon present in the spent mixture was also 1.2% revealing a very limited coking during reaction.

The TGA curve of fresh 80%MnO-Ref+20%SAPO-K mixture plotted in Fig.37 shows four main mass variations: first, a weak mass loss due to dehydration process occurred at 120 °C. Then, two gains of mass were observed at 310 and 450 °C and attributed to oxidation of MnO to Mn_3O_4 followed by the oxidation of a part of the formed Mn_3O_4 into Mn_5O_8 forming a mixed oxide composed of both Mn_3O_4 and Mn_5O_8. [73–75] Finally, a loss of mass was observed at 575 °C due to the formation of Mn_2O_3.[73–75] The final difference in mass between the fresh and spent arise from de-hydroxylation, decarboxylation or oxidation of carbonaceous species.

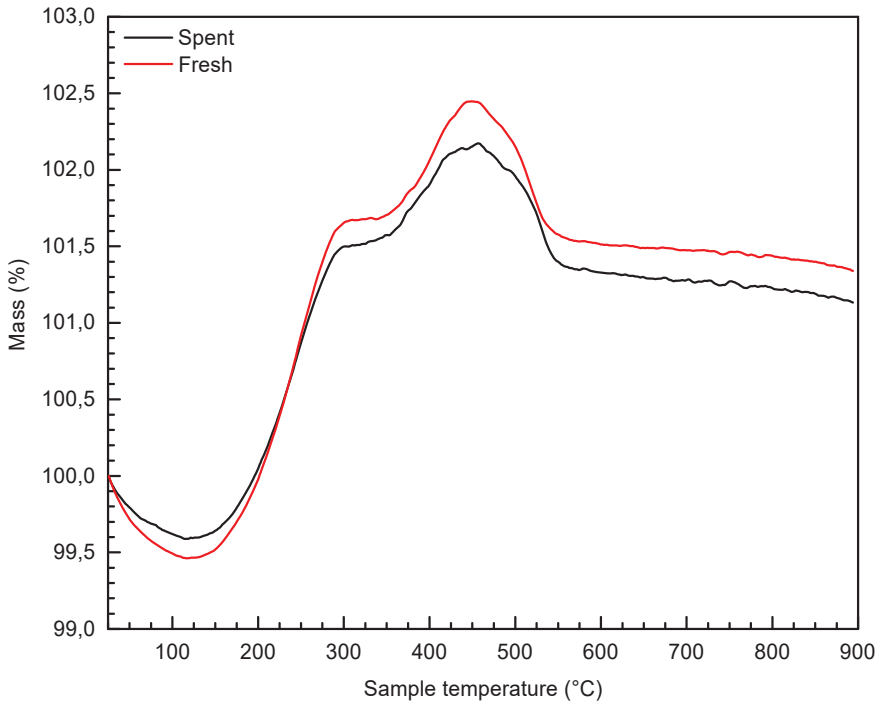

Figure 37: TGA curves in air of 80%MnO-Ref+20%SAPO-K before and after test.

The TGA curve of the spent mixture was quite similar since a difference of only 0.18% of the initial mass was observed at 900 °C. It confirms that a quite small quantity of carbon accumulates on the surface of MnOx-SAPO-34 mixtures during the Ox-Zeo process. This is surprising compared to the MTO process for which coke is easily formed on the zeolite surface leading to fast deactivation.[76–78]

GC-MS analysis of the trapped hydrocarbons in the spent 80%MnO-Ref+20%SAPO-K mixture confirms the presence of trapped hydrocarbon. Most of them are anthracene species that have already been observed in the spent Ox-Zeo catalysts.[26,79] Those anthracenes are known as precursors of coke in the MTO process.[77,78,80,81] However, the Ox-Zeo conditions strongly limit the formation of such species and thus prevent the deactivation as already shown in literature.[20] It was proposed that the presence of CO and H_2 during the Ox-Zeo process limits the formation of coke.[26,79]

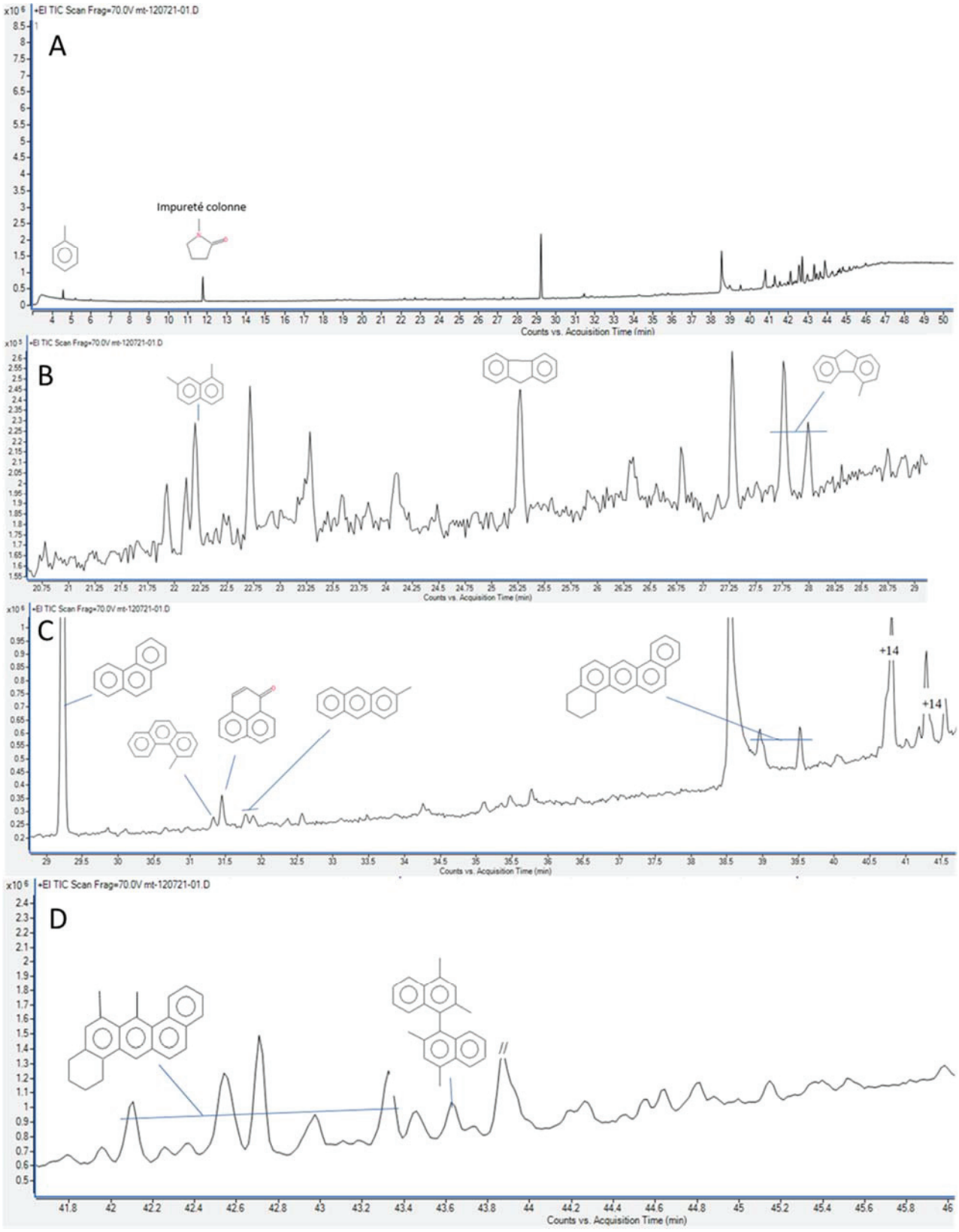

Figure 38: GC-MS analysis of extracted hydrocarbons from spent 80%MnO-Ref+20%SAPO-K mixture. A) Whole chromatograph, B) zoom on the 20.6 min to 29.1 min range, C) zoom on the 28.75 min to 41.75 min range and D) zoom on the 41.7 min to 46 min.

^{13}C NMR spectra of four spent catalyst are plotted in **Figure 39**. Those four spent catalysts were composed of 67% of MnO-Ref and 33 % of SAPO-K, SAPO-sK, SAPO-Gil or SAPO-com. The signal was noisy for all of them (in spite of 48 h counting) because of the small amount of carbon species. However, several bands can be distinguished that are in common for all the samples. The band at 128 ppm corresponds to aromatic molecules.[78,81] The band at 210 and 290 ppm are rotational bands of the aromatic compounds. The band at 19 ppm corresponds to aliphatic molecules that are trapped inside of the zeolite.[78,82,83] Those two bands together indicate the formation of methylbenzene like molecules that are known intermediates formed during the MTO reaction and lead to the formation of coke.[78,82,83] Finally the band at 49 ppm corresponds to methanol that is trapped inside of the zeolite structure.[78,82,83] It is worth noting that characteristic band of ketene at 194 ppm is not visible in our spectra for all the zeotypes.[84] Thus ketene, if formed in our system, have not been retained in the structure. Those analysis further confirm that methanol is our main intermediate.

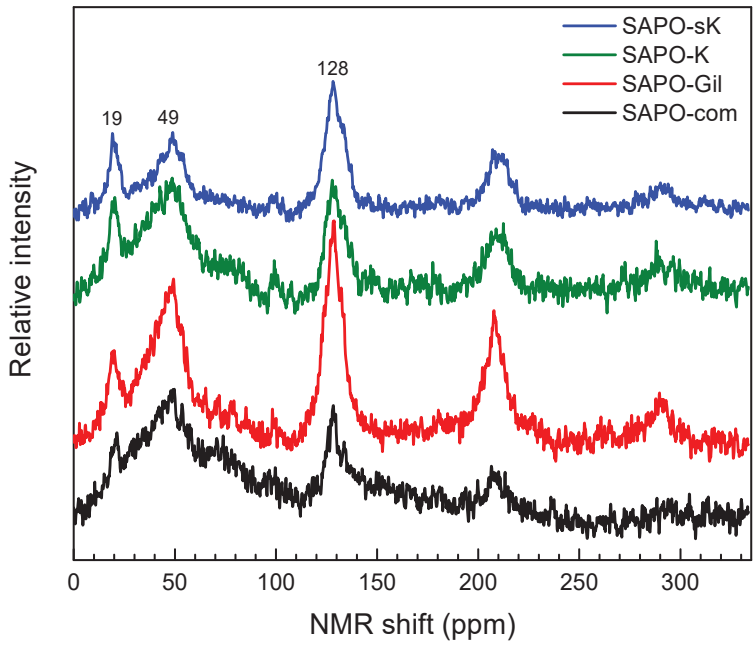

Figure 39 : ^{13}C NMR spectra of spent catalyst (14 h on stream) for SAPO-com, SAPO-K, SAPO-sK and SAPO-Gil with MnO-Ref (66 %). Reaction conditions: m(MnOx-Ref)=200 mg, m(SAPO-34)=100 mg, P=25 bar, T=410 °C, $H_2/CO/N_2$=60/30/10, WHSV 87 $mL.min^{-1}.g^{-1}$.

7) Conclusions

This reference study using MnOx+SAPO-34 bifunctional catalysts allowed to go further than the study of Zhu and coll.[1] and strengthen the scientific background on the Ox-Zeo process. Methanol is formed over MnO_x from CO and H_2 via formate route. However, at the reaction temperature of 400 °C, methanol is further hydrogenated to methane. When a small quantity of SAPO-34 is added to MnOx, methanol is consumed leading to formation of C2-C4 olefins in the SAPO-34 pores. The conversion is strongly increased by a shift of thermodynamic equilibrium and the CH_4 selectivity is damped probably because formation of olefins is much faster than formation of CH_4. C2-C4 olefins can be further hydrogenated to C2-C4 paraffins both over MnO_x which is hydrogenating and more surprisingly over SAPO-34. In agreement with the literature,[25,26,79] the O/P ratio was related to the density of acid sites of SAPO-34. This phenomenon can be explained by formation a hydrocarbon pool in the zeotype pores favoring hydrogen transfer [31–35,85–88]. CO_2 is a major by-product. It is not mainly formed by the Boudouart reaction as previously claimed[1,20,27] but by the WGS reaction. In that regard, it was shown that the CO_2 selectivity varies only if the temperature or the H_2 or CO partial pressure is varied. Finally, the Ox-Zeo process was confirmed to be stable with quite low coking in spite of a second step similar to MTO. This major difference could arise from the low concentration of methanol within the SAPO-34 pores and by the presence of CO and H_2 in the feed. All these results will be useful to investigate the effect of intimacy in the Ox-Zeo process.

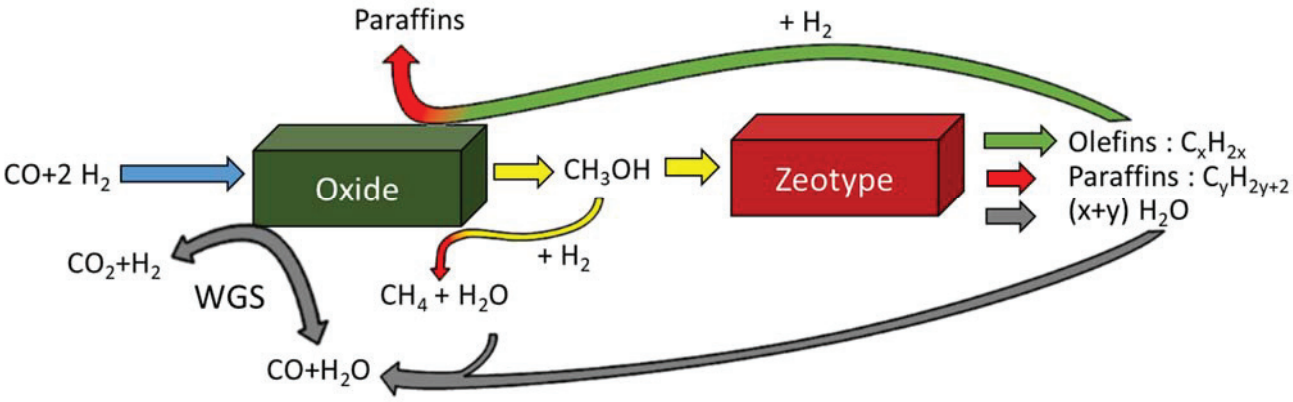

Figure 40: Reaction scheme of the Ox-Zeo process using MnOx+SAPO-34 mixtures.

8) References

1. Zhu, Y., Pan, X., Jiao, F., Li, J., Yang, J., Ding, M., Han, Y., Liu, Z., Bao, X. Role of Manganese Oxide in Syngas Conversion to Light Olefins. *ACS Catal.* **7**, 2800–2804 (2017).
2. Böttcher, M. E., Gehlken, P.-L., Usdowski, E. Infrared spectroscopic investigations of the calcite-rhodochrosite and parts of the calcite-magnesite mineral series. *Contr. Mineral. and Petrol.* **109**, 304–306 (1992).
3. Boulard, E., Goncharov, A. F., Blanchard, M., L. Mao, W. Pressure-induced phase transition in $MnCO_3$ and its implications on the deep carbon cycle: High-Pressure Phase Transition In $MnCO_3$. *J. Geophys. Res. Solid Earth* **120**, 4069–4079 (2015).
4. Regmi, R., Tackett, R., Lawes, G. Suppression of low-temperature magnetic states in Mn_3O_4 nanoparticles. *J. Magn. Magn. Mater.* **321**, 2296–2299 (2009).
5. Kaczmarczyk, J., Zasada, F., Janas, J., Indyka, P., Piskorz, W., Kotarba, A., Sojka, Z. Thermodynamic Stability, Redox Properties, and Reactivity of Mn_3O_4, Fe_3O_4, and Co_3O_4 Model Catalysts for N_2O Decomposition: Resolving the Origins of Steady Turnover. *ACS Catal.* **6**, 1235–1246 (2016).
6. Larbi, T., Doll, K., Manoubi, T. Density functional theory study of ferromagnetically and ferrimagnetically ordered spinel oxide Mn_3O_4. A quantum mechanical simulation of their IR and Raman spectra. J. Alloys Compd. **688**, 692–698 (2016).
7. Chou, H., Fan, H. Y. Light scattering by magnons in CoO, MnO, and α−MnS. *Phys. Rev. B* **13**, 3924–3938 (1976).
8. Mita, Y., Sakai, Y., Izaki, D., Kobayashi, M., Endo, S., Mochizuki, S. Optical Study of MnO under High Pressure. *Phys. Stat. Sol. (b)* **223**, 247–251 (2001).
9. Mironova-Ulmane, N., Kuzmin, A., Skvortsova, V., Chikvaidze, G., Sildos, I., Grabis, J., Jankoviča, D., Dindune, A., Maiorov, M. Synthesis and Vibration Spectroscopy of Nano-Sized Manganese Oxides. *Acta Phys. Pol. A* **133**, 1013–1016 (2018).
10. Kaplas, T., Svirko, Y. Direct deposition of semitransparent conducting pyrolytic carbon films. *J. Nanophoton* **6**, 061703 (2012).
11. Reich, S., Thomsen, C. Raman spectroscopy of graphite. *Philosophical Transactions of the Royal Society of London. Series A: Mathematical, Physical and Engineering Sciences* **362**, 2271–2288 (2004).
12. Pétaud, G., Gaillard, F., Tayakout, M., Gil, S., Giroir-Fendler, A. Spotlight on Large Surface Copper Cluster Role of Cu-SAPO-34 Catalyst in Standard NH_3-SCR Performances. *ChemCatChem* **12**, 2807–2822 (2020).
13. Potter, M. E. Down the Microporous Rabbit Hole of Silicoaluminophosphates: Recent Developments on Synthesis, Characterization, and Catalytic Applications. *ACS Catal.* **10**, 9758–9789 (2020).
14. Shen, W., Li, X., Wei, Y., Tian, P., Deng, F., Han, X., Bao, X. A study of the acidity of SAPO-34 by solid-state NMR spectroscopy. *Micropor. Mesopor. Mat.* **158**, 19–25 (2012).
15. Vomscheid, R., Briend, M., Peltre, M. J., Massiani, P., Man, P. P., Barthomeuf, D. Reversible modification of the Si environment in template-free SAPO-34 structure upon hydration-dehydration cycles below ca. 400 K. *J. Chem. Soc., Chem. Commun.* **6**, 544 (1993).
16. Buchholz, A., Wang, W., Xu, M., Arnold, A., Hunger, M. Thermal stability and dehydroxylation of Brønsted acid sites in silicoaluminophosphates H-SAPO-11, H-SAPO-18, H-SAPO-31, and H-

SAPO-34 investigated by multi-nuclear solid-state NMR spectroscopy. *Micropor. Mesopor. Mat.* **56**, 267–278 (2002).
17. Ashtekar, S., Chilukuri, S. V. V., Chakrabarty, D. K. Small-Pore Molecular Sieves SAPO-34 and SAPO-44 with Chabazite Structure: A Study of Silicon Incorporation. *J. Phys. Chem.* **98**, 4878–4883 (1994).
18. Sastre, G., Lewis, D. W., Catlow, C. R. A. Mechanisms of silicon incorporation in aluminophosphate molecular sieves. *J. Mol. Catal. A: Chem.* **119**, 349–356 (1997).
19. Liu, X., Wu, X., Weng, D., Si, Z., Ran, R. Evolution of copper species on Cu/SAPO-34 SCR catalysts upon hydrothermal aging. *Catal. Today* **281**, 596–604 (2017).
20. Jiao, F., Li, J., Pan, X., Xiao, J., Li, H., Ma, H., Wei, M., Pan, Y., Zhou, Z., Li, M., Miao, S., Li, J., Zhu, Y., Xiao, D., He, T., Yang, J., Qi, F., Fu, Q., Bao, X. Selective conversion of syngas to light olefins. *Science* **351**, 1065–1068 (2016).
21. Li, G., Jiao, F., Miao, D., Wang, Y., Pan, X., Yokoi, T., Meng, X., Xiao, F.-S., Parvulescu, A.-N., Müller, U., Bao, X. Selective conversion of syngas to propane over ZnCrO-SSZ-39 OX-ZEO catalysts. J. Energy Chem. **36**, 141–147 (2019).
22. Cheng, K., Gu, B., Liu, X., Kang, J., Zhang, Q., Wang, Y. Direct and Highly Selective Conversion of Synthesis Gas into Lower Olefins: Design of a Bifunctional Catalyst Combining Methanol Synthesis and Carbon–Carbon Coupling. *Angew. Chem.* **128**, 4803–4806 (2016).
23. Huang, Y., Ma, H., Xu, Z., Qian, W., Zhang, H., Ying, W. Role of nanosized sheet-like SAPO-34 in bifunctional catalyst for syngas-to-olefins reaction. *Fuel* **273**, 117771 (2020).
24. Huang, Y., Ma, H., Xu, Z., Qian, W., Zhang, H., Ying, W. Utilization of SAPO-18 or SAPO-35 in the bifunctional catalyst for the direct conversion of syngas to light olefins. *RSC Adv.* **11**, 13876–13884 (2021).
25. Liu, X., Zhou, W., Yang, Y., Cheng, K., Kang, J., Zhang, L., Zhang, G., Min, X., Zhang, Q., Wang, Y. Design of efficient bifunctional catalysts for direct conversion of syngas into lower olefins *via* methanol/dimethyl ether intermediates. *Chem. Sci.* **9**, 4708–4718 (2018).
26. Wang, M., Wang, Z., Liu, S., Gao, R., Cheng, K., Zhang, L., Zhang, G., Min, X., Kang, J., Zhang, Q., Wang, Y. Synthesis of hierarchical SAPO-34 to improve the catalytic performance of bifunctional catalysts for syngas-to-olefins reactions. *J. Catal.* **394**, 181–192 (2021).
27. Pan, X., Jiao, F., Miao, D., Bao, X. Oxide–Zeolite-Based Composite Catalyst Concept That Enables Syngas Chemistry beyond Fischer–Tropsch Synthesis. *Chem. Rev.* **121**, 6588–6609 (2021).
28. Zhou, W., Cheng, K., Kang, J., Zhou, C., Subramanian, V., Zhang, Q., Wang, Y. New horizon in C1 chemistry: breaking the selectivity limitation in transformation of syngas and hydrogenation of CO_2 into hydrocarbon chemicals and fuels. *Chem. Soc. Rev.* **48**, 3193–3228 (2019).
29. Fu, X., Li, J., Long, J., Guo, C., Xiao, J. Understanding the Product Selectivity of Syngas Conversion on ZnO Surfaces with Complex Reaction Network and Structural Evolution. *ACS Catal.* **11**, 12264–12273 (2021).
30. Huang, Z.-Q., Li, T.-H., Yang, B., Chang, C.-R. Role of surface frustrated Lewis pairs on reduced CeO_2(110) in direct conversion of syngas. *Chin. J. Catal.* **41**, 1906–1915 (2020).
31. Ebitani, K. Activation of molecular hydrogen into protonic acid sites over metal-free H-ZSM-5 catalyst. *J. Catal.* **138**, 750–753 (1992).

32. Gounder, R., Iglesia, E. Catalytic hydrogenation of alkenes on acidic zeolites: Mechanistic connections to monomolecular alkane dehydrogenation reactions. *J. Catal.* **277**, 36–45 (2011).
33. Kanai, J. On the nature of the active sites for ethylene hydrogenation in metal-free zeolites. *J. Catal.* **133**, 527–543 (1992).
34. Senger, S., Radom, L. Zeolites as Transition-Metal-Free Hydrogenation Catalysts: A Theoretical Mechanistic Study. *J. Am. Chem. Soc.* **122**, 2613–2620 (2000).
35. Vityuk, A., Khivantsev, K., Aleksandrov, H. A., Vayssilov, G. N., Alexeev, O. S., Amiridis, M. D. Room-Temperature Ethene Hydrogenation Activity of Transition-Metal-Free HY Zeolites. *ACS Catal.* **9**, 839–847 (2019).
36. Förtsch, D. On the basic effects on the gas composition governed by the water-gas shift equilibrium. *Energy* **205**, 117883 (2020).
37. Idriss, H., Scott, M., Subramani, V. Introduction to hydrogen and its properties. in *Compendium of Hydrogen Energy* 3–19 (Elsevier, 2015).
38. Marín, P., Ordóñez, S., Díez, F. V. Performance of reverse flow monolithic reactor for water–gas shift reaction. *Catal. Today* **147**, S185–S190 (2009).
39. Chen, W., Lin, M., Jiang, T., Chen, M. Modeling and simulation of hydrogen generation from high-temperature and low-temperature water gas shift reactions. *Int. J. Hydrog. Energy* **33**, 6644–6656 (2008).
40. Choi, Y., Futagami, K., Fujitani, T., Nakamura, J. The role of ZnO in Cu/ZnO methanol synthesis catalysts — morphology effect or active site model? *Appl. Catal. A: Gen.***208**, 163–167 (2001).
41. Zhou, Y., Qi, L., Wei, Y., Yuan, C., Zhang, M., Liu, Z. Methanol-to-olefin induction reaction over SAPO-34. *Chin. J. Catal.* **37**, 1496–1501 (2016).
42. Quílez-Pardo, J., Solaz-Portolés, J. J. Students' and teachers' misapplication of le chatelier's principle: Implications for the teaching of chemical equilibrium. *J. Res. Sci. Teach.* **32**, 939–957 (1995).
43. Fernandez-Prini, R. Le Châtelier's principle and the prediction of the effect of temperature on solubilities. *J. Chem. Educ.* **59**, 550 (1982).
44. Treptow, R. S. Le Châtelier's principle: A reexamination and method of graphic illustration. *J. Chem. Educ.* **57**, 417 (1980).
45. Wang, S., Wang, P., Shi, D., He, S., Zhang, L., Yan, W., Qin, Z., Li, J., Dong, M., Wang, J., Olsbye, U., Fan, W. Direct Conversion of Syngas into Light Olefins with Low CO_2 Emission. *ACS Catal.* **10**, 2046–2059 (2020).
46. Kirilin, A. V., Dewilde, J. F., Santos, V., Chojecki, A., Scieranka, K., Malek, A. Conversion of Synthesis Gas to Light Olefins: Impact of Hydrogenation Activity of Methanol Synthesis Catalyst on the Hybrid Process Selectivity over Cr–Zn and Cu–Zn with SAPO-34. *Ind. Eng. Chem. Res.* **56**, 13392–13401 (2017).
47. Liu, X., Wang, M., Yin, H., Hu, J., Cheng, K., Kang, J., Zhang, Q., Wang, Y. Tandem Catalysis for Hydrogenation of CO and CO_2 to Lower Olefins with Bifunctional Catalysts Composed of Spinel Oxide and SAPO-34. *ACS Catal.* **10**, 8303–8314 (2020).
48. Raveendra, G., Li, C., Cheng, Y., Meng, F., Li, Z. Direct transformation of syngas to lower olefins synthesis over hybrid Zn–Al_2O_3/SAPO-34 catalysts. *New J. Chem.* **42**, 4419–4431 (2018).
49. Chen, Z., Ni, Y., Wen, F., Zhou, Z., Zhu, W., Liu, Z. The carboxylates formed on oxides promoting the aromatization in syngas conversion over composite catalysts. *Chin. J. Catal.* **42**, 835–843 (2021).

50. Yuxuan Huang, Weixin Qian, Hongfang Ma, Haitao Zhang, Weiyong Ying. Impact Of Zn/Cr Ratio On ZnCrOx-Sapo-34 Bifunctional Catalyst For Direct Conversion Of Syngas To Light Olefins. *Int. j. chem. biomol. sci.* **12**, 557–563 (2018).
51. Fornero, E. L., Bonivardi, A. L., Baltanás, M. A. Isotopic study of the rates of hydrogen provision vs. methanol synthesis from CO_2 over Cu–Ga–Zr catalysts. *J. Catal.* **330**, 302–310 (2015).
52. Collins, S., Baltanas, M., Bonivardi, A. An infrared study of the intermediates of methanol synthesis from carbon dioxide over Pd/-GaO. *J. Catal.* **226**, 410–421 (2004).
53. Collins, S. E., Chiavassa, D. L., Bonivardi, A. L., Baltanás, M. A. Hydrogen Spillover in Ga_2O_3–Pd/SiO_2 Catalysts for Methanol Synthesis from CO_2/H_2. *Catal. Lett.* **103**, 83–88 (2005).
54. Zhang, P., Meng, F., Li, X., Yang, L., Ma, P., Li, Z. Excellent selectivity for direct conversion of syngas to light olefins over a Mn–Ga oxide and SAPO-34 bifunctional catalyst. *Catal. Sci. Technol.* **9**, 5577–5581 (2019).
55. Yang, G., Meng, F., Zhang, P., Yang, L., Li, Z. Effects of preparation method and precipitant on Mn–Ga oxide in combination with SAPO-34 for syngas conversion into light olefins. *New J. Chem.* **45**, 7967–7976 (2021).
56. Tsyganenko, A. A., Filimonov, V. N. Infrared spectra of surface hydroxyl groups and crystalline structure of oxides. *J. Mol. Struct.* **19**, 579–589 (1973).
57. Lavalley, J. C. Infrared spectrometric studies of the surface basicity of metal oxides and zeolites using adsorbed probe molecules. *Catal. Today* **27**, 377–401 (1996).
58. Goguet, A., Meunier, F. C., Tibiletti, D., Breen, J. P., Burch, R. Spectrokinetic Investigation of Reverse Water-Gas-Shift Reaction Intermediates over a Pt/CeO_2 Catalyst. *J. Phys. Chem. B* **108**, 20240–20246 (2004).
59. Bor, G., Sbrignadello, G. Infrared spectroscopic studies on metal carbonyl compounds. Part XVII. A comparative study of the vibrational spectrum of ditechnetium decacarbonyl and of the decacarbonyls of manganese and rhenium in the C–O stretching region. *J. Chem. Soc., Dalton Trans.* 440–448 (1974).
60. Wittrig, R. E., Kubiak, C. P. IR spectroelectrochemical studies of the metal carbonyl dimers $Mn_2(CO)_{10}$ and $[CpM(CO)_3]_2$ (M = W, Mo). Cross-coupling and ligand substitution reactions of electrochemically generated organometallic radicals. *J. Electroanal. Chem.* **393**, 75–86 (1995).
61. Steinhurst, D. A., Baronavski, A. P., Owrutsky, J. C. Transient infrared spectroscopy of Mn2(CO)10 with 400 nm excitation. *Chem. Phys. Lett.* **361**, 513–519 (2002).
62. Chein, R.-Y., Fung, W.-Y. Syngas production via dry reforming of methane over CeO_2 modified Ni/Al2O3 catalysts. *Int. J. Hydrog. Energy* **44**, 14303–14315 (2019).
63. Liao, C.-H., Chein, R. Thermodynamic analysis of syngas production from biodiesel via chemical looping reforming. *Int. J. Hydrog. Energy* **46**, 16591–16602 (2021).
64. Hunt, J., Ferrari, A., Lita, A., Crosswhite, M., Ashley, B., Stiegman, A. E. Microwave-Specific Enhancement of the Carbon–Carbon Dioxide (Boudouard) Reaction. *J. Phys. Chem. C* **117**, 26871–26880 (2013).
65. Busca, G., Lamotte, J., Lavalley, J. C., Lorenzelli, V. FT-IR study of the adsorption and transformation of formaldehyde on oxide surfaces. *J. Am. Chem. Soc.* **109**, 5197–5202 (1987).
66. Li, C., Sakata, Y., Arai, T., Domen, K., Maruya, K., Onishi, T. Adsorption of carbon monoxide and carbon dioxide on cerium oxide studied by Fourier-transform infrared spectroscopy. Part 2.—

Formation of formate species on partially reduced CeO_2 at room temperature. *J. Chem. Soc., Faraday Trans. 1* **85**, 1451 (1989).
67. Durand, J. P., Senanayake, S. D., Suib, S. L., Mullins, D. R. Reaction of Formic Acid over Amorphous Manganese Oxide Catalytic Systems: An *In Situ* Study. *J. Phys. Chem. C* **114**, 20000–20006 (2010).
68. Sivachandiran, L., Thevenet, F., Rousseau, A. Non-Thermal Plasma Assisted Regeneration of Acetone Adsorbed TiO_2 Surface. *Plasma Chem. Plasma Process* **33**, 855–871 (2013).
69. Daturi, M., Binet, C., Lavalley, J.-C., Galtayries, A., Sporken, R. Surface investigation on $Ce_xZr_{1-x}O_2$ compounds. *Phys. Chem. Chem. Phys.* **1**, 5717–5724 (1999).
70. Ouyang, F., Kondo, J. N., Maruya, K., Domen, K. Site Conversion of Methoxy Species on ZrO_2. *J. Phys. Chem. B* **101**, 4867–4869 (1997).
71. Vayssilov, G. N., Mihaylov, M., Petkov, P. St., Hadjiivanov, K. I., Neyman, K. M. Reassignment of the Vibrational Spectra of Carbonates, Formates, and Related Surface Species on Ceria: A Combined Density Functional and Infrared Spectroscopy Investigation. *J. Phys. Chem. C* **115**, 23435–23454 (2011).
72. Tan, J., Liu, Z., Bao, X., Liu, X., Han, X., He, C., Zhai, R. Crystallization and Si incorporation mechanisms of SAPO-34. *Micropor. Mesopor. Mater.* **53**, 97–108 (2002).
73. Augustin, M., Fenske, D., Bardenhagen, I., Westphal, A., Knipper, M., Plaggenborg, T., Kolny-Olesiak, J., Parisi, J. Manganese oxide phases and morphologies: A study on calcination temperature and atmospheric dependence. *Beilstein J. Nanotechnol.* **6**, 47–59 (2015).
74. Dessie, Y., Tadesse, S., Eswaramoorthy, R., Abebe, B. Recent developments in manganese oxide based nanomaterials with oxygen reduction reaction functionalities for energy conversion and storage applications: A review. J. Sci.: Adv. Mater. Devices **4**, 353–369 (2019).
75. Ullah, A. K. M. A., Kibria, A. K. M. F., Akter, M., Khan, M. N. I., Maksud, M. A., Jahan, R. A., Firoz, S. H. Synthesis of Mn_3O_4 nanoparticles via a facile gel formation route and study of their phase and structural transformation with distinct surface morphology upon heat treatment. *J. Saudi Chem. Soc.* **21**, 830–836 (2017).
76. Chen, D., Moljord, K., Holmen, A. A methanol to olefins review: Diffusion, coke formation and deactivation on SAPO type catalysts. *Micropor. Mesopor. Mater.* **164**, 239–250 (2012).
77. Borodina, E., Sharbini Harun Kamaluddin, H., Meirer, F., Mokhtar, M., Asiri, A. M., Al-Thabaiti, S. A., Basahel, S. N., Ruiz-Martinez, J., Weckhuysen, B. M. Influence of the Reaction Temperature on the Nature of the Active and Deactivating Species During Methanol-to-Olefins Conversion over H-SAPO-34. *ACS Catal.* **7**, 5268–5281 (2017).
78. Park, J. W., Lee, J. Y., Kim, K. S., Hong, S. B., Seo, G. Effects of cage shape and size of 8-membered ring molecular sieves on their deactivation in methanol-to-olefin (MTO) reactions. *Appl. Catal. A: Gen.* **339**, 36–44 (2008).
79. Li, G., Jiao, F., Pan, X., Li, N., Miao, D., Li, L., Bao, X. Role of SAPO-18 Acidity in Direct Syngas Conversion to Light Olefins. *ACS Catal.* **10**, 12370–12375 (2020).
80. Konnov, S. V., Pavlov, V. S., Kots, P. A., Zaytsev, V. B., Ivanova, I. I. Mechanism of SAPO-34 catalyst deactivation in the course of MTO conversion in a slurry reactor. *Catal. Sci. Technol.* **8**, 1564–1577 (2018).
81. Park, J. W., Kim, S. J., Seo, M., Kim, S. Y., Sugi, Y., Seo, G. Product selectivity and catalytic deactivation of MOR zeolites with different acid site densities in methanol-to-olefin (MTO) reactions. *Appl. Catal. A: Gen.* **349**, 76–85 (2008).

82. Wang, W., Jiang, Y., Hunger, M. Mechanistic investigations of the methanol-to-olefin (MTO) process on acidic zeolite catalysts by in situ solid-state NMR spectroscopy. *Catal. Today* **113**, 102–114 (2006).
83. Hunger, M. In situ NMR spectroscopy in heterogeneous catalysis. *Catal. Today* **97**, 3–12 (2004).
84. Firl, J., Runge, W. ^{13}C-NMR-Spektrum von Keten. *Angew. Chem.* **85**, 671–672 (1973).
85. Schulz, H. "Coking" of zeolites during methanol conversion: Basic reactions of the MTO-, MTP- and MTG processes. *Catal. Today* **154**, 183–194 (2010).
86. Xin, Y., Qi, P., Duan, X., Lin, H., Yuan, Y. Enhanced Performance of Zn–Sn/HZSM-5 Catalyst for the Conversion of Methanol to Aromatics. *Catal. Lett.* **143**, 798–806 (2013).
87. Yu, L., Huang, S., Zhang, S., Liu, Z., Xin, W., Xie, S., Xu, L. Transformation of Isobutyl Alcohol to Aromatics over Zeolite-Based Catalysts. *ACS Catal.* **2**, 1203–1210 (2012).
88. Müller, S., Liu, Y., Kirchberger, F. M., Tonigold, M., Sanchez-Sanchez, M., Lercher, J. A. Hydrogen Transfer Pathways during Zeolite Catalyzed Methanol Conversion to Hydrocarbons. *J. Am. Chem. Soc.* **138**, 15994–16003 (2016).

9) Supplementary

Equation S1 : Formula used for the WGS equilibrium constant calculation36

$$K_{WGS} = e^{(-3.732+\left(\frac{3850}{T}\right)+\left(\frac{470}{T}\right)^2)}$$

KWGS: equilibrium constant for the Water gas shift reaction

T: reaction temperature in K

Equation S2: Reaction coefficient of the WGS reaction in our system

$$Q = \frac{x_{CO2} * x_{H2}}{x_{CO} * x_{H2O}}$$

Xi: the molar proportion of i, i being either CO, CO2, H2O or H2.

Q : the reaction coefficient

Chapter 4 : Intimacy in the Ox-Zeo process

1) Introduction

The intimacy is one of the parameters that can affect the catalytic properties of the Ox-Zeo process. This intimacy was related in chapter 1 to the contact density between the oxide and the zeotype and the inter-function distance.

In this work, several methods have been used to study the intimacy from milli to nanometer scale: first the intimacy at the millimeter scale was studied through various bed arrangements. Then the micrometer scale was investigated by diluting the catalyst in an inert solid such as silica: this allowed to increase progressively the distance and decrease the contact density of the two solids. Then the particle size and the mixing method have been modified to improve the intimacy between the two solids. In those experiments, SEM images allowed to observe the intimacy of the mixture and possibly its evolution under stream.

In a second time, the impact of the inter-function distance at the nanometer scale has been studied by preparing and testing MnO@SiO_2 core-shell structures. They allowed to nullify the contact density by separating the two functions. The shell thickness defines the minimal distance existing between the two functions. It was determined from TEM images and the accessibility of the core was measured by liquid N_2-adsorption isotherm.

2) Milli and micro-metric intimacy

Milli and micro-metric intimacy can be studied in various ways. The easiest methods are catalyst dilution and bed arrangement. Bed arrangement allows to control the quantity of contact between the two functions precisely by multiplying the number of beds. An inert layer can be added between the two solids to nullify the contact density. Bed dilution will act on both the contact density and the inter-function distance. However, high dilution might be needed to reach low contact density and high inter-function distance.

Bed arrangement for the MnO_x-Ref+SAPO-K system has been studied by V. L'Hospital at IC2MP as part of ANR INCH project and is reported in Coudercy and coll.[1] The catalyst dilution has been performed at IRCELYON.

2.1) Bed arrangement

Various arrangements of MnO_x-Ref and SAPO-K layers were prepared in order to study the variation of the catalytic properties as a function of the contact density between the two functions. Three types of arrangement were prepared: separated double layer (SDL), double layer (DL) and multilayer (ML) with either three or four layers of MnO_x-Ref and SAPO-K. For the SDL, the separating inert layer was composed of SiC. For such arrangement, the contact between the oxide and the zeotype is nullified and their interaction is the smallest. The transition between DL to ML with four layers allow to increase gradually the contact density in the composite catalyst.

As shown in **Table 1** reprinted from Coudercy et al.[1], MnO_x-Ref pre-treated *in situ* at 410 °C for 30 min gave aCO conversion of 2.5% with a high selectivity (>30%) to CO_2 and CH_4. Interestingly, a significant selectivity to CH_3OH (8.1%) was determined. This difference compared to testing performed at IRCELYON (see Chapter 3, part 4.1.1) arises from the analytical system used at IC2MP which allowed CH_3OH quantification. It confirmed that CH_3OH is formed over MnO_x-Ref and further hydrogenated to CH_4 at 410 °C. The other by-products were C2+ hydrocarbons with an O/P ratio of 1.47 and traces of DME. Addition of SAPO-K to MnO_x-Ref as a separated double layer (see SDL in **Table 1**) led to a drastic decrease in the CH_3OH selectivity (and to a lesser extent, in the CH_4 one) while the selectivity to C2+ hydrocarbons and the O/P ratio were significantly increased. This trend was emphasized increasing proximity between MnO_x-Ref and SAPO-K as shown by the data obtained for double layer and multi-layer catalytic beds (DL, MLx3, MLx4 in **Table 1**). Furthermore, the CO conversion increased, which can be explained by a synergistic effect between MnO_x and SAPO-34. The slight increase in the CO_2 selectivity could arise from production of higher amount of H_2O favoring the water-gas shift reaction. The decrease in the CH_4 selectivity agrees with a limitation of consecutive hydrogenation of CH_3OH [2] over MnO_x-Ref when SAPO-34 is available to transform CH_3OH into C2+ hydrocarbons. Note that the decrease in the O/P ratio was observed with the increase of CO conversion as paraffins are consecutively produced from olefins by

hydrogenation.[3] Interestingly, the presence of an additional MnO_x-Ref layer in the lower part of the catalytic bed led to much higher amounts of DME and CH_3OH (compared MLx3 and DL in Table 1) clearly showing these compounds are reaction intermediates.

Table 1: Catalytic data obtained for MnO_x-Ref, MnO_x-Ref/SAPO-K separated double layer (SDL), double layer (DL) and Multi-Layer (ML) catalytic beds and reported in Coudercy and coll. [1]. Reaction conditions: m(MnO_x-Ref)=600 mg, m(SAPO-K)=300 mg, P=25 bar, T=410 °C, H_2/CO/Ar=63.8/25.6/10.6, WHSV=87 $mL.min^{-1}.g^{-1}$.

			Selectivity value (%)											
Sample	X_{CO}(%)[a]	O/P[b]	CO_2	CH_4	CH_3OH	DME	C2=	C2	C3=	C3	C4=	C4	C5=	C5
MnO_x-Ref	2.5	1.47	32.8	37.8	8.1	0.5	4.1	4.8	2.9	1.9	5.0	0.7	0.5	1.1
SDL	2.6	1.66	34.5	32.3	1.2	0	6.7	5.7	6.6	4.5	6.4	1.7	0.4	0.2
DL	3.3	1.33	38.1	24.4	0.9	0	7.3	5.9	8.1	7.3	5.6	2.1	0.3	0.2
MLx3	4.6	2.04	37.4	18.5	2.3	5.4	9.5	4.4	10.2	5.0	4.5	2.0	0.3	0.6
MLx4	4.7	1.31	37.8	18.5	0.8	0	8.3	6.5	11.5	8.8	4.2	2.9	0.3	0.3

[a]: CO conversion,

[b]: olefins to paraffins molar ratio.

2.2) Bed dilution

The second method used to study micro-metric intimacy was dilution of MnO_x-Ref+SAPO-K mechanical mixtures in silica prepared in the lab. The silica proportion was varied from 10% up to 94%.

2.2.1) Silica preparation

Shortly, 5 g of TEOS was added to 87 ml of ethanol and 18 ml of water under stirring. A second solution was prepared with 8 ml of 30% ammonia in water and 100 ml of ethanol. Then, the

ammonia solution was added to the TEOS one under vigorous stirring. The solution was kept at room temperature for 24 h under stirring. After that, the white suspension was centrifuged (3500 rpm) and washed with ethanol three times. The recovered solid was dried at 100 °C overnight and then calcinated at 430 °C for 10 h under air.

2.2.2)Catalytic results

It was previously checked that the prepared silica was catalytically inactive. Small addition of silica to MnO_x-Ref-SAPO-K mix leads to a decrease in conversion and O/P ratio from 5.7% to 5.2% and from 4.6 to 4.2, respectively (**Figure A**). At higher amount, the conversion and O/P exhibit a plateau up to 70% of silica. Above 70% of silica, the O/P decreases from 4.2 to 2.0. The conversion is only affected above silica proportion of 94% with a decrease in conversion from 4.7% to 3.1%. The addition of silica has other effects on the selectivity. The CH_4 selectivity continuously increases with the proportion of silica mainly at the expense of C2-C3 hydrocarbons. At 94% of silica, the CH_4 selectivity reaches 28.9% while the C2 and C3 selectivity drop from 19.9% to 17.4% and from 21.5% to 16.9%, respectively. The O/P ratios for C2, C3 and C4 hydrocarbons decrease with increasing proportion of silica (to a lesser extent for C3).

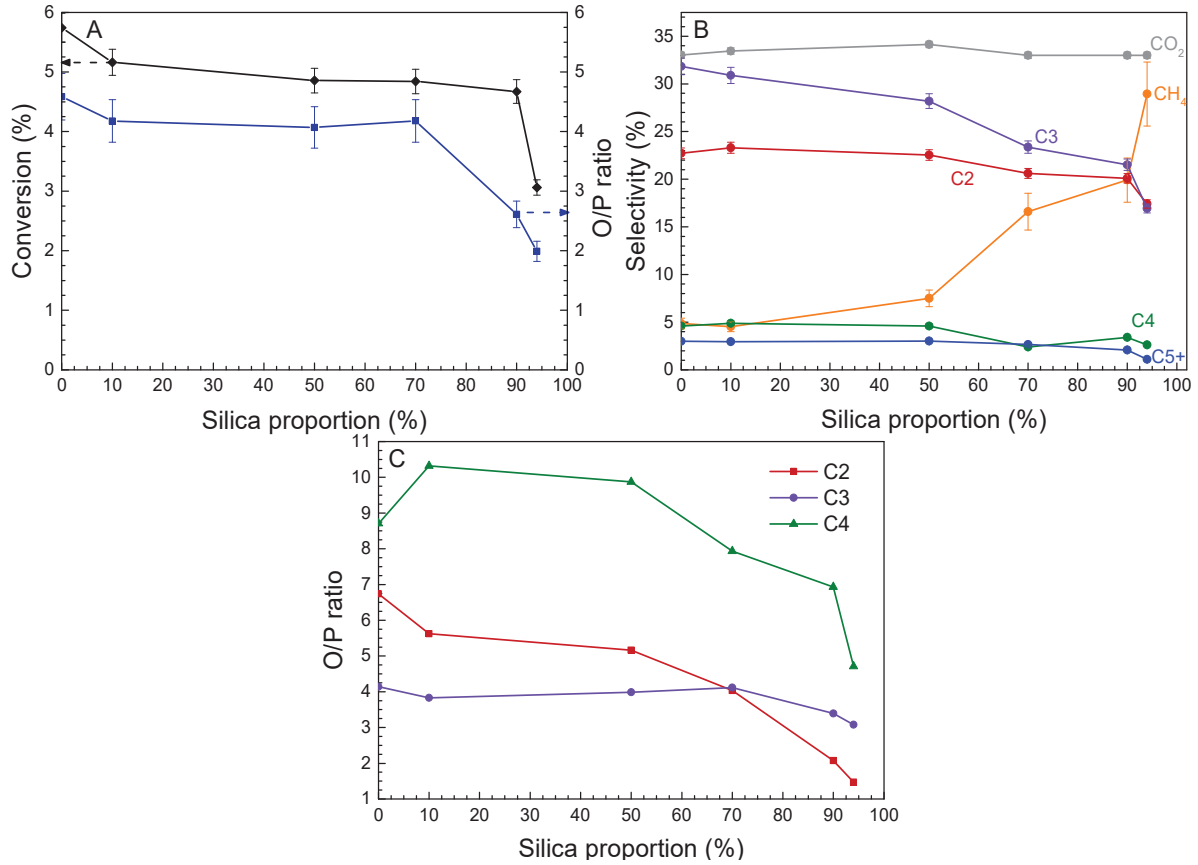

Figure 1: A) Evolution with the silica proportion of the conversion and the C2-C4 O/P ratio, B) evolution of the CO_2, CH_4 and hydrocarbon selectivity and C) evolution of the O/P ratio for C2, C3 and C4 hydrocarbons. Reaction conditions: m (MnO_x-Ref) =240 mg, m (SAPO-K) =60 mg, P=25 bar, T=410 °C, $H_2/CO/N_2$=60/30/10. WHSV 87 $mL.min^{-1}.g^{-1}$ (without silica). Data were taken after 14 h on stream.

As dilution up to 50% has a very limited impact on the catalytic properties, it confirms that silica is an inert diluent. However, the CH_4 selectivity increases above 50% of silica while the conversion remains constant. It suggests that the methanol diffusion flow begins to decrease due to the increase of inter-function distance and that formation of methane is favored by increasing the partial pressure of methanol at the MnO_x surface. The conversion is not affected because the increase in methane formation rate compensates the decrease in the apparent rate of formation of C2+ hydrocarbons.

At higher dilution (>90%), the diffusion flux of methanol from oxide to zeolite continues to decrease. However, the methane formation rate does not increase anymore, as the methane yield

shown in **Figure 2** leading to a decrease in conversion along with an increase in CH_4 selectivity. At this point the overall rate is limited by the diffusion of methanol.

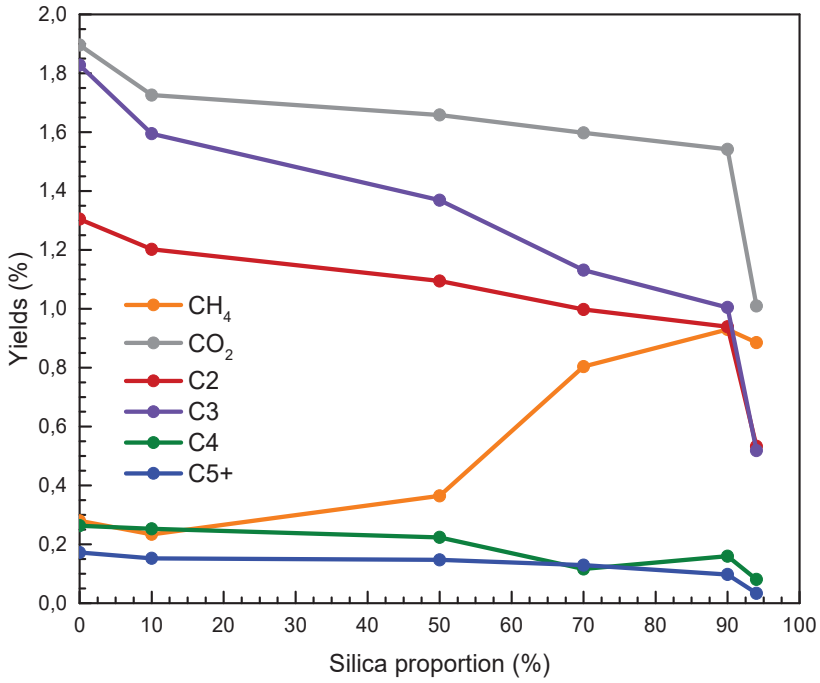

Figure 2 : Evolution of the CO_2, CH_4 and hydrocarbon yields. Reaction conditions: m (MnO_x-Ref) =240 mg, m (SAPO-K) =60 mg, P=25 bar, T=410 °C, $H_2/CO/N_2$=60/30/10. WHSV 87 $mL.min^{-1}.g^{-1}$ (without silica). Data were taken after 14 h on stream.

At the dilution of 94%, the O/P is lower than at 90% suggesting that the diffusion rate of the methanol is even lower. The quantity able to react with the zeotype decreases and the latter one acts as if less amount of oxide was present in the catalyst mixture. As evidenced in the literature[3–8] and in chapter 3, parts 4.2 and 4.3, an excess of SAPO-34 can lead to a decrease in the O/P ratio as the olefins are hydrogenated by the hydrocarbon pool.

In fact, the decrease in diffusion flux of methanol is more evidenced above 90% because a small variation of the silica proportion implies a big increase of its mass and thus of the bed length (**Figure 3**).

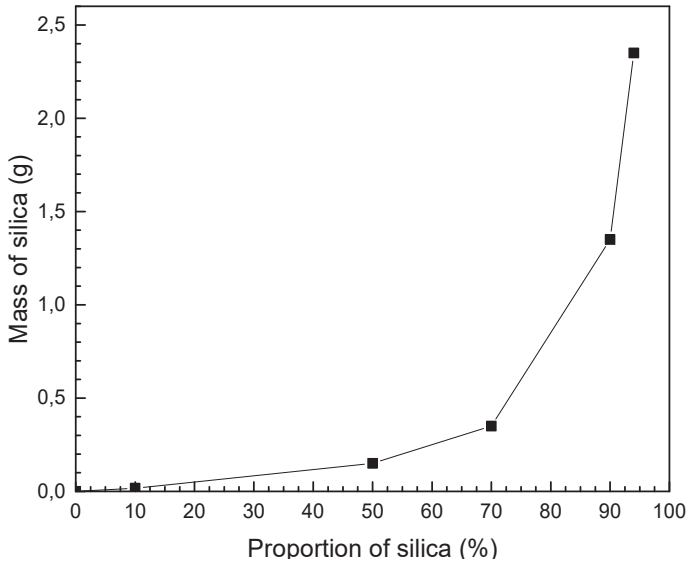

Figure 3: Mass of silica as a function of the silica proportion.

These results showed that the inter-function distance must remain at least at the micrometer scale to retain the catalytic properties of the mixture.

3) Nanometric intimacy

The study of the nanometric intimacy has been done through the preparation and testing of core-shell structures with an inert porous solid as shell. Those structures allow to nullify the contact density and to control precisely the distance introduced between the two functions.

3.1) Core-shell structure preparation

The core-shell structures prepared to study the nanometric intimacy need to have specific properties: first, the core should be as monodisperse as possible to get a precise distance between the two functions. Second, the shell must cover the whole surface of the core as a homogeneous layer so that the shell mean thickness corresponds to the minimal distance between the two functions. Third, the shell must be porous to allow CO and H_2 reactants to diffuse toward the inner core and its surface. For this last point, either a shell that is not in contact with the MnO_x surface, (commonly named yolk-shell structure), or a porous core can be prepared. With a porous core, it is likely that the mesoporous surface will not be covered by the shell leaving a part of the oxide surface accessible.

3.1.1) Dense core-shell structures

At the beginning of the thesis, the focus was put on the synthesis of monodisperse dense MnO_x core with a size of 10 nm order followed by deposit of a silica shell with a comparable thickness. The core was prepared by decomposition of the manganese oleate at high temperature, a known strategy for the preparation of monodisperse nanoparticles.[9–14] The silica shell was prepared either by direct deposit[15–17] or by using micro-emulsion[18–23] to encapsulate the MnO_x core.

a) MnO_x core

i) Reflux oleate route preparation

MnO_x nanoparticles were prepared by refluxing MnO in an oleic acid solution. The common protocol is as follows: first, 76.5 mmol of oleic acid (Fluka, Ref 75096, >99%) and 62 ml of 1-octadecene (Alfa Aesar, Ref L11004, 90%) were added into a round bottom flask. Then, 17.0 mmol of bulk MnO (Alfa Aesar, Ref 11870, 99%) was added. An inert gas (Ar) inlet was placed directly into the solution for bubbling: it avoided ODE ignition during the reaction. A refrigerant was mounted on the setup. After Ar bubbling for 30 min, the temperature was raised up to the ODE boiling point i.e. 320 °C. Reflux was maintained for 1h30 and the mixture was then cooled down.

During reflux, dissolution of MnO green particles by oleic acid can be observed within the first 30 min as the introduced green particles disappear leaving a clear yellowish solution in the round flask. Then, a green suspension appears as Mn oleate molecules decompose forming MnO nanoparticles. This suspension became brown at the end of the reaction probably due to surface oxidation of the MnO nanoparticles.[14,24,25] It is worth mentioning that dissolution of MnO by oleic acid produces water that circulated inside the reflux via condensation and evaporation cycle. However after condensation drops of water fell back into the ODE solution at 320 °C evaporating abruptly leading to the formation of an ODE mist inside the flask.

After cooling down, the nanoparticles were centrifuged (3500 rpm), washed with acetone three times and re-dispersed in hexane. The recovered colloidal suspension is named MnO-ODE in the following.

Later on, a paper was published highlighting problems with the ODE synthesis. It has shown that ODE easily formed oligomers at the reflux temperature (320 °C). Their solubility parameters are close to those of the formed MnO nanoparticles.[26] This impeaches easy separation of the nanoparticles from the oligomers and leads to degraded properties for the SiO_2 deposit.[26] Therefore, an alternative solvothermal oleate preparation route was used to produce MnO nanoparticles, as follows.

ii) Solvothermal oleate preparation route

In this protocol, similarly to the protocol using ODE reflux, Mn-oleate molecules are formed and decomposed during the synthesis to form the MnO nanoparticles. However, the synthesis conditions are different.

Shortly, 14.7 g of $Mn(CH_3COO)_2,2.4H_2O$ (Sigma-aldrich, Ref 63537, 99%), 7.2 g of oleic acid (Fluka, Ref 75096, >99%) and 100 ml methanol (Carlo Erba, Ref 414816, 99.9%) were introduced in a Teflon lined autoclave. The mixture was kept at room temperature under stirring for 2 h and then the closed autoclave was heated to 180 °C under autogenous pressure and stirring. The mixture was kept at this temperature for 24 h and the resulting suspension was then centrifuged (3500 rpm), washed with ethanol three times and re-dispersed into hexane.[18] The recovered colloidal suspension is named MnO-MeOH in the following.

iii) Characterizations

ATR-IR spectra of dried MnO-ODE and MnO-MeOH samples plotted in **Figure 4** contain absorption bands in the 3045-2745 cm^{-1} spectral range, attributed to stretching vibrations of aliphatic C-H bonds.[14,24] The band at 1735 cm^{-1} corresponds to $\nu_{as}(COO)$ stretching vibrations of free oleic acid.[14,24] The band at 1548 cm^{-1} was attributed to $\nu_{as}(COO^-)$ of adsorbed oleates[24] while the 1500-1300 cm^{-1} spectral range could correspond to $\delta(CH_2)$, $\delta_s(CH_3)$, or $\nu_s(COO)$ vibrations.[27] The band at 720 cm^{-1} was attributed to $\rho(CH_2)$.[27]

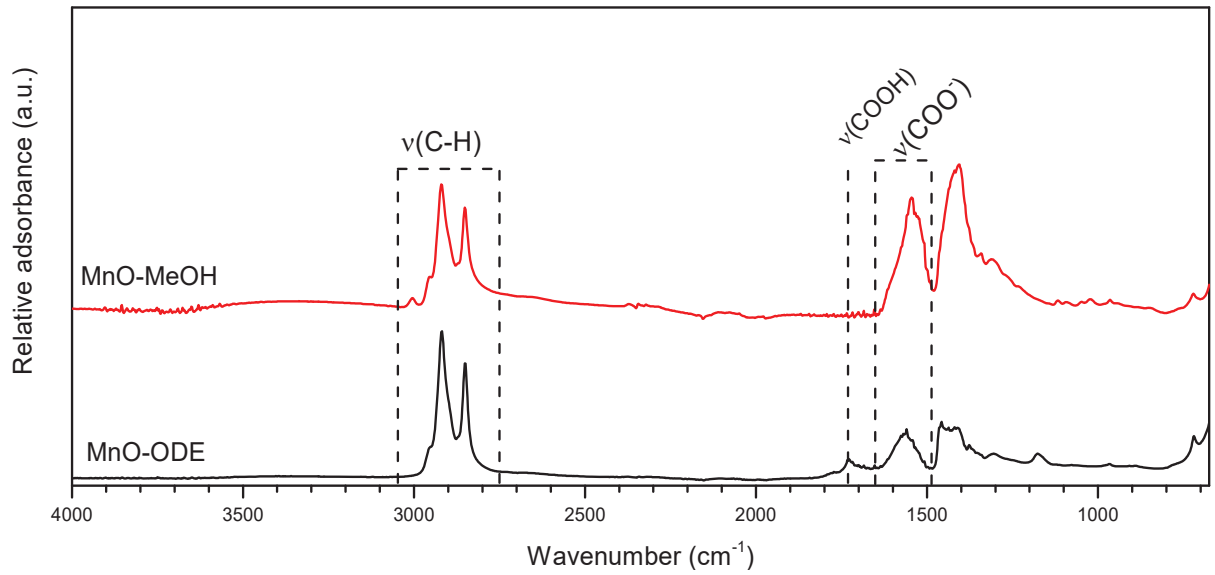

Figure 4: ATR-FTIR spectra of dried MnO-ODE and MnO-MeOH samples.

Both solids contained adsorbed oleates, as evidenced in litterature[9,14], while the MnO-ODE sample contained some amount of oleic acid compared with the MnO-MeOH. However, the ν(C-H)/ν (COO^-) ratio is higher for the MnO-ODE than the MnO-MeOH. This indicates that ODE oligomers or residual ODE are present in the MnO-ODE, confirming that ODE oligomers are formed during its synthesis and tend to pollute the MnO nanoparticles.

TEM images of the two MnO samples show that the MnO nanoparticles have octahedral shape in both cases, as shown in **Figure 5**. The size of MnO-MeOH particles seems to be more dispersed than those of MnO-ODE.

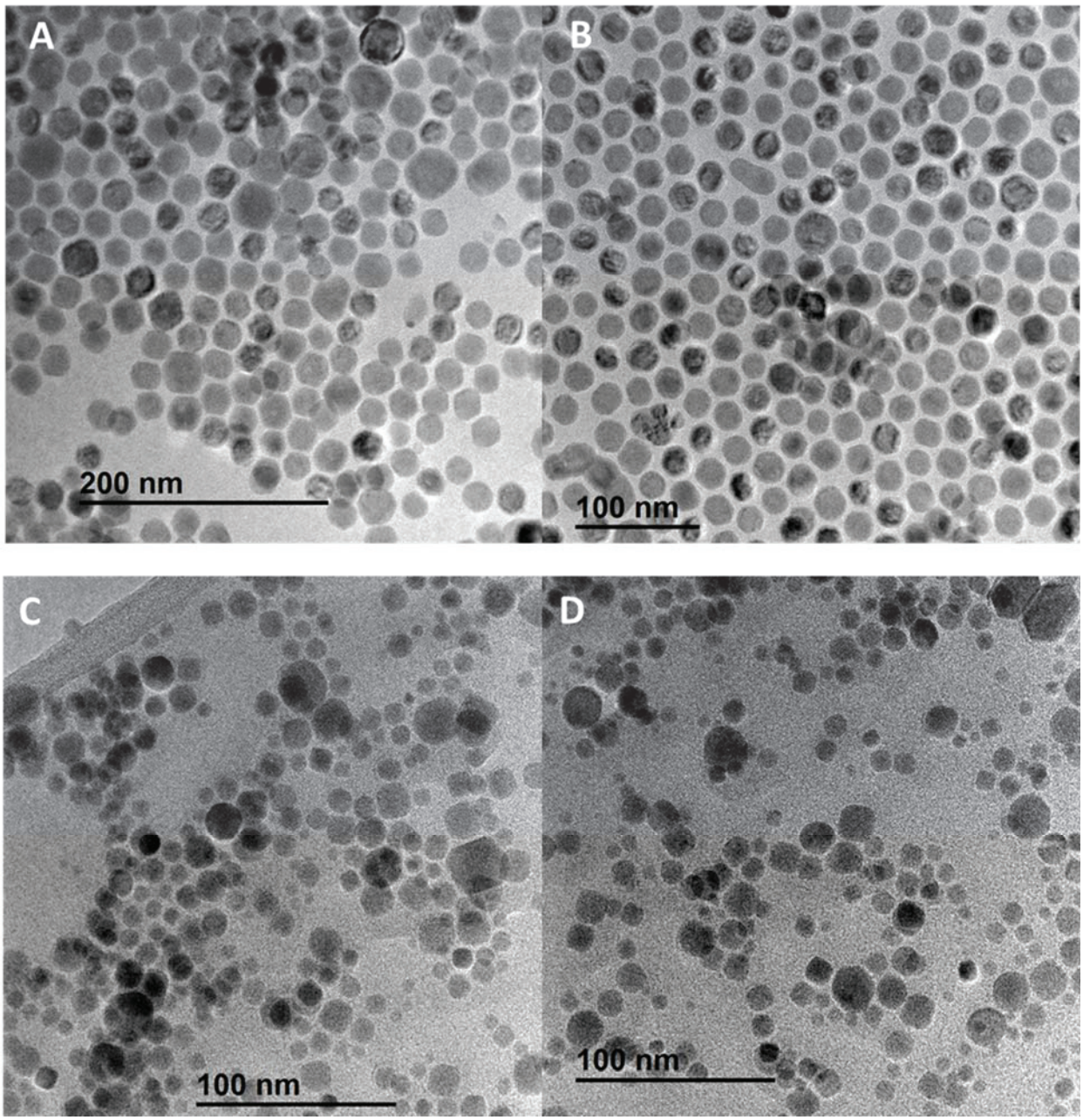

Figure 5: TEM images of the prepared MnO nanoparticles: A) and B) MnO-ODE; C) and D) MnO-MeOH.

Size distribution analysis of TEM images is represented in **Figure 6**. It shows that MnO-ODE and MnO-MeOH present a mean diameter of 12 nm with a standard deviation of 1 nm for MnO-ODE and of 4 nm for MnO-MeOH. The MnO-MeOH protocol leads to formation of more dispersed nanoparticles compared with the MnO-ODE one. However, the MnO-MeOH nanoparticles contain less residual species such as oleic acid and ODE oligomers, as shown by ATR-IR. Therefore, the

MnO-MeOH protocol has been retained to prepare dense MnO nanoparticles in the following. Note that the colloidal suspension is composed of hydrophobic MnO nanoparticles in hexane.

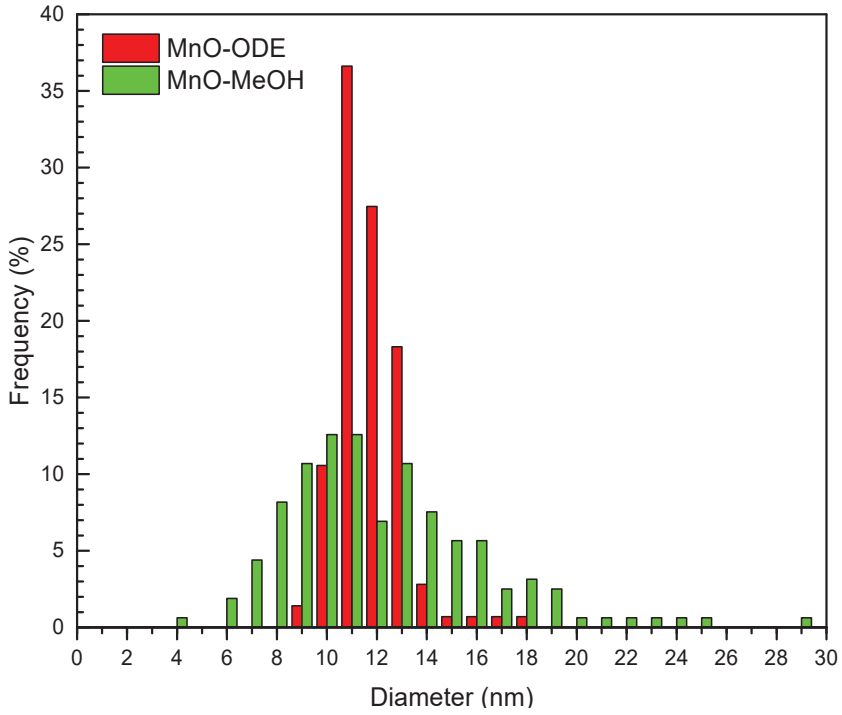

Figure 6: Statistical analysis of the particle diameter for MnO-ODE and MnO-MeOH samples.

b) Silica shell

To get a well-defined core-shell structure, the nanoparticles need to be well dispersed and not agglomerated in the synthesis solution. Usually, a TEOS/ethanol/water/NH_4OH solution is used for SiO_2 deposit. If the MnO nanoparticles are simply introduced in such a solution they will aggregate leading to the formation a multicore-shell structure. To avoid that, two strategies have been tested: first, we tried to render the MnO nanoparticles hydrophilic, replacing the surface oleates by shorter carboxylates and then performing a SiO_2 synthesis (mono-phasic synthesis). The second strategy used micro-emulsion to encase the hydrophobic nanoparticles in a surfactant and disperse them in the synthesis solution.

i) Mono-phasic synthesis

The MnO nanoparticles need to be hydrophilic, allowing dispersion in ethanol/water where TEOS hydrolysis is carried out. However, the long aliphatic chain of oleate has unfavorable interaction with water molecules, giving hydrophobic nanoparticles. To improve the dispersability

of nanoparticles in water, either the aliphatic chain length can be drastically shortened or bi/tri carboxylates can be adsorbed.[28,29]

Three carboxylic acids have been tested: acetic acid (Sigma-Aldrich, Ref 338826, 99.99%), citric acid (Sigma-Aldrich, Ref C0759, 99%) and glutaric acid (Sigma Aldrich, Ref G3407, 99%) with one, two or three carboxylic acid functions, respectively. They were chosen for their carbon chain length, their number of acid function and their pKa around 4.5. Such pKa was chosen to avoid dissolution of the MnO nanoparticles that was observed with oxalic acid which has the first pKa of 1.7.

Shortly, 0.43 mmol of MnO nanoparticles in 5 ml of hexane were placed in a beaker under stirring. Then, 1.75 mmol of the corresponding carboxylic acid was added. A high molar ratio was used for this step to favor the surface exchange between the surface oleate and the carboxylic acid. The solution was kept at room temperature under stirring for 1 h. At this point a black sediment was observed confirming the hydrophilic nature of the nanoparticles and thus the effectiveness of the treatment. The obtained suspension was centrifuged (3500 rpm) and washed first with diethyl ether to remove hexane and oleic acid and then re-dispersed in 10 ml of ethanol leading to a concentration of 3 mg/ml. Such suspensions are named as MnO-acetic, MnO-citric and MnO-glutaric in the following.

The ATR-IR spectra plotted in **Figure 7** suggest that the ν(C-H)/$\nu(COO^-)$ ratio (area in the 2985-2735 cm^{-1} region for ν(C-H) and in the 1665-1480 cm^{-1} $\nu(COO^-)$) is decreased compared to MnO-MeOH (**Figure 4**). They are 0.78, 0.49 and 0.03 for MnO-acetic, MnO-citric and MnO-glutaric, respectively vs 1.17 for MnO-MeOH. This indicates that the oleates present on the surface were successfully replaced with shorter carboxylates. However, the proportion of substitution was not determined.

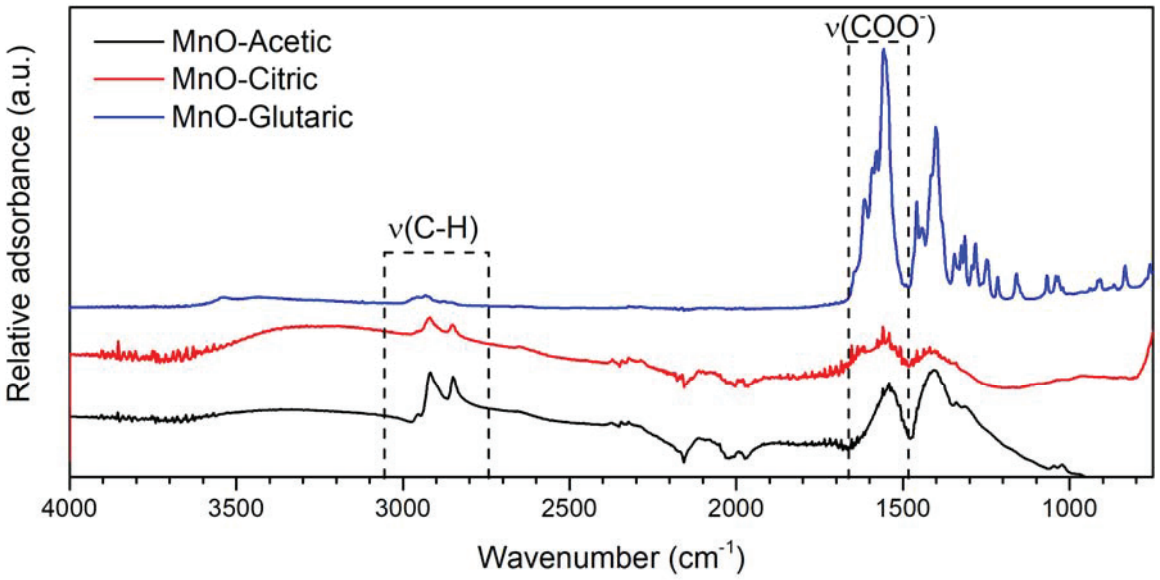

Figure 7: ATR-FTIR spectra of the dried MnO-Acetic, MnO-Citric and MnO-Glutaric.

The synthesized hydrophilic nanoparticles were directly used for the SiO_2 deposit. For that purpose, they were re-dispersed in 185 ml of ethanol with 2 mmol of TEOS (Sigma-Aldrich, Ref 13.190-3, 98%) under stirring. A NH_3 solution composed of 18 ml of 28% NH_4OH and 28 ml of H_2O was then added to this solution. The resulting solution was kept under stirring for 1 h at 50 °C. The measured pH was 10.8. Then, the solution was centrifuged (3500 rpm) and the recovered solid was washed with ethanol three times before drying at 100 °C overnight.

TEM images of MnO-glutaric covered by SiO_2 show that a thin silica shell has been formed on some MnO nanoparticles which were however agglomerated as shown in **Figure 8B**). Baton shaped nanoparticles also exhibit a thin silica shell as shown in **Figure 8C)**. However, the main part of nanoparticles is not covered (**Figure 8A**). Similar results were observed with two other carboxylic acids.

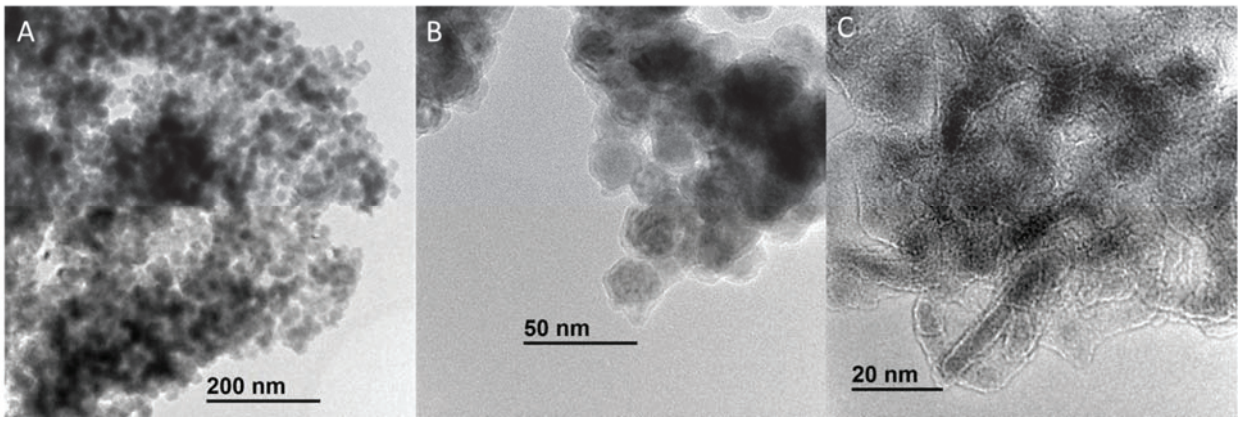

Figure 8: TEM images of MnO-glutaric after SiO_2 deposit: A) naked MnO particles, B) MnO@SiO_2 core-shell structure and C) baton shaped nanoparticles covered by SiO_2.

Overall, the syntheses in one liquid phase produce aggregates of MnO nanoparticles covered with a thin layer of silica that do not correspond to well defined core-shell structure. After this conclusion, a micro-emulsion synthesis was undertaken.

ii) Micro-emulsion synthesis

With this method, the MnO nanoparticles are encapsulated in hydrophobic droplets dispersed inside an ethanol/water solution and a SiO_2 shell is formed in the aqueous solution around each droplet. Two surfactants have been tested for this protocol: CTAB[19] and Triton-X-100[20–23] with protocol inspired by literature. As the Triton-X-100 based micro-emulsion gave the best results, only this synthesis is presented.

First, a solution composed of 400 mg of the MnO-MeOH nanoparticles in 200 ml of hexane, 2300 ml of cyclohexane, 480 ml of heptanol, a co-surfactant, 600 ml of Triton-X-100 , the surfactant (Fluka, 93426, 100%) and 100 ml of water were mixed together with 10 ml of TEOS (Sigma-Aldrich, 13.190-3, 98%). After 6 h of stirring at room temperature, 10 ml of 30% NH_4OH was added and the solution was kept under stirring for 24 h at room temperature. The solution was then centrifuged (4500 rpm for 2 h) and the recovered solid washed with ethanol three times.

TEM images of the recovered solid in **Figure 9** show well defined core-shell nanoparticles that are separated from each other similar to what is obtained in literature.[20–23] Statistical analysis of the TEM images, summed up in **Figure 10**, shows that core-shell structures were mostly (>95%)

obtained with one core per shell. Few multiple core-shell structures were observed but no naked core or empty shell. For the one core per shell structure, the mean core diameter is of 11±3 nm with a shell of 10±2 nm. The core size seems to have been preserved during the SiO_2 deposit.

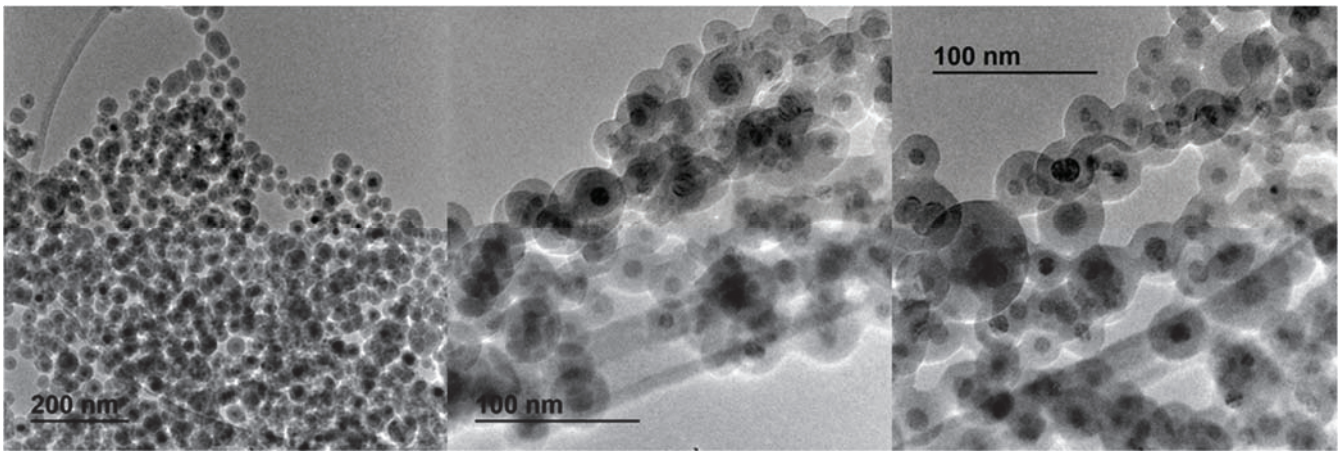

Figure 9: TEM images of MnO@SiO_2 sample prepared via micro-emulsion using Triton-X-100.

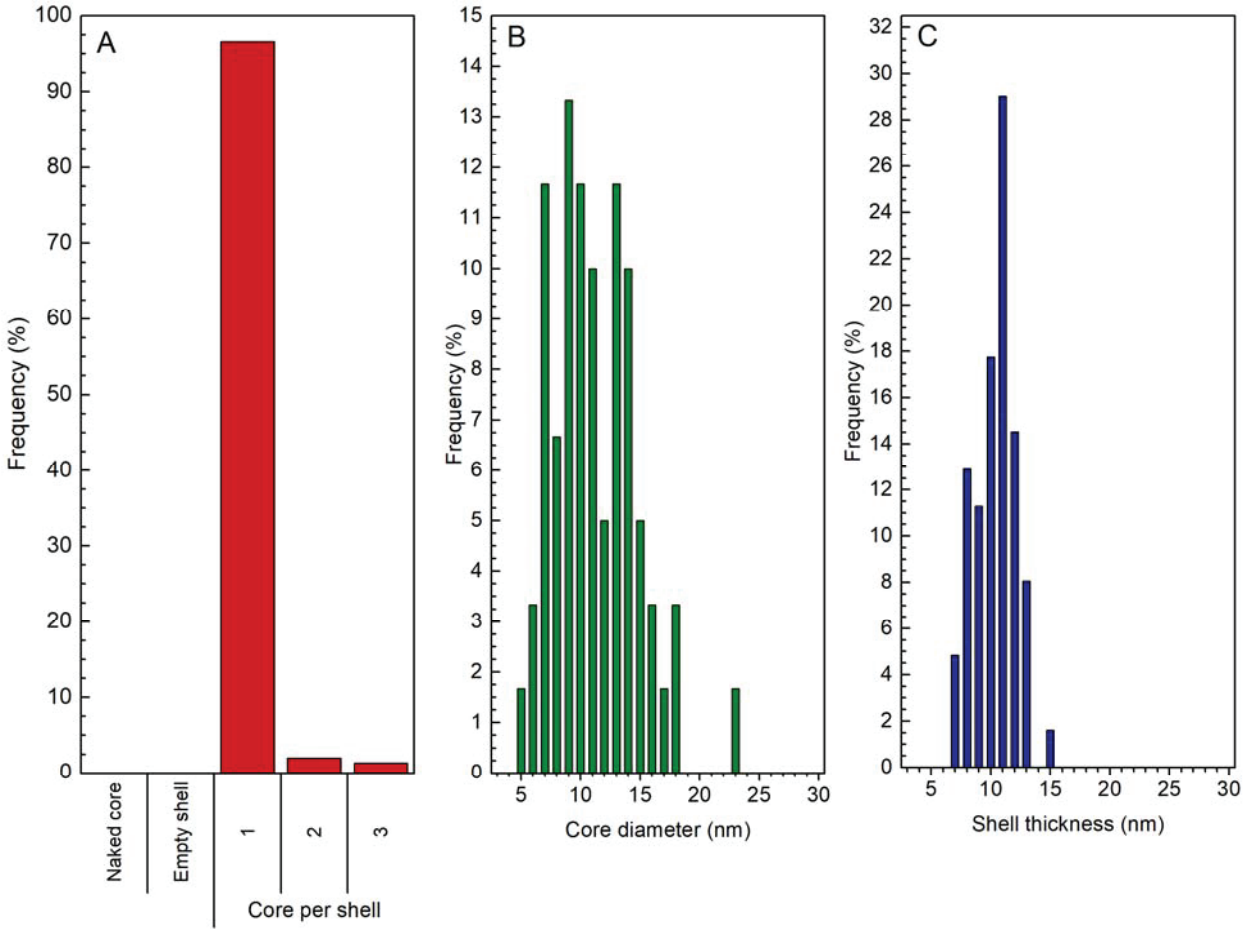

Figure 10: Statistical analysis of A) the type of structure observed between naked core, empty shell and core-shell with 1, 2 or 3 cores per shell, B) distribution of the MnO core diameter and C) of the SiO_2 shell thickness.

This protocol allowed to produce well defined nanoparticles with a shell thickness of ca 10 nm. However, the nanoparticle concentration in the synthesis medium is too low, only 0.1 g/L. At least 2 L of solution is needed to produce enough coated MnO for one catalytic test leading to time consuming purification step especially centrifugation. Thus, a less expensive and time-consuming protocol was needed.

c) Conclusion

Various strategies have been attempted to obtain dense MnO@SiO_2 core-shell structures.

MnO dense cores were prepared by formation and decomposition at high temperature of manganese oleate either in 1-octadecene or methanol. Using 1-octadecene allowed to get highly monodispersed octahedral nanoparticles. However, 1-octadecene undergoes oligomerization

during the synthesis of nanoparticles. The formed polymer was not easily separable from the nanoparticles pushing us to find another solvent for the synthesis. The solvothermal synthesis leads to nanoparticles with close mean size, but wider size distribution. For both methods, MnO nanoparticles are hydrophobic since the surface is covered by oleates.

Two methods have been tested to carry out the SiO_2 deposit on the MnO dense cores. First, a surface exchange has been done to replace the oleates by hydrophilic surface species. Three carboxylic acids have been tested all showing good exchange capability. However, the succeeding SiO_2 deposit has shown a common problem. The particles were aggregated during the synthesis leading to formation of undesired multi core-shell structures. The second strategy consisted in using micro-emulsion to disperse the nanoparticles and then depositing SiO_2 on the surface. Such strategy allowed to obtain well-defined core-shell nanoparticles with mainly a single core structure. However, the concentration of nanoparticles during the SiO_2 deposit was too low leading to the usage of large volume of solvent and time-consuming centrifugation.

From those results, the dense core-shell synthesis using MnO nanoparticles formed from manganese oleate were not used for catalytic test and our focus shifted toward preparation of porous core-shell structures.

3.1.2) Porous core-shell structures

In the development of a more robust and scalable preparation method, porous MnO spherical nanoparticles were synthesized to ensure access to the oxide surface. For that purpose, $MnCO_3$ nanoparticles were used as precursor for the core. Then, direct deposition of SiO_2 was carried out to form core-shell structures.

a) Porous MnO_x

$MnCO_3$ was used as the precursor for the synthesis due to its facile thermal decomposition and its capacity to retain its morphology.[30,31] We developed an original method of preparation for $MnCO_3$ nanospheres, using precipitation in mixed solvents. In order to form $MnCO_3$ spheres of desirable size, we adjusted conditions of precipitation in water-glycerol mixtures. Indeed, if a Mn(II) soluble salt (sulfate, nitrate..) is mixed with carbonate solution in aqueous medium, then

immediate precipitation occurs, leading to large (tens to hundreds microns) and shapeless $MnCO_3$ particles. On the other hand, while both Mn salts and inorganic carbonates are soluble in small polyols such as glycerol, or ethylene glycol, mixing of their solutions does not produce precipitation. Apparently, polyol Mn complexes are formed that hinder nucleation of Mn carbonate. The idea was therefore to apply mixed polyol-water solvents in order to find optimal precipitation conditions. That conditions would provide a compromise between fast incontrollable growth in water and the absence of precipitation in polyols. This way, relatively slow nucleation and growth would be achieved in mixed solvents. After certain number of trials and errors we come up with the preparation that afforded narrowly distributed 0.3-0.5 size particles of Mn(II) carbonate, as follows.

i) Synthesis

First, two 0.5 M aqueous solutions of $(NH_4)_2CO_3$ (Alfa aesar, Ref 36229, NH_3 30,0+%) and $MnSO_4$ (Prolabo, Ref 25-301, 98%) were prepared. 5 ml of each solution were sampled and 6.35 ml of glycerol (Sigma-Aldrich, Ref G7893, 99.5%) were added to each of them and stirred until homogenization. The $(NH_4)_2CO_3$ solution was added to the $MnSO_4$ solution under stirring and left at room temperature under stirring for 1 h. Upon addition of the carbonate solution to the sulfate solution, a white suspension was formed. After 1 h of reaction, the suspension was centrifuged (3500 rpm) and washed three times with water.

The next step depends on whether the naked particles were used to prepare uncovered porous MnO_x or to prepare MnO_x@SiO_2 core shell structures. In the former case, the recovered $MnCO_3$ solid was dried at 100 °C overnight. Then the obtained powder was treated under H_2/N_2:20/80 (100 mL. min^{-1}) at 410 °C for 12 h to produce MnO particles. After the treatment, MnO was exposed to flowing air at room temperature to control the surface reoxidation as for MnO_x-Ref (cf chapter 3). This solid is called MnO_x-pore in the following. For SiO_2 deposit, the solid was used immediately and in totality after centrifugation without drying to avoid aggregation of the nanoparticles.

ATR-IR spectra of the dried solid before and after calcination were recorded and represented in **Figure 11**. Before calcination, the ν_3 and ν_2 bands of carbonates can be observed between 1570

cm^{-1} and 1240 cm^{-1} and at 861 cm^{-1}, respectively.[5] Those typical bands disappeared upon thermal treatment under H_2 showing the carbonate structure has been completely decomposed.

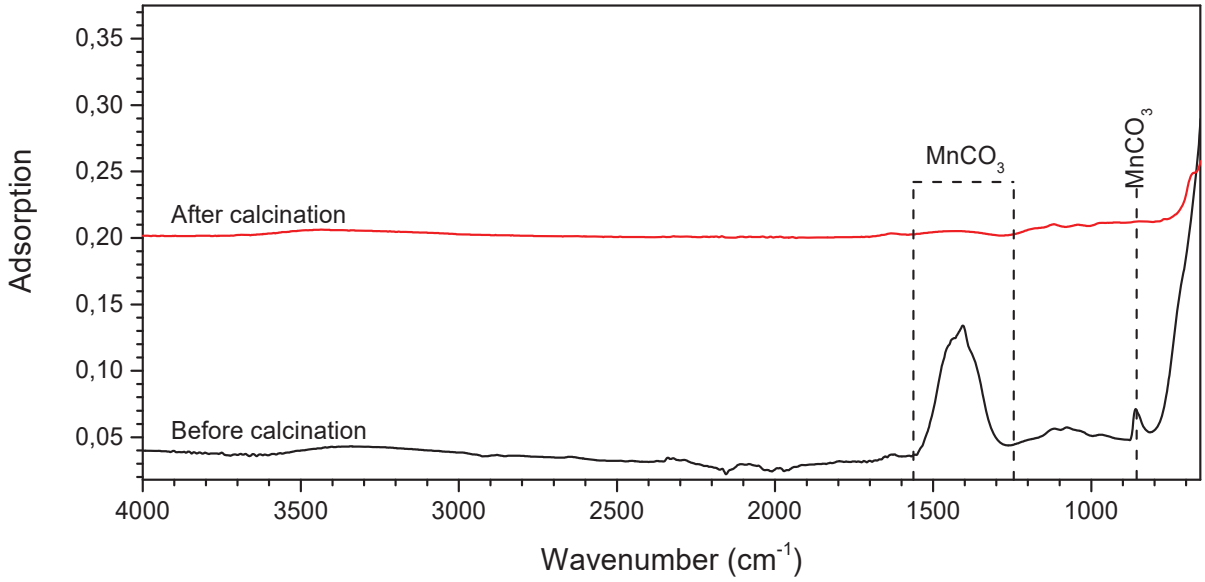

Figure 11: ATR-FTIR spectra of the prepared MnO_x-pore nanoparticles before and after calcination.

XRD analysis of MnO_x-pore after calcination (**Figure 12**) show that all $MnCO_3$ crystallites have been decomposed while crystalline MnO and Mn_3O_4 phases were present in the solid. Compared with MnO_x-Ref (see the XRD diffractogram in chapter 3 part 2.1), the badly crystallized Mn_3O_4 overlayer is more present. The crystallite size was around 12 nm which is two times smaller than the one of MnO_x-Ref.

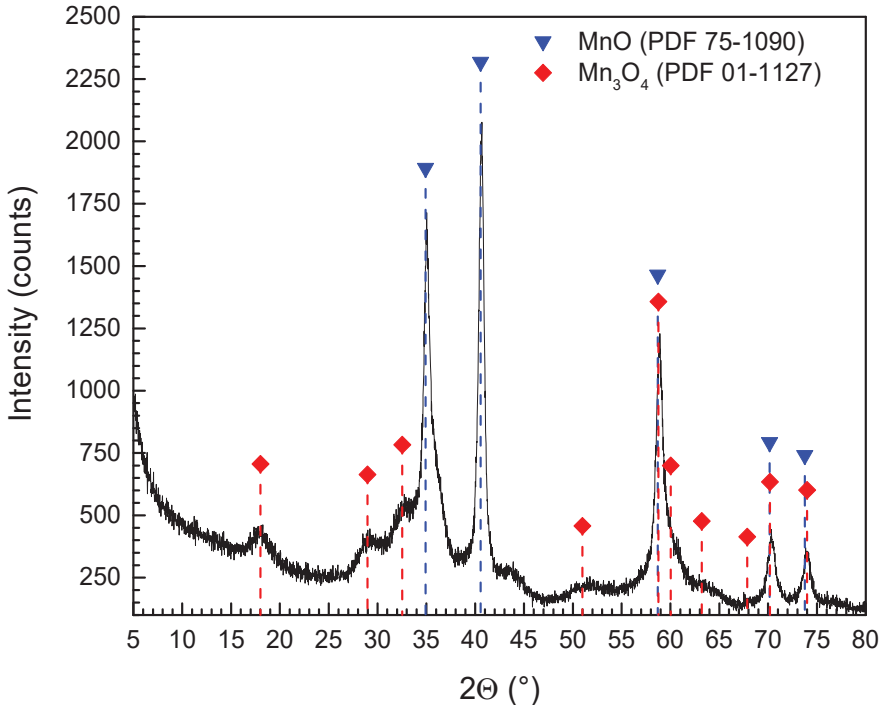

Figure 12: XRD diffractogram of MnO_x-pore after calcination.

TEM images of the solid before calcination show well defined spherical nanoparticles with a mean diameter of 466±44 nm (**Figure 13 A and B**). The nanoparticles composed of smaller nanoparticles are porous (**Figure 13 C**). SEM images of the same solid after calcination (**Figure 14**) show that the structure has been retained and further confirm that the porous spheres are composed of smaller nanoparticles as shown in literature when treatment temperature remain below 900 °C.[30]

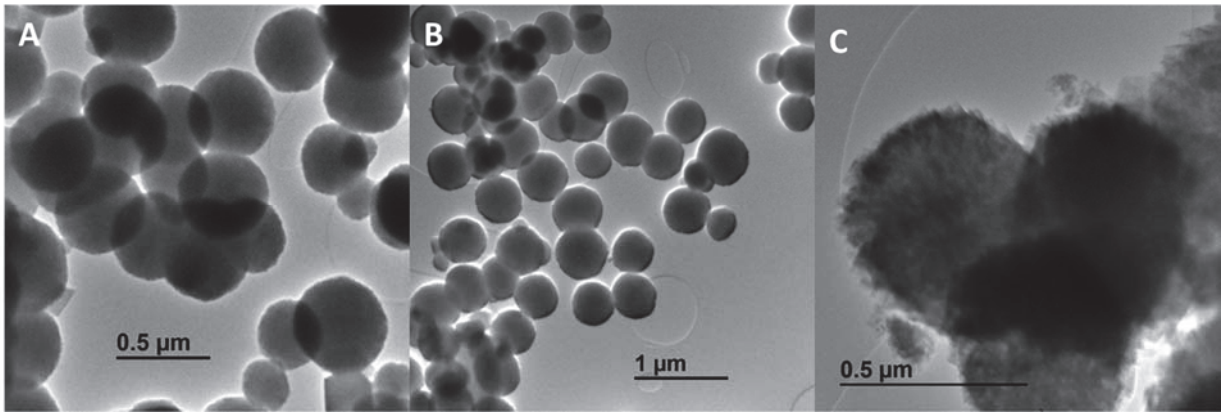

Figure 13: TEM images of the prepared MnO_x-pore nanoparticles before calcination. A) and B) pictures showing the variety of size and shape obtained, C) zoom on a single nanoparticle showing that the nanoparticle is porous and constituted of secondary nanoparticles.

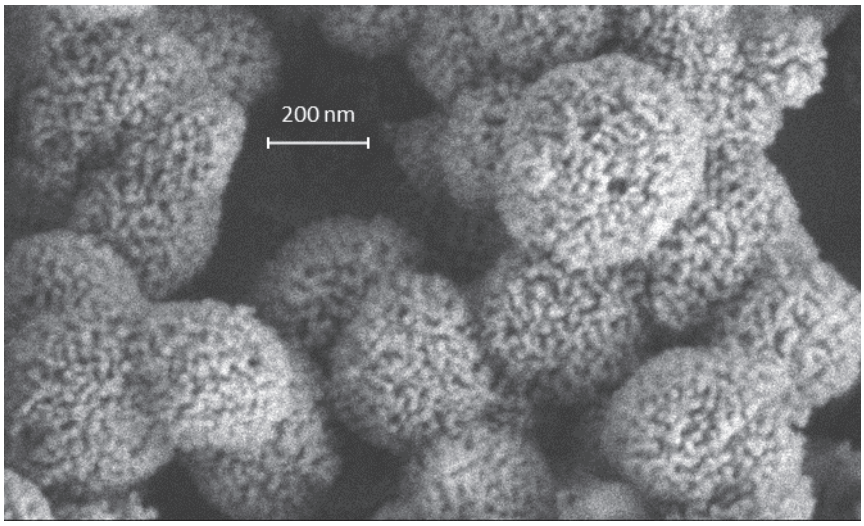

Figure 14: SEM images of the prepared MnO_x-pore nanoparticles after calcination.

N_2 adsorption isotherms have been performed on the sample before and after calcination. Both samples exhibit mainly mesoporosity with a BET surface area of 103 m^2/g before calcination and of 53 m^2/g after calcination. Both solids exhibit a type V isotherm adsorption with H_2 hysteresis (**Figure 15**)[32–34] indicating the presence of mesoporosity in the solid even after calcination. Small quantity of microporosity 8 m^2/g is present in the solid after calcination. The mesopore radius strongly increased due to calcination, from 4 nm to 12 nm, **Figure 16**. A fraction of the mesopores under 3 nm are preserved during calcination. The difference in specific surface areas observed here allows us to clearly explain the higher proportion of Mn_3O_4 overlayer observed by XRD.

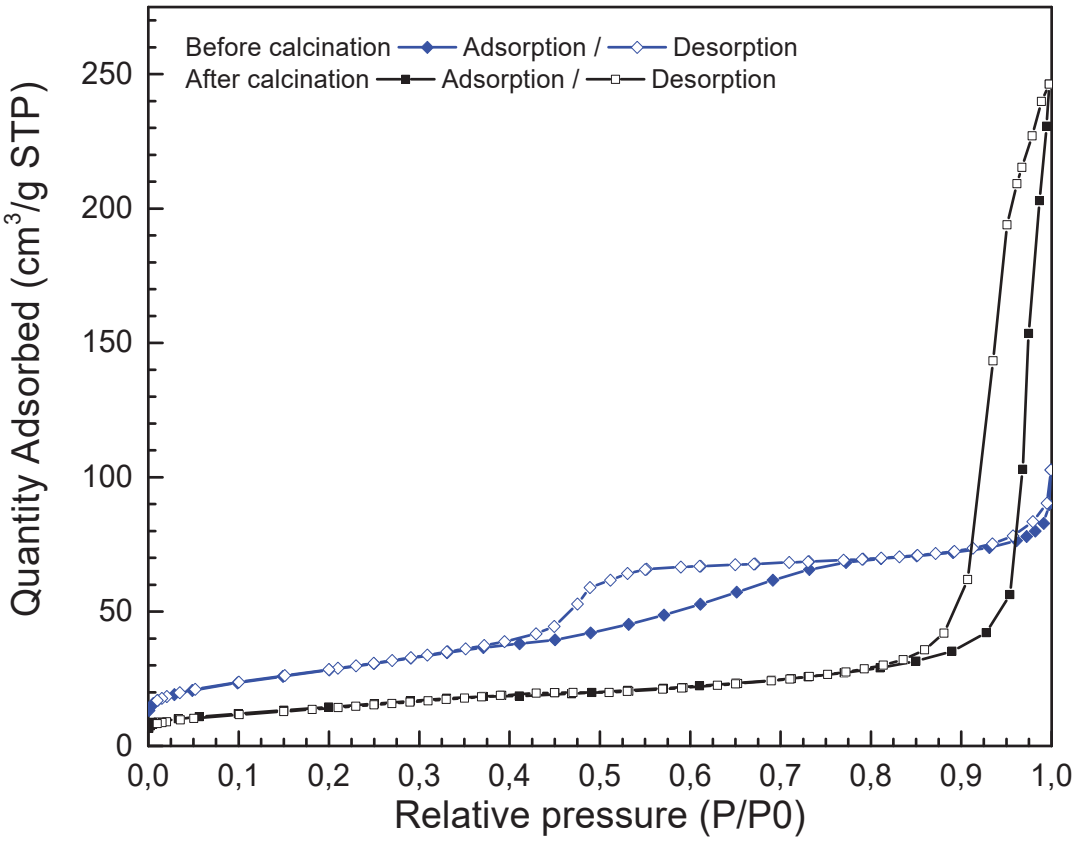

Figure 15: N_2 adsorption isotherms of the prepared MnO_x-pore nanoparticles before and after calcination.

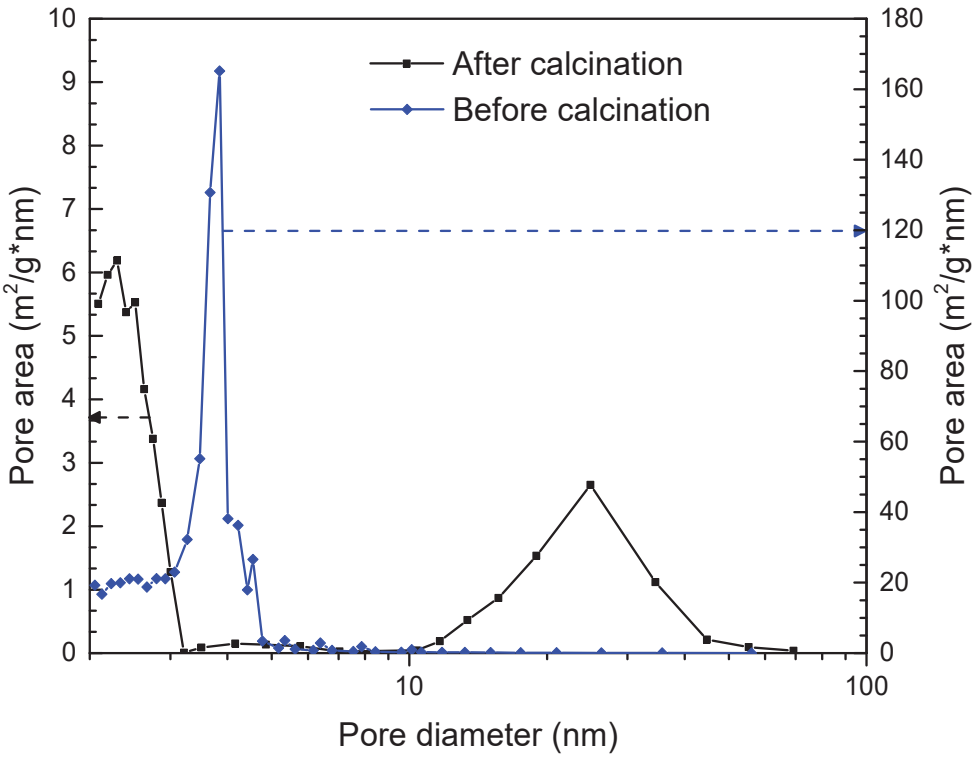

Figure 16: Pore area distribution as function of pore diameter of the prepared MnO_x-pore nanoparticles before and after calcination.

b) Silica deposit

i) Stöber

After centrifuging and washing 4 mmol of the $MnCO_3$ porous spheres, were re-dispersed in 374 ml of ethanol with 48.1 mmol of TEOS. After 1 h of stirring an ammonia solution, composed of 16 ml of 30% NH_4OH and 32 ml of water, was added under vigorous stirring. The solution was kept at room temperature under stirring for 1 day. The suspension was centrifuged (3500 rpm) and washed three times with ethanol before drying the recovered solid at 100 °C overnight. The solid was then calcinated at 450 °C for 12 h under synthetic air (100 $mL.min^{-1}$). The temperature was slowly raised from room temperature to 450 °C with a heating rate of 0.5 $°C.min^{-1}$. Three core shell materials have been prepared with 48.1 mmol of TEOS, 6.5 mmol TEOS and 2.9 mmol of TEOS and are named $MnO_x@SiO_2$-48.1, $MnO_x@SiO_2$-6.5 and $MnO_x@SiO_2$-2.9, respectively.

For $MnO_x@SiO_2$-48.0 and $MnO_x@SiO_2$-6.5, a white deposit was observed on top of the main solid indicating formation of free silica. Its amount was higher for $MnO_x@SiO_2$-48.0.

The XRD diffractogram of MnO_x@SiO_2-48.0 after calcination plotted in **Figure 17** contains peaks of crystalline MnO_2 (PDF 12-0713) and of amorphous SiO_2. It shows that $MnCO_3$ is decomposed and oxidized upon calcination.

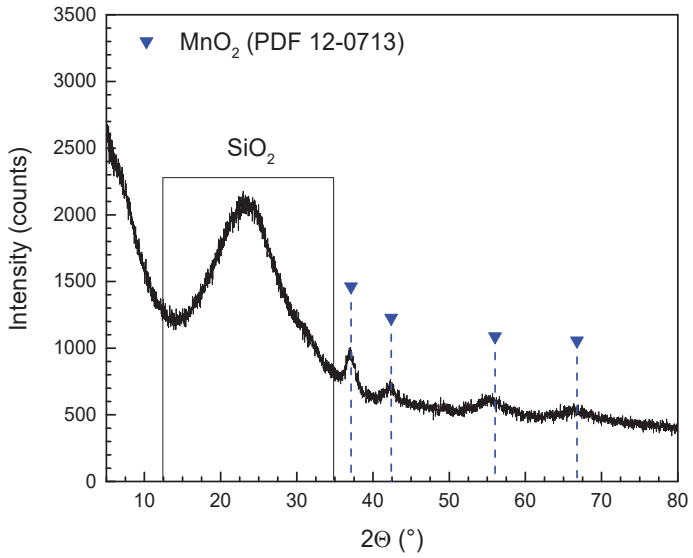

Figure 17: XRD diffractogram of MnO_x@SiO_2-48.0 sample after calcination.

ATR-IR spectra of MnO_x@SiO_2-48.0 before and after calcination are represented in **Figure 18**. Before calcination, the bands characteristic of $MnCO_3$ are observed between 1570 cm^{-1} and 1300 cm^{-1} and at 861 cm^{-1}.[35] The broad bands between 1295 cm^{-1} to 980 cm^{-1} were attributed to SiO_2.[36] After calcination, the bands characteristic of $MnCO_3$ are not observed confirming the decomposition of $MnCO_3$ upon calcination. The bands due to SiO_2 remain unchanged.

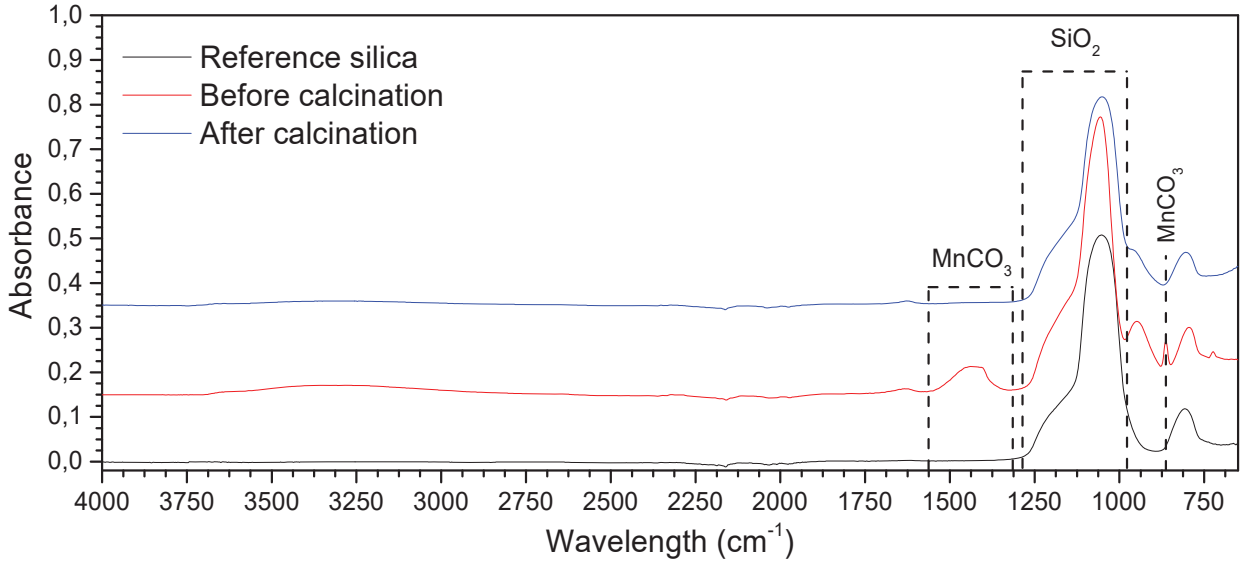

Figure 18: ATR-FTIR spectra of the MnO_x@SiO_2-48.0 sample before and after calcination and of reference silica.

TEM images of MnO_x@SiO_2-48.0 before and after calcination (**Figure 19** and **Figure 20**, respectively) show that the deposition of SiO_2 on the $MnCO_3$ cores leads to well defined core-shell structures. The shell thickness is consistent around the core and of 95±12 nm. Free silica particles can be observed for MnO_x@SiO2-48.0 as shown in **Figure 19 C** and **Figure 20 C**. Little quantity of free silica is observed for MnO_x@SiO_2-6.5, as shown in **Figure 21 C**, **Figure 22 B** and **C**, and no free silica is visible in MnO_x@SiO_2-2.9. The core structure and its size was retained after the deposition of the SiO_2 layer for every solid, with 442±56 nm, 428±41 nm, 460±64 nm for MnO_x@SiO_2-48.0, MnO_x@SiO_2-6.5 and MnO_x@SiO_2-2.9 respectively. Porosity cannot be observed. In particular, no broken shell was observed after calcination. Similar conclusions can be drawn from the TEM images of MnO_x@SiO_2-6.5 (**Figure 21** before calcination and **Figure 22** after calcination) and MnO_x@SiO_2-2.9 (**Figure 23**). Their shell thicknesses were 62±13 nm and 40±7 nm, respectively.

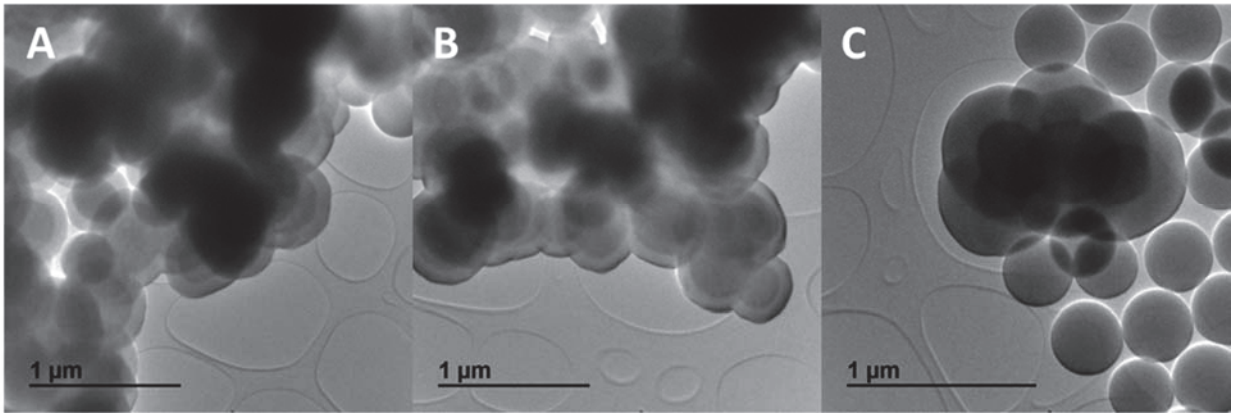

Figure 19: TEM images of the prepared MnO_x@SiO_2-48.0 sample before calcination. A) and B) showing core-shell structures that are agglomerated, C) showing core-shell structures surrounded by free silica nanoparticles.

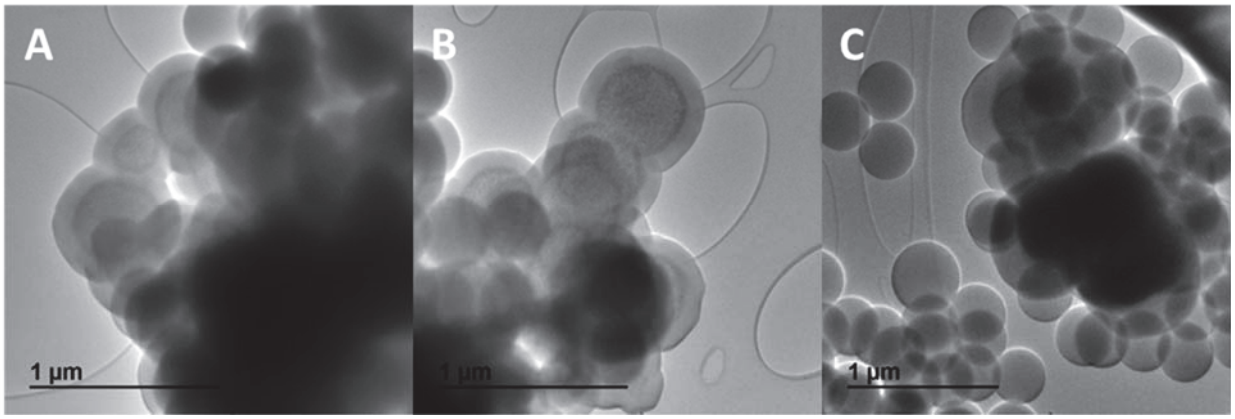

Figure 20: TEM images of the prepared MnO_x@SiO_2-48.0 sample after calcination. A) and B) showing core-shell structures that are agglomerated, C) showing core-shell structures surrounded by free silica nanoparticles.

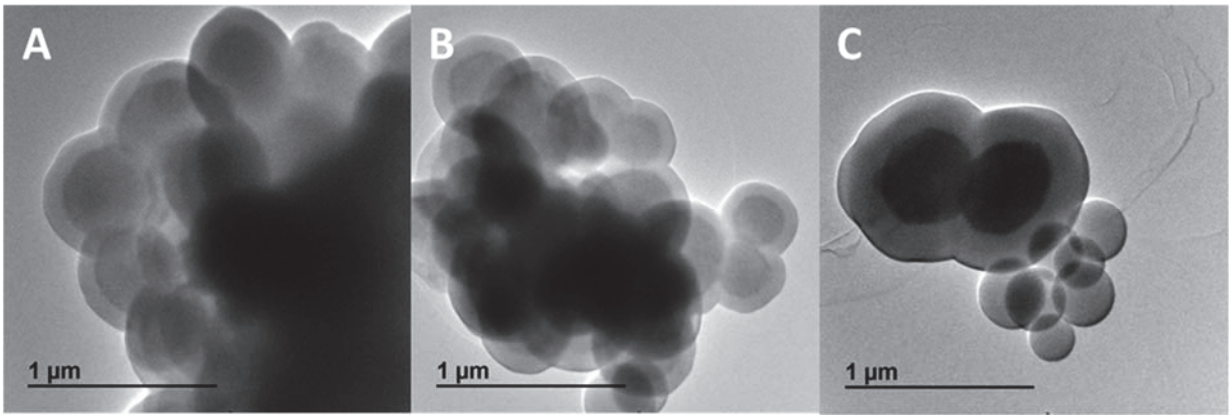

Figure 21: TEM images of the prepared MnO_x@SiO_2-6.5 sample before calcination. A) and B) showing core-shell structures that are agglomerated, C) showing core-shell structures surrounded by free silica nanoparticles.

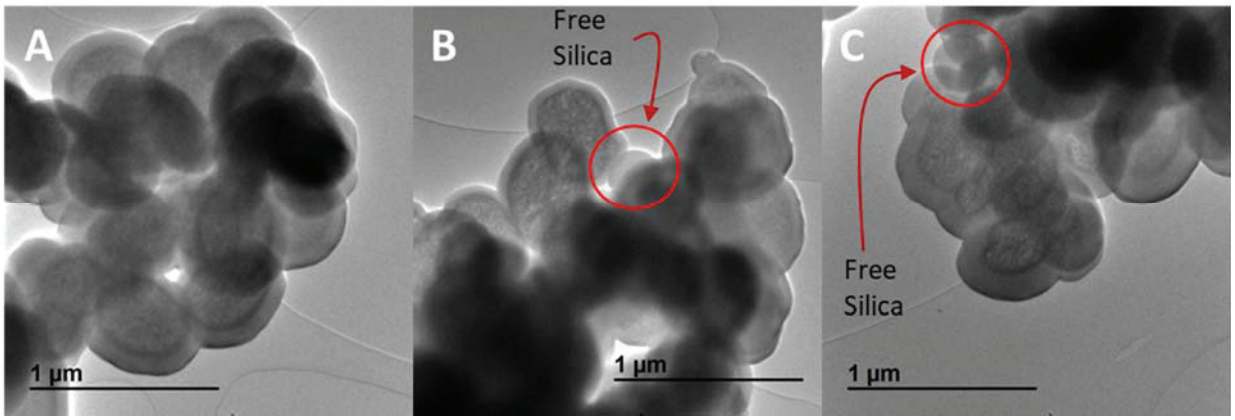

Figure 22: TEM images of the prepared MnO_x@SiO_2-6.5 sample after calcination showing the core-shell structure. Free silica nanoparticles are circled in red in B) and C).

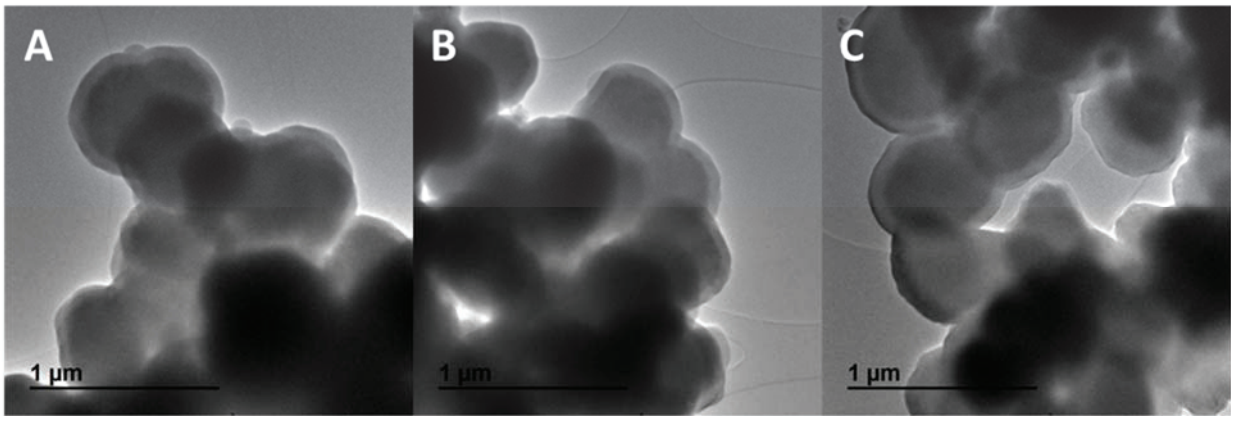

Figure 23: TEM images of the prepared MnO_x@SiO_2-2.9 sample before calcination showing the core-shell structures.

For the sake of clarity, the three samples are re-labelled MnO_x@SiO_2-95 nm, MnO_x@SiO_2-62 nm, MnO_x@SiO_2-40 nm in the following.

Using FX analysis and TEM images, the proportion of free silica in the samples was estimated and is represented in **Figure 24** : first, the shell thickness and the core diameter were evaluated from the TEM images by doing a statistical measurement (see above). Then, by using a dense sphere model, the $\frac{Si}{Mn}^{CS}$ molar ratio was determined considering MnO_2 and SiO_2 as oxides present in the solid. Finally, by using the Si and Mn proportion (x_{Si}^T and x_{Mn}^T , respectively with T for the proportion in total) determined by FX analysis, the proportion of free silica x_{SiO2}^f can be determined using Eqn. 1. (details in annex S1).

$$x_{SiO2}^f = \left(x_{Si}^T - x_{Mn}^T * \frac{Si}{Mn}^{CS}\right) * M_{SiO2}/M_{Si} \quad (1)$$

With M_{SiO2} and M_{Si} the molar mass of SiO_2 and Si, respectively.

A theoretical shell thickness was determined using a dense sphere model, the core diameter determined by TEM and assuming that all the TEOS introduced during the deposit reacted forming the shell. With those data the theoretical thickness was determined using Eqn.2. (Details in annex S2).

$$m_{TEOS} = \frac{M_{TEOS}}{M_{SiO2}} * \frac{4\pi\rho_{SiO2}}{3} * ((R_S + R_C)^3 - R_C^3) \quad (2)$$

With m_{TEOS}, the mass of TEOS introduced during the deposit, M_{TESOS} its molar mass, ρ_{SiO2} the specific mass of SiO_2 (2.65 g.cm^{-3}), R_s and R_c the shell and core radii, respectively.

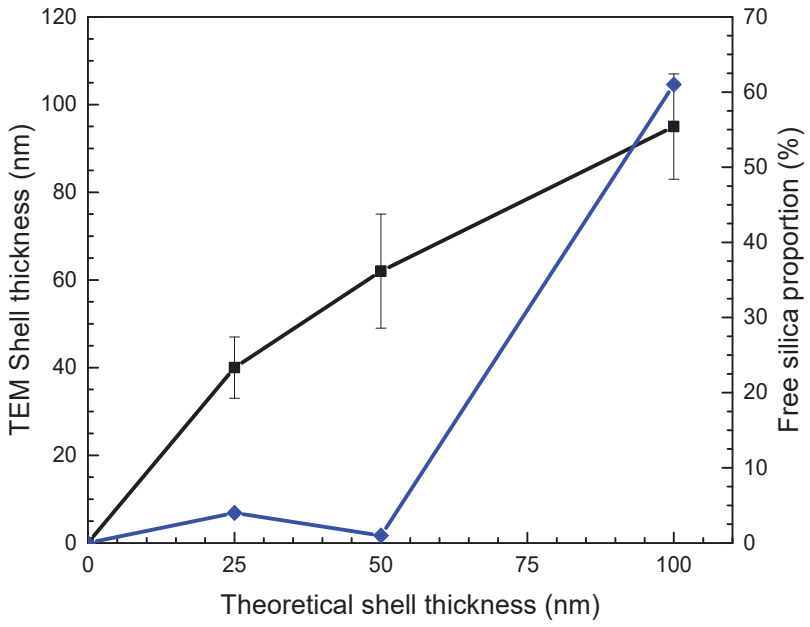

Figure 24: shell thickness determined from the TEM images and free silica proportion as a function of the theoretical shell thickness based on a dense sphere model and complete conversion TEOS into SiO_2 shell.

It can be observed that the shell thicknesses determined from TEM images are higher than expected, except for MnO_x@SiO_2-95 nm (95 nm instead of 100 nm). Initially the quantity of TEOS was determined supposing 100 % yield for the $MnCO_3$ synthesis implying the production of 5 mmol of $MnCO_3$. However it seems that the yields were around 80% leading to this gap between the theoretical and measured thickness. The only sample containing mainly free silica is MnO_x@SiO_2-95 nm in high quantity as suggested by the white deposit observed. This might be due to high TEOS concentration (0.11 $mol.l^{-1}$ against 0.015 $mol.l^{-1}$ for MnO_x@SiO_2-62 nm) leading to homogeneous nucleation during the SiO_2 deposit.

N_2 adsorption isotherms were measured for the three core-shell samples, as depicted in **Figure 25**. The determination of the adsorbed quantity at low relative pressure was difficult for all of them indicating difficulty to access the porosity. Furthermore, the quantitative measurements were not repeatable for the same sample. However, the shapes of the curves were similar. All core-shell structures present a type VI isotherm curve[32–34] with a specific shape indicating that the mesopores might be only accessible through microporosity. This type of porosity is called 'bottle shaped' generally leading to difficult access to the mesoporosity.[33,34]

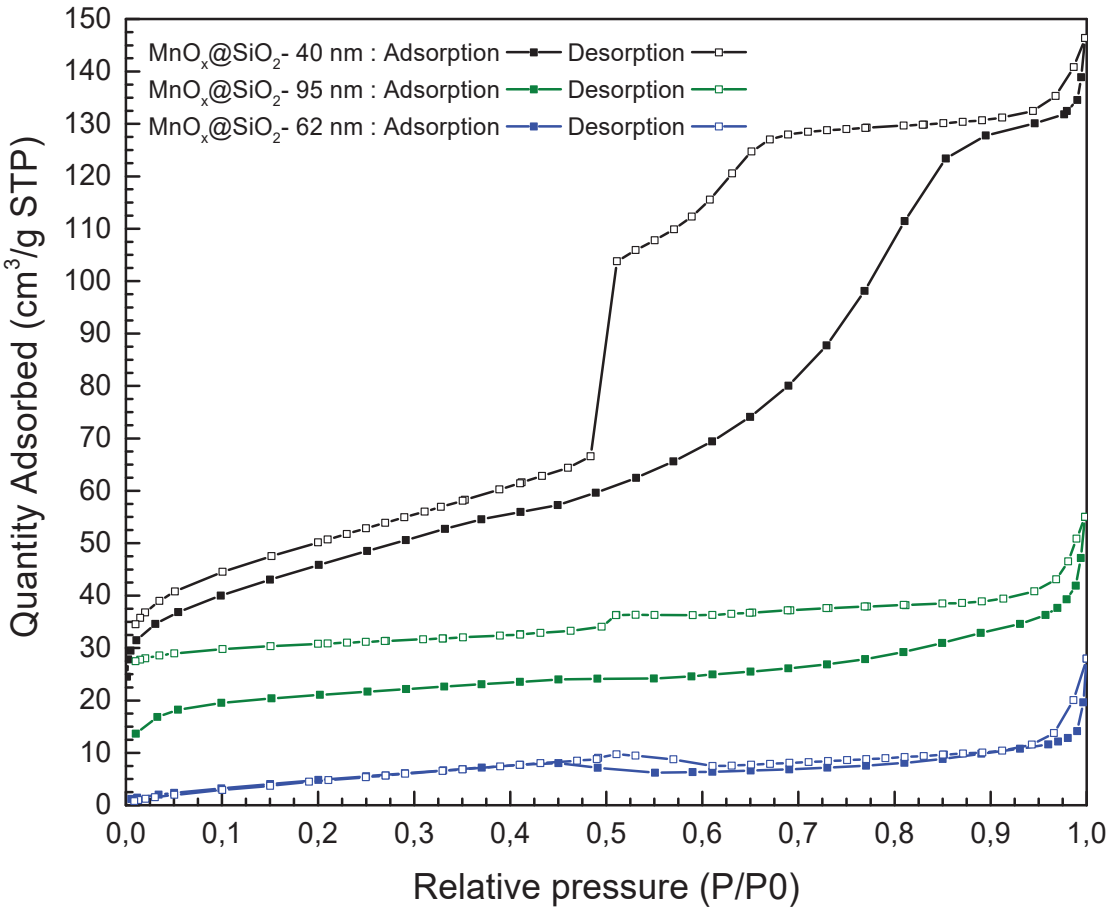

Figure 25: N_2-asdorption isotherm curves for $MnO_x@SiO_2$-95 nm, $MnO_x@SiO_2$-62 nm and $MnO_x@SiO_2$-40 nm samples.

3.2) Catalytic results

In this section, the catalytic properties of the core-shell structures will be presented. Before understanding those results, it is needed to determine the intrinsic activity of MnO_x-pore mixed with SAPO-K. This allows to compare similar Ox-Zeo mixtures and to get a better understanding of the impact of the shell on the catalytic properties.

3.2.1) *MnOx-pore*

MnO_x-pore was tested alone to compare its catalytic properties with those of MnO_x-Ref.

a) MnO_x-pore alone

MnO_x-pore was tested alone as a function of contact time in the same reaction conditions as MnO_x-Ref (P=25 bar, T=410 °C, feed $H_2/CO/N_2$=60/30/10). Catalytic performances are plotted in

Figure 26. The conversion was only 1.4% for the contact time 3.4 s. It was higher than for MnO_x-Ref in the same conditions (0.9%). This difference could be linked to the difference in S_{BET} value (53 and 28 $m^2.g^{-1}$, respectively). However, the increase in conversion is not proportional to the increase in S_{BET} value.

Similarly to MnO_x-Ref, MnO_x-pore produced mainly CH_4 and CO_2 with selectivity values of 52% and 33%, respectively. The selectivity values to C2, C3, C4 and C5+ were low (sum below 15%). The selectivity does not depend on the conversion in the range of contact time studied.

The C2-C4 O/P ratio was 1.1 for the contact time 3.4 s which is lower than for MnO_x-Ref with 1.7. The O/P ratios for C2, C3 and C4 hydrocarbons were 1.0, 2.9 and almost 0, respectively.

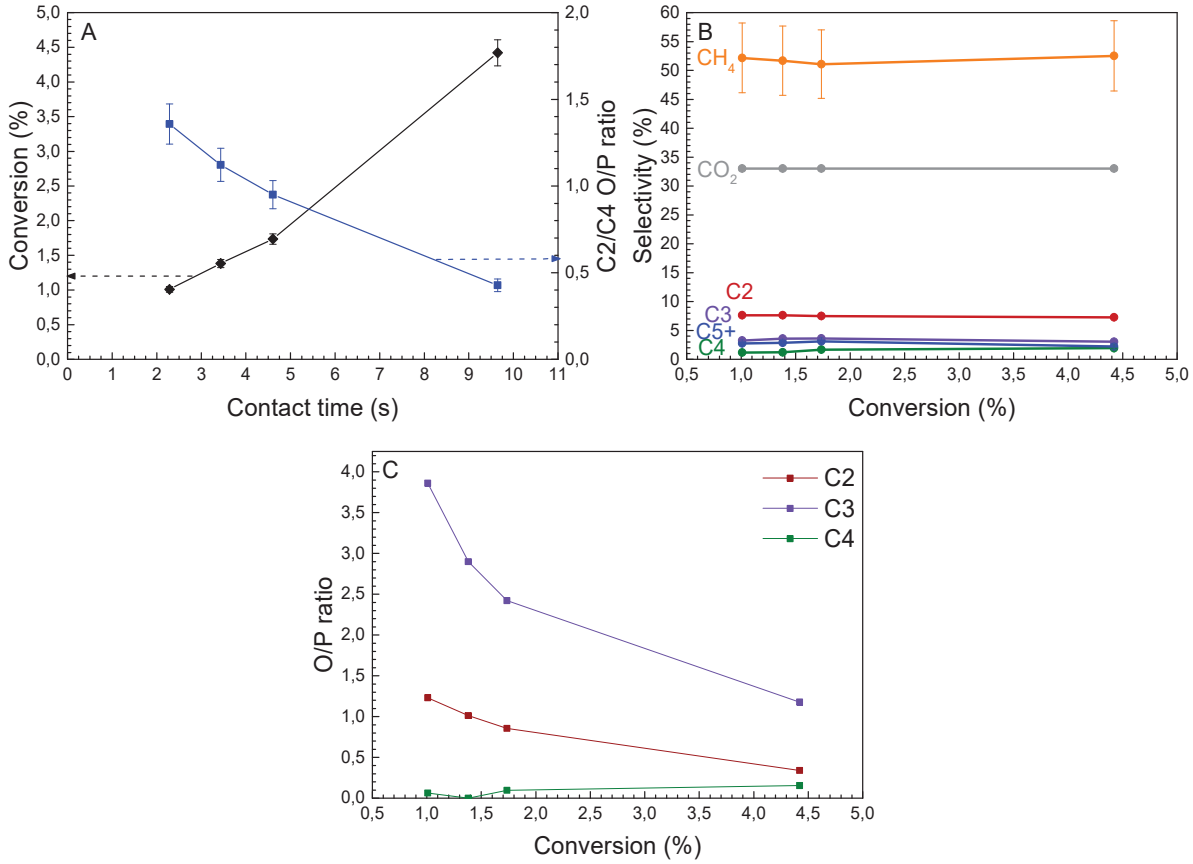

Figure 26: A) Evolution of the conversion and the C2-C4 O/P ratio with contact time and B) evolution of the CO_2, CH_4 and hydrocarbon selectivity and C) evolution of the O/P ratio for C2, C3 and C4 hydrocarbons with conversion. Reaction conditions: m (MnO_x-pore) =200 mg, P=25 bar, T=410 °C, $H_2/CO/N_2$=60/30/10. Data were taken after 14 h on stream.

b) MnO_x-pore+SAPO-K

As shown in **Figure 27**, 80% MnO_x-pore+ 20% SAPO-K mixture exhibits a conversion of 3.9% at contact time 3.4 s (87 $mL.min^{-1}.g^{-1}$) which is lower than using MnO_x-Ref as oxide (5.7%). This difference might be due to a higher proportion of active sites located far from the outer surface, leading to a decrease in the diffusion flow of methanol and hence a decrease in conversion.

As for 80% MnO_x-Ref+20% SAPO-K mixture, this sample produced mainly C2 and C3 hydrocarbons and CO_2 with the selectivity values of 23.6%, 33.0% and 32.4%, respectively. The by-products were CH_4 (4.9%), C4 (4.6%) and C5+ hydrocarbons (1.5%). However, a higher C5+ selectivity was obtained using MnO_x-Ref.

The C2-C4 O/P ratio was slightly higher compared with MnO_x-Ref+SAPO-K (6.3 vs 5.3). This difference could be explained by the lower conversion. However, the O/P ratios for C2, C3 and C4 hydrocarbons were ranked in a different order. Indeed, the C2 O/P ratio was the highest while it was the C4 one for MnO_x-Ref+SAPO-K. Unfortunately, our understanding of the system does not allow to have a solid explanation of that difference at the moment.

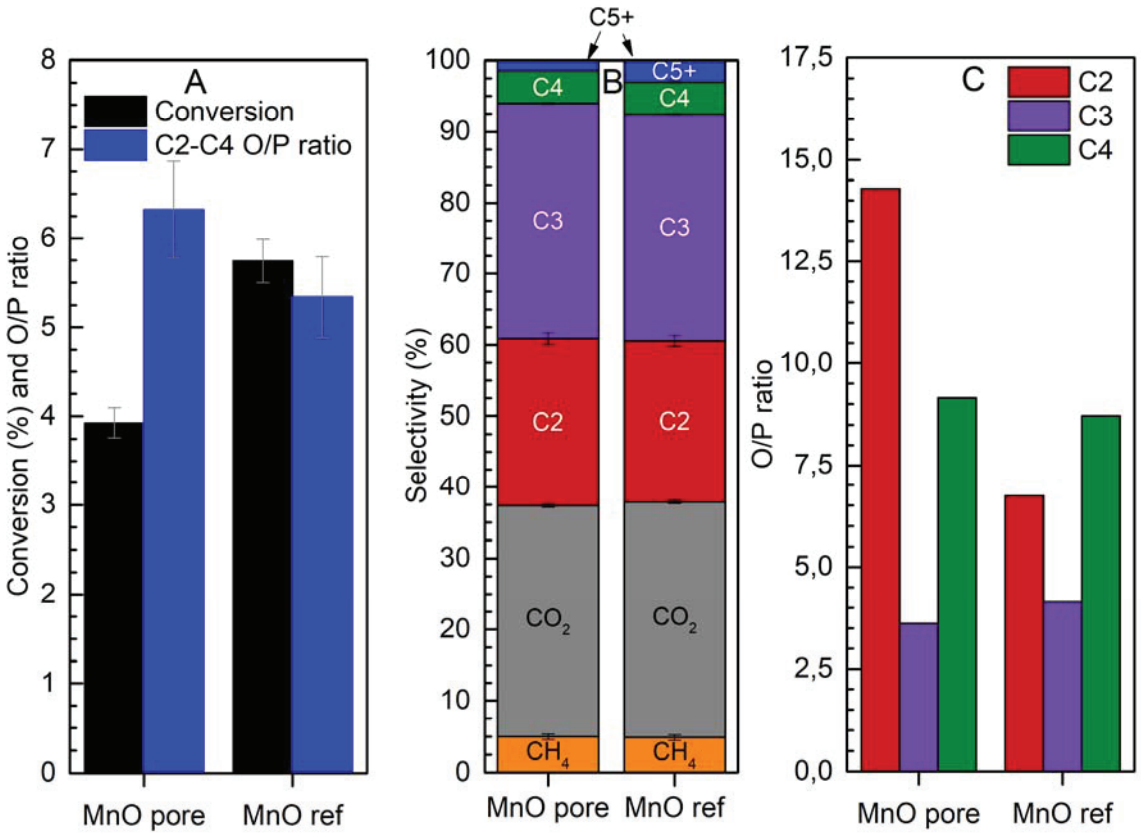

Figure 27: A) Conversion and C2-C4 O/P ratio and B) CO_2, CH_4 and hydrocarbon selectivity and C) O/P ratio for C2, C3 and C4 hydrocarbons for 80%MnO_x-pore+20%SAPO-K and , 80%MnO_x-Ref+20%SAPO-K. Reaction conditions: m(MnO-pore) or m(MnO_x-Ref)=240 mg, m(SAPO-K)=60 mg, P=25 bar, T=410 °C, $H_2/CO/N_2$=60/30/10, WHSV 87 $mL.min^{-1}.g^{-1}$. Data were taken after 14 h on stream.

From these results we see that the MnO-pore has slightly different catalytic properties as compared with MnO-ref, both in pure state and in the mixture with SAPO. The reasons of this difference might be related to morphology as well as to the difference in genesis of these two solids that would modify the surface density of active sites. However the general trends are the same for two manganese oxide samples.

3.2.2) *Core-shell structures*

The three core-shell structures were tested in a mechanical mixture with SAPO-K in the standard conditions (P=25 bar, T=410 °C, $H_2/CO/N_2$=60/30/10, WHSV=87 $mL.min^{-1}.g^{-1}$). The evolution of their catalytic properties along those of MnO_x-pore also mixed with SAPO-K are presented in **Figure 28** and **Figure 29** as a function of time on stream.

It can be seen in **Figure 28 A** that the conversion was systematically lower using the three core-shell structures compared with MnO_x-pore. Among the core-shell structures, $MnO_x@SiO_2$-95 nm led to the highest conversion (2.5% after 14 h) and $MnO_x@SiO_2$-40 nm the lowest one (0.4% after 14 h). In fact, the conversion seems to increase with the shell thickness which is counterintuitive. Indeed, one would expect that the thickest shell (100 nm) would hinder the diffusion of intermediate at the highest degree. We must suppose therefore that other factors that we do not control play role like, the resistivity of the shell to formation of cracks. However, we can merely speculate on the reasons of such behavior and from the data of characterizations we possess, this result has no clear explanation.

$MnO_x@SiO_2$-95 nm and $MnO_x@SiO_2$-62 nm exhibited a maximum of conversion after 1.5 h on stream, of 3.3% and 1.6% respectively. The conversion decreased after this time, as it was the case for MnO_x-pore alone. For $MnO_x@SiO_2$-40 nm, the conversion increased continuously. Hence, the evolution of the conversion under flow does not seem to be related to the shell thickness.

Concerning the C2-C4 O/P ratio, all the core-shell structures exhibited an O/P ratio lower than for MnO_x-pore, in spite of a lower conversion. $MnO_x@SiO_2$-40 nm led to the lowest O/P ratio, 1.1, after 14 h on stream while $MnO_x@SiO_2$-95 nm and $MnO_x@SiO_2$-62 nm led to similar ratios, 3.8 and 3.9, respectively. The O/P ratio decreased with time on stream for $MnO_x@SiO_2$-95 nm and $MnO_x@SiO_2$-40 nm while a maximum of 7.0 was observed for $MnO_x@SiO_2$-62 nm after 30 min on stream before a continuous decrease. Hence, the shell thickness had a smaller impact on the O/P ratio after 14 h on stream. However the evolution of the O/P ratio was greatly affected by the shell thickness. The introduction of a shell seems to impeach the increase of the O/P ratio during the first 14 h, as observed for MnO_x-pore+SAPO-K and MnO_x-Ref+SAPO-K.

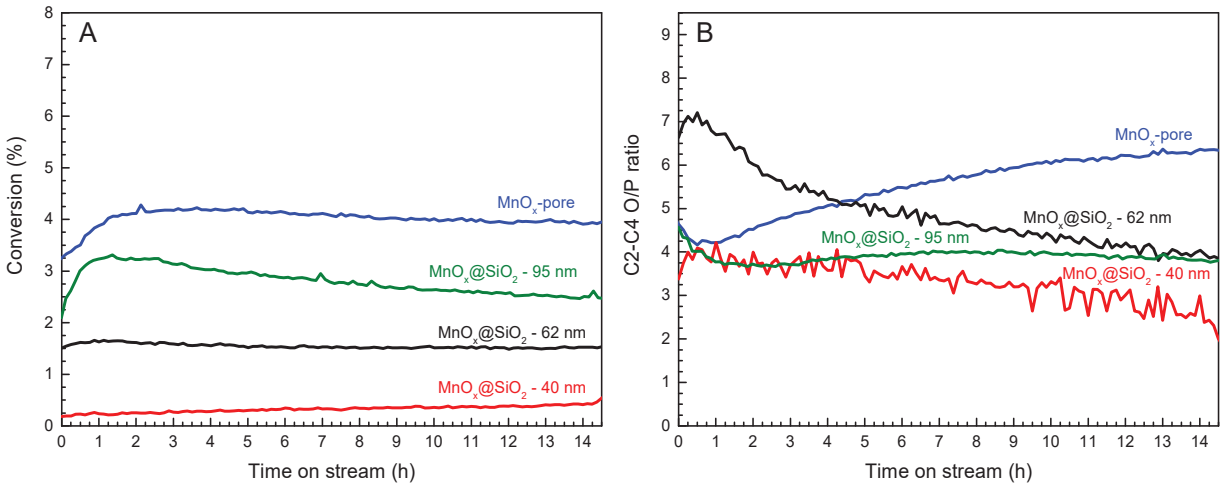

Figure 28: A) Evolution of the conversion and B) the O/P ratio with time on stream for MnO-pore, $MnO_x@SiO_2$-95 nm, $MnO_x@SiO_2$-62 nm and $MnO_x@SiO_2$-40 nm. Reaction conditions: m(SAPO-K)=30 mg with oxide mass of 120 mg, 1083 mg, 310 mg and 254 mg respectively to get 120 mg of MnO in the mixture, P=25 bar, T=410 °C, $H_2/CO/N_2$=60/30/10, WHSV 87 $mL.min^{-1}.g^{-1}$.

The evolutions of selectivity as function of time on stream are plotted for the four samples in **Figure 29**. For each core-shell structure mixed with SAPO-K, the CH_4 selectivity increased continuously under flow, contrary to MnO_x-pore mixed with SAPO-K. This increase was associated to a decrease in C3 and C2 selectivity values while the CO_2 selectivity did not vary with time on stream.

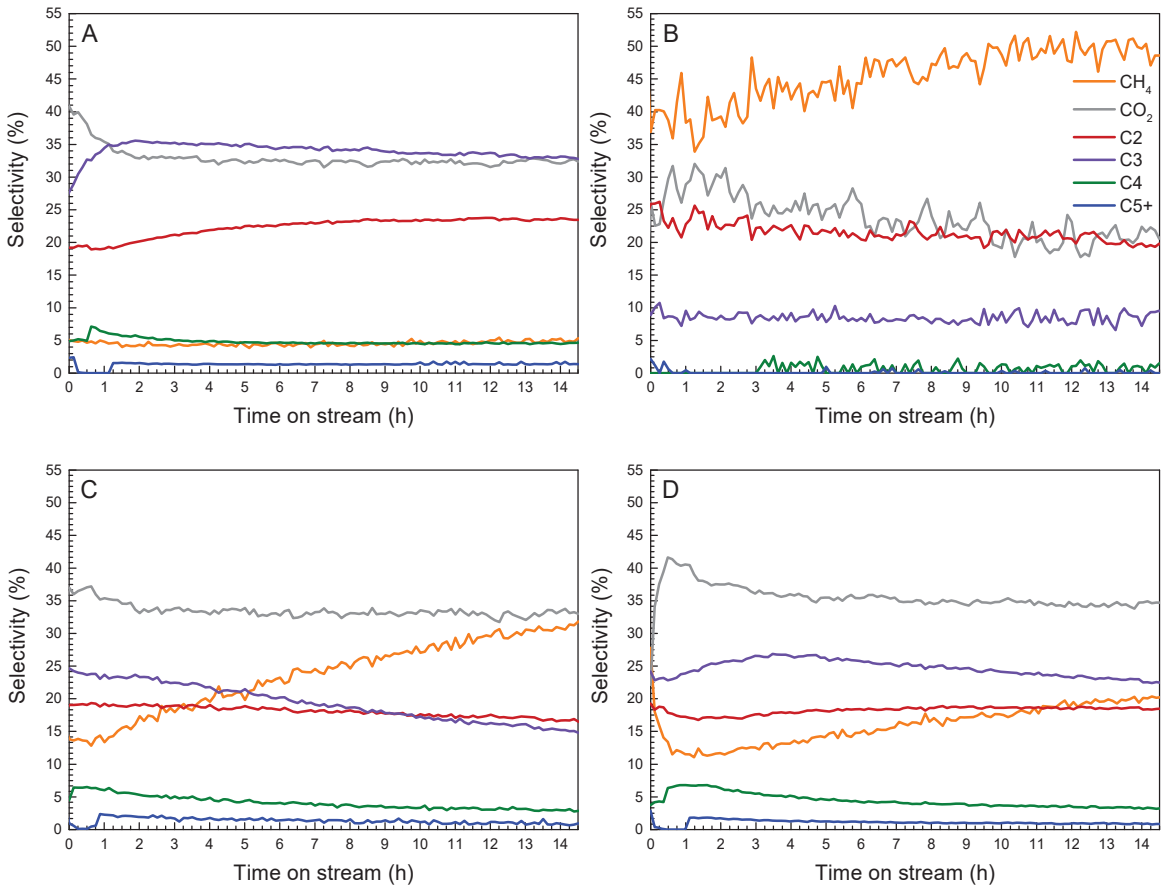

Figure 29: Evolution of the CO_2, CH_4 and hydrocarbon selectivity with time on stream for A) MnO_x-pore, B) MnO_x@SiO_2-40 nm, C) MnO_x@SiO_2-62 nm and D) MnO_x@SiO_2-95 nm in mechanical mixture with SAPO-K. Reaction conditions: m(SAPO-K)=30 mg with oxide mass of 120 mg, 254 mg, 310 mg and 1083 mg respectively to get 120 mg of MnO in the mixture, P=25 bar, T=410 °C, $H_2/CO/N_2$=60/30/10, WHSV 87 $mL.min^{-1}.g^{-1}$.

Concerning the individual hydrocarbon O/P ratios, their evolutions were similar to those observed for the C2-C4 O/P ratio as depicted in **Figure 30**.

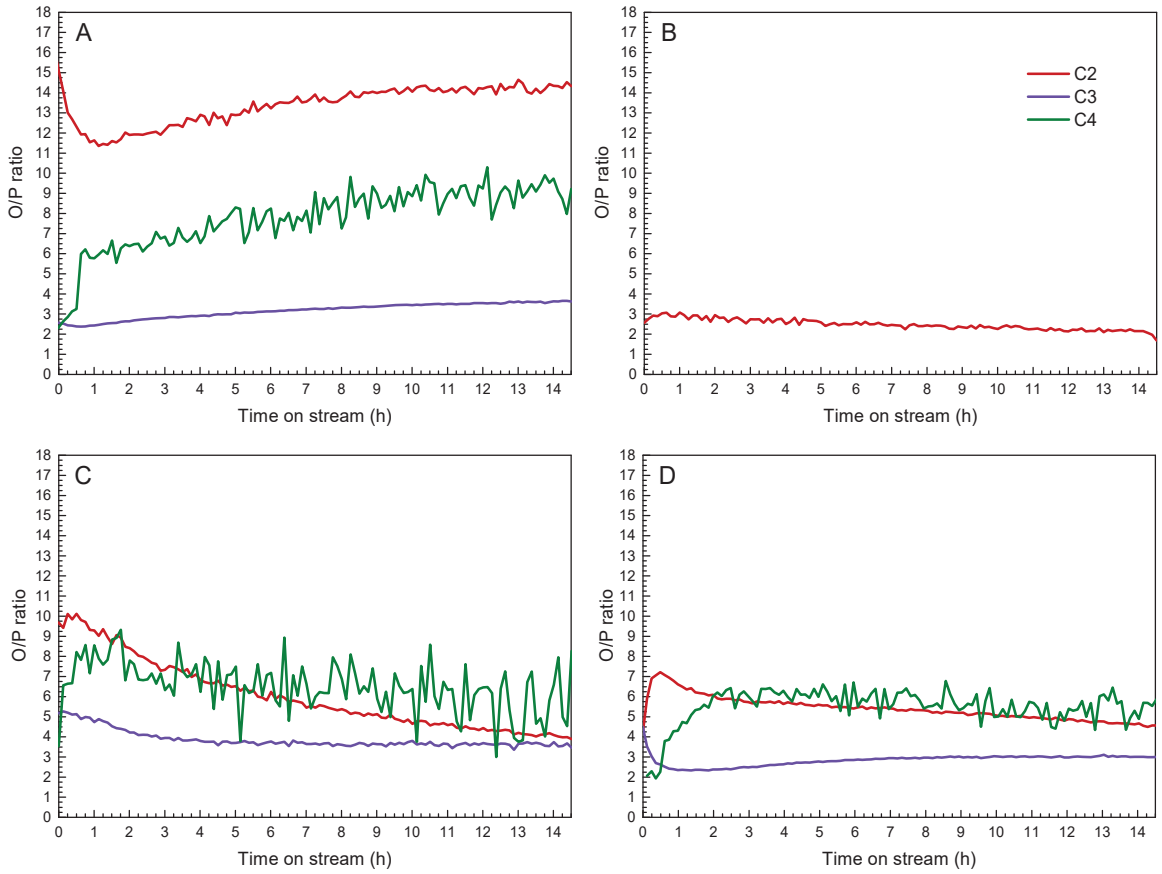

Figure 30: Evolution of the O/P ratio for C2, C3 and C4 hydrocarbons with time on stream for A) MnO_x-pore, B) $MnO_x@SiO_2$-40 nm, C) $MnO_x@SiO_2$-62 nm and D) $MnO_x@SiO_2$-95 nm in mechanical mixture with SAPO-K. Reaction conditions: m(SAPO-K)=30 mg with oxide mass of 120 mg, 254 mg, 310 mg and 1083 mg ,respectively to get 120 mg of MnO in the mixture, P=25 bar, T=410 °C, $H_2/CO/N_2$=60/30/10, WHSV 87 $mL.min^{-1}.g^{-1}$.

From those results and the N_2-adsorption isotherms (part 3.1.2.b), it can be proposed that the shell reduces greatly the diffusion of methanol and hence the global reaction rate. Indeed, most of porosity is only accessible through small mesopores or micropores.

This bottle shaped porosity implies the presence of a diffusion barrier around the oxide which decreases greatly the diffusion flow of the methanol. This decrease has two major effects: first the quantity of methanol reaching the zeotype is greatly decreased leading to a decrease in C2 and C3 selectivity. Secondly, the partial pressure of methanol increases inside the core-shell structure. This increase promotes the hydrogenation of methanol into methane as represented in **Figure 31**. Thus the methanol formation rate is no longer drawn by the zeotype but by the hydrogenation of

methanol, as with the oxide alone. However this hydrogenation is much slower than the conversion of methanol on the zeolite leading to a strong decrease in conversion.

This result is in accordance with the reaction mechanism proposed in the conclusion of Chapter 3. The decrease of the diffusion flow of methanol toward the zeotype is detrimental to the conversion and C2+ hydrocarbon selectivity. A beneficial effect could only occur if the diffusion coefficient of methanol was higher than that of the C2 + hydrocarbons. The use of a selectively permeable shell, prepared from a specific material, could allow to resolve this problem, by decreasing the diffusion coefficient of olefin at a value lower than methanol. This would allow for the existence of an optimum shell thickness where conversion is maintained and hydrogenation on the oxide is reduced.

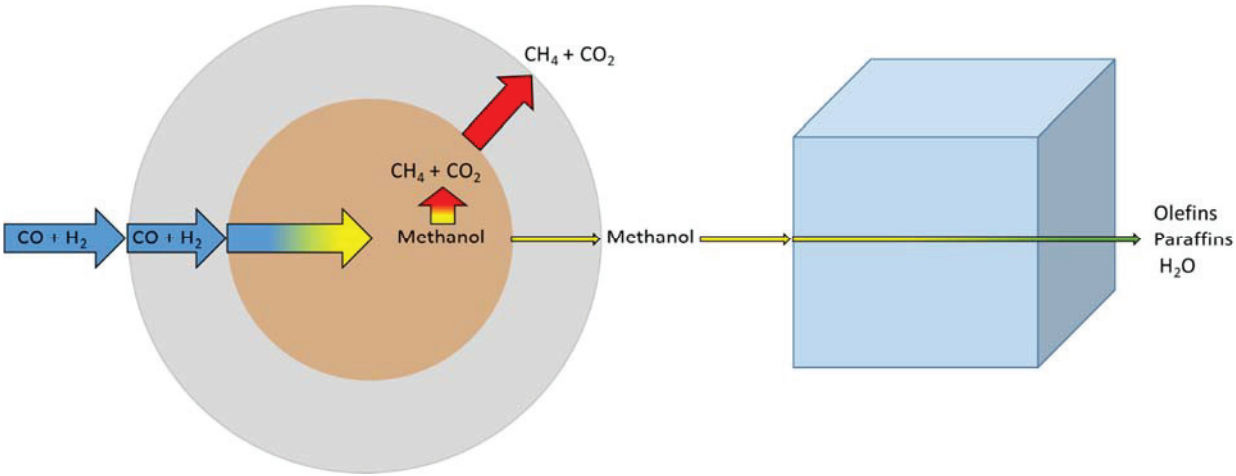

Figure 31 : Schematic representation of the diffusion flow and conversion taking place inside of the $MnO_x@SiO_2$ system coupled with SAPO-34

4) Suspension Mixture

As shown in part 2, at the grain agglomerate (micrometer) scale, the closer the oxide and the zeotype are, the higher the conversion. To improve intimacy at the primary grain (nanometer) scale, we prepared a random mixture of SAPO-sK crystals and MnO_x-pore nanoparticles. To ensure the dispersion of SAPO-sK nanoparticle, the mixture was prepared by combining suspensions of both solids. This idea was based on the fact that during drying the particles always considerably agglomerate. Then if two solids are dried separately and then mixed, many agglomerates of the same type particles would persist in the mixture. On the contrary we expected that mixing of liquid

suspensions prior to drying would ensure lesser agglomeration of the same type particles and better intimacy as it have been shown in literature for $BaTiO_2$ preparation.[37,38]

4.1) Preparation

143 mg of calcined SAPO-sK was finely grinded and added to 5 ml of ethanol and stirred vigorously. The obtained suspension was then treated in an ultrasound bath for 15 min to favor dispersion of SAPO-sK particles. A $MnCO_3$ suspension was prepared as previously described for MnO_x-pore (see part 3.1.2). After washing, 1.700 g of $MnCO_3$ nanoparticles were re-dispersed in 50 ml of ethanol passed in an ultrasound bath for 15 min producing a suspension. Then, the two suspensions were mixed together and dried at 100 °C over day. It would lead after calcination to a mixture composed of 1.286 g of MnO and 0.143 g of SAPO-sK (10% of zeotype). During the drying step, the suspension was periodically shacked at 30 min interval to ensure that no segregation between the SAPO-sK and $MnCO_3$ particles occurred. After drying, the obtained powder was treated thermally under 20%H_2-N_2 at 410 °C for 12 h. The resulting solid is named MnO_x-pore+SAPO-sK-SM in the following.

ATR-IR spectra recorded on the solid before and after calcination to follow the decomposition of $MnCO_3$ are presented in **Figure 32**. Before calcination, the solid exhibits characteristic bands of $MnCO_3$ between 1570 cm^{-1} and 1250 cm^{-1} region and at 861 cm^{-1}.[35] The T-O-T (framework linkage with T being either Al, Si or P) bands typical of SAPO-34 are also observed between 1250 cm^{-1} and 940 cm^{-1}.[39] The bands corresponding to $MnCO_3$ disappeared upon calcination indicating that $MnCO_3$ has been decomposed into MnO.

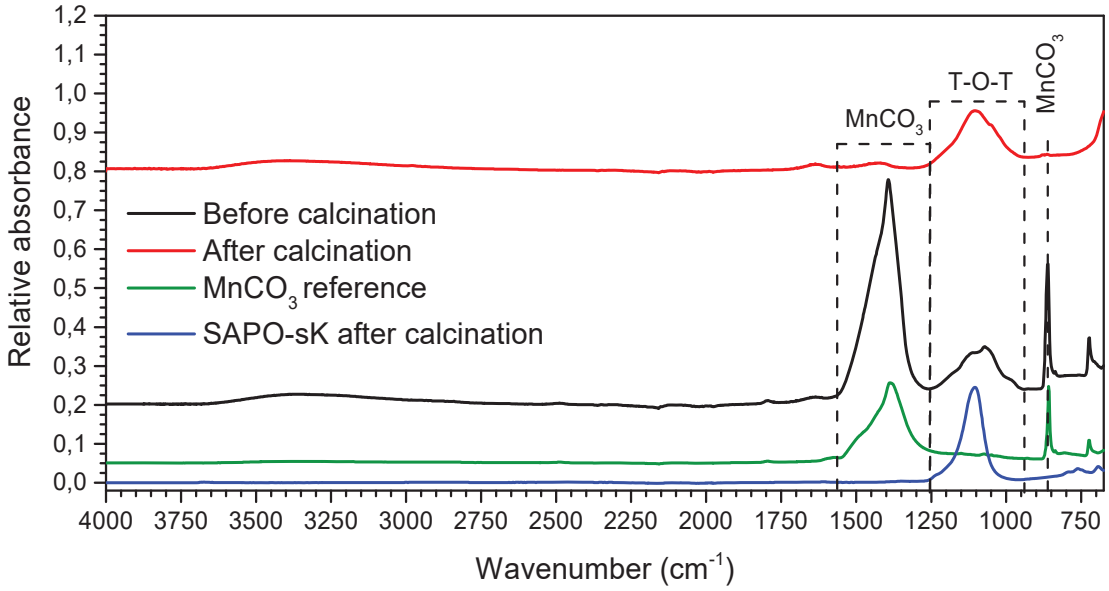

Figure 32: ATR-FTIR spectra of 90%MnO_x-pore+10%SAPO-sK-SM before and after calcination.

XRD pattern of the sample was recorded after calcination and ambient air conditioning. The solid exhibits characteristic diffraction peaks of MnO manganosite phase (PDF 75-1090 pattern) and of crystalline SAPO-34 (PDF 85-1049 pattern) as shown in **Figure 33**. Additional small broad peaks revealed the presence of Mn_3O_4 amorphous layer (PDF 01-1127) over MnO. The MnO crystallite size was 11 nm which is comparable to the value measured for MnO_x-pore alone.

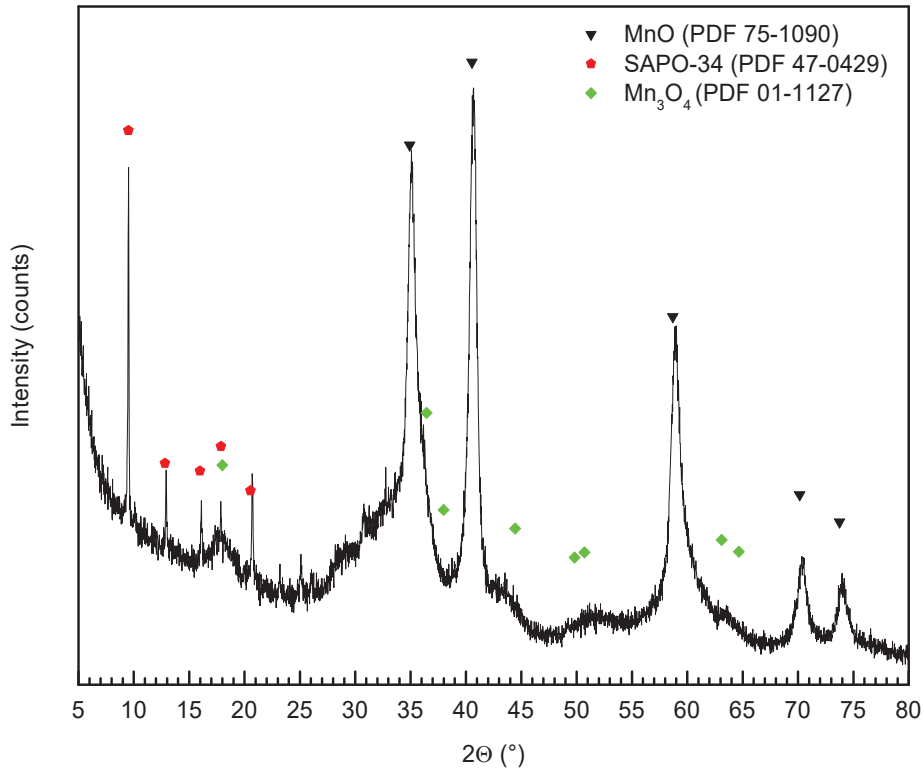

Figure 33: XRD diffractogram of 90%MnO_x-pore+10%SAPO-sK-SM sample after calcination.

SEM images of the sample after calcination were acquired to observe the dispersion of the SAPO-sK crystals in the mixture. **Figure 34** shows various size aggregates. No MnO_x nanoparticles or SAPO-sK agglomerates can be clearly distinguished as expected.

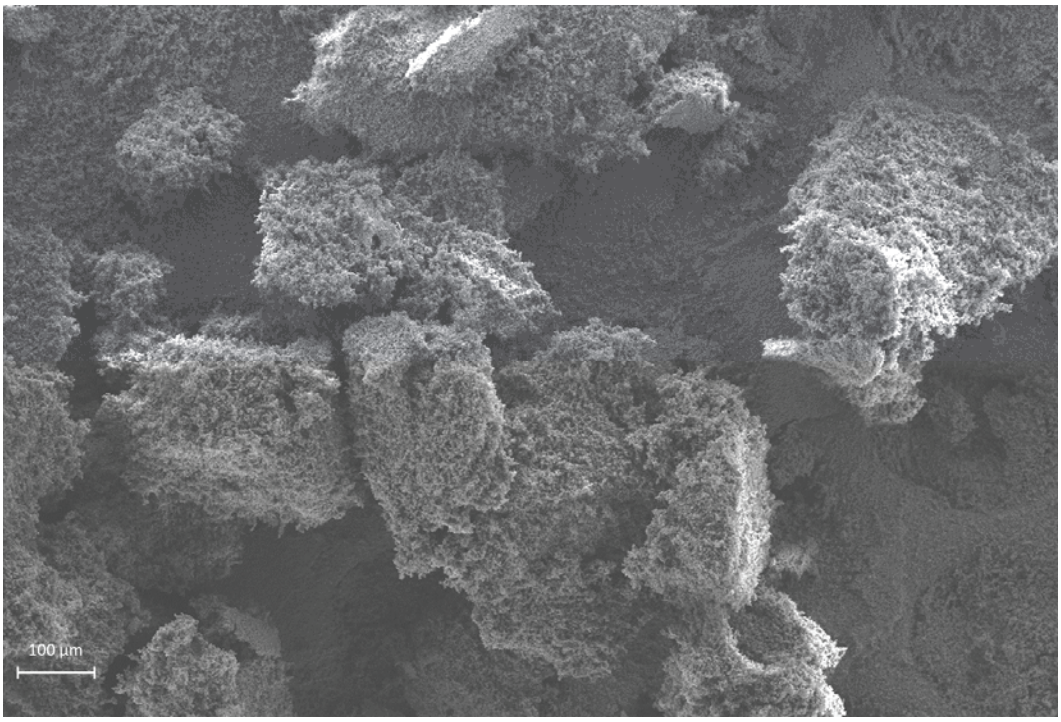

Figure 34: SEM image of 90%MnO_x-pore+10%SAPO-sK-SM sample after calcination.

In **Figure 35** a zoom of the image allows to observe clearly the MnO_x spherical particles and the SAPO-sK crystals: the SAPO-sK crystals are highly dispersed among the MnO_x nanoparticles. Therefore suspension mixing method seems to be effective to get a high contact density between the two functions.

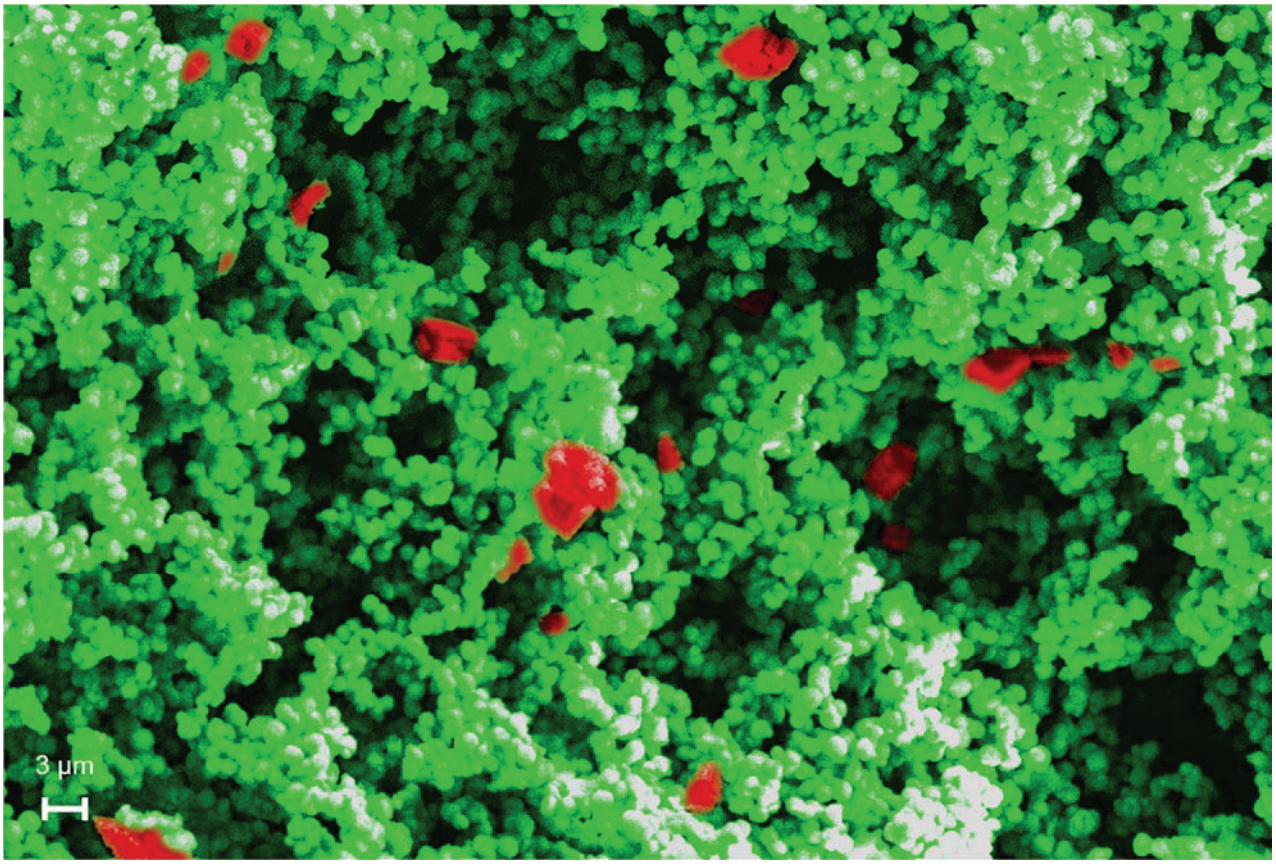

Figure 35: SEM image of 90%MnO_x-pore+10%SAPO-sK-SM sample after calcination. Zeolite particles are surrounded with red circles.

On the contrary, 90%MnO_x-pore+10%SAPO-sK was a mixture of MnO_x-pore and SAPO-sK, separately sieved between 180 µm and 105 µm before mechanical mixing. SEM images of this fresh mixture are shown in **Figure 36** and **Figure S1**. Large agglomerates of around 100-200 µm can be observed. Most of them are aggregates of MnO_x composed of spherical agglomerate of crystallite. In the down right corner of **Figure 36A**, a SAPO-sK aggregate seems to be covered by primary agglomerates of MnO_x which is confirmed by the zoom in **Figure 36A**. **Erreur ! Source du renvoi introuvable.** showing two images recorded at the surface of this aggregate. **Erreur ! Source du renvoi introuvable.B** evidenced aggregation of SAPO-sK crystals while **Erreur ! Source du renvoi introuvable.B** shows that some areas of this aggregate are covered by MnO_x agglomerate. Hence, this mixture is mostly composed of MnO_x and SAPO-sK aggregates even if a small quantity of MnO_x agglomerate partly covers SAPO-sK aggregates. The intimacy of the two catalytic functions is lower than that of the corresponding suspension mixture.

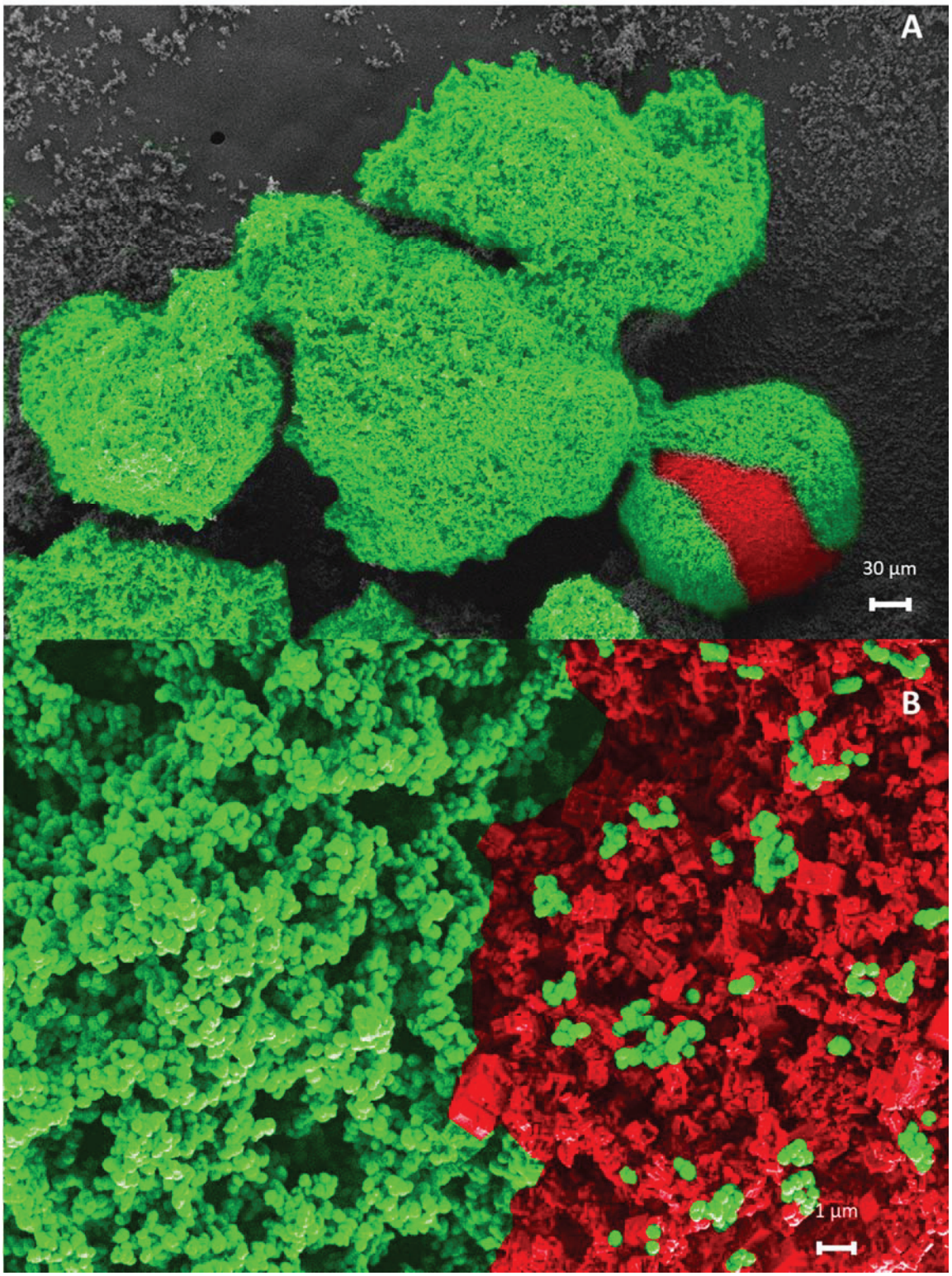

Figure 36: freshly prepared 90%MnO_x-pore+10%SAPO-sK mixture: A) Picture showing Four aggregates, three of oxide on the left and one of zeotype on the down right corner, B) MnO_x-pore and SAPO-sK separation.

4.2) Catalytic results

First, catalytic properties of MnO_x-pore+SAPO-sK mixture were determined. They are compared to those of MnO_x-Ref+SAPO-sK in **Figure 37**. When combined with SAPO-K, a lower conversion was obtained using MnO_x-pore instead of MnO_x-Ref (4.1% vs 6.7%). In parallel, the C2-C4 O/P ratio was 16.3 which is quite high. In fact all the O/P ratios were much higher than for MnO_x-Ref+SAPO-sK. In particular, the C3 O/P reaches 27.3. These high values can be mostly explained by lower conversion: for instance, the O/P ratio was increased from 3.0 to 4.8 when the conversion was decreased from 7.7% to 4.7% for 80%MnO_x-Ref-20%SAPO-K (**Figure 20, Chapter 3**). The O/P increase seems to be even higher for MnO_x-pore-SAPO-sK mixture for which the balance was optimized and the size of SAPO-sK crystals could limit consecutive hydrogenation of olefins.

The CO_2 selectivity values are comparable, around 33% for both MnO_x-pore+SAPO-sK and MnO_x-Ref+SAPO-sK mixtures. However, the CH_4 selectivity is higher with MnO_x-pore (12.1%) than with MnO_x-Ref (8.8%). Again, it was explained by a higher diffusion path of methanol leading to hydrogenation to CH_4. Consequently, the C2 and C3 selectivity values were slightly lower while the C4 and C5+ ones were quite similar (around 4.2% and 1.9%, respectively). Note that the difference of porosity between MnO_x-pore and MnO_x-Ref does not seem to impact the hydrogenation of C2-C4 olefins.

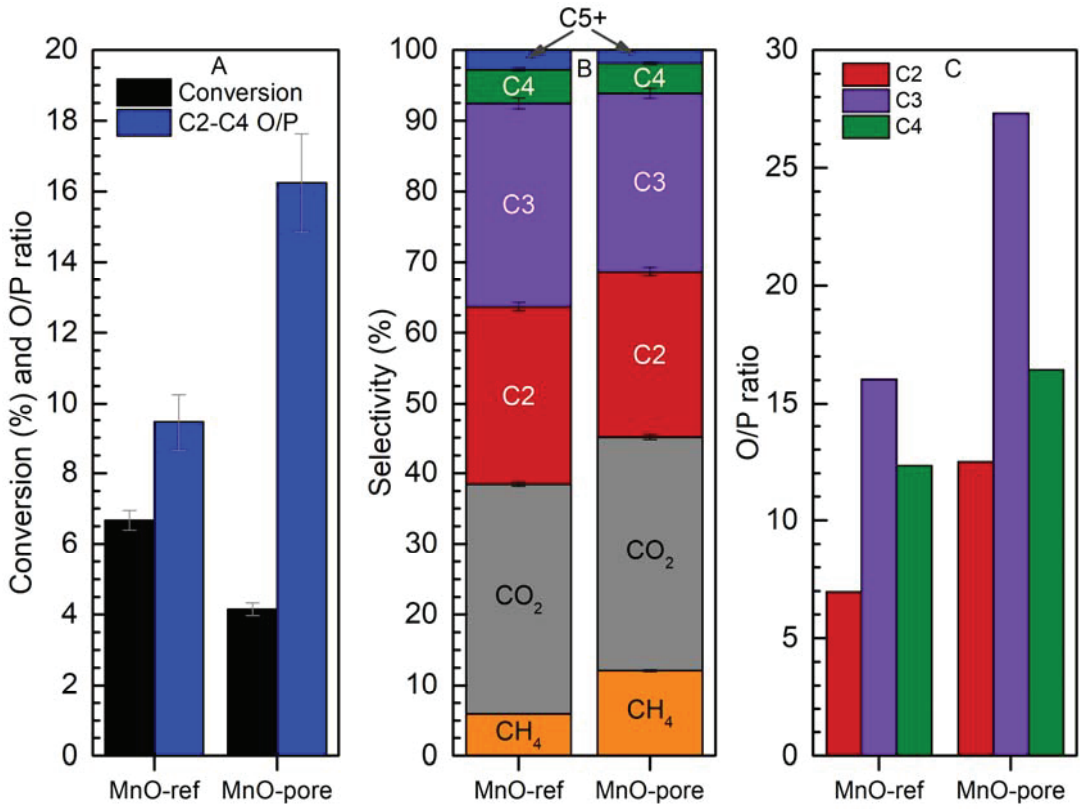

Figure 37: A) Conversion and C2-C4 O/P ratio and B) CO_2, CH_4 and hydrocarbon selectivity and C) O/P ratio for C2, C3 and C4 hydrocarbons for MnO_x-pore+SAPO-sK and MnOx-Ref+SAPO-sK mixture. Reaction conditions: m(MnO_x-pore) or m(MnO_x-Ref)=270 mg, m(SAPO-sK)=30 mg, P=25 bar, T=410 °C, $H_2/CO/N_2$=60/30/10, WHSV 87 $mL.min^{-1}.g^{-1}$. Data were taken after 14 h on stream.

Catalytic properties of MnO_x-pore+SAPO-sK-SM were assessed in the reaction conditions similar to those of MnO_x-pore+SAPO-sK mixture and compared in **Figure 38** to evaluate the impact of the difference of intimacy at the grain scale. After 14 h on stream, the two solids exhibited similar catalytic properties. The conversion was around 4.4% with an O/P ratio of 16.8 for MnO_x-pore+SAPO-sK-SM. A slightly lower CH_4 selectivity (8.8% vs 12.1%) was obtained in favor of the other hydrocarbons. The O/P ratio for C2, C3 and C4 hydrocarbons were 13.8, 25.2 and 12.2, respectively.

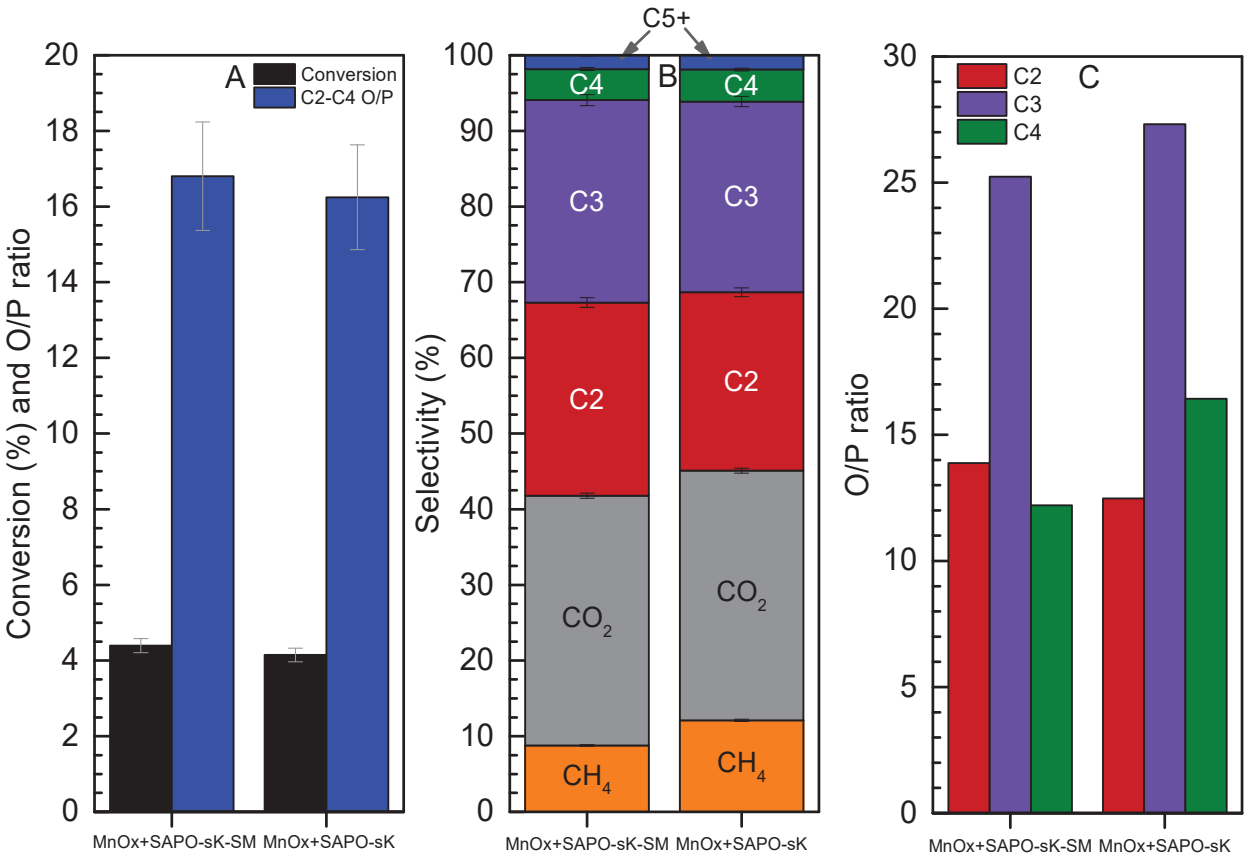

Figure 38: A) Conversion and C2-C4 O/P ratio, B) CO_2, CH_4 and hydrocarbon selectivity and C) O/P ratio for C2, C3 and C4 hydrocarbons for MnO_x-pore+SAPO-sK-SM and MnO_x-pore+SAPO-sK. Reaction conditions: m (MnO_x-pore) =270 mg, m (SAPO-sK) =30 mg, P=25 bar, T=410 °C, $H_2/CO/N_2$=60/30/10, WHSV 87 $mL.min^{-1}.g^{-1}$. Data were taken after 14 h on stream.

The evolutions of the O/P ratio with time on stream were different for MnO_x-pore+SAPO-sK-SM and MnO_x-pore+SAPO-sK. As shown in **Figure 39**, the O/P ratio reaches its maximum after 4 h for the former and after 6 h for the latter. It is worth noting that the maximum reached for MnO_x-pore+SAPO-sK-SM, 18.7, is higher than for MnO_x-pore+SAPO-sK, 16.6. Then, the two curves converge toward similar value at 14 h on stream. This difference of evolution is also evidenced for the C3 O/P ratio (**Figure 40 C and D**) with a quicker stabilization for MnO_x-pore+SAPO-sK-SM (6 h) than for MnO_x-pore+SAPO-sK (10 h). Concerning the evolutions of selectivity, no significant difference can be observed (**Figure 37**). It is worth noting that the early evolution of catalytic properties are often not discussed in literature.[2,4,7,40] Usually focus is placed on the long term stability of the catalytic system.

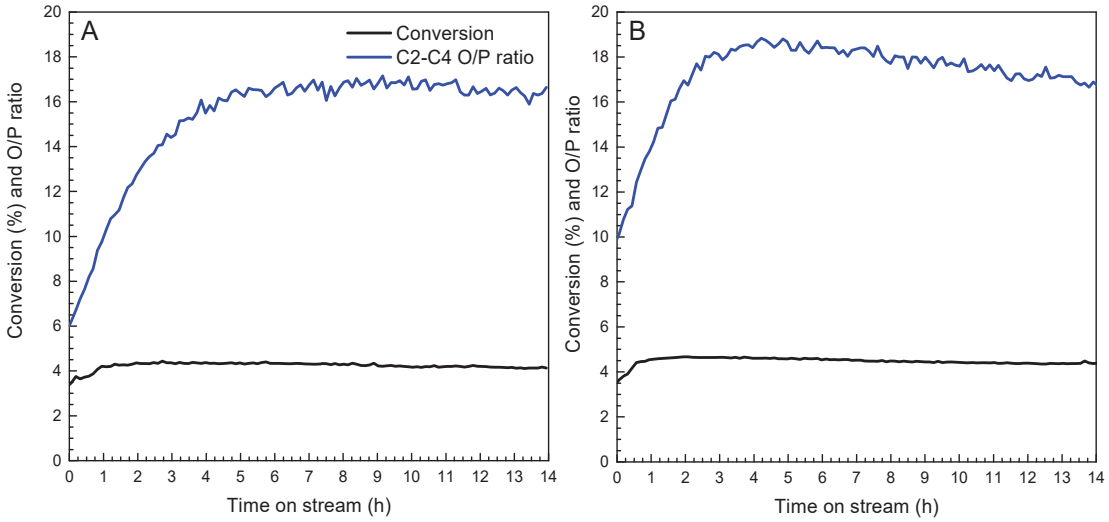

Figure 39: Evolution of the conversion and the O/P ratio with time on stream for A) MnO_x-pore+SAPO-sK and B) MnO_x-pore+SAPO-sk-SM. Reaction conditions: m (MnO_x-pore) =270 mg, m (SAPO-sK) =30 mg, P=25 bar, T=410 °C, $H_2/CO/N_2$=60/30/10, WHSV 87 $mL.min^{-1}.g^{-1}$.

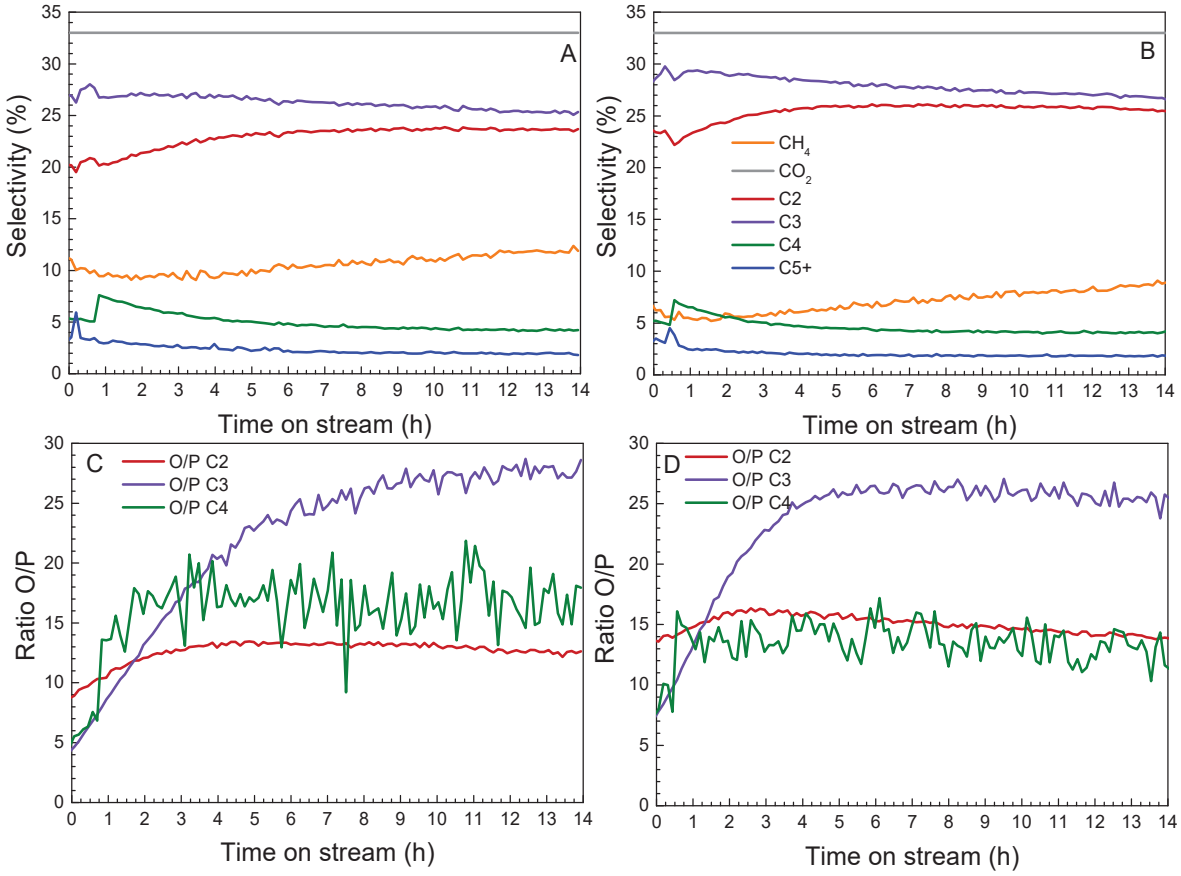

Figure 40: Evolution of the hydrocarbon and CO_2 selectivity with time on stream for A) MnO_x-pore+SAPO-sK and B) MnO_x-pore+SAPO-sk-SM and the O/P ratio for C2, C3 and C4 hydrocarbons with time on stream for C) MnO_x-pore+SAPO-sK and D) MnO_x-pore+SAPO-sk-SM. Reaction conditions: m (MnO_x-pore) =270 mg, m (SAPO-sK) =30 mg, P=25 bar, T=410 °C, $H_2/CO/N_2$=60/30/10, WHSV 87 $mL.min^{-1}.g^{-1}$.

Those results suggest that a specific property of the catalyst mixture, initially different between the two solids, converges with time. SEM images of MnO_x-pore+SAPO-sK mixture were recorded right after activation under H_2. **Figure 41A** shows the presence of well-defined zeotype aggregates of ca 100-200 μm size, that seems to be covered by MnO_x primary particles, it is confirmed by the zoom in **Figure 41A**. **Figure 41B** shows a zoom of another zeotype aggregate that is also covered by MnO_x primary particles. Conversely, only few SAPO-sK crystals were distinguished among MnO_x primary particles of MnO_x aggregates (**Figure S1B**). Hence, SEM analysis revealed that intimacy of MnO_x-pore+SAPO-sK mixture after activation was similar to that of the fresh state.

SEM images were also recorded after 2 h on stream: large aggregates of zeotype are still visible as shown in **Figure 42A**. However, they seem to begin to lose their shape as revealed by **Figure 42B**: SAPO-sK crystals begin to separate from each other and the transition with MnO_x domains is less sharp. As shown in **Figure S2A**, more zeotype crystals are dispersed inside the MnO_x domains. However, some domains of pure MnO_x are still visible as shown in **Figure S2B**. Those images suggest that a textural evolution takes place under stream improving intimacy and it is a slow phenomenon.

Finally, SEM images were recorded after 14 h on stream for both MnO_x-pore+SAPO-sK and MnO_x-pore+SAPO-sK-SM. It appears that the intimacy of MnO_x-pore+SAPO-sK mixture greatly improved with time on stream: no zeotype aggregates are still observed and only a homogeneous powder is visible at the 100 µm scale as shown in **Figure 43A**. **Figure 43B** and **Figure S3** clearly show that the powder is composed of SAPO-sK crystals well dispersed among MnO_x agglomerate (see the red circles). Hence, a high intimacy was obtained for MnO_x-pore+SAPO-sK mixture. Such intimacy is similar to that of the fresh MnO_x-pore+SAPO-sK-SM. Note that the intimacy of MnO-pore+SAPO-sK-SM is similar after 14 h on stream and right after calcination: as shown in **Figure 44** no specific aggregates could be identified while some SAPO-sK crystals were well dispersed in the MnO_x powder.

The temporal evolution of the O/P ratio and the value reached after 14 h could be related to the evolution of intimacy. Indeed, improvement of intimacy probably decreases the diffusion path of methanol toward the zeotype and of olefins outward it. However, the methanol conversion is not limited by diffusion inside the zeotype aggregate, otherwise the conversion should increase as a function of time on stream which is not observed experimentally. The apparent syngas consumption rate is kinetically limited by the formation of methanol on the oxide and not by the diffusion of methanol. In a similar manner, because the oxide aggregates do not change in size under stream, selectivity related to the oxide is not affected. Here, the methanol diffusion flow inside of the oxide is not modified and thus the methane selectivity is not impacted by the intimacy evolution that occurs on the zeotype.

Those explanations are in accordance with the experimental data since no significant evolution of conversion and of methane selectivity was evidenced. On the other hand, the improvement of intimacy leads to a decrease of the contact time of the olefins with the zeotype. This helps to reduce the proportion of olefins that is converted into paraffins and hence to improve the O/P ratio. However the intimacy reached after 14 h on stream seems to not be the optimum as a maximal value of O/P, higher that the value at 14 h for both solid, is obtained after 4 h under stream with MnO_x-pore+SAPO-sK. Such maxima do not exist with MnO_x-pore+SAPO-sK-SM suggesting that this level of intimacy is not an optimum. Intermediate intimacy between fresh MnO_x-pore+SAPO-sK and MnO_x-pore+SAPO-sK-SM should give better results. Confirming results can be found in the literature were both the oxide and zeolite particle size are modified. Such work was done by Ding and coll. [41]who studied the MnO_x/SAPO-34 system with grain size ranging from 900 µm to 200 µm (we do not consider the result for the 50-20 nm mix due to a lack of preparation description and MEB/TEM image confirming that such intimacy is effectively obtained with a combination of sieving and hand shaking). They observed an improvement of the O/P confirming such link. It is worth noting that their SAPO-34 aggregates kept their shape under stream unlike ours.

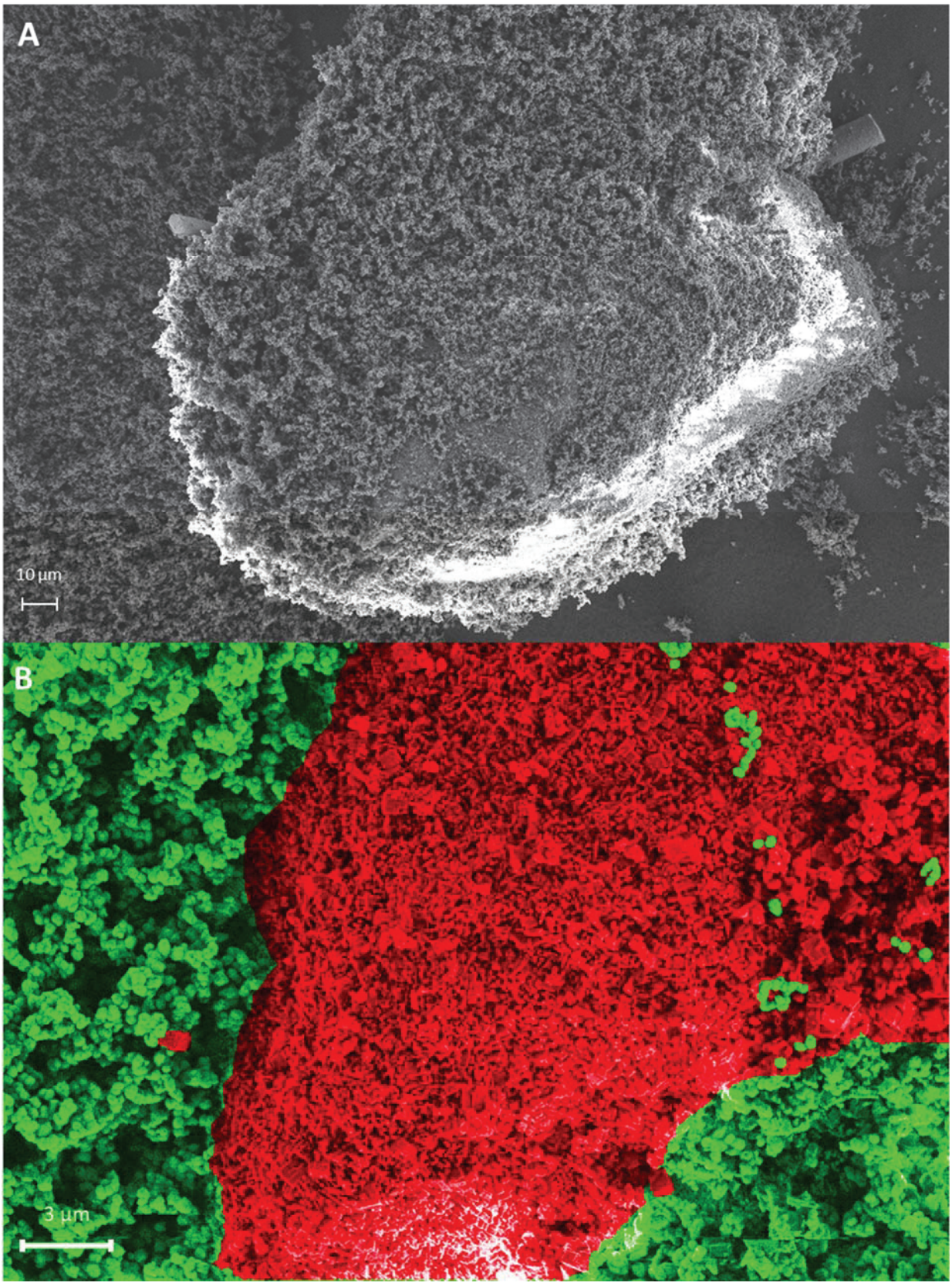

Figure 41: 90%MnO_x-pore+10%SAPO-sK mixture after activation under 20 nml/min of H_2 at 430 °C for 4 h A) a zeotype aggregate, B) zoom on the zeotype aggregate exposed surface. Colored with MnO-pore in green and SAPO-sK in red

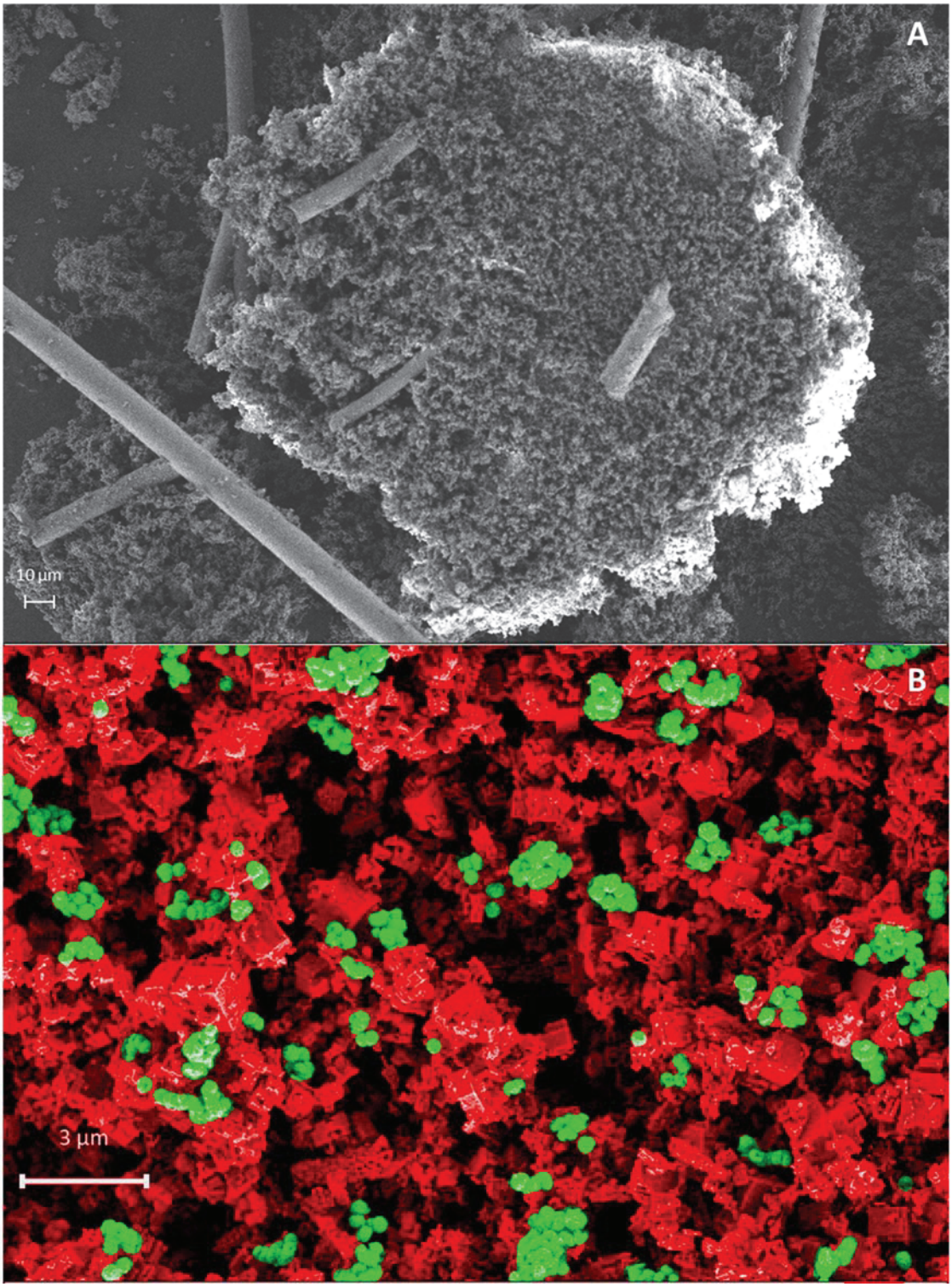

Figure 42: 90%MnO_x-pore+10%SAPO-sK mixture after activation under 20 nml.min^{-1} of H_2 at 430 °C for 4 h and 2 h on stream, A) zeotype aggregate, the needles correspond to quart wool added to the catalytic bed B) zoom on the zeotype aggregate showing the beginning of the aggregate structure deterioration. Colored with MnO-pore in green and SAPO-sK in red. Reaction conditions: m (MnO_x-pore) =270 mg, m (SAPO-sK)=30 mg, P=25 bar, T=410 °C, H_2/CO/N_2=60/30/10, WHSV 87 mL.min^{-1}.g^{-1}. Picture were taken after 2 h on stream.

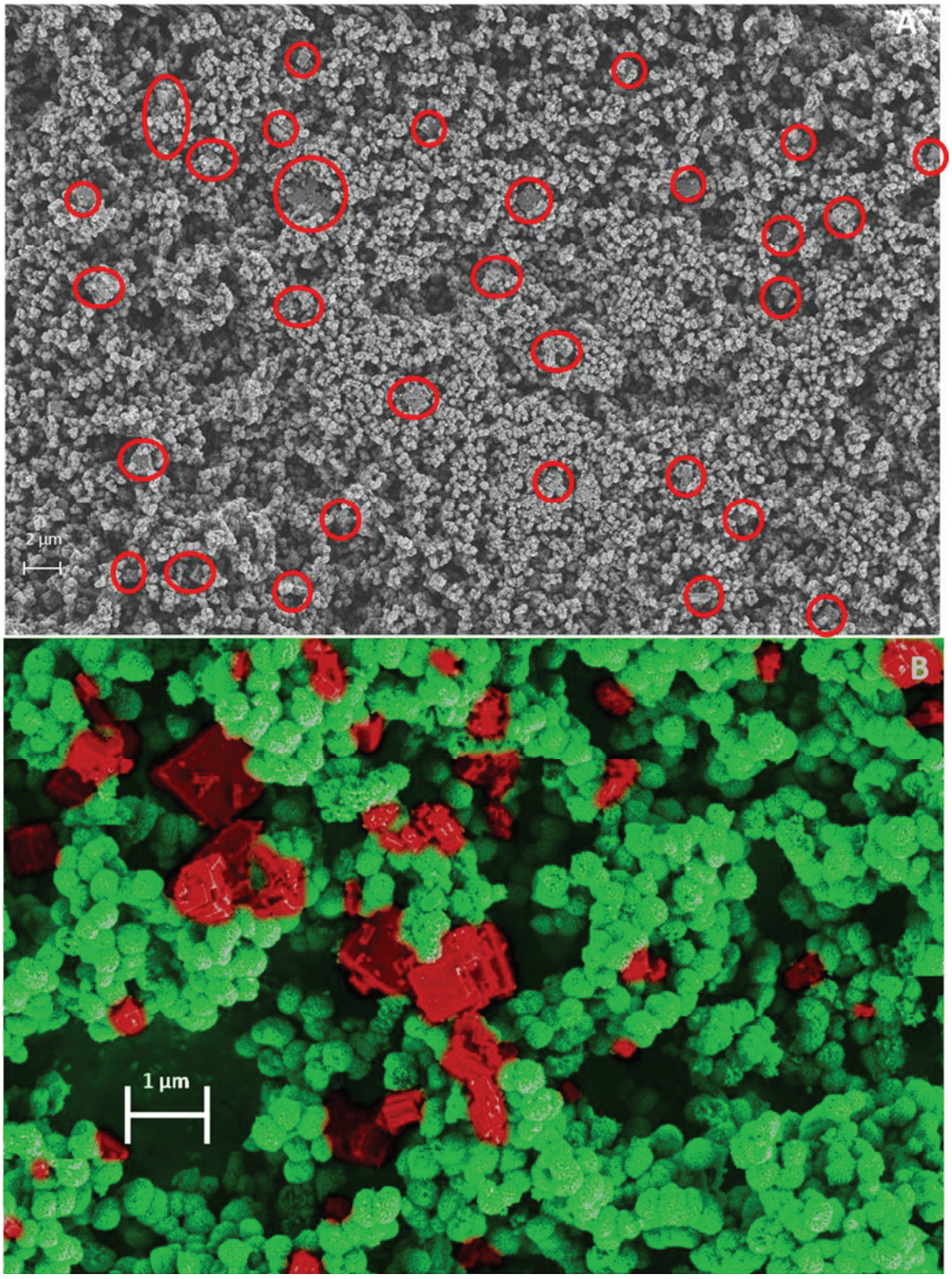

Figure 43: 90%MnO_x-pore+10%SAPO-sK mixture after activation under 20 nml.min^{-1} of H_2 at 430 °C for 4 h and 14 h on stream, A) zoom on the mixed aggregate showing high dispersion of zeotype crystals, B) zoom on dispersed zeotype crystals. Colored with MnO-pore in green and SAPO-sK in red. Reaction conditions: m(MnO_x-pore)=270 mg, m(SAPO-sK)=30 mg, P=25 bar, T=410 °C, H_2/CO/N_2=60/30/10, WHSV 87 mL.min^{-1}.g^{-1}. Data were taken after 14 h on stream.

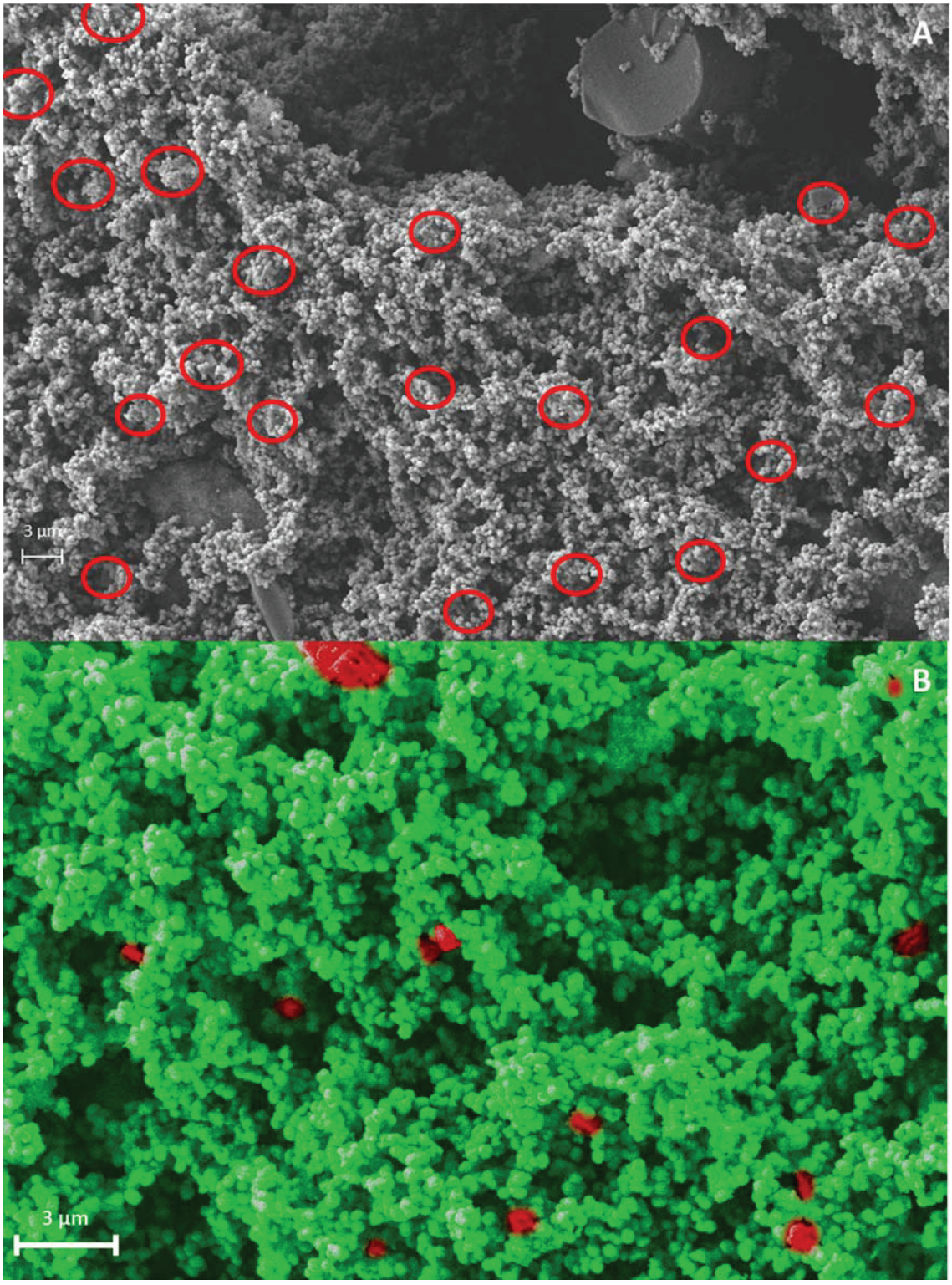

Figure 44: 90%MnO_x-pore+10%SAPO-sK-SM mixture after activation under 20 nml.min^{-1} of H_2 at 430 °C for 4 h and 14 h on stream, A) zeotype crystals highly dispersed in the oxide, B) zoom on dispersed zeotype crystals. Colored with MnO-pore in green and SAPO-sK in red. Reaction conditions: m (MnO_x-pore) =270 mg, m (SAPO-sK) =30 mg, P=25 bar, T=410 °C, H_2/CO/N_2=60/30/10, WHSV 87 mL.min^{-1}.g^{-1}. Data were taken after 14 h on stream.

5) Beyond intimacy

The previous experiments have shown that high intimacy is needed to increase the O/P ratio. However, the decrease in the interfunction distance and the increase in contact density could potentially favor formation of a new site by solid-state diffusion of Mn species into the SAPO-34 micropores leading to a partially ion-exchanged zeotype. Therefore, H-SAPO-34 ion exchanged with manganese was prepared and tested in order to check possible effect of Mn migration into zeolite.

5.1) SAPO-34 ionic exchange

The ionic exchange of SAPO-sK was carried out by dispersing a calcinated H-SAPO-sK sample into a manganese sulfate solution.

5.1.1) Preparation

The protocol was inspired by literature works.[42,43] 0.5 g of SAPO-sK were re-dispersed into 25 ml of 0.05 M $MnSO_4$. The suspension was kept at room temperature under stirring for 24 h before being centrifuged (3500 rpm) and dried at 100 °C overnight. Later on, the obtained solid was calcined at 550 °C for 6 h to decompose sulfate anions which might remain in the structure. The obtained solid is denoted SAPO-Mn in the following.

The XRD diffractogram of SAPO-Mn is compared with the diffractogram of SAPO-sK in **Figure 45**. It reveals that the SAPO-34 structure was retained after the ionic exchange. No significant peak shift was observed as reported in the literature.[42–44] Moreover, no diffraction peaks of any manganese oxides was observed. An FX elemental analysis confirmed that 0.8% wt. of Mn was present in the solid.

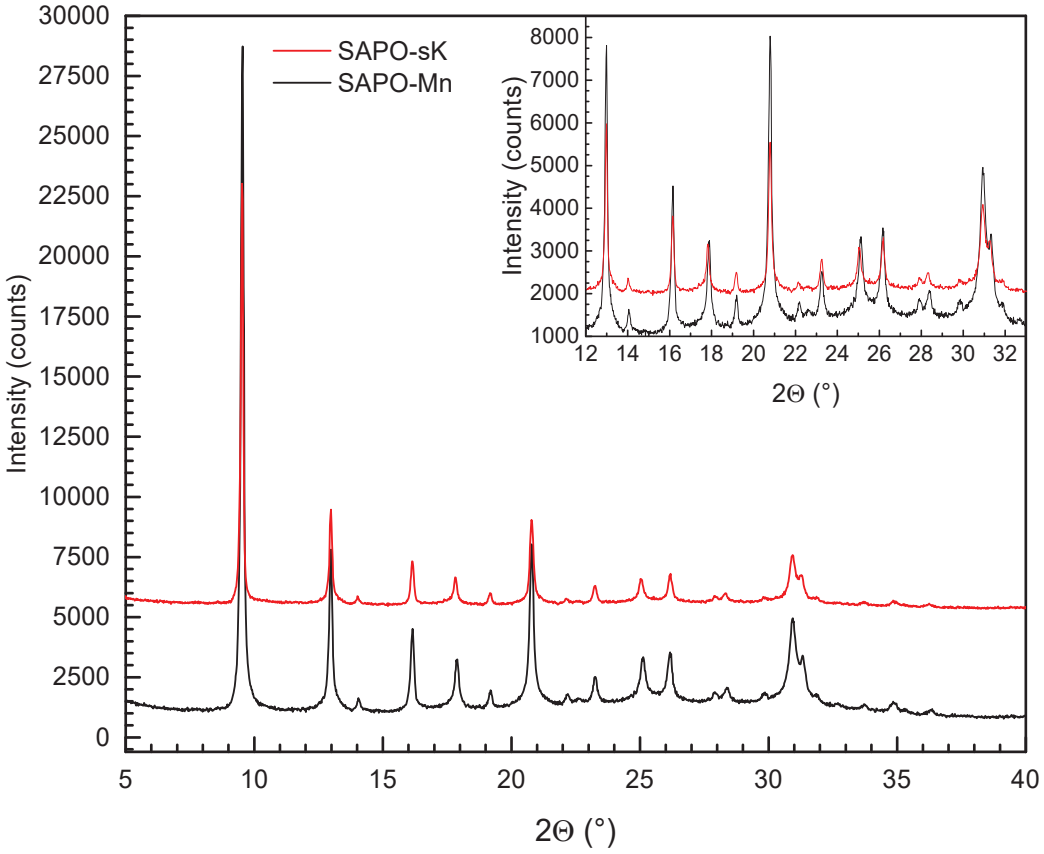

Figure 45: Comparison of XRD patterns of SAPO-Mn and SAPO-sK samples after calcination.

5.2) Catalytic results

300 mg of SAPO-Mn were tested in the standard conditions (P=25 bar, T=410 °C, $H_2/CO/N_2$=60/30/10, WHSV 87 $mL.min^{-1}.g^{-1}$) and the catalytic result is depicted in **Figure 46**. A conversion of only 1% was obtained which is close to the value measured during a blank test (see Chapter 2, Part 3.5). The O/P ratio was 0.87 and the selectivity values were as follows: 46.6% for CH_4, 33.0% for CO_2, 13.3% for C2, 6.3% for C3, 0.9 for C4+. The O/P ratio for C2, C3 and C4 hydrocarbons were 0.9, 0.9 and 0.2, respectively.

From those results, one can conclude that the SAPO-Mn is inactive for the OX-ZEO process and that no new active site is formed during reaction by diffusion of Mn species into the SAPO-34 structure. Probably, Mn ions incorporated in the SAPO structure do not bear hydrogenating properties necessary to convert syngas. The two active sites for the conversion of syngas into light olefins are definitely the MnO_x surface and the acid sites of the SAPO-34 crystals. Such results have been confirmed by Ding and coll. [41] who quantified migration of Mn within SAPO-34. It was shown

that such migration was negligible. However it has been shown that for the $ZnCrO_x$/SAPO-34 system migration of Zn ions occurs in non-negligible quantity decreasing the Brønsted acid site density in the SAPO-34. This migration was related to an increase in hydrogenation properties and a decrease in O/P ratio. Thus the importance and impact of the metal migration in the oxide should be studied for every system to get a better understanding of the Ox-Zeo activity.

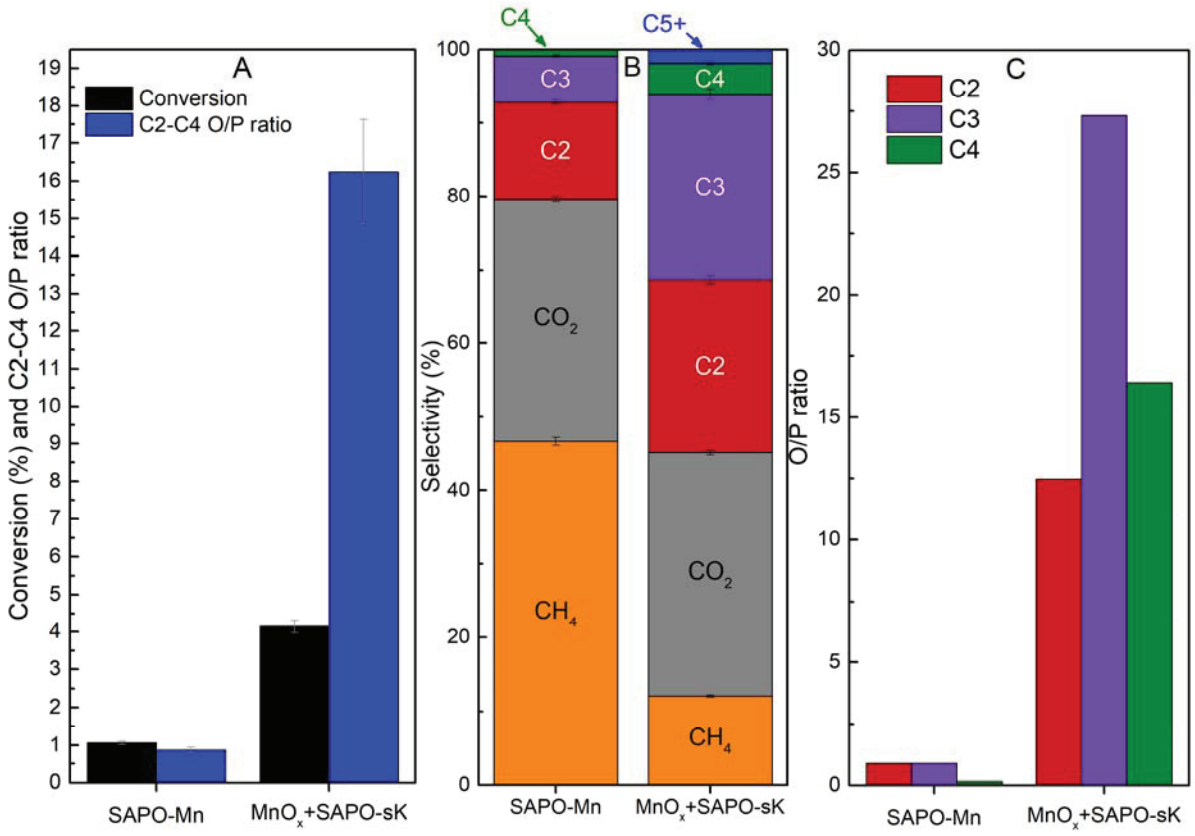

Figure 46: A) Conversion and C2-C4 O/P ratio, B) CO_2, CH_4 and hydrocarbon selectivity and C) O/P ratio for C2, C3 and C4 hydrocarbons for SAPO-Mn and MnO_x-pore+SAPO-sK. Reaction conditions: either m (SAPO-Mn) = 300 mg or, m (MnOx-pore) =270 mg, m (SAPO-sK) =30 mg, P=25 bar, T=410 °C, H_2/CO/N_2=60/30/10, WHSV 87 mL.min^{-1}.g^{-1}. Data were taken after 14 h on stream.

6) Conclusion

In this chapter, we have studied the intimacy at various scales. At the millimeter scale, probed through different bed arrangements, the effects of intimacy are strong. The conversion and hydrocarbons selectivity are improved by decreasing the interfunction distance achieved by suppressing the spacing between the layers and by increasing the number of layers. Clearly, the

millimeter scale defines a superior limit of the interfunction distance. At this distance the cooperation between MnO_x and SAPO-34 is insufficient and should be improved.

The micrometer scale has been probed through bed dilution by inert SiO_2 and its effect is more discrete. Progressive dilution first increases the methane selectivity and then decreases the O/P ratio and finally decreases the total conversion. High dilution is needed to impact the two later parameters. Hence, no dilution is required to get good cooperation between the MnO_x and SAPO-34 and high catalytic performances.

The nanoscale intimacy has been studied by preparing and testing $MnO@SiO_2$ core-shell structures with different shell thicknesses. All these structures exhibited degraded catalytic properties (lower CO conversion, O/P ratio and C2+ hydrocarbon selectivity) which are close to those of MnO_x alone. We assume that the shell is not permeable enough to allow the diffusion of methanol, thus degrading the conversion. Further work is needed to get mesoporous shell and to better study the nanoscale intimacy. However, the reaction scheme drawn from the results of Chapter 3 suggests that the closer the MnO_x and SAPO-34 functions, the better the catalytic performances.

In that regard, we have shown that the intimacy of a mechanical mixture composed of MnO_x and SAPO-34 agglomerates improves during the first 14 h on stream with dispersion of SAPO-34 crystal among MnO_x primary particles. The increase of O/P ratio with time on stream seems to be related to this improvement. After 14 h, the intimacy reached was close to that obtained for a suspension, mixture leading to similar catalytic properties. It clearly shows that high intimacy at the micrometer scale is required to get high performances for the Ox-Zeo process and intimacy optimization is further needed.

7) References

1. Coudercy, C., L'hospital, V., Checa, R., Le Valant, A., Afanasiev, P. & Loridant, S. On the reaction mechanism of MnO_x/SAPO-34 bifunctional catalysts for the conversion of syngas to light olefins. *Catal. Sci. Technol.* **11**, 7844–7849 (2021).
2. Su, J., Wang, D., Wang, Y., Zhou, H., Liu, C., Liu, S., Wang, C., Yang, W., Xie, Z. & He, M. Direct Conversion of Syngas into Light Olefins over Zirconium-Doped Indium(III) Oxide and SAPO-34 Bifunctional Catalysts: Design of Oxide Component and Construction of Reaction Network. *ChemCatChem* **10**, 1536–1541 (2018).
3. Zhu, Y., Pan, X., Jiao, F., Li, J., Yang, J., Ding, M., Han, Y., Liu, Z. & Bao, X. Role of Manganese Oxide in Syngas Conversion to Light Olefins. *ACS Catal.* **7**, 2800–2804 (2017).
4. Liu, X., Zhou, W., Yang, Y., Cheng, K., Kang, J., Zhang, L., Zhang, G., Min, X., Zhang, Q. & Wang, Y. Design of efficient bifunctional catalysts for direct conversion of syngas into lower olefins *via* methanol/dimethyl ether intermediates. *Chem. Sci.* **9**, 4708–4718 (2018).
5. Liu, X., Wang, M., Yin, H., Hu, J., Cheng, K., Kang, J., Zhang, Q. & Wang, Y. Tandem Catalysis for Hydrogenation of CO and CO_2 to Lower Olefins with Bifunctional Catalysts Composed of Spinel Oxide and SAPO-34. *ACS Catal.* **10**, 8303–8314 (2020).
6. Cheng, K., Gu, B., Liu, X., Kang, J., Zhang, Q. & Wang, Y. Direct and Highly Selective Conversion of Synthesis Gas into Lower Olefins: Design of a Bifunctional Catalyst Combining Methanol Synthesis and Carbon–Carbon Coupling. *Angew. Chem.* **128**, 4803–4806 (2016).
7. Jiao, F., Li, J., Pan, X., Xiao, J., Li, H., Ma, H., Wei, M., Pan, Y., Zhou, Z., Li, M., Miao, S., Li, J., Zhu, Y., Xiao, D., He, T., Yang, J., Qi, F., Fu, Q. & Bao, X. Selective conversion of syngas to light olefins. *Science* **351**, 1065–1068 (2016).
8. Zhang, P., Meng, F., Li, X., Yang, L., Ma, P. & Li, Z. Excellent selectivity for direct conversion of syngas to light olefins over a Mn–Ga oxide and SAPO-34 bifunctional catalyst. *Catal. Sci. Technol.* **9**, 5577–5581 (2019).
9. Sun, S., Zeng, H., Robinson, D. B., Raoux, S., Rice, P. M., Wang, S. X. & Li, G. Monodisperse MFe_2O_4 (M = Fe, Co, Mn) Nanoparticles. *J. Am. Chem. Soc.* **126**, 273–279 (2004).
10. Hufschmid, R., Arami, H., Ferguson, R. M., Gonzales, M., Teeman, E., Brush, L. N., Browning, N. D. & Krishnan, K. M. Synthesis of phase-pure and monodisperse iron oxide nanoparticles by thermal decomposition. *Nanoscale* **7**, 11142–11154 (2015).
11. Park, J., Lee, E., Hwang, N.-M., Kang, M., Kim, S. C., Hwang, Y., Park, J.-G., Noh, H.-J., Kim, J.-Y., Park, J.-H. & Hyeon, T. One-Nanometer-Scale Size-Controlled Synthesis of Monodisperse Magnetic Iron Oxide Nanoparticles. *Angew. Chem. Int. Ed.* **44**, 2872–2877 (2005).
12. Seo, W. S., Jo, H. H., Lee, K., Kim, B., Oh, S. J. & Park, J. T. Size-Dependent Magnetic Properties of Colloidal Mn3O4 and MnO Nanoparticles. *Angew. Chem. Int. Ed.* **43**, 1115–1117 (2004).
13. Zhang, H., Jing, L., Zeng, J., Hou, Y., Li, Z. & Gao, M. Revisiting the coordination chemistry for preparing manganese oxide nanocrystals in the presence of oleylamine and oleic acid. *Nanoscale* **6**, 5918 (2014).
14. Lin, C.-C., Chen, C.-J. & Chiang, R.-K. Facile synthesis of monodisperse MnO nanoparticles from bulk MnO. *J. Cryst. Growth* **338**, 152–156 (2012).
15. Fu, W., Yang, H., Chang, L., Li, M., Bala, H., Yu, Q. & Zou, G. Preparation and characteristics of core–shell structure nickel/silica nanoparticles. *Colloids Surf. A: Physicochem. Eng. Asp.* **262**, 71–75 (2005).

16. Demirörs, A. F., van Blaaderen, A. & Imhof, A. Synthesis of Eccentric Titania−Silica Core−Shell and Composite Particles. *Chem. Mater.* **21**, 979–984 (2009).
17. Han, K., Zhao, Z., Xiang, Z., Wang, C., Zhang, J. & Yang, B. The sol–gel preparation of ZnO/silica core–shell composites and hollow silica structure. *Mater. Lett.* **61**, 363–368 (2007).
18. Xu, J., Deng, Y.-Q., Zhang, X.-M., Luo, Y., Mao, W., Yang, X.-J., Ouyang, L., Tian, P. & Han, Y.-F. Preparation, Characterization, and Kinetic Study of a Core–Shell Mn_3O_4@SiO_2 Nanostructure Catalyst for CO Oxidation. *ACS Catal.* **4**, 4106–4115 (2014).
19. Peng, Y.-K., Lui, C. N. P., Chen, Y.-W., Chou, S.-W., Raine, E., Chou, P.-T., Yung, K. K. L. & Tsang, S. C. E. Engineering of Single Magnetic Particle Carrier for Living Brain Cell Imaging: A Tunable T_1-/T_2-/Dual-Modal Contrast Agent for Magnetic Resonance Imaging Application. *Chem. Mater.* **29**, 4411–4417 (2017).
20. Lai, C.-W., Wang, Y.-H., Lai, C.-H., Yang, M.-J., Chen, C.-Y., Chou, P.-T., Chan, C.-S., Chi, Y., Chen, Y.-C. & Hsiao, J.-K. Iridium-Complex-Functionalized Fe3O4/SiO2 Core/Shell Nanoparticles: A Facile Three-in-One System in Magnetic Resonance Imaging, Luminescence Imaging, and Photodynamic Therapy. *Small* **4**, 218–224 (2008).
21. Ren, Y., Zhao, Y., Zhang, Y., Tang, W., Xin, X., Shen, J. & Wang, L. Facile synthesis of Au@SiO2 core–shell nanoparticles with multiple Au nanodots by a reverse microemulsion (water-in-oil) method. *Colloids Surf. A: Physicochem. Eng. Asp.* **486**, 14–20 (2015).
22. Zhang, X. F., Mansouri, S., Clime, L., Ly, H. Q., Yahia, L. 'H. & Veres, T. Fe3O4–silica core–shell nanoporous particles for high-capacity pH-triggered drug delivery. *J. Mater. Chem.* **22**, 14450 (2012).
23. Han, D. Y., Wang, C. Q., Li, D. D. & Cao, Z. B. NiO/ZnO Core-Shell Nanoparticles *In Situ* Synthesis Via Microemulsion Method. *Synthesis and Reactivity in Inorganic, Metal-Organic, and Nano-Metal Chemistry* **46**, 794–797 (2016).
24. Schladt, T. D., Graf, T. & Tremel, W. Synthesis and Characterization of Monodisperse Manganese Oxide Nanoparticles−Evaluation of the Nucleation and Growth Mechanism. *Chem. Mater.* **21**, 3183–3190 (2009).
25. Yin, M. & O'Brien, S. Synthesis of Monodisperse Nanocrystals of Manganese Oxides. *J. Am. Chem. Soc.* **125**, 10180–10181 (2003).
26. Dhaene, E., Billet, J., Bennett, E., Van Driessche, I. & De Roo, J. The Trouble with ODE: Polymerization during Nanocrystal Synthesis. *Nano Lett.* **19**, 7411–7417 (2019).
27. Dou, Q. & Ng, K. M. Synthesis of various metal stearates and the corresponding monodisperse metal oxide nanoparticles. *Powder Technol.* **301**, 949–958 (2016).
28. Zaytseva, M. P., Muradova, A. G., Sharapaev, A. I., Yurtov, E. V., Grebennikov, I. S. & Savchenko, A. G. Fe3O4/SiO2 Core Shell Nanostructures: Preparation and Characterization. *Russ. J. Inorg. Chem.* **63**, 1684–1688 (2018).
29. Zeininger, L., Portilla, L., Halik, M. & Hirsch, A. Quantitative Determination and Comparison of the Surface Binding of Phosphonic Acid, Carboxylic Acid, and Catechol Ligands on TiO_2 Nanoparticles. *Chem. Eur. J.* **22**, 13506–13512 (2016).
30. Škapin, S. D., Čadež, V., Suvorov, D. & Sondi, I. Formation and properties of nanostructured colloidal manganese oxide particles obtained through the thermally controlled transformation of manganese carbonate precursor phase. *J. Colloid and Interface Sci.* **457**, 35–42 (2015).

31. Fei, J. B., Cui, Y., Yan, X. H., Qi, W., Yang, Y., Wang, K. W., He, Q. & Li, J. B. Controlled Preparation of MnO2 Hierarchical Hollow Nanostructures and Their Application in Water Treatment. *Adv. Mater.* **20**, 452–456 (2008).
32. Zeng, Y., Prasetyo, L., Tan, S. J., Fan, C., Do, D. D. & Nicholson, D. On the hysteresis of adsorption and desorption of simple gases in open end and closed end pores. *Chem. Eng. Sci.* **158**, 462–479 (2017).
33. Wang, Z., Jiang, X., Pan, M. & Shi, Y. Nano-Scale Pore Structure and Its Multi-Fractal Characteristics of Tight Sandstone by N2 Adsorption/Desorption Analyses: A Case Study of Shihezi Formation from the Sulige Gas Filed, Ordos Basin, China. *Minerals* **10**, 377 (2020).
34. Cychosz, K. A. & Thommes, M. Progress in the Physisorption Characterization of Nanoporous Gas Storage Materials. *Engineering* **4**, 559–566 (2018).
35. Nour, E. M., Teleb, S. M., AL-Khsosy, N. A. & Refat, M. S. A Novel Method for the Synthesis of Metal Carbonates. I. Synthesis and Infrared Spectrum of Manganese Carbonate, $MnCO_3.H_2O$, Formed by the Reaction of Urea with Manganese(II) Salts. *Synthesis and Reactivity in Inorganic and Metal-Organic Chemistry* **27**, 505–508 (1997).
36. Li, Z. & Zhu, Y. Surface-modification of SiO2 nanoparticles with oleic acid. *Applied Surface Science* **211**, 315–320 (2003).
37. Buscaglia, M. T., Bassoli, M., Buscaglia, V. & Alessio, R. Solid-State Synthesis of Ultrafine BaTiO3 Powders from Nanocrystalline BaCO3 and TiO2. *J. Am. Ceram. Soc.* **88**, 2374–2379 (2005).
38. Buscaglia, M. T., Bassoli, M., Buscaglia, V. & Vormberg, R. Solid-State Synthesis of Nanocrystalline $BaTiO_3$: Reaction Kinetics and Powder Properties. *J. Am. Ceram. Soc.* **91**, 2862–2869 (2008).
39. Tan, J., Liu, Z., Bao, X., Liu, X., Han, X., He, C. & Zhai, R. Crystallization and Si incorporation mechanisms of SAPO-34. *Micropor. Mesopor. Mater.* **53**, 97–108 (2002).
40. Li, N., Jiao, F., Pan, X., Ding, Y., Feng, J. & Bao, X. Size Effects of ZnO Nanoparticles in Bifunctional Catalysts for Selective Syngas Conversion. *ACS Catal.* **9**, 960–966 (2019).
41. Ding, Y., Jiao, F., Pan, X., Ji, Y., Li, M., Si, R., Pan, Y., Hou, G. & Bao, X. Effects of Proximity-Dependent Metal Migration on Bifunctional Composites Catalyzed Syngas to Olefins. *ACS Catal.* **11**, 9729–9737 (2021).
42. Yang, X., Wu, Z., Moses-Debusk, M., Mullins, D. R., Mahurin, S. M., Geiger, R. A., Kidder, M. & Narula, C. K. Heterometal Incorporation in Metal-Exchanged Zeolites Enables Low-Temperature Catalytic Activity of NO_x Reduction. *J. Phys. Chem. C* **116**, 23322–23331 (2012).
43. Huang, L., Wang, X., Yao, S., Jiang, B., Chen, X. & Wang, X. Cu–Mn bimetal ion-exchanged SAPO-34 as an active SCR catalyst for removal of NO from diesel engine exhausts. *Catal. Commun.* **81**, 54–57 (2016).
44. Hong, M., Li, S., Funke, H. F., Falconer, J. L. & Noble, R. D. Ion-exchanged SAPO-34 membranes for light gas separations. *Micropor. Mesopor. Mater.* **106**, 140–146 (2007).

8) Supplementary

Equation S3: Free silica proportion determination

$$x_{Si}^{f} = x_{Si}^{T} - x_{Si}^{CS}$$

$$x_{Si}^{CS} = x_{Mn}^{T} * \frac{Si}{Mn}^{CS}$$

$$x_{Si}^{f} = x_{Si}^{T} - x_{Mn}^{T} * \frac{Si}{Mn}^{CS}$$

$$x_{SiO2}^{f} = x_{Si}^{f} * \frac{M_{SiO2}}{M_{Si}}$$

Equation S4: Determination of the TEOS mass from the shell thickness

$$m_{TEOS} = M_{TEOS} * n_{TEOS}$$

$$n_{SiO2} = n_{TEOS}$$

$$n_{SiO2} = \frac{m_{SiO2}}{M_{SiO2}}$$

$$m_{SiO2} = V_{SiO2} * \rho_{SiO2}$$

$$V_{SiO2} = V_{CS} - V_{C} = \frac{4}{3}\pi((W_S + R_C)^3 - R_C^3)$$

$$m_{TEOS} = \frac{M_{TEOS}}{M_{SiO2}} * \frac{4\pi\rho_{SiO2}}{3} * ((W_S + R_C)^3 - R_C^3)$$

With

x_i^j: mass proportion of i in j. i being either Si, Mn or SiO_2 and j being either T, for the global proportion, or CS for the core-shell structure,

x_i^f: mass proportion of free i either Si or SiO_2,

M_i: molar mass in g/mol of i, i being either Si, SiO_2 or TEOS,

$\frac{Si}{Mn}^{CS}$: ratio of mass proportion in the core-shell structure,

m_i: mass in gram of i with i being either TEOS or SiO_2,

n_i: quantity of matter in mol of i. i being either TEOS or SiO_2,

V_i: volume in ml of i. i being either SiO_2, CS for core-shell or C for Core,

ρ_{SiO2}: density of dense SiO_2 g/ml,

R_C: radius of the core in nm,

W_S: width of the shell in nm.

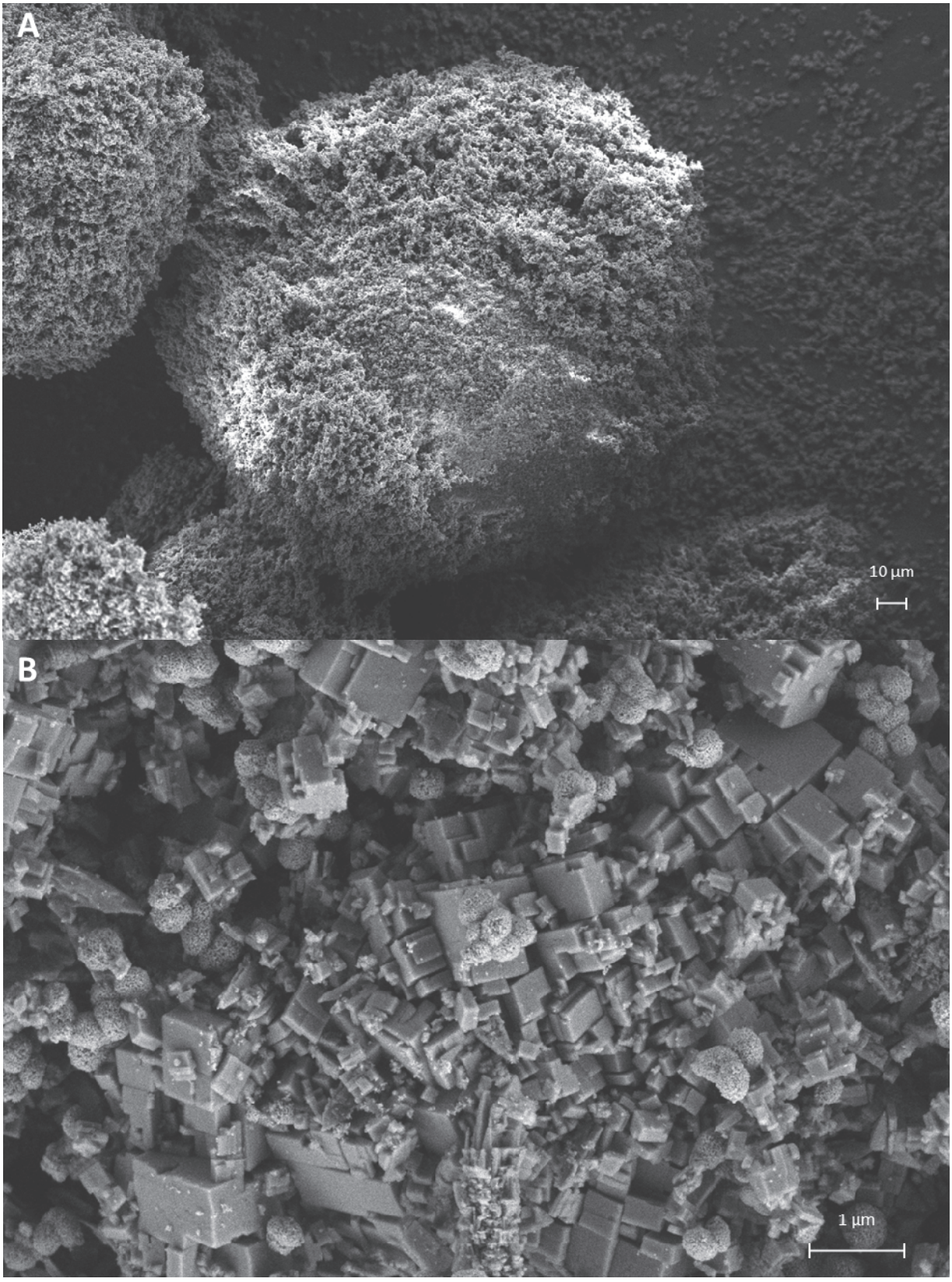

Figure S1 : freshly prepared 90%MnOx-pore+10%SAPO-sK mixture, zoom on a zeotype aggregate, A) Zoom on the zeotype aggregate at the down right corner of Figure 36A), B) Exposed zeotype aggregate surface.

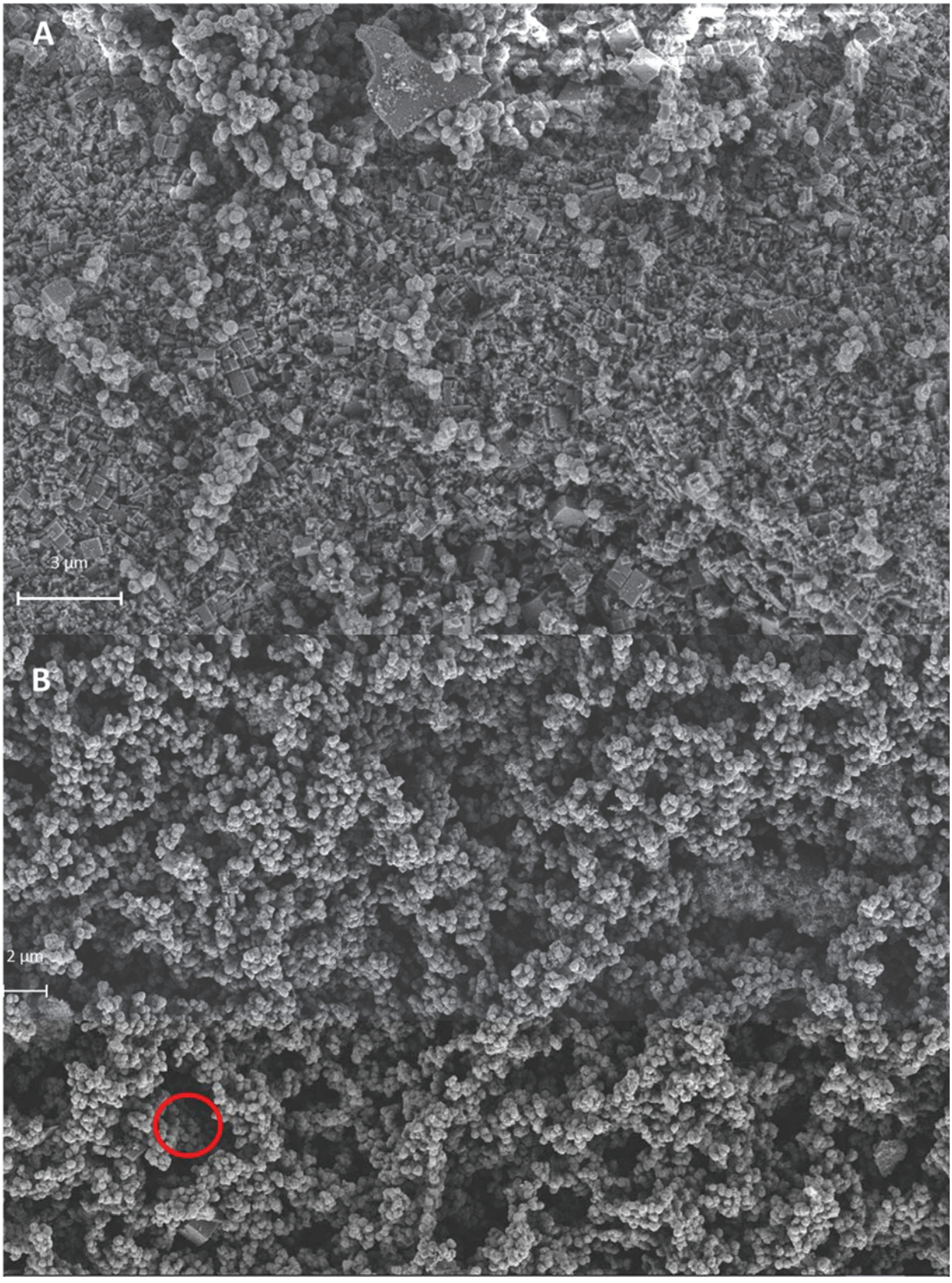

Figure S2 : 90%MnOx-pore+10%SAPO-sK mixture after activation under 20 nml.min-1 of H2 at 430 °C for 4 h A) zoom on the zeotype aggregate exposed surface B) oxide domain with small quantity of zeotype.

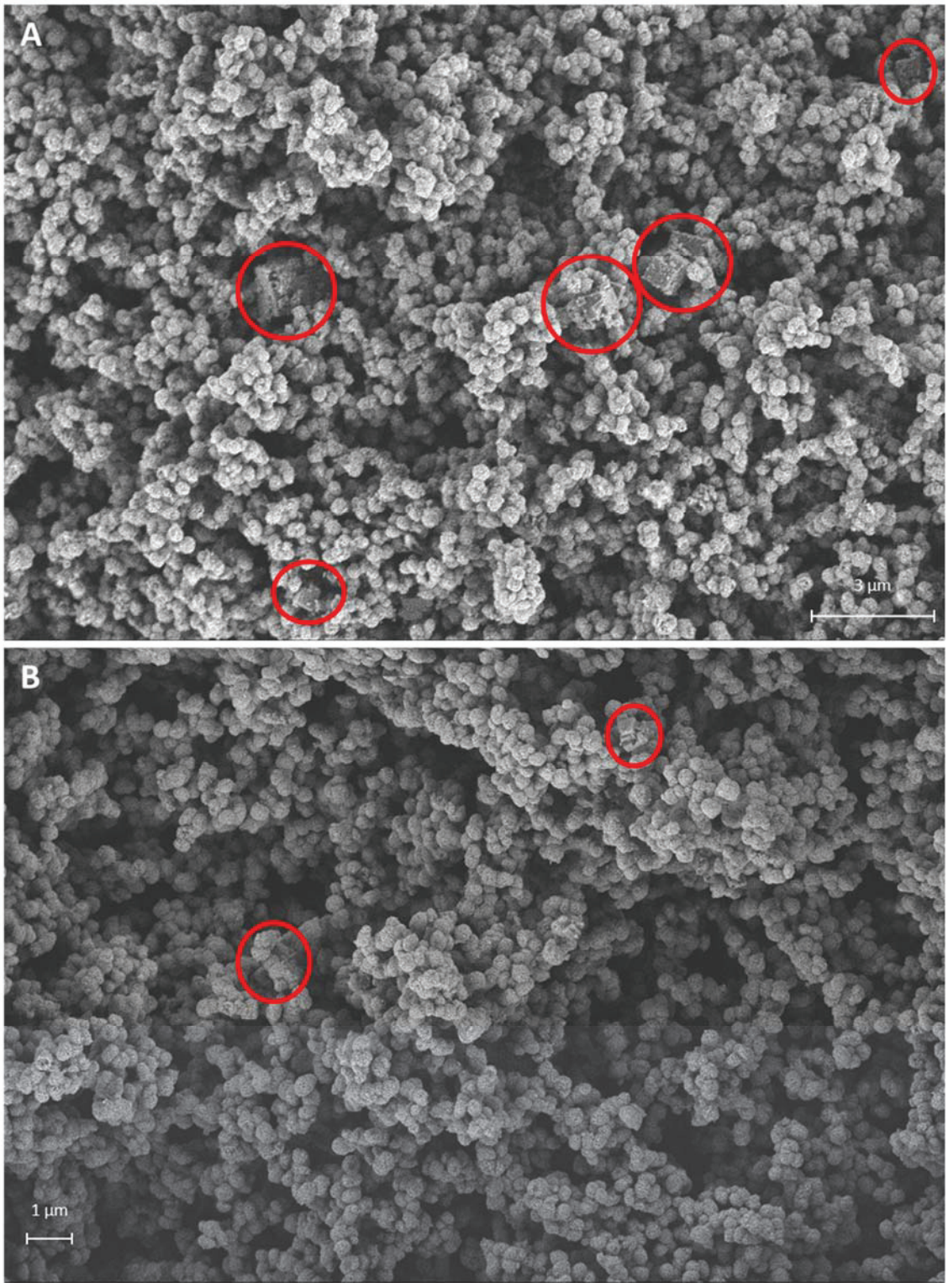

Figure S3: 90%MnOx-pore+10%SAPO-sK mixture after activation under 20 nml.min-1 of H2 at 430 °C for 4 h and 2 h on stream, A) oxide domain with dispersed zeotype crystals, B) oxide domain with small quantity of zeotype crystals. Reaction conditions: m(MnOx-pore)=270 mg, m(SAPO-sK)=30 mg, P=25 bar, T=410 °C, H2/CO/N2=60/30/10, WHSV 87 mL.min-1.g-1. Data were taken after 2 h on stream.

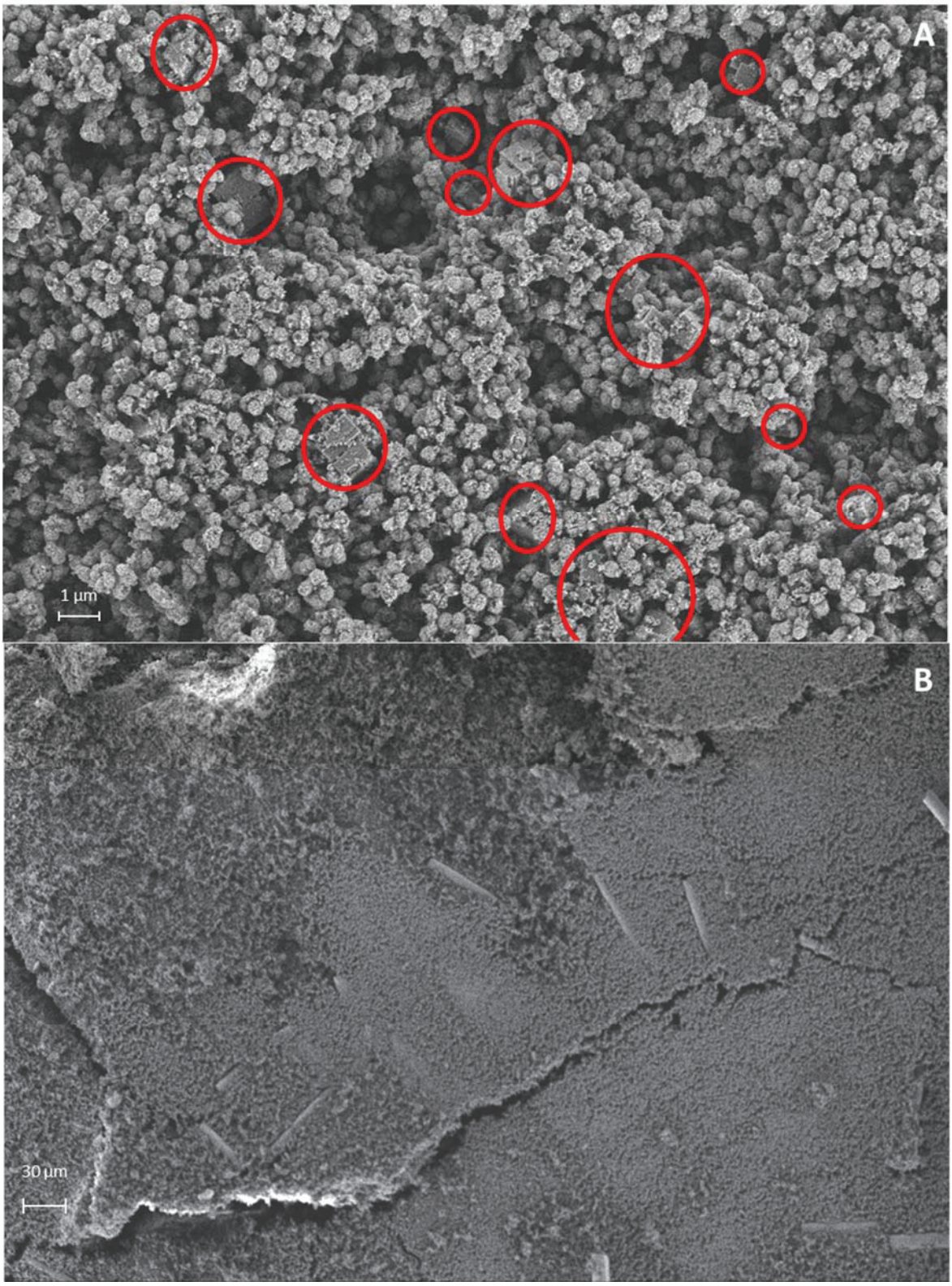

Figure S4: 90%MnOx-pore+10%SAPO-sK mixture after activation under 20 nml.min-1 of H2 at 430 °C for 4 h and 14 h on stream, A) zeotype crystals highly dispersed in the oxide, B) aggregate of oxide and zeotype. Reaction conditions: m(MnOx-pore)=270 mg, m(SAPO-sK)=30 mg, P=25 bar, T=410 °C, H2/CO/N2=60/30/10, WHSV 87 mL.min-1.g-1. Data were taken after 14 h on stream.

General conclusion and outlook

The increasing demand for light olefins and the evolution of the raw materials used for vapocracking and FCC processes lead to the development of on-purpose processes. Among them, the Ox-Zeo process appears as a promising one. Since its definition in 2016 by the Bao group[1] as a combination of a hydrogenating oxide and an acidic zeotype to selectively and stably convert syngas to light olefins, numerous papers on this process were published. The versatility of the process has been largely demonstrated using various oxide and zeotype combinations.[2,3] Beyond the search for performances, the literature highlights that numerous parameters influence catalytic properties. However the role of intimacy has been rarely addressed and only concerned the micrometer scale and above.

In this PhD work, we selected the MnO_x + SAPO-34 system previously studied by Zhu and coll.[4] as using a simple oxide and standard SAPO-34 zeotype to produce C2-C4 hydrocarbons. Before deep investigation of the role of intimacy, we studied a reference system to fix some parameters influencing catalytic properties. This study confirmed that this bifunctional system is selective to C2-C4 hydrocarbons (>60%) with a high O/P ratio (up to 9.5 for MnO-Ref+ SAPO-sK mechanical mixture).

Different reaction parameters such as the contact time, the time on stream, the activation and the reaction temperature, the Ox/Zeo balance, the CO and H_2 pressures were investigated. No effect of the activation temperature was evidenced in the investigated range (410-450 °C). The conversion is rather stable over time (small deactivation) but the O/P ratio was shown to increase slowly but significantly, before reaching a steady state. Such evolution also observed for other Ox-Zeo systems (often not commented)[1,5–8] was attributed to settling down of hydrocarbon pool within the zeotype pores. The mass ratio of zeotype in the mixture plays a crucial role. Adding small amount of SAPO-34 strongly increases the conversion. On the conversion vs. zeotype amount curve, a plateau was reached above 10-20% wt. of zeotype in the mixture. In parallel, a sharp optimum for the O/P ratio was evidenced for 5-10% of SAPO-34. The optimal amount of zeotype appears to be much lower than in the study of Zhu and coll.[4] (around 30%), which can be explained

by different properties of MnOx and SAPO-34. The conversion linearly increased with the contact while the O/P ratio strongly decreases. The same trend is observed while increasing the temperature. The apparent activation energy was 72 kJ.mol^{-1} which is close to the value reported for MTO synthesis. In that regard, experiments achieved at IC2MP clearly revealed that methanol is formed with MnO_x-Ref alone and that addition of SAPO-34 consumed methanol, leading to formation of C2-C4 olefins.[9] *In situ* DRIFT measurements revealed the presence of formate species on the oxide surface under H_2/CO flow. These species which have been reported as intermediates leading to methanol formation[5,7,10] are destabilised by the addition of SAPO-34 indicating that they are linked to the reaction intermediate. Therefore, methanol was proposed as the key intermediate for the Ox-Zeo process using MnOx+SAPO-34 system. However, minor participation of ketene cannot be ruled out, this intermediate was supposed in some oxides.[1,3,4] It appears that the key intermediate (ketene versus methanol) may vary with metal oxides and reaction conditions[3] and both mechanisms could occur in parallel.[11] Future work should focus on determining the proportions of ketene and methanol that are produced by the oxide in the Ox-Zeo conditions. It will allow to gain a better understanding of the overall process and to precisely model the catalytic properties.

The reaction order for the production of olefins with respect to H_2 was determined to be 0.5. It suggests that the dissociation of H_2 or reaction of dissociated species is a limiting step in methanol formation. It supports the strategy used in the literature for the development of new Ox-Zeo system by preparing mixed oxides containing elements such as Zn[5,12–15] or Ga [6,16] which favour H_2 dissociation. The strong increase in conversion and C2+ yield observed after adding SAPO-34 to MnOx was explained by a shift of thermodynamic equilibrium of the intermediate formation from syngas. The associated decrease in CH_4 selectivity probably arises from a C-C coupling in the zeotype pores much faster than hydrogenation of methanol to CH_4 over MnOx.

By comparison of catalytic properties obtained combining MnO_x-Ref with four different SAPO-34, we also confirm that olefins can be hydrogenated within the zeotype and that its acidic sites strongly affect the O/P ratio.[7,13,17] In the future, a comprehensive investigation of the role of acidity (nature, strength, density) on the reaction mechanism within SAPO-34 should be undertaken.

The major drawback of the Ox-Zeo process is its high CO_2 selectivity (35-45%).[2,3] For the MnOx+SAPO-34 system, a CO_2 selectivity around 30% was obtained. It seems to be related to relatively harsh reaction conditions (T=410 °C, P=25 bar) needed to convert syngas but simultaneously promoting the Water-Gas-Shift (WGS) reaction, as far as water becomes present in the system due to C-C coupling reaction and CH_4 formation.[5] In fact, the WGS reaction would allow for the formation of CO_2 in these conditions without necessarily reaching the equilibrium depending on the oxide used.[7] In agreement with this hypothesis we observed that the CO_2 selectivity does not vary with the contact time, but increases with the CO pressure and decreases with that of H_2. For future development, oxides able to convert syngas at lower temperature and pressure are needed to avoid WGS and decrease the CO_2 selectivity.

Finally, we confirmed that the Ox-Zeo process is stable, with quite low coking after tens of hours on stream. This major difference as compared with the MTO synthesis could arise from the presence of both H_2 and CO in the feed. In that regard, it was recently proposed that H_2, CO and CO_2 modify the MTO process within the zeotype.[18,19]

Based on this reference study on the Ox-Zeo process, the activation and reaction conditions were fixed to investigate the effect of intimacy through the distance between the two functions. This investigation encompassed several scales of spatial proximity between two catalytic phases, from macroscopic to nanoscopic.

In the framework of the ANR INCH project, catalytic properties of different bed arrangements of MnOx-Ref and SAPO-K were studied at IC2MP. A significant increase in conversion was obtained increasing the number of layers while the O/P ratio was slightly decreased. It shows that at the millimeter scale, the distance is important and has to be sufficiently low to convert synergistically methanol produced over MnO_x into C2+ olefins within the zeotype pores.

The conversion and the O/P ratio are strongly improved for a random mechanical mixture of particles (micrometer-scale proximity), as compared with any bed arrangements. This trend was also reported for $ZnCrO_x$+MSAPO[1] and $ZnZrO_x$+SSZ-13[7] catalytic systems. Hence, intimacy at the micrometer scale is needed to optimize catalytic properties as it was confirmed by dilution by SiO_2 of MnO_x+SAPO-34 mixtures. However the first significant effect was an increase in the CH_4

selectivity for dilution around 70%. The conversion and O/P ratio decreased only for the highest dilution rate (>90%). The CH_4 formation is then prominent impeding methanol to be converted into C2+ hydrocarbons. MnO_x acts then as if it was alone. Hence, dilution should be avoided and again the best performances were obtained for the closest distance in the studied range. The "closer the better" rule is valid therefore down to few micrometer distance, which is the characteristic particle size in our systems.

We studied the nanoscale intimacy by preparing $MnO_x@SiO_2$ core-shell structures with different shell thicknesses. This part of the PhD work was arguably the hardest task since monodispersed cores, homogeneous and porous shells were required for this study. Among numerous methods tried, preparation of $MnCO_3$ porous cores followed by Stöber deposit of SiO_2 and calcination led to the best results. However, all these structures exhibited degraded catalytic properties (much lower CO conversion, O/P ratio and C2+ hydrocarbon selectivity) which were close to those of MnO_x alone. Even if microporosity of the shells can explain those results by diffusion limitation of methanol, a similar trend should be observed for mesoporous shells especially for large thicknesses since the reaction scheme strongly suggest that a quick transfer of methanol toward the zeotype pores is required to obtain high C2+ yields.

Following this principle we tried to make the particles even closer using the suspension method to mix two phases. However, catalytic performances were not improved preparing a suspension mixture in spite of improved intimacy. Interestingly, SEM images clearly evidenced a strong change of morphology of simple mechanical mixtures containing agglomerates of ca 100 μm during the first 14 h on stream. Indeed, SAPO-34 agglomerates disappear and primary crystals of half of micrometer are dispersed among MnO_x primary particles. After 14 h, the intimacy reached was close to that obtained for a suspension mixture leading to similar catalytic properties. This self-generated intimacy does not impact the conversion. However, the increase of O/P ratio with time on stream seems to be partly related to it, as suggested by the difference of evolution with time between suspension and simple mechanical mixtures. The evolution of the O/P ratio seems to arise from the hydrogenation properties of the zeotype[20–22] as de-agglomeration of SAPO-34 leads to a decrease in the diffusion path of produced olefins diminishing the proportion of olefins that are hydrogenated in the zeotypes pores. It has no effect on other catalytic properties

because the zeotype mostly convert methanol formed over MnO_x and hydrogenate the olefins. However, one cannot rule out that formation of hydrocarbon pool also modify hydrogenating properties of the zeotype. Such formation should be better characterized in future works. Textural properties of MnOx have also to be considered. Indeed, a lower conversion and higher CH_4 selectivity were obtained for MnO_x-pore compared with MnO_x-Ref. Indeed, the longer diffusion path in MnO_x-pore due to its porosity leads to preferential hydrogenation of methanol compared with C-C coupling in the zeotype pores.

As already suggested in Chapter 4, a diffusion flux must be considered instead of the distance or the diffusion path suggested in Chapter 1. The quite poor catalytic properties of MnO_x@SiO_2-40 nm combined with SAPO-K clearly illustrate this point. To go further, a diffusion flux of methanol and olefins could be determined using the Fick's law. However, it requires to determine its diffusion coefficients in reaction conditions and the difference of concentration between MnO_x and SAPO-34 which is not trivial and requires operando techniques. Such data would allow to develop a comprehensive model necessary to rationalize the effects of intimacy and design more efficient Ox-Zeo catalytic systems.

From these experiences, we obtained a glaring demonstration that the intimacy is first of all related to the diffusion flux of the reactants and not to the spatial proximity of the catalytic phase's particles. Variations of diffusion coefficient can occur in the core-shell structures, which might have much greater impact than the distance between particles (observed by microscopies).

Moreover, the distance between the functions is usually poorly defined and often only qualitatively estimated from TEM images, without any statistical treatment.[23,24] The distance distribution could be misconceived from the TEM images and lead to false results.

From the above said, we suggest that a sufficient definition should be given to the intimacy, considering both the distribution of geometric distances in the reactor and the diffusion coefficients of reactants in the respective materials that are needed to estimate the diffusion flux as it has been suggested in literature.[25] Without giving any expression of such generalised intimacy parameter, we can illustrate it to give the first intuitions in our case. Thus, the increase of intimacy in the MnO–SAPO mixtures would correspond first of all to the decrease of zeotype particle size

because the diffusion coefficient stay constant. On the contrary, in the materials containing core-shell particles, the intimacy parameter will be related primarily to the shell permeability and secondly to the thickness due to a low permeability.

References

1. Jiao, F., Li, J., Pan, X., Xiao, J., Li, H., Ma, H., Wei, M., Pan, Y., Zhou, Z., Li, M., Miao, S., Li, J., Zhu, Y., Xiao, D., He, T., Yang, J., Qi, F., Fu, Q. & Bao, X. Selective conversion of syngas to light olefins. *Science* **351**, 1065–1068 (2016).
2. Zhou, W., Cheng, K., Kang, J., Zhou, C., Subramanian, V., Zhang, Q. & Wang, Y. New horizon in C1 chemistry: breaking the selectivity limitation in transformation of syngas and hydrogenation of CO_2 into hydrocarbon chemicals and fuels. *Chem. Soc. Rev.* **48**, 3193–3228 (2019).
3. Pan, X., Jiao, F., Miao, D. & Bao, X. Oxide–Zeolite-Based Composite Catalyst Concept That Enables Syngas Chemistry beyond Fischer–Tropsch Synthesis. *Chem. Rev.* **121**, 6588–6609 (2021).
4. Zhu, Y., Pan, X., Jiao, F., Li, J., Yang, J., Ding, M., Han, Y., Liu, Z. & Bao, X. Role of Manganese Oxide in Syngas Conversion to Light Olefins. *ACS Catal.* **7**, 2800–2804 (2017).
5. Wang, S., Wang, P., Shi, D., He, S., Zhang, L., Yan, W., Qin, Z., Li, J., Dong, M., Wang, J., Olsbye, U. & Fan, W. Direct Conversion of Syngas into Light Olefins with Low CO_2 Emission. *ACS Catal.* **10**, 2046–2059 (2020).
6. Yang, G., Meng, F., Zhang, P., Yang, L. & Li, Z. Effects of preparation method and precipitant on Mn–Ga oxide in combination with SAPO-34 for syngas conversion into light olefins. *New J. Chem.* **45**, 7967–7976 (2021).
7. Liu, X., Zhou, W., Yang, Y., Cheng, K., Kang, J., Zhang, L., Zhang, G., Min, X., Zhang, Q. & Wang, Y. Design of efficient bifunctional catalysts for direct conversion of syngas into lower olefins *via* methanol/dimethyl ether intermediates. *Chem. Sci.* **9**, 4708–4718 (2018).
8. Su, J., Zhou, H., Liu, S., Wang, C., Jiao, W., Wang, Y., Liu, C., Ye, Y., Zhang, L., Zhao, Y., Liu, H., Wang, D., Yang, W., Xie, Z. & He, M. Syngas to light olefins conversion with high olefin/paraffin ratio using ZnCrOx/AlPO-18 bifunctional catalysts. *Nat Commun* **10**, 1297 (2019).
9. Coudercy, C., L'hospital, V., Checa, R., Le Valant, A., Afanasiev, P. & Loridant, S. On the reaction mechanism of MnO_x/SAPO-34 bifunctional catalysts for the conversion of syngas to light olefins. *Catal. Sci. Technol.* **11**, 7844–7849 (2021).
10. Liu, X., Wang, M., Yin, H., Hu, J., Cheng, K., Kang, J., Zhang, Q. & Wang, Y. Tandem Catalysis for Hydrogenation of CO and CO_2 to Lower Olefins with Bifunctional Catalysts Composed of Spinel Oxide and SAPO-34. *ACS Catal.* **10**, 8303–8314 (2020).
11. Huang, Z.-Q., Li, T.-H., Yang, B. & Chang, C.-R. Role of surface frustrated Lewis pairs on reduced CeO_2(110) in direct conversion of syngas. *Chinese Journal of Catalysis* **41**, 1906–1915 (2020).
12. Yuxuan Huang, Weixin Qian, Hongfang Ma, Haitao Zhang & Weiyong Ying. Impact Of Zn/Cr Ratio On Zncrox-Sapo-34 Bifunctional Catalyst For Direct Conversion Of Syngas To Light Olefins. *International Journal of Chemical, Materials and Biomolecular Sciences* **12**, 557–563 (2018).
13. Cheng, K., Gu, B., Liu, X., Kang, J., Zhang, Q. & Wang, Y. Direct and Highly Selective Conversion of Synthesis Gas into Lower Olefins: Design of a Bifunctional Catalyst Combining Methanol Synthesis and Carbon–Carbon Coupling. *Angew. Chem.* **128**, 4803–4806 (2016).
14. Kirilin, A. V., Dewilde, J. F., Santos, V., Chojecki, A., Scieranka, K. & Malek, A. Conversion of Synthesis Gas to Light Olefins: Impact of Hydrogenation Activity of Methanol Synthesis Catalyst on the Hybrid Process Selectivity over Cr–Zn and Cu–Zn with SAPO-34. *Ind. Eng. Chem. Res.* **56**, 13392–13401 (2017).

15. Raveendra, G., Li, C., Cheng, Y., Meng, F. & Li, Z. Direct transformation of syngas to lower olefins synthesis over hybrid Zn–Al_2O_3/SAPO-34 catalysts. *New J. Chem.* **42**, 4419–4431 (2018).
16. Zhang, P., Meng, F., Li, X., Yang, L., Ma, P. & Li, Z. Excellent selectivity for direct conversion of syngas to light olefins over a Mn–Ga oxide and SAPO-34 bifunctional catalyst. *Catal. Sci. Technol.* **9**, 5577–5581 (2019).
17. Wang, M., Wang, Z., Liu, S., Gao, R., Cheng, K., Zhang, L., Zhang, G., Min, X., Kang, J., Zhang, Q. & Wang, Y. Synthesis of hierarchical SAPO-34 to improve the catalytic performance of bifunctional catalysts for syngas-to-olefins reactions. *Journal of Catalysis* **394**, 181–192 (2021).
18. Huang, Y., Ma, H., Xu, Z., Qian, W., Zhang, H. & Ying, W. Direct Conversion of Syngas to Light Olefins over a $ZnCrO_x$ + H-SSZ-13 Bifunctional Catalyst. *ACS Omega* **6**, 10953–10962 (2021).
19. Xie, J., Firth, D. S., Cordero-Lanzac, T., Airi, A., Negri, C., Øien-Ødegaard, S., Lillerud, K. P., Bordiga, S. & Olsbye, U. MAPO-18 Catalysts for the Methanol to Olefins Process: Influence of Catalyst Acidity in a High-Pressure Syngas (CO and H_2) Environment. *ACS Catal.* **12**, 1520–1531 (2022).
20. Li, N., Jiao, F., Pan, X., Chen, Y., Feng, J., Li, G. & Bao, X. High-Quality Gasoline Directly from Syngas by Dual Metal Oxide–Zeolite (OX-ZEO) Catalysis. *Angew. Chem. Int. Ed.* **58**, 7400–7404 (2019).
21. Vityuk, A., Khivantsev, K., Aleksandrov, H. A., Vayssilov, G. N., Alexeev, O. S. & Amiridis, M. D. Room-Temperature Ethene Hydrogenation Activity of Transition-Metal-Free HY Zeolites. *ACS Catal.* **9**, 839–847 (2019).
22. Gounder, R. & Iglesia, E. Catalytic hydrogenation of alkenes on acidic zeolites: Mechanistic connections to monomolecular alkane dehydrogenation reactions. *Journal of Catalysis* **277**, 36–45 (2011).
23. Zecevic, J., Vanbutsele, G., de Jong, K. P. & Martens, J. A. Nanoscale intimacy in bifunctional catalysts for selective conversion of hydrocarbons. *Nature* **528**, 245–248 (2015).
24. Samad, J. E., Blanchard, J., Sayag, C., Louis, C. & Regalbuto, J. R. The controlled synthesis of metal-acid bifunctional catalysts: The effect of metal:acid ratio and metal-acid proximity in Pt silica-alumina catalysts for n-heptane isomerization. *Journal of Catalysis* **342**, 203–212 (2016).
25. Cheng, K., Wal, L. I., Yoshida, H., Oenema, J., Harmel, J., Zhang, Z., Sunley, G., Zečević, J. & Jong, K. P. Impact of the Spatial Organization of Bifunctional Metal–Zeolite Catalysts on the Hydroisomerization of Light Alkanes. *Angew. Chem. Int. Ed.* **59**, 3592–3600 (2020).

Abstract: Light olefins which are key intermediates for the petrochemical industry are produced mainly by steam cracking and catalytic cracking. The increasing demand and the evolution of the raw materials require the development of novel on-purpose processes. This is the case of the Ox-Zeo process which combines a hydrogenating oxide catalyst and an acid zeotype, generally SAPO-34, to produce light olefins, very selectively and stably. Previous studies have focused on the improvement of the properties of the oxide and the zeotype, but little attention was paid to the role of the intimacy between the two functions. The main objective of this work was to study the impact of the inter-functional distance on the catalytic properties of the MnO_x+SAPO-34 catalytic system in the Ox-Zeo process. Previous studies showed that many reaction parameters influence the catalytic properties and in particular the olefin/paraffin ratio (O/P). It was therefore necessary to fix these parameters in order to study the role of intimacy. The study of kinetic parameters associated with *in situ* DRIFT measurements allowed to better define the reaction scheme and to identify CH_3OH as a key intermediate. Then, the inter-functional distance was modulated from millimeter to atomic scale notably through catalytic bed arrangements, dilution by SiO_2, preparation of MnO_x@SiO_2 core-shell structures possessing a porous SiO_2 shell of variable thickness. It was shown that a fine mechanical mixture of MnO_x and SAPO-34 allows to obtain a higher conversion than any bed arrangements. In fact, high intimacy improves the catalytic properties and dense separation between functions decreases the conversion and selectivity to olefins. Finally, it has been shown that morphology of the mixtures evolves and intimacy is generated *in situ* during the catalyst activation and initial period of reaction, at the scale of primary MnO_x particles and SAPO-34 crystals.

Title: Role of intimacy in bifunctionnal catalysts for the production of light olefins: application to the Ox-Zeo process

Résumé : Les oléfines légères sont des intermédiaires clés pour l'industrie pétrochimique qui sont produites essentiellement par craquage à la vapeur et craquage catalytique. L'augmentation croissante de la demande et l'évolution des matières premières nécessite de développer des procédés dédiés. C'est le cas du procédé Ox-Zeo qui combine un catalyseur oxyde hydrogénant et un zéotype acide, généralement la SAPO-34 pour produire très sélectivement et de manière stable les oléfines légères. Les études précédentes ont porté essentiellement sur l'amélioration des propriétés de l'oxyde et du zéotype et peu sur rôle de l'intimité entre les deux fonctions. L'objectif principal de ce travail était d'étudier l'impact de la distance inter-fonction sur les propriétés catalytiques du procédé Ox-Zeo. Il s'est focalisé sur le système catalytique MnOx+SAPO-34. Une étude préalable a montré que de nombreux paramètres de réaction influent sur les propriétés catalytiques et notamment le rapport oléfines/paraffines (O/P). Il convenait donc de fixer ces paramètres pour pouvoir étudier le rôle de l'intimité. L'étude de paramètres cinétiques associée à des mesures DRIFT *in situ* ont permis de mieux définir le schéma réactionnel et d'identifier CH_3OH comme intermédiaire clé. La distance inter-fonction a été modulée depuis l'échelle millimétrique à atomique notamment à travers des arrangements de lits catalytiques, des dilutions par SiO_2, la préparation de structure cœur coquille MnO_x@SiO_2 possédant une coquille poreuse de SiO_2 d'épaisseur variable. Il a été montré qu'un mélange de MnO_x et SAPO-34 permet d'obtenir une conversion plus élevée que des arrangements de lits. En fait, une intimité élevée permet donc d'améliorer les propriétés catalytiques et l'ajout d'une séparation dense entre les fonctions diminue la conversion et la sélectivité en oléfines. Enfin, Il a été montré qu'une intimité se génère *in situ* à l'échelle des particules primaires de MnO_x et des cristaux de SAPO-34.

Key words : Catalysis, Ox-Zeo, Syngas, Olefin, Intimacy, Core-shell, MnO, SAPO-34